Application of Dynamical System Methods to Galactic Dynamics: from Warps to Double Bars

Patricia Sánchez-Martín

Departament de Matemàtica Aplicada I (UPC)

Dirigida por: Josep J. Masdemont, Mercè Romero-Gómez

Memoria presentada para aspirar al grado
de doctor en Ciencias Matemáticas

Programa de Doctorat de Matemàtica Aplicada
Universitat Politècnica de Catalunya

Barcelona, Mayo del 2015

Abstract

Most galaxies have a warped shape when they are seen from an edge-on point of view. In this work we apply dynamical system methods to find an explanation of this phenomenon that agrees with its abundance among galaxies, its persistence in time and the angular size of observed warps.

Starting from a simple, but realistic, 3D galaxy model formed by a bar and a flat disc, we study the effect produced by a small misalignment between the angular momentum of the system and its angular velocity. To this end, a precession model is developed and considered, assuming that the bar behaves like a rigid body. In order to study the behaviour of the rigid body, we solve its Euler equations. We study the resulting solution in a precessing reference system, selected in such a way to make the angular momentum and angular velocity of the body time independent. After checking that the periodic orbits inside the bar keep being the skeleton of the inner system, even after inflicting a precession to the potential, we compute the invariant manifolds of the unstable periodic orbits departing from the equilibrium points at the ends of the bar to get evidence of their warped shapes. As is well known, from previous studies with 2D galaxy models, the invariant manifolds associated with these periodic orbits drive the arms and rings of barred galaxies and constitute the skeleton of these building blocks. Now, looking at them from an edge-on viewpoint, we find that these manifolds present warped shapes such as those recognized in observations with a close concordance in angles.

In addition, test particle simulations have been performed to determine how the stars are affected by the applied precession, confirming in this way the theoretical results obtained.

Once the behaviour of the precessing model is known, we develop the model with a more complex potential, including a spherical halo, in order to study the influence of each parameter that gives shape to the potential and to determine the effect of the halo in the formation of galaxy warps. We have observed that the presence of the halo helps to increase the resulting warp angle.

The theory of invariant manifolds is also applied to the study of the existence of galaxies with four spiral arms, such as ESO 566-24 and possibly the Milky Way. A double-barred galaxy model is tested as a plausible explanation of the formation of four spiral arms in a galaxy. This is checked through the method of invariant manifolds in various double-barred systems, not restricting ourselves to the Milky Way. We find that

the double-barred model is not sufficient by itself to give rise to the shape of four spiral arms as observed, and we suggest possible refinements of the galaxy model in order to better match the experimental observations.

The most promising of these model refinements is to consider the galaxy as a non-autonomous system, with two bars which are rotating with different pattern speeds. Dealing with non-autonomous systems leads to the study of their dynamics by means of Lagrange Coherent Structures (LCS). This is a recent, still developing theory, in which the LCS behave analogously to the invariant manifolds in autonomous systems, organizing the evolution of the flow. We have developed our own code for the computation of LCS, which can be applied to parametrized surfaces in systems of any dimension. To establish the comparison between LCS and invariant manifolds, we apply both methods to the pendulum problem, in its autonomous and non-autonomous versions. After this, we compute the LCS for our galaxy model formed by a disc and bar, without precession. We demonstrate that the LCS show the same behaviour as the stable invariant manifolds, and that they exhibit more information in a wide region of the space.

Acknowledgements

First and foremost I want to thank my doctoral advisors, Josep J. Masdemont for sharing with me the main idea of this thesis, which I have enjoyed a lot, and for his patience when discussing all the problems that I have found, and Mercè Romero-Gómez for introducing me to the world of astronomy, helping me with all the details I did not know, and for her constant help and support.

I am indebted to all the people from the department of MA1 who have helped me to spend long hours in the university, and to my colleagues for all the entertaining chats together. I want to express my gratitude to Oriol Guasch for his considerable patience in waiting for the completion of this work. Also, I would like to thank Zubin for his great work.

Of course many thanks to my friends, the mathematicians and the not, for the happy days (and nights) we have spent together and for making me laugh at all moments.

Mis padres se merecen una mención especial, por estar siempre ahí, intentando entenderme aunque a veces no fuera fácil, y sobre todo, por su amor. Gracias por todo.

With all of my heart I want to thank Jaume, because he knows what he means for me.

Contents

1 Introduction **1**

1.1 Barred galaxies 6

1.1.1 Identifying the components 6

1.1.2 Periodic orbits as building blocks 8

1.2 Warped galaxies 9

1.3 Thesis outline 11

2 Galaxy models and equations of motion **13**

2.1 Potential-density pairs for barred galaxy models 14

2.1.1 Origin and characteristics of the potentials 16

2.2 Angular momentum and angular velocity of a rigid body 20

2.2.1 The moment of inertia tensor 20

2.2.2 The case of axially symmetric barred galaxies 23

2.3 Equations of motion associated with barred galaxies 32

2.3.1 Zero velocity surfaces and equilibrium points 35

2.4 Lyapunov orbits 38

2.4.1 Invariant manifolds associated to Lyapunov orbits 42

3 The dynamics of the precessing model **45**

3.1 The structure of periodic orbits inside the bar 46

3.1.1 Other family orbits emanating from L_3 51

3.2 Dynamics close to corotation 54
3.2.1 Warp angles 69
3.3 Test particle simulations 72
3.4 The case of the tilted bar model 74

4 The dynamics of the precessing model with halo 83
4.1 Components and description of the model 84
4.2 Characteristics of the model 85
4.3 Dynamics close to corotation 89
4.3.1 Warp angles 93
4.4 The effect of a strong bar in the dynamics close to corotation 94

5 Double-barred systems 101
5.1 Components and description of the model 103
5.2 Equilibrium points for different parameter configurations 104
5.2.1 The role of the semi-minor axis of the main bar 105
5.2.2 The role of the mass ratio between bars 107
5.2.3 The role of the pattern speed 109
5.2.4 The role of density for a fixed separation angle 111
5.3 Dynamics close to corotation 112

6 Towards the non-autonomous problem 119
6.1 Lagrangian Coherent Structures 120
6.2 The computation of Lagrangian Coherent Structures 123
6.2.1 Basic test examples 127
6.3 Lagrangian Coherent Structures in the precessing model 132
6.3.1 Lagrangian Coherent Structures in the non-autonomous case 136

7 Conclusions 145
7.1 Future work 150

Chapter 1

Introduction

For a general vision of galaxies, a first step is trying to understand the different shapes they acquire. Observations made on galaxies (Hubble, 1958) indicate they can be elliptical, spiral, lenticular or irregular. This classification system reflects their composition, mass distribution and kinematics.

The main morphological types are described in Hubble's "tuning-fork" diagram (see Fig. 1.1). Spiral galaxies split up into two families, normal spirals (Sa, Sb and Sc) and barred spirals (SBa, SBb and SBc). From left to right in the tuning-fork diagram, the disc does not exist in elliptical galaxies and becomes important in lenticular and spiral ones gradually, as also does the proportion of gas and young stars.

The progression from left to right in the tuning-fork diagram was originally believed to reflect the life cycle of galaxies, which would evolve from an elliptical origin to a spiral final stage. This evolution paradigm was later disproved, but the terms 'early type' and 'late type' are still used to refer to the position of galaxies to the left or right side of the diagram, even though 'early type' galaxies can be full of old stars, and vice versa.

Elliptical galaxies (E) are seen as more or less flattened ellipses, according to the ratio of the axes which varies from 1 to 3. The ellipticity $\epsilon = (a - b)/a$, where a is the major axis and b the minor one, is in the range $[0, 0.7]$. Thus, ellipticals are classified by an index 10ϵ, from E0 to E7. The most massive galaxies known are the ellipticals, most of which are more luminous than the spirals. However, elliptical galaxies do not have a specific substructure, since their luminosity decreases very regularly from centre to edge.

Spiral galaxies (S) have spiral arms that wind around in a thin disc, and meet towards the central bulge. This bulge is the brightest component and its shape is ellipsoidal and less flattened than the disc. Hubble's classification of spiral galaxies depends mainly on three

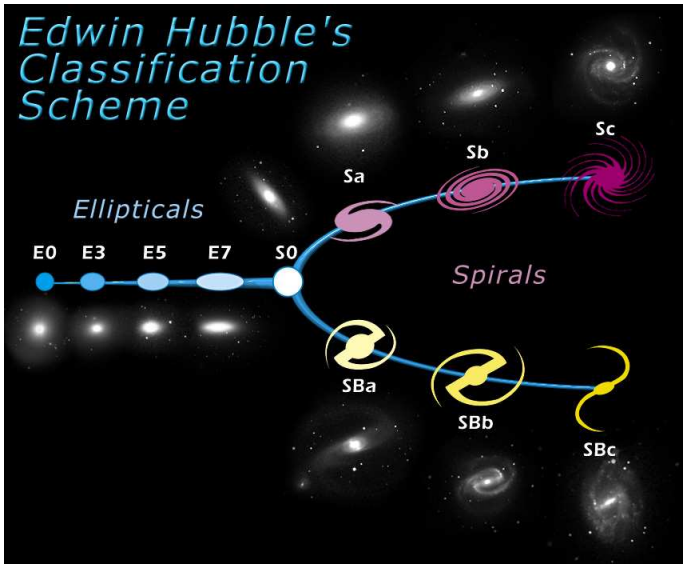

Figure 1.1: The main morphological types of galaxies represented by Hubble in the "tuning-fork" diagram.

parameters: first, the size of the bulge relative to the disc length; second, the tightness of the winding of the spiral arms; finally, the degree of resolution of the disc into stars is considered. In this classification, spirals are denoted by the letter S followed by a, b or c subdivisions for galaxies with big bulges and tight arms down to galaxies with small bulges and more open arms.

In addition, Hubble separates some spiral galaxies which have bar-shaped stellar configurations, where the nucleus is crossed by a bar of stars at the ends of which the spiral arms begin. The bar rotates like a solid rigid, maintaining its shape as the stars orbit the galactic center. To distinguish these galaxies from the non-barred spiral galaxies, he called them SB, with a similar subdivision as for the non-barred galaxies.

De Vaucouleurs (1959) expanded and supplemented the Hubble classification system. He also defines the irregular galaxies, which do not have well-defined structures, with no nucleus, no disc and no spiral arms, but containing much gas.

The lenticular galaxies (S0) are the intermediate ones placed between ellipticals and spirals. They have a large central bulge and a flattened disc of stars. The disc differentiates the lenticular galaxies from the ellipticals, but they do not contain spiral arms nor gas or dust.

Moreover, galaxies are inclined with respect to our line-of-sight, acquiring a different shape depending on the view point. This inclination is the angle between the disc and the

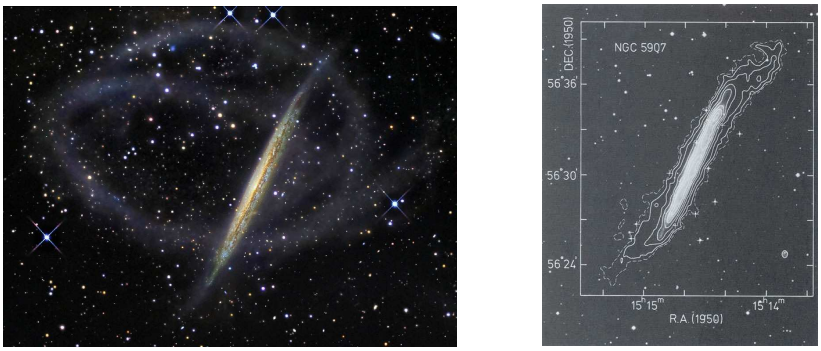

Figure 1.2: Warped galaxy NGC 5907 and its HI warp as observed by Sancisi (1976) with the Westerbork Synthesis Radio Telescope.

perpendicular plane to our line-of-sight, calling *edge-on* to galaxies with 90° of inclination and *face-on* those with 0°.

Due to the fact that generally we can only see a galaxy from a single view point, warped galaxies have been detected when they are seen edge-on. These are galaxies whose outer parts are not aligned with the inner plane of the disc. As with galaxies, warps are classified by its shape. The S-shaped or grand-design warps, in which the surface of the galaxy takes the shape of an integral sign rising in one side and symmetrically descending on the other. The U-shaped warps, where the two sides rise symmetrically, which is generally related to a large asymmetry parameter suggesting that dust is hiding the far side of the galaxy (Reshetnikov & Combes, 1998). In addition, Sánchez-Saavedra et al. (2003), García-Ruiz et al. (2002) introduced L-shaped or lopsided warps, where only one side is warped.

As is detailed in Giovanelli & Haynes (1988), warps are commonly studied through the distribution of neutral hydrogen (HI), which in the outer regions of galaxies tends to follow a curved surface instead of the flatness seen in the inner regions. It is well known that the Milky Way displays a clear warp, which was long attributed to a close tidal interaction with the Magellanic Clouds. However, warped galaxies are a common phenomenon, as a large fraction of the edge-on galaxies where HI distribution has been studied present a warped shape. Figure 1.2 shows the warped galaxy NGC 5907 (left), whose warp is clearly visible in the HI distribution (right), and which has no visible nearby neighbour that could produce perturbations. Figure 1.3 presents the galaxies NGC 4565 and NGC 7814 where a slight warp is observed in the stellar disc.

In addition, if the discs are face-on, warped galaxies can also be detected by the characteristics of the rotation velocity fields. Namely, deviations from circular rotation, related with the gas in warps, are marked in isovelocity contour maps. These are called

Figure 1.3: Warped galaxies NGC 4565 and NGC 7814 (images taken from SDSS).

kinematic warps. Figure 1.4 presents the isovelocity contour maps of several galaxies, some of them warped. For example, in galaxy M83 (top left part of the panel) we observe a change in the inclination of the warp reproducing a S-shaped warp. This fact is also observed in NGC 5055 (middle left part of the panel), but less remarked. The most detailed warp seen kinematically is possibly in the galaxy M31 (bottom left part), which is not a typical warp due to the higher inclination of the disc (about 77°). Therefore, the velocity fields show that a warp is a perturbation which affects the outer regions of the disc.

In order to understand the observations and the above classification, galactic shapes have been studied by means of two main methods: the qualitative method (periodic orbits, invariant manifolds and density waves) and the quantitative method (test particle simulations and self-consistent N-body simulations). Even though test particle simulations can provide real time information of the potential and morphology of the galaxy, analytical models allow us to study in detail the building blocks of the potential.

Our thesis is devoted to the study of S-shaped warps in barred galaxies, and we use a standard analytical model that describes them. Its potentials determine equations of motion and vector fields that have been taken up to the present as time-independent fields (autonomous problem). In addition, the present work introduces the non-autonomous problem in the study of the analytical model.

The autonomous problem has been extensively studied, analyzing the periodic orbits of the system. For example, in Athanassoula (1992), there is a complete study of the periodic orbits in a standard barred galaxy potential which we will use in our work. Former studies, e.g. Pfenniger (1984), Contopoulos (1980), compute the families of periodic orbits around the central equilibrium point. These are mainly stable, which is important for the structure of the bar. The periodic orbits of the equilibrium points located at the end of

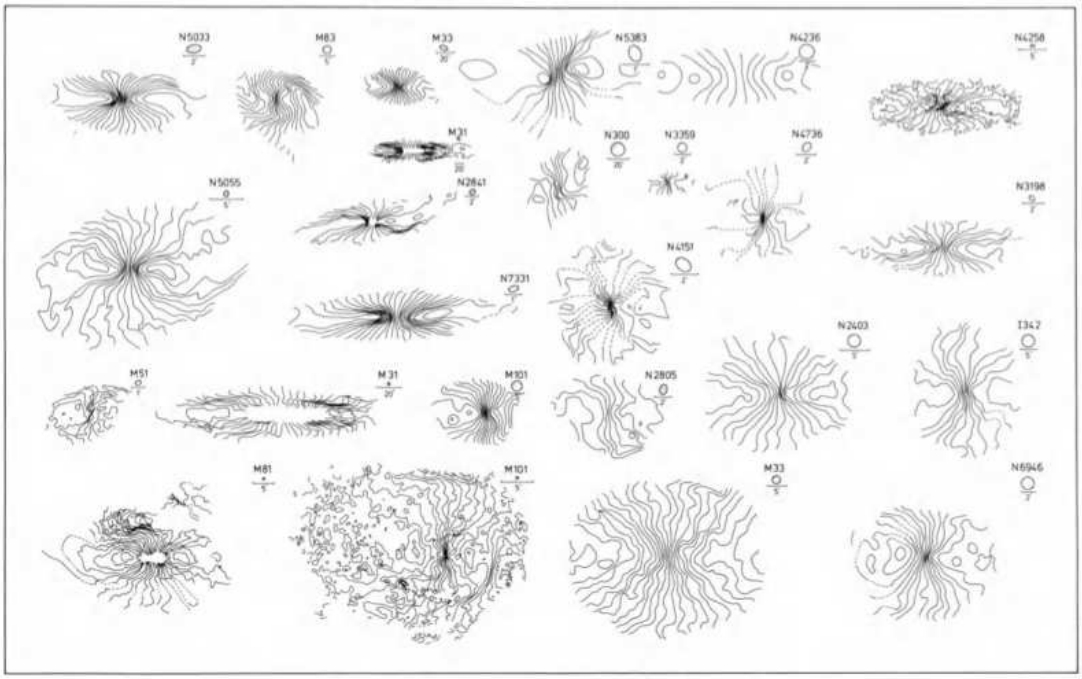

Figure 1.4: Selection of velocity fields of spiral galaxies, assembled by Bosma (1981).

the bar are unstable for a long energy range and this is why they were not considered physically important, until Romero-Gómez et al. (2006, 2007), Athanassoula et al. (2009) introduce a different approach to the study of spiral arms and rings in barred galaxies. They claim that these are results of the orbital motion driven by the invariant manifolds associated to periodic orbits around the unstable equilibrium points. This idea came from celestial mechanics, at Gómez et al. (2004), where dynamical system theory, in particular the invariant manifolds of periodic orbits, was applied to the restricted three body problem in order to study the design of low cost orbits.

On the other hand, the non-autonomous problem has been sparsely studied from an analytical view point. The approach to develop the non-autonomous problem in this work is to study the Lagrangian Coherent Structures (LCS), hitherto used in problems of fluid flows and in instances of the three body problem to identify transport barriers in time-dependent velocity fields, in order to analyze the dynamics of the galaxy in time-dependent models.

1.1 Barred galaxies

The central part of this thesis focuses on the formation of warps in barred galaxies. In this section we shall just discuss their main features and detection procedures. For a further review we refer to Combes et al. (1995), Sparke & Gallagher (2000), Binney & Tremaine (2008).

Barred galaxies are very common, but the fraction of disc galaxies that are barred varies with the selection criterion. Optical observation is still the most reliable detection method. It shows that about 30 per cent of spiral galaxies are strongly barred, but this fraction increases to 50 per cent at least if weak bars are included. Bars appear still more prominently in near infrared images, Eskridge et al. (2000) found in a sample of 186 spiral galaxies observed in the near infrared that 56% of them are strongly barred, while an additional 6% are weakly barred; only 27% can be classified as non-barred.

In the case of warped galaxies, these statistics have to be assumed because warps become visible only when the galaxy is seen edge-on, which makes the bar difficult to detect.

Bars can be biaxially or triaxially structured, so we consider them as ellipsoids with two or three different axes. In the galactic plane their axial ratio is about 2.5 to 5, and in the perpendicular direction they are flattened systems, but it is plausible that the two minor axes are similar since when the galaxy is seen edge-on the bar is difficult to spot. There are central bulges that are seen edge-on, usually boxy or "peanut-shaped", for which there is good evidence that they are really bars seen at an inclination of 90°.

The bar structure behaves differently than the spiral arms, in the sense that for example a bar can persist even if the disc is empty of gas. As the spiral part, the bar is not static, but rotates with a pattern speed Ω. Stars and gas no longer follow near-circular paths inside the bar, but they stay close to orbits that close on themselves as seen by an observer moving with the rotation of the bar. Within the corotation radius a family of closed orbits appear, which line up with the long axis of the bar. In a stable bar, most of the stars remain near these orbits, and outside the corotation radius all the closed orbits lie perpendicular to the bar. For this reason, it is likely that bars rotate slowly enough so that corotation falls beyond the end of the bar.

1.1.1 Identifying the components

The detection of the components of a galaxy becomes more complicated as the galaxy is more complex. The existence of the basic components, such as bars, discs or bulges,

has been established through surface photometry and luminosity distributions. Since the mass luminosity ratio varies from the centre to the edge of galaxies, kinematic observations become also necessary to determine the mass distribution of galaxies.

Barred galaxies are composed by a flattened disc that extends to a large distance from the centre, a bar in the central part and maybe a bulge. This bulge closely resembles an elliptical galaxy, they are similar in terms of morphology, luminosity profile and colour, but some characteristics difference them from ellipticals: the rotation speed is greater for bulges than for elliptical galaxies, as the luminosity profiles are equally represented along the major axis but not along the minor one. In addition, the bulges have a smaller surface luminosity and a greater characteristic radius, and they are usually more flattened than elliptical galaxies.

The surface brightness of the disc obeys the exponential law (de Jong, 1996)

$$I(r) = I_0 e^{-r/r_0},$$

where I_0 is the luminosity extrapolated to the centre and r_0 the characteristic radius. However, the distribution of light in the disc depends on the model selected for the bulge, and this analysis is only certain when the bulge does not dominate the luminosity. Other factors, such as spiral arms and bars, contribute to the difficulty of analyzing the luminosity and give rise to many exceptions to the exponential law.

The age of the stars which constitute galaxies also helps to determine the structure of galaxies. The idea of classifying stars into populations was introduced by Baade in 1940. He distinguishes between population I, where the most luminous stars are blue, very hot, massive and young, and population II where they are cool, red, giant and very old. This classification has been refined and now there are five types depending on star temperature, luminosity and metallicity.

Moreover, every star has a specific colour according to its spectral type, determined by the nature of the lines appearing in its spectrum, its mass and age. This photometry gives information about the stellar populations, star formation and evolution of galaxies. The colours are defined in the standard UBV photometric system, where U represents the magnitude in the ultraviolet, B in the blue and V is the visible magnitude. The effects of evolution can be detected with this photometry, since for example irregular galaxies are the least evolved systems and they appear in blue, while elliptical galaxies are composed almost entirely of old red stars.

1.1.2 Periodic orbits as building blocks

Periodic orbits inside the bar have been widely studied, proving that they behave as the blocks which are responsible for the bar structure and constitute its backbone, and answering a great number of questions. For instance, in Contopoulos (1981), Athanassoula et al. (1983) the authors study a series of periodic orbits according to their energy and thus to the distance from the centre.

Papayannopoulos & Petrou (1983) explored the families of orbits perpendicular to the bar and classified them in order to obtain the main features of an inhomogeneous ellipsoidal bar. Their results agree with the research of Contopoulos (1980), who studied how far bars extend in terms of the resonances in the rotation curve.

Athanassoula et al. (1983) compute the main families of periodic orbits inside the corotation radius. They study the individual orbits in a realistic bar potential in order to characterize the morphology and features of barred galaxies. They assert that families of periodic orbits are the backbone of all their orbital structure. If they are stable they are followed by quasi-periodic orbits, while if, on the contrary, they are unstable they detonate in chaotic motion. Skokos et al. (2002) study the morphology of three dimensional bars and find all families of periodic orbits, either two dimensional or three dimensional, around the stable Lagrangian points.

We shall summarize the families obtained in the above studies. Let us suppose that the bar is realized as a symmetric gravitational potential which rotates in the galaxy at a pattern speed. In this system five stationary points appear, L_1 to L_5, called Lagrangian points. In the next chapter we explain in depth the characteristics of these points, but now we just place them into the model. The points L_1 and L_2 are in the ends of the bar, L_3 is in its centre, and L_4 and L_5 are placed perpendicularly to the bar (left part of Fig. 1.5). The four points L_1, L_2, L_4 and L_5 correspond to the corotation, delimiting a region called the corotation zone.

There are several families of periodic orbits along the bar which give structure to it (right part of Fig. 1.5). Close to the centre, the x_1 family is found. This family is formed at low energies by elongated orbits, parallel to the bar. There also exists a x_4 family of retrograde orbits which is sparsely populated in spiral galaxies. The x_2 family is a set of elongated orbits perpendicular to the bar, and stable. There is also a set of orbits of the same type as x_2 but unstable, they are the x_3 family.

But, if we take a bar with practically no axisymmetric component, the x_2 family disappears. The extinction of this family depends on the angular velocity of the bar, at lower velocity the bar must be less axisymmetric.

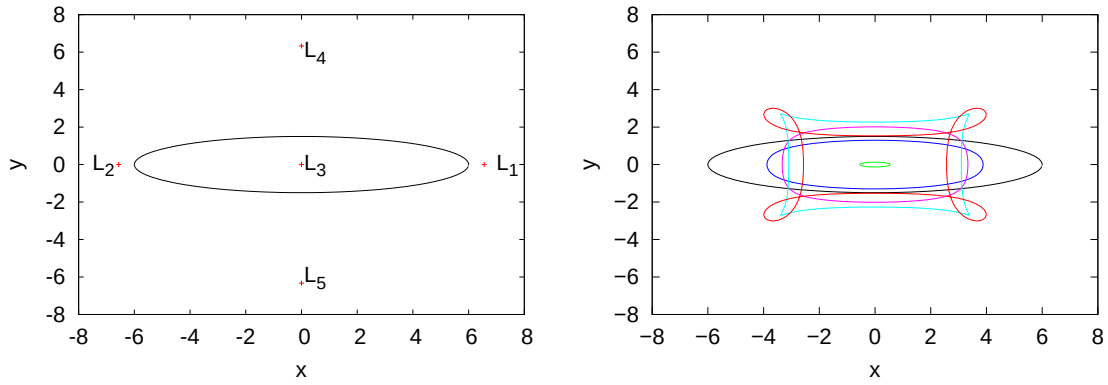

Figure 1.5: Left: Position of the Lagrangian points in a bar potential. Right: Representative periodic orbits inside the bar.

Before corotation we find elongated orbits of the x_1 family parallel to the bar, but they have lobes at their limits. These orbits then become rounder, having more complex forms near corotation. Also there exist families of periodic orbits at corotation, enveloping the Lagrangian points L_4 and L_5, so they do not revolve around the centre.

Therefore, all of these families of orbits do not construct the bar, although some of them are important to it. The orbits of the x_1 family, which are aligned parallel to the bar, spend most of their time in the potential well of the bar and amplify it. But the x_2 family is perpendicular to the bar and tends to weaken and even destroy it if the angular velocity is small.

1.2 Warped galaxies

The main goal in our work is to study the formation of warps observed in some galaxies when seen edge-on. Thanks to the images of the Hubble Space Telescope and taking into account the probability of non-detection of warps when the line of nodes lies in the plane of the sky, it has been observed that nearly all galaxies are warped, confirming the suggestion made by Bosma (1981) for HI warps (Sánchez-Saavedra et al., 2003). Although there is abundant literature about this subject, the reason for these warps is not known yet. They have been observed in the distribution of stars (e.g. Sanchez-Saavedra et al. (1990)) and in the study of neutral hydrogen (Bosma, 1981), confirming that it is a very common phenomenon. In general, warps are viewed commonly as an integral sign as seen edge-on, manifesting themselves in the shape of the outer disc bending away from the plane defined by the inner disc (like the galaxy shown in Fig. 1.6). This could suggest that

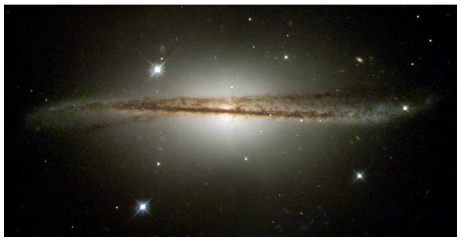

Figure 1.6: Galaxy ESO 510-G13 photographed by Hubble telescope.

the angular momentum of some material in warps is misaligned with that of material in the inner disc. In this direction, Debattista & Sellwood (1999) make simulations in which the warp is formed when a misalignment between the angular momenta of the disc and the halo occurs.

Several assumptions have been made in the literature about the formation of warps. Briggs (1990) establishes some rules based on observational studies in external galaxies to determine the behaviour of galactic warps, telling us that warps appear from isophotal radius $R_{26.5}$. After that, Cox et al. (1996) studied the observations of the galaxy UGC 7170 concluding that due to the similarities between the stellar and gaseous warps, these could be produced by means of a gravitational origin. And more recently, Sellwood (2013) determines that because of warps being really common, they are either repeatedly regenerated or long-lived.

From a theoretical viewpoint, numerous approaches have been made to understand the mechanisms responsible for warp generation. One of these mechanisms, explained in Lynden-Bell (1965), proposes that warps could be produced by internal bending modes in the disc as a long-lived phenomenon, but this proposal held only in a disc with an unrealistic mass truncation (Hunter & Toomre, 1969). In this context, Sparke & Casertano (1988) found warp modes inside rigid halos by means of discrete modes of bending. In Revaz & Pfenniger (2004) this discussion has been revived by identifying short-lived bending instabilities as a possible cause of the formation of warps obtaining, however, warp angles of less than 5°. Nevertheless, Binney et al. (1998) argued that the inner halo would realign with the disc, and so the warp would dissipate.

Another possible explanation for the existence of warps is a tidal interaction between galaxies, this theory has been studied to explain the Milky Way's warp mainly, because of the proximity of the Large Magellanic Clouds (see e.g. Levine et al., 2006). Nevertheless, in López-Corredoira et al. (2002) a method to calculate the amplitude of the galactic warp generated by a torque due to external forces is developed, and applied to discard the tidal theory because it would lead to the formation of warps of very low amplitude. In fact,

the authors propose that the warp is formed due to the accretion of material over the disc (i.e. the accretion of angular momentum). Read et al. (2008) agree that the warp is an indicator of the merger activity. If the impact angle is larger than 20°, the stellar disc can be warped.

As we can observe, the explanation of why warped galaxies exist represents a challenge. Our approach is based on the fact that warps are long-lived and, by means of dynamical system tools, we use a simple but widely used model to show that introducing a natural misalignment between the angular momentum and the angular velocity, the resulting model is consistent and it is able to reproduce warped shapes. To check its consistency, we apply the fact that the periodic orbits are the backbone of galactic bars (Athanassoula et al., 1983) since these orbits are mainly stable, and therefore they mostly determine the structure of the bar. We then study the set of orbits that depart from the Lyapunov orbits, proving that they acquire the form of warps with varying angles. The line of our study follows the analysis of the invariant objects which cause in a similar dynamic way the formation of rings and spiral arms in barred galaxies (Romero-Gómez et al., 2006, 2007, Athanassoula et al., 2009). Again the purpose is to use the invariant manifolds associated to these objects and how they are affected by a precessing model to explain the apparition of galactic warps. Since invariant manifolds are determined by the potential of the galaxy, they exist for as long as this potential does not change significantly and thus they are long-lived objects.

1.3 Thesis outline

The work in this thesis is developed as follows. In Chapter 2 we justify the consistency of the misalignment between the angular momentum vector and the angular velocity vector and we derive the equations of motion of the precessing model. We also describe the galactic potential used and the characteristics of the potential under the precessing model. In Chapter 3 we use a model composed by a bar and a disc to describe the types of orbits inside the bar, observe how they are modified with the tilt angle and check that they are the skeleton of the model. The formation of warps through our model also is described in this chapter, where we study the invariant manifolds of the system. In addition we perform test-particle simulations of the model which, although they are collisionless simulations, serve to demonstrate that the model behaves as we have predicted. In Chapter 4 we add to the previous model a halo to confirm the results obtained, we compare the results obtained in the two models and analyze the warps reached with the invariant manifolds. We claim that warps are formed with our model independently of the potentials used and observe

that the halo favours higher warp angles. In Chapter 5 we apply the theory of invariant manifolds to four-armed galaxies, studying whether it is plausible that a model with two bars makes this type of galaxy appear. The results are not convincing and we come to the conclusion that, at least, a more complex potential with outer spiral arms is needed. Chapter 6 is centered in the study of the non-autonomous version of the precessing model by means of the Lagrangian Coherent Structures (LCS), finding that LCS describe the motion of the problem in a similar way as the invariant manifolds in the autonomous case. Our conclusions and expectations for future work are described in Chapter 7.

Chapter 2

Galaxy models and equations of motion

In principle, to compute the potential of a big set of stars it would be enough to add the point-mass potentials of all the stars in the set. But, actually, this is not possible because of the number of stars of a typical galaxy. For that, in most of cases, it is sufficient to model the potential by smoothing the mass density in stars on a scale that is small compared to the size of the galaxy, but large compared to the mean distance between stars.

In the literature one can find several potential-density pairs to model the main components of a galaxy. It is well-known that disc galaxies are made of different morphological components such as a disc and, occasionally, a bulge, a lens, a bar, inner rings, outer rings, and spiral arms. In our work we consider barred galaxies. They contain a disc and may have also a bulge, but their special feature is the non-axisymmetric component with a bar shape in the central part. These components are described in Binney & Tremaine (2008), but here we show the potentials that we use in order to describe the galaxy model of our work.

Our study is based in the use of analytical potentials to describe each of the main components of a barred galaxy: the bar, the disc and a spheroid to model the halo. Since we integrate the equations of motion to investigate the orbital structure, we need the expanded form of the potentials, including its first and second derivatives.

2.1 Potential-density pairs for barred galaxy models

In Chapter 3, as in Romero-Gómez et al. (2006), we essentially consider the same potential as in Pfenniger (1984), consisting in two components. We assume that the barred galaxies we want to study have a bar and a disc. The disc component is modelled by a Miyamoto-Nagai potential (Miyamoto & Nagai, 1975),

$$\phi_d = -\frac{GM_d}{\sqrt{R^2 + (A + \sqrt{B^2 + z^2})^2}}\,, \tag{2.1}$$

where $R^2 = x^2 + y^2$ is the cylindrical coordinate radius in the disc plane, and z denotes the distance in the out-of-plane component. The parameter G is the gravitational constant and M_d is the mass of the disc. The parameters A and B characterize the shape of the disc. Parameter A measures the radial scale length of the disc while B is a measure of the disc thickness in the z direction. Since galactic discs are larger in the radial direction than in the vertical one, in our models A is greater than B.

By means of Poisson's equation, $\nabla^2\phi = 4\pi G\rho$, we obtain the density of the disc potential

$$\rho_d(R,z) = \left(\frac{B^2 M_d}{4\pi}\right) \frac{AR^2 + (A + 3\sqrt{z^2 + B^2})(A + \sqrt{z^2 + B^2})^2}{\left[R^2 + (A + \sqrt{z^2 + B^2})^2\right]^{5/2} (z^2 + B^2)^{3/2}}\,. \tag{2.2}$$

From this equation, we can deduce that close enough to the center ($R = 0$, $z = 0$) the density is almost constant (see Fig. 2.1). Equation (2.1) shows that at very large values of R and $|z|$, the potential becomes similar to that of a point mass. The dependence of the potential on the two constants A and B may be inferred from the two limiting cases. If $A = 0$ then this density-potential pair becomes the case known as the Plummer potential, in which the axial symmetry is changed to the spherical one. On the other hand, if $B = 0$ the pair becomes Kuzmin-Toomre case, for which the system has a collapse so that the density dependence on z follows the Dirac delta function. Therefore, the ratio A/B regulates the flattening of the system, from zero (no flattening) to infinity (collapse into the plane of symmetry).

The barlike component of the galaxy is modelled by a Ferrers ellipsoid (Ferrers, 1877), which is a realistic model where the bar is described as a finite homogeneous ellipsoid with density function

$$\rho = \begin{cases} \rho_0(1 - m^2)^{n_h}, & m \leq 1\,, \\ 0, & m > 1\,, \end{cases} \tag{2.3}$$

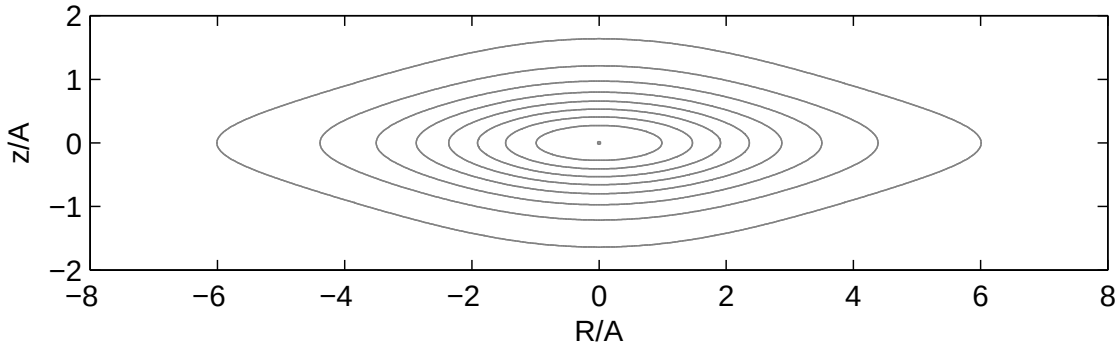

Figure 2.1: Isodensity curves of the Miyamoto-Nagai disc.

where $m^2 = x^2/a^2 + y^2/b^2 + z^2/c^2$, the parameters a (semi-major axis), b (intermediate axis), c (semi-minor axis) determine the shape of the bar, and the parameter n_h determines the homogeneity degree for the mass distribution. The parameter ρ_0 is the density at the origin and, thus, depends on the degree of homogeneity n_h selected. The Ferrers potential agrees fairly well with observations of barred galaxies and N-body simulations. For $n_h = 0$ the bar is completely homogeneous, whereas if $n_h = 1$ the bar has an inhomogeneous mass distribution. For higher values of n_h the density falls off sharply and the gravitational potential becomes a polynomial of higher, even degree on the coordinates. Since we are interested in a bar that ends sharply, which fits with observations as we detail in the next subsection 2.1.1, we choose $n_h = 2$ for our computations.

The density at the origin ρ_0 is related to the bar mass, determining the density distribution function. The mass of the bar is defined for a general case as:

$$M_b = 8\int_0^{2\pi}\int_0^{2\pi}\int_0^1 abcr^2\sin(\theta)\rho_0(1-m^2)^{n_h}drd\theta d\phi = 2^{2n_h+3}\pi abc\frac{\Gamma(n_h+1)\Gamma(n_h+2)}{\Gamma(2n_h+4)}, \tag{2.4}$$

where Γ is the Euler Gamma function. Therefore, setting the mass to be M_b the density at the origin depending on n_h is:

$$n_h = 0 \Rightarrow \rho_0 = \frac{3}{4}\frac{M_b}{\pi abc}; \quad n_h = 1 \Rightarrow \rho_0 = \frac{15}{8}\frac{M_b}{\pi abc}; \quad n_h = 2 \Rightarrow \rho_0 = \frac{105}{32}\frac{M_b}{\pi abc} \tag{2.5}$$

Again, the density of the bar potential is related with its potential, ϕ_b, by means of the Poisson equation ($\nabla^2\phi = 4\pi G\rho$):

$$\phi_b = -\pi\, G\, abc\frac{\rho_0}{n_h+1}\int_\lambda^\infty \frac{du}{\sqrt{\Delta(u)}}(1-m^2(u))^{(n_h+1)}, \tag{2.6}$$

where G is the gravitational constant, $\Delta(u) = (a^2+u)(b^2+u)(c^2+u)$ and λ the unique positive solution of $m^2(\lambda) = 1$ if $m \geq 1$, (that is, if the particle lies outside the bar), and zero otherwise.

Another special feature of barred galaxies is a bulge or spheroid. In Chapter 4 we add to the above model a Plummer spheroid in order to introduce dark matter in the galaxy since, as we explain later, the rotation curve of the system is normally nearly flat due to the presence of dark mass. The analytical potential of the spheroid has the characteristic of being a spherical distribution of matter with high densities at the centre and decreasing fast when the radius increases. This model, as we have mentioned before, has a potential of the form:

$$\phi_p = -\frac{GM}{\sqrt{r^2+b^2}}, \tag{2.7}$$

where b characterises the radial scale length of the spheroid and M its mass. This potential was used by Plummer in 1911 to fit observations of globular clusters. From Poisson's equation, we obtain the density distribution of the Plummer spheroid,

$$\rho_p(r) = \frac{3M}{4\pi b^3}\left(1+\frac{r^2}{b^2}\right)^{-5/2}. \tag{2.8}$$

2.1.1 Origin and characteristics of the potentials

We have just defined the analytical potentials used in our models to describe the morphological components of galaxies. But, since these potentials do not have simple equations, let us explain how they have been obtained (following Binney & Tremaine (2008)).

Let us start by the easier components such as the disc and bulge. As we have been able to appreciate, the Miyamoto-Nagai potential is a combination of the Plummer and the Kuzmin-Toomre models. A region R with density ρ induces a gravitational potential

$$\phi(x) = -G\int_R \frac{\rho(x')}{|x'-x|}\,dx'. \tag{2.9}$$

By Newton's first and second theorems, the gravitational attraction of a spherically symmetric density distribution $\rho(r')$ on a unit mass is

$$\mathbf{F}(r) = -\frac{GM(r)}{r^2}\hat{\mathbf{e}}_{\mathbf{r}}, \tag{2.10}$$

being r the distance from the mass to the centre of the sphere, and

$$M(r) = 4\pi\int_0^r r'^2\rho(r')\,dr' \tag{2.11}$$

is the mass of the sphere up to radius r.

We can think of the total gravitational potential of a spherically symmetric density distribution as the sum of the potentials of spherical shells of mass $dM(r) = 4\pi\rho(r)r^2dr$.

In this way, we obtain the potential at distance r

$$\phi(r) = -\frac{G}{r}\int_0^r dM(r') - G\int_r^\infty \frac{dM(r')}{r'} \tag{2.12}$$

where the two parts of the equation are produced by shells with $r' < r$ and with $r' > r$, respectively.

We can observe that this last equation gives the potential of a symmetric spherical system as a function of the mass or density distribution. From this equation, we may obtain the Plummer potential since it has to be proportional to $r^2 + cte$ at small radii and to r^{-1} at large radii. And, in the same manner, the Miyamoto-Nagai potential is obtained considering that it represents domains varying from an infinitesimally thin disk to a spherical system.

On the other hand, note that equation 2.12 is reversible taking into account Poisson's equation, $\nabla^2\phi = 4\pi G\rho$, which yields the density distribution of a system from its potential.

Regarding the Ferrers bar, the way to obtain it is more complicated since the bar part is a non-axisymmetric potential. We make here a brief explanation on how to obtain it, but for more details we refer to Binney & Tremaine (2008). Assuming that the isodensity surfaces in an ellipsoid are similar, we could define its gravitational potential breaking the body down into thin triaxial ellipsoidal shells. So, in a body in which $\rho = \rho(\mu)$, where $\mu = m^2$,

$$\phi(x) = -\pi G\,\frac{b\,c}{a}\int_0^\infty d\tau \frac{\psi(\infty) - \psi(am)}{\sqrt{(\tau + a^2)(\tau + b^2)(\tau + c^2)}} \tag{2.13}$$

being $m \equiv m(\mathbf{x}, \tau)$ defined by

$$m^2 = \frac{x^2}{a^2 + \tau} + \frac{y^2}{b^2 + \tau} + \frac{z^2}{c^2 + \tau} \tag{2.14}$$

where $\tau \geq 0$ labels the surfaces of the ellipsoid. And $\psi(m)$ is defined as

$$\psi(m) = \int_0^{m^2} \rho(\mu')\, d\mu'. \tag{2.15}$$

Once we get this formula, it is easy to observe that if we apply the density distribution of the Ferrers ellipsoid, we obtain equation 2.6. This density distribution has been chosen because of the main features of the galaxy bars which have been widely observed (Lynden-Bell, 1979, Miller & Smith, 1979, Athanassoula & Martinet, 1980, Contopoulos, 1980, Sellwood, 1980, 1981, Combes & Sanders, 1981, Kormendy, 1982, van Albada & Sanders, 1982, Duval & Athanassoula, 1983), and the Ferrers bar is the one that best fits their characteristics:

- Bars are centrally condensed, extend up to about corotation and end sharply.

- They rotate fast.
- The volume of the bar extends over the rising or linear part of the rotation curve.
- The mass of bars typically ranges around 1/4 of the mass of the disc of the same extension.
- The horizontal axis ratio a/b of bars is in the range 3-5.
- The vertical axis ratio a/c is around 10.

The corotation radius, r_L, is defined as the distance from the centre to the Lagrangian equilibrium point L_1 (or L_2). This corotation radius is the radius at which a star can move on a circular orbit at the same angular frequency as the pattern speed Ω of the bar. In addition, the pattern speed is related to r_L through the expression $\Omega^2 = r_L \left(\frac{\partial\phi(r)}{\partial r}\right)_{|\, r_L}$ where $\phi(r)$ is the potential on the equatorial plane.

Lastly, an important property in the study of the matter distribution in potential models is the rotation curve or circular-speed $v_{rot}(r)$, defined as the speed of a particle of negligible mass in a circular orbit at radius r. For a potential $\phi(r)$, we define v_{rot} as

$$v_{rot}^2 = r\frac{d\phi}{dr}\,. \tag{2.16}$$

This circular speed measures the mass interior to r. In addition, the circular frequency is the associated angular frequency defined by

$$\omega = \frac{v_{rot}}{r}\,. \tag{2.17}$$

And the escape speed v_e measures the speed at which a star can escape from the gravitational field,

$$v_e(r) = \sqrt{2|\phi(r)|}\,. \tag{2.18}$$

Rotation curves are the primary tool for determining the dynamical mass distribution in spiral galaxies. They have played a key role in the evidence that galaxies have a great amount of dark matter. Figure 2.2 shows different rotation curves obtained for spiral galaxies, which were obtained from the emission lines of ionized gas. The main feature of these rotation curves is that they climb rapidly towards a maximal value, and then become flat as far as they have been determined by observations.

It follows from observations that most spiral galaxies have a nearly flat rotation curve. It is remarkable that the rotation curves still remain flat even at radii well beyond the outer edge of the visible galaxy, thus implying the presence of invisible or dark mass

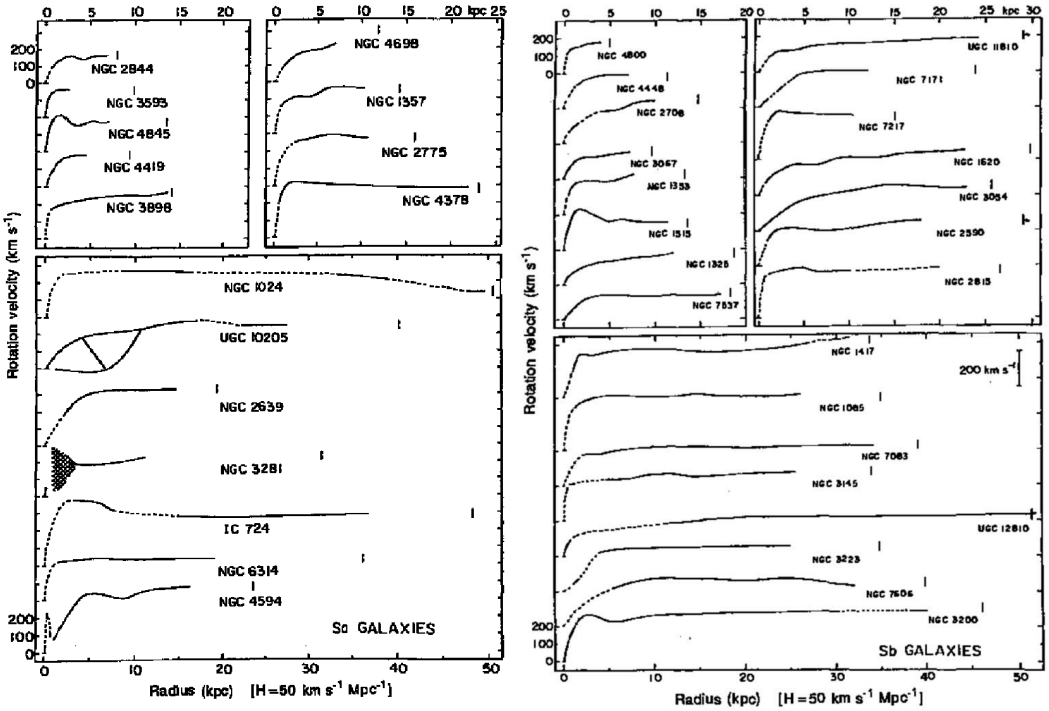

Figure 2.2: Rotation curves for spiral galaxies of type Sa and Sb. Image taken from Rubin et al. (1985).

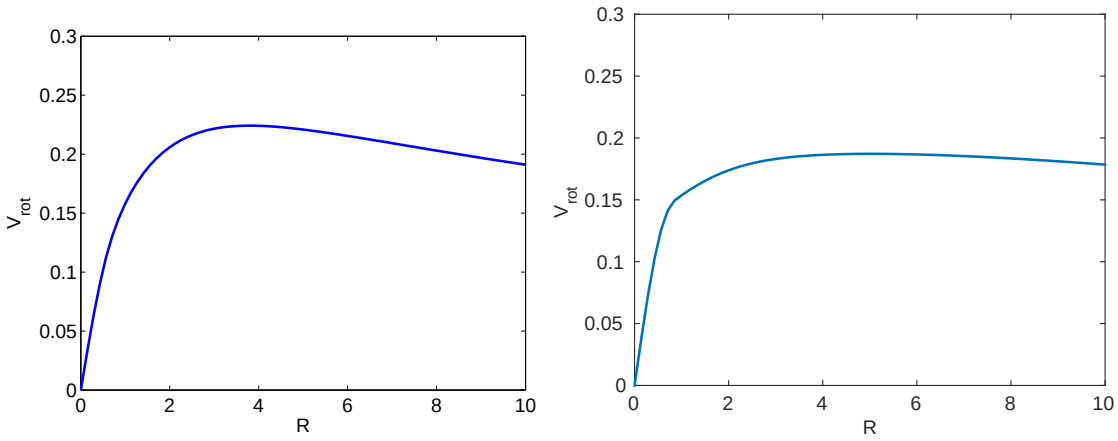

Figure 2.3: Rotation curve of the potential. Left: $\phi = \phi_{bar} + \phi_{disc}$. Right: $\phi = \phi_{bar} + \phi_{disc} + \phi_{bulge}$.

in the outer parts of the galaxy. In our first model, composed by a Ferrers bar and a Miyamoto-Nagai disc, although we have not imposed a halo potential, the rotation curve of the system is rather flat in the outer parts (see left part of Fig. 2.3). On the contrary, when we add a Plummer bulge to the first model, which performs as dark matter, we observe that the rotation curve remains flat up to a radius of 20 kpc (see right part of Fig. 2.3).

2.2 Angular momentum and angular velocity of a rigid body

2.2.1 The moment of inertia tensor

Before explaining how we have modelled the movement of our system it is necessary to clarify some preliminary concepts. The moment of inertia tensor characterizes rotation, in the sense that two bodies with totally different shapes, but having the same inertia tensor, have identical rotational dynamics. We treat the bar of our galaxy system as a rigid body, in order to apply a usual simplification for a rigid body motion. This is, the separation of the rotational degrees of freedom from those of the center of mass motion, with respect to which the body behaves like a point with all of its mass located at the center of mass. The inertia tensor gives us a relation between the angular velocity $\boldsymbol{\omega}$ and the angular momentum $\mathbf{L}$. Both vectors are proportional in magnitude but in general point out to different directions. The alignment of the angular momentum and the angular velocity would be assured only in the case that the rigid body had a spherical symmetry with uniform density. But, in our theory, the rigid body is the bar, which is an ellipsoid, therefore a misalignment between the angular momentum and the angular velocity is produced provided that the rotation axis is not any of the main axes of the bar.

Let us proceed now to describe the construction of our model. First of all, let us recall that for a rigid body B with density ρ, the kinetic energy in inertial coordinates (X, Y, Z) is given by

$$T = \frac{1}{2} \int_B \rho v^2, \tag{2.19}$$

where $v = ||\mathbf{v}(X, Y, Z)||$ is the pointwise speed in inertial coordinates.

If we choose the origin in body coordinates to be the center of mass (see Fig. 2.4), the kinetic energy divides into $T = T_{trans} + T_{rot}$, where the first term is the translational kinetic energy and the second term is the kinetic energy associated with the rotation. Actually, we are only interested in the motion of the body about the center of mass for

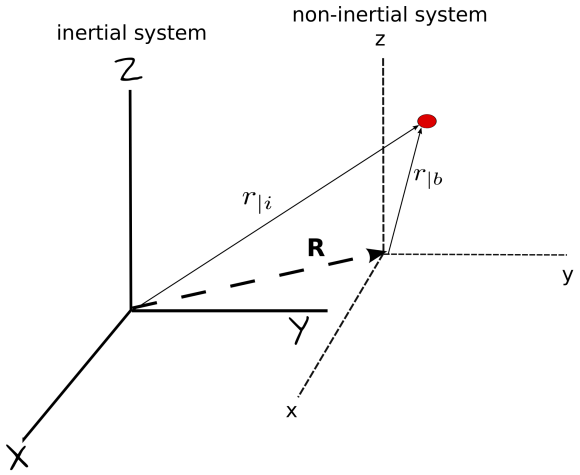

Figure 2.4: Change of coordinates between the inertial and non-inertial system.

our problem, i.e. in T_{rot}. This rotational part of the kinetic energy is

$$T_{rot} = \frac{1}{2}\int_B \rho ||\boldsymbol{\omega} \times \mathbf{r}||^2, \tag{2.20}$$

where $\boldsymbol{\omega}$ is the angular velocity vector of the system and $\mathbf{r} = (x, y, z)$ is the position in body (or non-inertial) coordinates. Using vector identities, this equation can be written in matrix notation as:

$$T_{rot} = \frac{1}{2}\omega^T \mathbf{I} \omega, \tag{2.21}$$

where the matrix $\mathbf{I}$ is called the moment of inertia tensor, which is defined as,

$$\mathbf{I} = \begin{pmatrix} \int_B \rho \cdot (y^2+z^2)\, dxdydz & -\int_B \rho\, x\, y\, dxdydz & -\int_B \rho\, x\, z\, dxdydz \\ -\int_B \rho\, x\, y\, dxdydz & \int_B \rho \cdot (x^2+z^2)\, dxdydz & -\int_B \rho\, y\, z\, dxdydz \\ -\int_B \rho\, x\, z\, dxdydz & -\int_B \rho\, y\, z\, dxdydz & \int_B \rho \cdot (x^2+y^2)\, dxdydz \end{pmatrix}. \tag{2.22}$$

Let us apply now this theory to a rigid body B which is an ellipsoid with parameters a, b, c and homogeneous mass distribution with constant density $\rho(x, y, z) = \rho$. Moreover, we select the body reference choosing as axes the main axes of the ellipsoid. When we calculate one of the components of the tensor, for example I_{33}, we obtain the following equation,

$$\begin{aligned} I_{33} &= \int_B \rho \cdot (x^2+y^2) dxdydz = \rho \int_B [(ax')^2 + (by')^2] \left| \frac{\partial(x,y,z)}{\partial(x',y',z')} \right| dx'dy'dz' \\ &= abc\rho \int_0^1 \int_0^{2\pi} \int_0^{\pi} (a^2 r^2 cos(\theta)^2 \sin(\phi)^2 + b^2 r^2 sin(\theta)^2 \sin(\phi)^2) r^2 sin(\phi) d\phi d\theta dr \\ &= \frac{4}{15}\pi\rho abc(a^2+b^2), \end{aligned} \tag{2.23}$$

where we made the coordinate change $x' = \frac{x}{a}$, $y' = \frac{y}{b}$ and $z' = \frac{z}{c}$, and we used spherical coordinates.

Let us suppose that the density of the ellipsoid is $\rho = \frac{M}{\frac{4}{3}\pi abc}$, where M is the mass of the ellipsoid. Note that this density matches with the Ferrers density (Ferrers, 1877) when the degree of homogeneity n_h is equal to 0. Then,

$$I_{33} = \frac{1}{5}M(a^2 + b^2), \tag{2.24}$$

and due to symmetry,

$$I_{11} = \tfrac{1}{5}M(b^2 + c^2),\ I_{22} = \tfrac{1}{5}M(a^2 + c^2). \tag{2.25}$$

If we compute the other components in the same way, we obtain that $I_{ij} = 0, \forall i \neq j$. Thus, we write the moment of inertia tensor as a diagonal matrix, where the principal values are called the principal moments of inertia,

$$\mathbf{I}_b = \begin{pmatrix} I_1 & 0 & 0 \\ 0 & I_2 & 0 \\ 0 & 0 & I_3 \end{pmatrix}. \tag{2.26}$$

Moreover, these values will be all positive, so, since all of the eigenvalues of $\mathbf{I}$ are positive, $\mathbf{I}$ is a positive definite matrix, and this fact guarantees, as expected, that the kinetic energy will be always positive, no matter what $\boldsymbol{\omega}$ is.

Finally, we are going to see the relation between the tensor of inertia and the angular momentum, which is what we will use to compute the angular velocity of our system. First, let us define the total angular momentum as

$$\mathbf{L}_{tot} = \int_B \rho(\mathbf{r}_b \times \mathbf{v}_b), \tag{2.27}$$

using body coordinates with the center of mass as the origin, so that $\mathbf{r}_b$ is the position of each point and $\mathbf{v}_b$ is the velocity of each point in the inertial reference frame expressed in the body frame. The total angular momentum can be written as $\mathbf{L}_{tot} = \mathbf{L}_{cm} + \mathbf{L}_{rot}$, the first term being the angular momentum due to the motion of the center of mass, and the second term the intrinsic angular momentum due to the rotation of the body. The rigid body of which we study the motion has its center of mass in a fixed position. Because of this, $\mathbf{L}_{tot} = \mathbf{L}_{rot}$. Therefore,

$$\mathbf{L} = \mathbf{L}_{rot} = \int_B \rho(\mathbf{r} \times (\boldsymbol{\omega} \times \mathbf{r})) = \int_B \rho(r^2\boldsymbol{\omega} - (\boldsymbol{\omega} \cdot \mathbf{r})\mathbf{r}), \tag{2.28}$$

in matrix notation:

$$\mathbf{L} = \mathbf{I} \cdot \boldsymbol{\omega}. \tag{2.29}$$

Let us remark that the above formulas are valid for any orthonormal frame, provided that the body center of mass is static in the inertial frame.

Note that, only when $\mathbf{I}$ is proportional to the identity matrix, which for an ellipsoid happens only if it is a sphere, does this formula give a perfect alignment between the intrinsic angular momentum and the instantaneous angular velocity.

2.2.2 The case of axially symmetric barred galaxies

There are some theories which seek to explain the formation of warps through a misalignment between the angular momenta of the components of the models. Usually they assume that this is produced by the contribution of a third element. For instance, as an accretion of material due to the cosmic infall (see e.g. Ostriker & Binney, 1989, Jiang & Binney, 1999, López-Corredoira et al., 2002), and also possibly aided by dynamical frictions between the components (see e.g. Debattista & Sellwood, 1999). Although this could be one of the reasons, we think that even the dynamics in the formation of the bar and other blocks of the galaxy could be responsible of a small misalignment between the angular velocity, $\boldsymbol{\omega}$, and the angular momentum, $\mathbf{L}$. Taking into account that the bar rotates as a rigid body, the well known equation relating both magnitudes is $\mathbf{L} = \mathbf{I} \cdot \boldsymbol{\omega}$, where $\mathbf{I}$ is the inertia tensor, a tensor that is diagonal in the orthogonal basis related to the principal axis of the body frame.

If we understand the galaxy and bar formation as an accretion of material from a spinning mass distribution, the total angular momentum will be preserved during the process. But for the angular velocity of its building blocks, even though the dominant component will be in the direction of the angular momentum, a small component can appear in the orthogonal direction when the bar is forming. In fact, and probabilistically speaking, it is natural that it occurs in this way, moreover it is reinforced by the existence of any other external perturbations or internal frictions. So the result of having angular momentum and angular velocity slightly misaligned is a common fact in the motion of rigid bodies.

Combes et al. (1995) speculated about the relation between the precession of the angular momentum of a galactic disc and the formation of a warp as a vibration of the disc, but did not study this idea any further. Although we reached the idea of studying the misalignment of the angular momentum and the angular velocity independently of Combes et al. (1995), the work carried out in this dissertation may be considered, to some extent, a detailed study of the original idea.

The purpose of this section is to study the effect of a small misalignment between

the angular momentum of the system and its angular velocity. We are going to consider a galactic potential generated by an axisymmetric disc plus an ellipsoidal bar. The bar is precessing in a cone about the inertial Z axis, with a small tilt angle ε with respect to the XY plane, as is shown in Fig. 2.6 in page 32. The disc follows the movement of the bar, i.e. its normal vector precesses exactly as the bar forming an angle ε with the inertial Z axis.

First reference system: the body frame

As mentioned above, our bar can be modeled as a rigid body. Following Hand & Finch (1998) let us recall the basic properties of the motion of rigid bodies. If no torque is applied to the rigid body, its angular momentum obeys

$$\frac{d\mathbf{L}}{dt} = 0, \tag{2.30}$$

in an inertial reference system. Although the angular momentum is constant, this fact does not imply that the angular velocity $\boldsymbol{\omega}$ will be so. An easy way to analyze the behaviour of our system is to work in a *body reference frame* (which is a non-inertial reference system) aligned with the main axes of the body. In this system, the equation (2.30) becomes

$$\frac{d\mathbf{L}}{dt} = \frac{d\mathbf{L}_b}{dt} + \boldsymbol{\omega}_b \times \mathbf{L}_b, \tag{2.31}$$

where $\boldsymbol{\omega}_b = (\omega_1, \omega_2, \omega_3)$ is the angular velocity of the rigid body respect to the non-inertial system of the main axes, and

$$\mathbf{L}_b = \begin{pmatrix} I_1\omega_1 \\ I_2\omega_2 \\ I_3\omega_3 \end{pmatrix} \tag{2.32}$$

where

$$\mathbf{I}_b = \begin{pmatrix} I_1 & 0 & 0 \\ 0 & I_2 & 0 \\ 0 & 0 & I_3 \end{pmatrix} \tag{2.33}$$

is the tensor of inertia in the non-inertial frame. To obtain the equations of our precessing galactic model, we consider that the bar behaves as a rigid body with principal moments of inertia $I_1 = \frac{1}{5}M_b(b^2 + c^2)$, $I_2 = \frac{1}{5}M_b(a^2 + c^2)$ and $I_3 = \frac{1}{5}M_b(a^2 + b^2)$, where M_b is the mass of the bar, and the parameters a, b (the semi-major axes) and c (semi-minor axis) define the shape of the ellipsoid of the bar. Assuming that there is no torque applied to it, from equations (2.30), (2.31) and (2.32) it can be derived that the angular velocity of the bar with respect to the static inertial axes, expressed in the body frame, $\boldsymbol{\omega} = (\omega_1, \omega_2, \omega_3)$,

is a solution of Euler's equations:

$$\begin{cases} I_1 \frac{d\omega_1}{dt} = \omega_2\omega_3(I_2 - I_3), \\ I_2 \frac{d\omega_2}{dt} = \omega_1\omega_3(I_3 - I_1), \\ I_3 \frac{d\omega_3}{dt} = \omega_1\omega_2(I_1 - I_2). \end{cases} \tag{2.34}$$

We study Eq. (2.34) in the case of an axially symmetric bar along the x axis, with parameters $a > b = c$. Since the major axis of the bar is along the x axis in body coordinates, we have $I_1 \neq I_2 = I_3$. Thus, solving system (2.34) we deduce the angular velocity of the body in the body reference system,

$$\boldsymbol{\omega}_b = \begin{pmatrix} \omega_1 \\ A\sin(\lambda t) \\ A\cos(\lambda t) \end{pmatrix}. \tag{2.35}$$

where we have defined,

$$\lambda = \frac{I_T - I_1}{I_T}\omega_1, \qquad (I_T := I_2 = I_3), \tag{2.36}$$

which is the precession rate of $\boldsymbol{\omega}_b$ in the body cone and A, ω_1 are constants of the motion.

The angular momentum of the body is given in the body reference by,

$$\mathbf{L}_b = I_b \cdot \boldsymbol{\omega}_b = \begin{pmatrix} I_1\omega_1 \\ I_T A\sin(\lambda t) \\ I_T A\cos(\lambda t) \end{pmatrix}. \tag{2.37}$$

The modulus of the angular momentum $L = ||\mathbf{L}_b|| = \sqrt{I_1^2\omega_1^2 + I_T^2A^2}$ is a constant of the motion. Let ε be the angle from the angular momentum $\mathbf{L}_b$ to the yz plane in the body reference, i.e. the angle from the body x axis to the angular momentum $\mathbf{L}$ is $\frac{\pi}{2} - \varepsilon$ (see left panel of Fig. 2.5). The first component of $\mathbf{L}_b$ is thus $I_1\omega_1 = -L\sin(\varepsilon)$ and the constant $I_T A$ is $I_T A = \sqrt{L^2 - I_1^2\omega_1^2} = L\cos(\varepsilon)$. Therefore the angular momentum in body reference can be written as,

$$\mathbf{L}_b = \begin{pmatrix} -L\sin(\varepsilon) \\ L\cos(\varepsilon)\sin(\lambda t) \\ L\cos(\varepsilon)\cos(\lambda t) \end{pmatrix}. \tag{2.38}$$

Let us observe that the modulus of $\mathbf{L}_b$ does not vary with ε, always being $||\mathbf{L}_b|| = L$. Also note that $\mathbf{L}_b$ has a small constant component, $-L\sin(\varepsilon)$, in the x direction of the body frame and a big one of modulus $L\cos(\varepsilon)$ describing a circle in the yz plane of the body

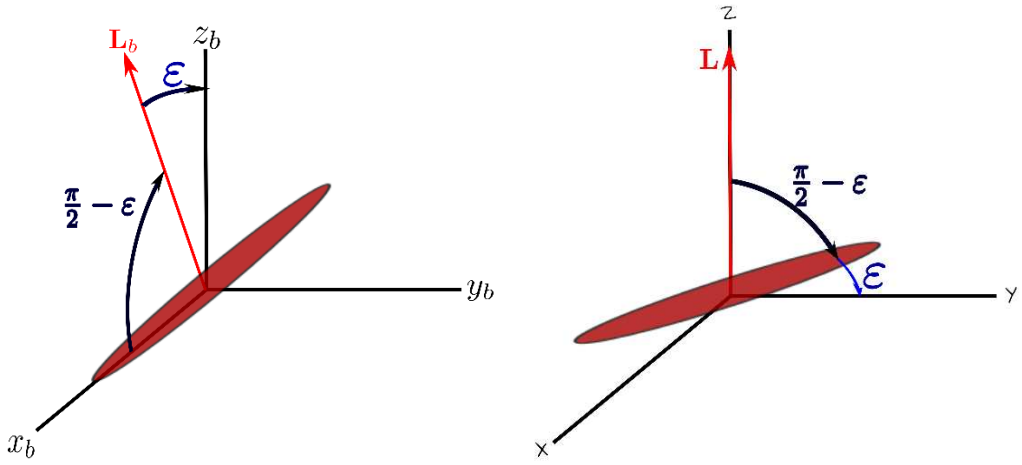

Figure 2.5: Left: Bar in the body reference frame, where the angular momentum $\mathbf{L}$ and the $y_b z_b$ plane form an angle ε. Right: Bar in the inertial reference frame, where the angular momentum is aligned with the Z axis and the main axis of the bar forms an angle ε with the XY plane.

frame. Thus, the angular velocity in the body frame is given by,

$$\boldsymbol{\omega}_b = I_b^{-1} \cdot \mathbf{L}_b = \begin{pmatrix} -\frac{L}{I_1}\sin(\varepsilon) \\ \frac{L}{I_T}\cos(\varepsilon)\sin(\lambda t) \\ \frac{L}{I_T}\cos(\varepsilon)\cos(\lambda t) \end{pmatrix}. \tag{2.39}$$

It follows from Eqs. (2.36) and (2.39) that $\lambda = -\frac{I_T - I_1}{I_T}\frac{L}{I_1}\sin(\varepsilon)$. Since the main axis, a, of the ellipsoid is much greater than the other axes, b and c, we have that $I_1 << I_T$. Moreover, for small values of ε, $\sin(\varepsilon) \approx \varepsilon$, and therefore $\lambda \approx -\frac{L}{I_1}\varepsilon$.

Since the angular momentum is preserved, we can select the inertial reference system so that its Z axis is given by the angular momentum $\mathbf{L}$. Then the angle ε is the angle formed by the main axis of the bar and the XY plane of the inertial reference system, and will be referred to as the *tilt angle* of the motion of the bar (see right panel of Fig. 2.5). When $\varepsilon = 0$ the angular momentum and angular velocity are aligned, but the two vectors become misaligned when $\varepsilon > 0$.

Second reference system: the precessing frame

Note that, in body reference, the angular momentum and angular velocity vectors rotate around the main axis of the bar (x axis in the body frame) with angular speed λ. We define a new reference, henceforth called the *precessing reference system*, applying to the

body reference the rotation,

$$R_p^b(t) = \begin{pmatrix} 1 & 0 & 0 \\ 0 & \cos(\lambda t) & -\sin(\lambda t) \\ 0 & \sin(\lambda t) & \cos(\lambda t) \end{pmatrix}, \tag{2.40}$$

where $R_p^b(t)$ is also the transformation of coordinates from the body reference to the precessing reference system. This rotation along the main axis of the bar is intended to "cancel out" the rotations of the angular momentum and angular velocity in the body frame, so that they become constant vectors in the new precessing reference system,

$$\boldsymbol{\omega}_p = R_p^b \cdot \boldsymbol{\omega}_b = \begin{pmatrix} -\frac{L}{I_1}\sin(\varepsilon) \\ 0 \\ \frac{L}{I_T}\cos(\varepsilon) \end{pmatrix}, \qquad \mathbf{L}_p = R_p^b \cdot \mathbf{L}_b = \begin{pmatrix} -L\sin(\varepsilon) \\ 0 \\ L\cos(\varepsilon) \end{pmatrix}. \tag{2.41}$$

Let us remark that for small ε the constant vector $\mathbf{L}_p$ has a small component in the x direction, which in the precessing reference is still the main axis of the bar, and a big component in the z direction.

We proceed to derive from our solution to Euler's equations (2.34) the motion of the bar in the three employed reference systems: body, precessing and inertial reference systems, where the inertial frame has been selected so that its Z axis is aligned with the angular momentum of the bar $\mathbf{L}$. We shall denote the space coordinates of a point in the bar in the body, precessing and inertial frames as $\mathbf{r}_b$, $\mathbf{r}_p$, $\mathbf{r}_i$ respectively, and we will follow the notation $\dot{} = \frac{d}{dt}$, $\ddot{} = \frac{d^2}{dt^2}$.

The body frame is fixed with respect to the body, so in this frame there is no apparent movement, i.e. $\dot{\mathbf{r}}_b = 0$.

The precessing coordinates of a bar point are given by,

$$\mathbf{r}_p = R_p^b \cdot \mathbf{r}_b, \tag{2.42}$$

where R_p^b is the change of reference matrix given in Eq. (2.41). Let us derive with respect of time Eq. (2.42),

$$\begin{aligned} \dot{\mathbf{r}}_p &= \dot{R}_p^b \mathbf{r}_b + R_p^b \dot{\mathbf{r}}_b = \dot{R}_p^b (R_p^b)^t R_p^b \mathbf{r}_b = (\boldsymbol{\omega}_p^b)^* \mathbf{r}_p \\ &= \boldsymbol{\omega}_p^b \times \mathbf{r}_p, \end{aligned} \tag{2.43}$$

where we have used that $\dot{\mathbf{r}}_b = 0$, and that, as R_p^b is an orthonormal change of frames, the matrix $(\boldsymbol{\omega}_p^b)^* = \dot{R}_p^b (R_p^b)^t$ is antisymmetric and its effect on a vector is the cross product by a vector $\boldsymbol{\omega}_p^b$. This vector is uniquely determined by $(\boldsymbol{\omega}_p^b)^*$, and it can be interpreted as the angular velocity of the body frame with respect to the precessing frame, expressed in the precessing reference.

The matrix $(\boldsymbol{\omega}_p^b)^*$, and therefore the vector $\boldsymbol{\omega}_p^b$, can be computed explicitly from the change of reference R_p^b,

$$(\boldsymbol{\omega}_p^b)^* = \dot{R}_p^b (R_p^b)^t = \begin{pmatrix} 0 & 0 & 0 \\ 0 & 0 & -\lambda \\ 0 & \lambda & 0 \end{pmatrix}, \tag{2.44}$$

and this antisymmetric matrix corresponds to cross product by the vector $\boldsymbol{\omega}_p^b = (\lambda, 0, 0)$.

Third reference system: the inertial frame

Let us recall from a theoretical view point the movement of the bar in the inertial system. If the center of mass of the rigid body remains fixed, as in our case, the position of a given point of the body at time t is given by $\mathbf{r}_i(t) = Q(t) \cdot \mathbf{r}_i(0)$, where $Q(t)$ is the time dependent orthogonal matrix that expresses the rotation of the rigid body from time 0 to time t. Differentiating this expression with respect to time, we obtain the well known defining formula for the instantaneous angular velocity,

$$\dot{\mathbf{r}}_i = \dot{Q}\mathbf{r}_i(0) = \dot{Q}Q^t Q\mathbf{r}_i(0) = (\boldsymbol{\omega}_i)^* \mathbf{r}_i(t) = \boldsymbol{\omega}_i \times \mathbf{r}_i, \tag{2.45}$$

where $\boldsymbol{\omega}_i$ is the angular velocity of the body in the inertial frame, determined by the antisymmetric matrix $(\boldsymbol{\omega}_i)^* = \dot{Q}Q^t$.

Next, we perform a comparison between the movement of the bar in the inertial and precessing frames. The relation between the coordinates of a bar point in these systems is given by,

$$\mathbf{r}_i = R_i^p \cdot \mathbf{r}_p, \tag{2.46}$$

where R_i^p is the orthonormal, time dependent, change from precessing to inertial coordinates. The time derivative of Eq. (2.46) is,

$$\dot{\mathbf{r}}_i = \dot{R}_i^p \mathbf{r}_p + R_i^p \dot{\mathbf{r}}_p. \tag{2.47}$$

The left hand side is $\dot{\mathbf{r}}_i = (\boldsymbol{\omega}_i)^* \mathbf{r}_i$, where $\boldsymbol{\omega}_i$ is the body angular velocity in the inertial frame given by Eq. (2.45). Thus, we can rewrite Eq. (2.47) as,

$$(\boldsymbol{\omega}_i)^* \mathbf{r}_i = \dot{R}_i^p (R_i^p)^t R_i^p \mathbf{r}_p + R_i^p \dot{\mathbf{r}}_p. \tag{2.48}$$

Multiplying both sides of this equation by the matrix of the change from inertial to precessing frame $(R_i^p)^t$, and applying that $\dot{R}_i^p (R_i^p)^t = (\boldsymbol{\omega}_i^p)^*$, which corresponds to the angular velocity of the precessing frame with respect to the inertial one (expressed in the inertial frame), we get

$$(R_i^p)^t (\boldsymbol{\omega}_i)^* R_i^p (R_i^p)^t \mathbf{r}_i = (R_i^p)^t (\boldsymbol{\omega}_i^p)^* R_i^p \mathbf{r}_p + \dot{\mathbf{r}}_p. \tag{2.49}$$

Let us note that the left hand side can be split in two factors: $(R_i^p)^t(\boldsymbol{\omega}_i)^* R_i^p = (\boldsymbol{\omega}_p)^*$, where $\boldsymbol{\omega}_p$ is the angular velocity of the body $\boldsymbol{\omega}_i$ changed to the precessing reference; and $(R_i^p)^t \mathbf{r}_i = \mathbf{r}_p$. In the right hand side we obtained $(R_i^p)^t(\boldsymbol{\omega}_i^p)^* R_i^p = (\boldsymbol{\omega}_i^p)_p^*$, where $(\boldsymbol{\omega}_i^p)_p$ is the angular velocity $\boldsymbol{\omega}_i^p$ expressed in the precessing frame. Therefore the last equation becomes,

$$\boldsymbol{\omega}_p \times \mathbf{r}_p = (\boldsymbol{\omega}_i^p)_p \times \mathbf{r}_p + \dot{\mathbf{r}}_p. \tag{2.50}$$

From this equation we deduce the equation of motion for the rigid body in the precessing reference system,

$$\dot{\mathbf{r}}_p = (\boldsymbol{\omega}_p - (\boldsymbol{\omega}_i^p)_p) \times \mathbf{r}_p, \tag{2.51}$$

where $\boldsymbol{\omega}_p$ is the angular velocity of the body in precessing reference (that is the inertial angular velocity of the body expressed in the precessing frame), and $(\boldsymbol{\omega}_i^p)_p$ is the angular velocity of the change of precessing to inertial frame expressed in the precessing frame. Remark that the angular velocity $(\boldsymbol{\omega}_i^p)_p$ is necessary in Eq. (2.51) because the precessing reference is neither inertial nor adapted to the body.

Comparing equations (2.51) and (2.43) we find that the vectors $\boldsymbol{\omega}_p^b$ and $\boldsymbol{\omega}_p - (\boldsymbol{\omega}_i^p)_p$ that multiply $\mathbf{r}_p$ on the right hand side must be equal modulo a multiple of $\mathbf{r}_p$. But both vectors are independent of $\mathbf{r}_p$ because the vectors $\boldsymbol{\omega}_p^b$ and $(\boldsymbol{\omega}_i^p)_p$ are determined by the change of reference transformations, which depend only on time, and $\boldsymbol{\omega}_p$ has been computed in Eq. (2.41) and found to be constant. Since $\boldsymbol{\omega}_p^b$ has also been computed, we obtain,

$$(\boldsymbol{\omega}_i^p)_p = \boldsymbol{\omega}_p - \boldsymbol{\omega}_p^b = \begin{pmatrix} -\lambda - \frac{L}{I_1}\sin(\varepsilon) \\ 0 \\ \frac{L}{I_T}\cos(\varepsilon) \end{pmatrix}. \tag{2.52}$$

The vector $(\boldsymbol{\omega}_i^p)_p$ is the angular velocity that is required in the equations of motion of the bar in the precessing reference frame as we shall see in Eq. (2.60). It is preferable to rewrite this vector in polar form as,

$$(\boldsymbol{\omega}_i^p)_p = \begin{pmatrix} -\lambda - \frac{L}{I_1}\sin(\varepsilon) \\ 0 \\ \frac{L}{I_T}\cos(\varepsilon) \end{pmatrix} = \begin{pmatrix} -\Omega\sin(\bar{\varepsilon}) \\ 0 \\ \Omega\cos(\bar{\varepsilon}) \end{pmatrix}, \tag{2.53}$$

where $\Omega = ||(\boldsymbol{\omega}_i^p)_p|| = \dfrac{L}{I_T}$, $\sin(\bar{\varepsilon}) = \dfrac{\lambda + \frac{L}{I_1}\sin(\varepsilon)}{\Omega}$ and $\cos(\bar{\varepsilon}) = \dfrac{\frac{L}{I_T}\cos(\varepsilon)}{\Omega}$. Substituting λ for its value $-\frac{I_T - I_1}{I_T}\frac{L}{I_1}\sin(\varepsilon)$, one immediately checks that $\bar{\varepsilon} = \varepsilon$.

We henceforth rename the vector $(\boldsymbol{\omega}_i^p)_p$ as $\boldsymbol{\Omega}_p$. This is the angular velocity that we

will use in the equations of motion of our model. Therefore,

$$\mathbf{\Omega_p} = \begin{pmatrix} -\Omega\sin(\varepsilon) \\ 0 \\ \Omega\cos(\varepsilon) \end{pmatrix}. \tag{2.54}$$

We can now determine the movement of the rigid body seen by an observer in the inertial frame. Our rigid body is already an ellipsoid whose movement is described by Poinsot's theorem (see Arnold, 1989), which states that the ellipsoid rolls without sliding on a stationary plane which is normal to the angular momentum $\mathbf{L}$. If the ellipsoid has axial symmetry as in our case, this movement is the superposition of a rotation of the ellipsoid along its symmetry axis with constant angular velocity and a precession with constant pattern speed around the axis of the angular momentum. The tilt angle formed by the symmetry axis of the ellipsoid and the stationary plane remains constant.

Since our inertial frame has the angular momentum of the bar $\mathbf{L}$ along its Z axis, the stationary plane over which the bar rolls is parallel to the XY plane. The tilt angle from the symmetry axis of the bar to the XY plane is the angle ε defined in Eq. (2.38). Since we know the motion of the rigid body in the precessing reference, we can deduce the complete movement in the inertial frame from Eq. (2.47) and therein, where we see that it is determined by the change of reference matrix R_i^p. As we have discussed, this matrix is the solution of the differential equation,

$$(R_i^p)^t \dot{R}_i^p (R_i^p)^t R_i^p = (\boldsymbol{\omega}_i^p)_p^* = \mathbf{\Omega_p}^*, \tag{2.55}$$

where $\mathbf{\Omega_p} = (-\Omega\sin(\varepsilon), 0, \Omega\cos(\varepsilon))$ as seen above. The solution of this equation becomes unique if one imposes as initial condition that at time $t = 0$ the precessing reference is a rotation of the inertial reference by an angle $-\varepsilon$ along the inertial Y axis, which we can impose because we have seen that the tilt angle is ε and we can choose the inertial X axis so that at time $t = 0$ the main axis of the body is contained in the inertial XZ plane. The solution to the differential equation satisfying this initial condition is,

$$R_i^p(t) = \begin{pmatrix} \cos\Omega t & -\sin\Omega t & 0 \\ \sin\Omega t & \cos\Omega t & 0 \\ 0 & 0 & 1 \end{pmatrix} \cdot \begin{pmatrix} \cos\varepsilon & 0 & \sin\varepsilon \\ 0 & 1 & 0 \\ -\sin\varepsilon & 0 & \cos\varepsilon \end{pmatrix}. \tag{2.56}$$

This means not only that the change from precessing to inertial frame is the matrix R_i^p, but also that we have identified all constants in the Poinsot's theorem description of the

bar motion: the change of reference from the body to the inertial frame is the product,

$$R_i^b(t) = \begin{pmatrix} \cos\Omega t & -\sin\Omega t & 0 \\ \sin\Omega t & \cos\Omega t & 0 \\ 0 & 0 & 1 \end{pmatrix} \cdot \begin{pmatrix} \cos\varepsilon & 0 & \sin\varepsilon \\ 0 & 1 & 0 \\ -\sin\varepsilon & 0 & \cos\varepsilon \end{pmatrix} \cdot \begin{pmatrix} 1 & 0 & 0 \\ 0 & \cos\lambda t & -\sin\lambda t \\ 0 & \sin\lambda t & \cos\lambda t \end{pmatrix}, \tag{2.57}$$

where the third factor indicates the rotation of the bar along its main axis with angular speed λ, the second factor shows the tilt angle ε between the main bar axis and the inertial XY plane, and the first factor is the precession of the bar along the inertial Z axis (which contains the angular momentum), with angular speed which is our pattern speed Ω.

The angular velocity of the bar in the inertial frame is,

$$\boldsymbol{\omega}_i = R_i^p \boldsymbol{\omega}_p = \begin{pmatrix} L(\frac{1}{I_T} - \frac{1}{I_1})\sin(\varepsilon)\cos(\varepsilon)\cos(\Omega t) \\ L(\frac{1}{I_T} - \frac{1}{I_1})\sin(\varepsilon)\cos(\varepsilon)\sin(\Omega t) \\ \frac{L}{I_1}\sin^2(\varepsilon) + \frac{L}{I_T}\cos^2(\varepsilon) \end{pmatrix}. \tag{2.58}$$

The constant Z component of $\boldsymbol{\omega}_i$ and the circular motion described by its X and Y components mean that the angular velocity $\boldsymbol{\omega}_i$ precesses in a cone around the Z axis, i.e. around the angular momentum,

$$\mathbf{L} = R_i^p \mathbf{L}_p = \begin{pmatrix} 0 \\ 0 \\ L \end{pmatrix}, \tag{2.59}$$

with pattern speed Ω as shown in Fig. 2.6. When $\varepsilon = 0$, the misalignment between the angular velocity and the angular momentum disappears and we recover the classical model with pattern speed Ω and $\boldsymbol{\omega}_i = (0, 0, \Omega)$.

We have to emphasize here that this solution is valid for an axially symmetric rigid body, which in the case of the bar implies that the components b and c are equal and therefore the moments of inertia I_2 and I_3 take the same value. If we want to solve the problem for the triaxial bar ($b \neq c$), the equations of motion (2.62) become non-autonomous and this would introduce a non-essential added difficulty. We will show, however, that although the model is initially considered for a symmetric bar, the results can be extended to a model with $b \neq c$ keeping the main properties and results of our system.

Summary: body motion

To complete this discussion, let us describe the motion of the rigid body as seen in the three reference systems that we have used.

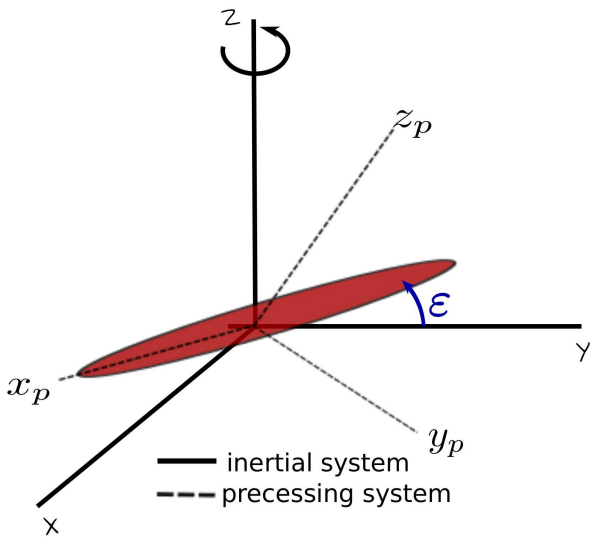

Figure 2.6: The major axis of the bar is aligned with the precessing x axis and the precessing z axis describes a cone about the inertial Z axis, where (x_p, y_p, z_p) denotes the precessing reference frame and (X, Y, Z) the inertial one.

An observer in the body reference sees a static body, because this reference frame is fixed to the body, i.e. $\mathbf{r}_b$ is constant for every point in the body.

An observer in the precessing reference sees the body rotating along its main axis (x axis in the precessing reference) with angular speed λ, because this rotation is the transformation between the precessing frame and the body frame where the body is static.

An observer in the inertial reference sees the body tilted a constant angle ε with respect to the XY plane, rotating along its main, symmetry axis with constant angular speed λ, and simultaneously precessing around the Z axis with constant angular velocity (pattern speed) Ω.

2.3 Equations of motion associated with barred galaxies

The equation of motion of a particle in the precessing model, in a non-inertial system is

$$\ddot{\mathbf{r}} = -\nabla\phi - 2(\mathbf{\Omega_p} \times \dot{\mathbf{r}}) - \mathbf{\Omega_p} \times (\mathbf{\Omega_p} \times \mathbf{r}), \tag{2.60}$$

where $\mathbf{r} = (x, y, z)$ is the position vector of a star or a particle, $\phi = \phi_d + \phi_b$ is the potential of the system, which in our case is the sum of the potentials ϕ_d, ϕ_b of the disc and bar

respectively, that compose the system, and $\mathbf{\Omega_p}$ is the angular velocity given in Eq. (2.54). The second term of the right hand side corresponds to Coriolis acceleration, and the last term to centrifugal acceleration.

From Eq. (2.60), by multiplying by $\dot{\mathbf{r}}$ we can derive the Jacobi constant $C_J = \frac{1}{2}\left|\dot{\mathbf{r}}\right|^2 + \phi - \frac{1}{2}\left|\mathbf{\Omega_p} \times \mathbf{r}\right|^2$ which is a constant of the motion. We can also define the effective potential as $\phi_{\text{eff}} = \phi - \frac{1}{2}\Omega^2 R^2$, taking into account that $-\frac{1}{2}\left|\mathbf{\Omega_p} \times \mathbf{r}\right|^2 = -\frac{1}{2}\Omega^2 R^2$, where $\Omega = |\mathbf{\Omega_p}|$ and R is the radius in cylindrical coordinates.

Our purpose is to study the effect of a small misalignment between the angular momentum of the system and its angular velocity. We are going to consider that the system, formed by a bar and a disc (and optionally a spheroid), is precessing in a cone about the inertial Z axis where the tilt angle with respect to the XY plane is ε. This tilt angle ε admits only small values, because it affects both bar and disc and tilting such a massive system soon leads to instability. Let us recall that to study the trajectories of stars under this potential, we consider the precessing reference frame defined in the previous section, where the x axis is aligned with the major axis of the bar, as shown in Fig. 2.6.

The components of our model are placed in the following way in the precessing reference system: the bar has the x axis as its main axis and rotates around it with constant angular speed, the disc is placed in the xy plane and the possible dark matter halo is a sphere with center at the origin of the system. Both the disc and the possible dark matter halo are static in this reference system. Therefore, from the inertial reference system viewpoint, the bar is precessing around the Z axis with tilt angle ε and the disc precesses solidarily with the bar and with the xy plane of the precessing frame, forming a constant angle ε with the inertial XY plane.

Let us remark that the disc has no effect in the angular velocity of Eq. (2.54). When the bar is forming from the disc the accumulation of particles in the bar makes it precess very slowly. Due to the bar having a greater density than the disc, its gravitational pull drags disc particles, making the disc follow the precession movement of the bar rather than affect this movement. By this reason, the movement of the disc is that of the bar given by Eq. (2.54). The fact that the movement of the disc is the same as that of the bar forces the angle ε to be small, because as the disc has a large size, a greater tilting angle would cause the unravelling of the disc.

The equations of motion for the precessing model are obtained by substituting the

pattern speed (2.54) in equation (2.60),

$$\begin{cases} \ddot{x} = 2\Omega\cos(\varepsilon)\dot{y} + \Omega^2\cos^2(\varepsilon)x + \Omega^2\sin(\varepsilon)\cos(\varepsilon)z - \phi_x \\ \ddot{y} = -2\Omega\cos(\varepsilon)\dot{x} - 2\Omega\sin(\varepsilon)\dot{z} + \Omega^2 y - \phi_y \\ \ddot{z} = 2\Omega\sin(\varepsilon)\dot{y} + \Omega^2\sin(\varepsilon)\cos(\varepsilon)x + \Omega^2\sin^2(\varepsilon)z - \phi_z \end{cases} \tag{2.61}$$

where ε is the tilt angle, Ω the modulus of the pattern speed and ϕ the potential ($\phi = \phi_b + \phi_d$).

By setting $(x_1, x_2, x_3, x_4, x_5, x_6) = (x, y, z, \dot{x}, \dot{y}, \dot{z})$, system (2.61) can be written as a system of first order differential equations,

$$\begin{cases} \dot{x_1} = x_4 \\ \dot{x_2} = x_5 \\ \dot{x_3} = x_6 \\ \dot{x_4} = 2\Omega\cos(\varepsilon)x_5 + \Omega^2\cos^2(\varepsilon)x_1 + \Omega^2\sin(\varepsilon)\cos(\varepsilon)x_3 - \phi_{x_1} \\ \dot{x_5} = -2\Omega\cos(\varepsilon)x_4 - 2\Omega\sin(\varepsilon)x_6 + \Omega^2 x_2 - \phi_{x_2} \\ \dot{x_6} = 2\Omega\sin(\varepsilon)x_5 + \Omega^2\sin(\varepsilon)\cos(\varepsilon)x_1 + \Omega^2\sin^2(\varepsilon)x_3 - \phi_{x_3} \end{cases} \tag{2.62}$$

where we recover the classical model when $\varepsilon = 0$. As stated, hereafter we refer to this model (2.62) as the **precessing model**. It is also worth mentioning that the precessing model has a Jacobi first integral given by,

$$\begin{aligned} C(x_1, x_2, x_3, x_4, x_5, x_6) = &-(x_4^2 + x_5^2 + x_6^2) + 2\Omega^2\sin(\varepsilon)\cos(\varepsilon)x_1x_3 \\ &+ (\Omega^2\cos^2(\varepsilon)x_1^2 + \Omega^2 x_2^2 + \Omega^2\sin^2(\varepsilon)x_3^2) - 2\phi, \end{aligned} \tag{2.63}$$

and the effective potential (see Fig. 2.7) is defined by,

$$\phi_{\text{eff}} = \phi - \frac{1}{2}\Omega^2(\cos^2(\varepsilon)x_1^2 + x_2^2 + \sin^2(\varepsilon)x_3^2) - \Omega^2\sin(\varepsilon)\cos(\varepsilon)x_1x_3. \tag{2.64}$$

The Jacobi integral is related with the Hamiltonian character of this system. In fact, and as in the non-precessing case, $C = -2H$.

Once the Jacobi integral is known in the precessing reference system, we compute the momenta and Hamiltonian in this reference system. In order to do this, we start by computing the kinetic energy T in the precessing reference system from its expression in inertial coordinates using the change of reference matrix R_i^p from the precessing to the inertial reference system determined in the last section.

Let us note that the Hamiltonian and the Lagrangian can be expressed as $H = T+V$, $L = T-V$, respectively, where V is the potential energy, and the Hamiltonian is $H = -\frac{1}{2}C$ in the precessing system. From these expressions, we deduce in the precessing system the

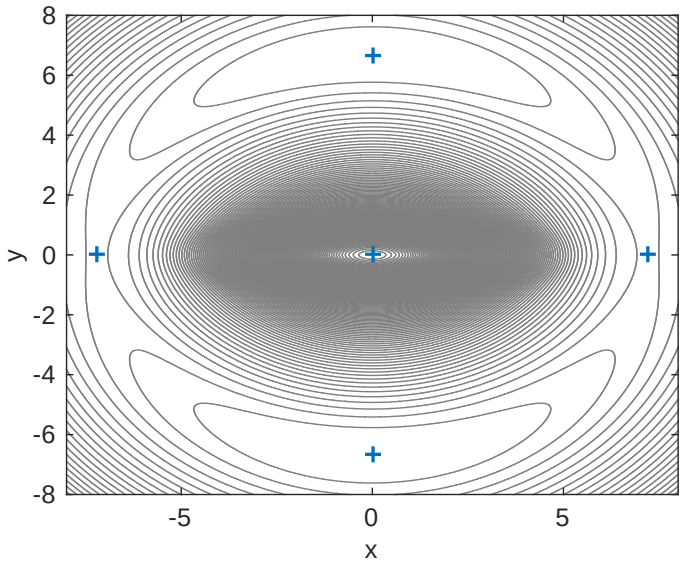

Figure 2.7: Contours of the effective potential for a model composed by a Miyamoto-Nagai disc and a Ferrers bar, where '+' denotes the Lagrange equilibrium points of the system.

expression of the Lagrangian L, from which the momenta are determined. And therefore we infer the canonical expression of the Hamiltonian in our precessing reference system,

$$\begin{aligned} H(q_1,q_2,q_3,p_1,p_2,p_3) &= \frac{1}{2}(p_1^2+p_2^2+p_3^2) \\ &+ 2\Omega\left(\cos(\varepsilon)p_1q_2 - \cos(\varepsilon)p_2q_1 - \sin(\varepsilon)p_2q_3 + \sin(\varepsilon)p_3q_2\right) \\ &+ \frac{3}{2}\Omega^2\left(q_2^2 + \cos^2(\varepsilon)q_1^2 + \sin^2(\varepsilon)q_3^2 + 2\sin(\varepsilon)\cos(\varepsilon)q_1q_3\right) \\ &+ \phi(q_1,q_2,q_3), \end{aligned} \tag{2.65}$$

being (p_i,q_i) the momenta and positions, respectively, in Hamiltonian coordinates defined as

$$\begin{aligned} q_1 &= x_1\,, & p_1 &= \dot{q_1} - 2\Omega\cos(\varepsilon)q_2\,, \\ q_2 &= x_2\,, & p_2 &= \dot{q_2} + 2\Omega\cos(\varepsilon)q_1 + 2\Omega\sin(\varepsilon)q_3\,, \\ q_3 &= x_3\,, & p_3 &= \dot{q_3} - 2\Omega\sin(\varepsilon)q_2\,. \end{aligned} \tag{2.66}$$

2.3.1 Zero velocity surfaces and equilibrium points

We define zero velocity surfaces of the precessing model as the manifold $(x_1, x_2, x_3) \in \mathbb{R}^3$ defined by Eq. (2.63) with $x_4 = x_5 = x_6 = 0$ for a given value of the Jacobi integral C. Their intersection with the $z = 0$ plane defines zero velocity curves. Regions where $\phi_{\text{eff}} > C$ are forbidden regions for a star of the given energy, whereas regions where

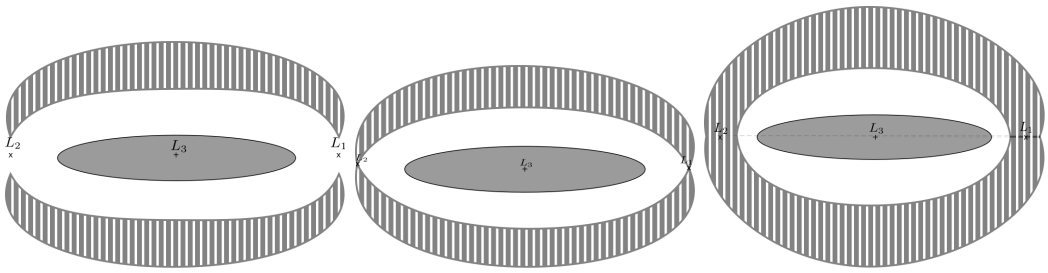

Figure 2.8: Hill regions of the precessing model, from left to right if: $E_J > E_{L_i}$, $E_J = E_{L_i}$, $E_J < E_{L_i}$. Being E_J the energy level taken and E_{L_i} the energy in the equilibrium points L_1 and L_2 ($E_{L_1} = E_{L_2}$).

$\phi_{\text{eff}} \leq C$ are possible places of movement called Hill regions. In Fig. 2.8 we show the Hill regions according to the energy level. Depending on whether this energy is greater or smaller than the energy of the equilibrium points L_1 and L_2, Hill regions consist in one or two connected components which form the complement of the forbidden regions, marked by striped zones in Fig. 2.8. Moreover, with this rank of energies, two possible movement zones are always delimited, one inner (where the bar is, shown as a grey ellipsoid) and another exterior surrounding the forbidden regions.

As in the case $\varepsilon = 0$, our precessing model in rotating coordinates has five Lagrangian equilibrium points (L_i, $i = 1 \ldots 5$), solutions of $\nabla\phi_{\text{eff}} = 0$. These are represented in Figs. 2.9 and 2.10. As for the properties of these libration points when $\varepsilon = 0$, L_1 and L_2 lie on the x-axis and are symmetric with respect to the origin. L_3 lies on the origin of coordinates, and, L_4 and L_5 lie on the y-axis and they are also symmetric with respect to the origin (see the left panel of Fig. 2.9). The two equilibrium points, L_1 and L_2 are unstable while L_3 is linearly stable and it is surrounded by the x_1 family of periodic orbits which is responsible for maintaining the bar structure, while the stable points L_4 and L_5 when $\varepsilon = 0$ have been thoroughly examined and are surrounded by families of periodic banana orbits (Contopoulos, 1981, Athanassoula et al., 1983, Skokos et al., 2002).

In our precessing model we notice that whereas L_3, L_4, L_5 maintain their coordinates fixed independently of ε, L_1 and L_2 vary as ε changes. Of relevant importance is the out-of-plane z-component for L_1 and L_2 (see right panel of Fig. 2.9). In Fig. 2.10 we detail the evolution of the coordinates of the equilibrium point L_1 when the parameter ε varies from $\varepsilon = 0$ to $\varepsilon = 0.2$.

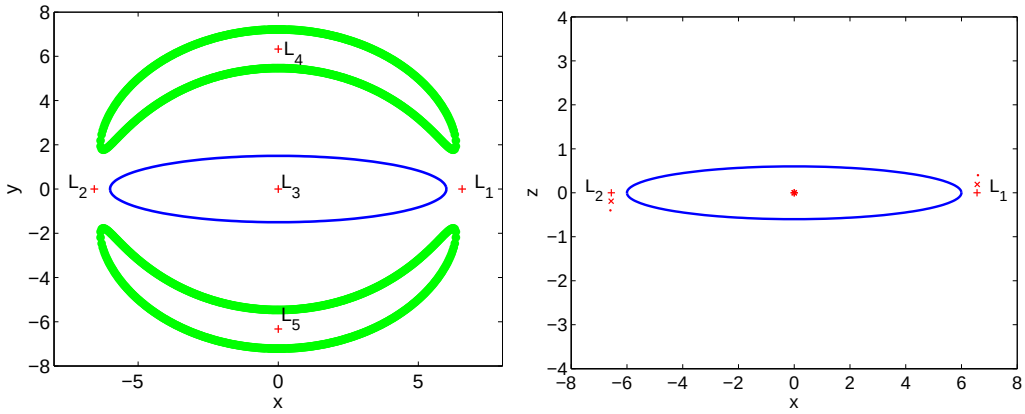

Figure 2.9: Equilibrium points of the precessing model with $GM_b = 0.1$. Left: xy plane with zero velocity curves. Right: xz plane,'+' for $\varepsilon = 0$, '$\times$' for $\varepsilon = 0.1$, '$\bullet$' for $\varepsilon = 0.2$, while the '$*$' shows the position of the central L_3 point. The blue curve in both panels outlines the triaxial Ferrers bar along the x axis.

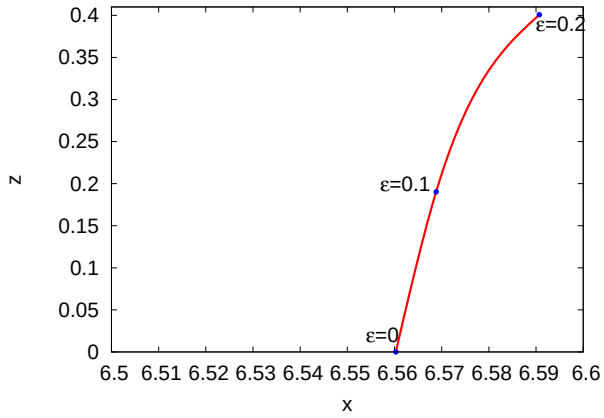

Figure 2.10: This plot shows the variation of the xz coordinates of L_1 as ε varies within the range $\varepsilon \in [0, 0.2]$ for the precessing model with $GM_b = 0.1$. The marked dots show the L_1 coordinates for three specific values of ε: $\varepsilon = 0$ (bottom part of the plot) $\varepsilon = 0.1$ (middle) and $\varepsilon = 0.2$ (top).

2.4 Lyapunov orbits

Before studying the invariant manifolds associated with periodic orbits around L_1 and L_2, we show how the periodic orbits around L_3 keep the bar structure in our precessing model. A thing to bear in mind is that, although the model is tilted, the equilibrium points and, consequently, periodic orbits, qualitatively remain the same as if the model were without tilt, except that their z-component varies. Finally, the orbits around L_4 and L_5 have been well studied for many models and we do not study them here because they are not relevant for the purpose of this work. These orbits are linearly stable and are commonly called banana orbits, but their shape does not constitute any characteristic of the galaxy (Patsis et al., 2003). On the contrary, the orbits around L_1 and L_2 are unstable and so they can not capture matter around them for long periods of time. For this reason they were not studied before. But (Romero-Gómez et al., 2006, 2007, Athanassoula et al., 2009) proved that invariant manifolds emanating from L_1 and L_2 perform as tubes transporting matter and make visible the external structures of the galaxies.

As common in Celestial Mechanics systems, in our case Lyapunov orbits are the family of periodic orbits which arises from infinitesimal librations in the central part of an equilibrium point. Taking an energy level close to the one of the equilibrium point, there exists a unique planar and a unique vertical periodic orbit around it.

As we just have explained, we are interested in the behaviour around the unstable equilibrium points L_1 and L_2, since they are located near the bar ends and it has been clearly proved that spiral arms and rings in barred galaxies emanate from the ends of the bar.

The general linear motion around L_1 (L_2 is symmetrical), is obtained by the addition of a hyperbolic exponential part to the in-plane and out-of-plane oscillations, which has both stable and unstable components with exponents of opposite sign. The linearized system has solutions

$$\begin{cases} x(t) = X_1 e^{\lambda t} + X_2 e^{-\lambda t} + X_3 \cos(\omega t + \theta) \\ y(t) = X_4 e^{\lambda t} + X_5 e^{-\lambda t} + X_6 \sin(\omega t + \theta) \\ z(t) = X_7 \cos(\nu t + \psi), \end{cases} \tag{2.67}$$

where X_i, $i = 1, ..., 7$ and θ,ψ represent amplitudes and phases.

Now we consider the motion of our equations of motion (2.61) in the neighbourhood of the equilibrium point, expanding the potential around this point and retaining only

first order terms,

$$\begin{cases} \ddot{x} = 2\Omega\cos(\varepsilon)\dot{y} + \Omega^2\cos(\varepsilon)^2 x + \Omega^2\sin(\varepsilon)\cos(\varepsilon)z + \phi_{xx}x + \phi_{xy}y + \phi_{xz}z \\ \ddot{y} = -2\Omega\cos(\varepsilon)\dot{x} - 2\Omega\sin(\varepsilon)\dot{z} + \Omega^2 y + \phi_{xy}x + \phi_{yy}y + \phi_{yz}z \\ \ddot{z} = 2\Omega\sin(\varepsilon)\dot{y} + \Omega^2\sin(\varepsilon)\cos(\varepsilon)x + \Omega^2\sin(\varepsilon)^2 z + \phi_{xz}x + \phi_{yz}y + \phi_{zz}z \end{cases} \tag{2.68}$$

where $x \equiv x_{L_i}$, $y \equiv y_{L_i}$ and $z \equiv z_{L_i}$, being x_{L_i}, y_{L_i} and z_{L_i} the coordinates of the equilibrium point L_i.

Substituting equations (2.67) into the differential equations obtained (2.68), we can find the terms X_i interrelated,

$$\begin{aligned} X_1 &= \frac{2\Omega\cos(\varepsilon)\lambda + \phi_{xy}}{\lambda^2 - \Omega^2\cos(\varepsilon)^2 - \phi_{xx}} X_4 \\ X_2 &= \frac{-2\Omega\cos(\varepsilon)\lambda + \phi_{xy}}{\lambda^2 - \Omega^2\cos(\varepsilon)^2 - \phi_{xx}} X_5 \\ X_3 &= -\frac{2\Omega\cos(\varepsilon)\omega}{\omega^2 + \Omega^2\cos(\varepsilon)^2 + \phi_{xx}} X_6. \end{aligned} \tag{2.69}$$

Therefore, if we define A_1, A_2 and A_3 in such way that $X_1 = A_1 X_4$, $X_2 = A_2 X_5$ and $X_3 = A_3 X_6$, equations (2.67) become

$$\begin{cases} x(t) = A_1 X_4 e^{\lambda t} + A_2 X_5 e^{-\lambda t} + A_3 X_6\cos(\omega t + \theta) \\ y(t) = X_4 e^{\lambda t} + X_5 e^{-\lambda t} + X_6\sin(\omega t + \theta) \\ z(t) = X_7\cos(\nu t + \psi), \end{cases} \tag{2.70}$$

where A_1 and A_2 depend on λ, and A_3 depends on ω.

Now we can already define the initial conditions at $t = 0$, taking $X_1 = X_2 = 0$:

$$\begin{aligned} &(x(0), y(0), z(0), \dot{x}(0), \dot{y}(0), \dot{z}(0)) = \\ &= (A_3 X_6\cos(\theta), X_6\sin(\theta), X_7\cos(\psi), -A_3 X_6\omega\sin(\theta), X_6\omega\cos(\theta), -X_7\nu\sin(\psi)) \end{aligned} \tag{2.71}$$

for selected values of X_3, X_6, θ and ψ.

In this way, we are able to deduce from the linearization of the system initial conditions for the periodic motion of the Lyapunov orbit when time evolves,

$$\begin{aligned} x_0(t) &= (x(t), y(t), z(t), \dot{x}(t), \dot{y}(t), \dot{z}(t)) = \\ &= (A_3 X_6\cos(\omega t + \theta), X_6\sin(\omega t + \theta), X_7\cos(\nu t + \psi), \\ &\quad - A_3 X_6\omega\sin(\omega t + \theta), X_6\omega\cos(\omega t + \theta), -X_7\nu\sin(\nu t\psi)) \end{aligned} \tag{2.72}$$

Note that here we have defined a linear approximation of a Lyapunov orbit. Since we want to obtain some orbits of the family of Lyapunov orbits, we need to refine this

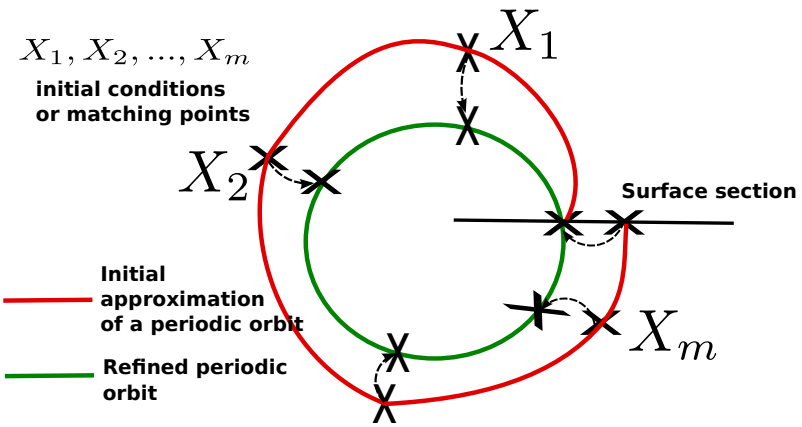

Figure 2.11: Schematic view of the multiple shooting method.

approximation and continue the orbits of the family. The reason to get the family is that we are studying periodic orbits around an equilibrium point in galaxies, and the stars cover a wide range of energies so that the orbits can be visible.

The manner of refining the linear approximation is using the method of multiple shooting, since these periodic orbits are unstable and we want to avoid difficulties in their integration. So, we have used the technique described in (Simó, 1990, Masdemont & Mondelo, 2004). The main idea of this method is to integrate the equations from one initial condition to the next one, making the last one close the orbit and imposing on the new orbit to have the desired energy or period (see Fig. 2.11).

We continue the family by following either the period or the energy of the periodic orbits. So, we need the Jacobian energy function $H(\mathbf{x})$, with vector field $X_H(\mathbf{x})$ and flow $\phi_t(\mathbf{x})$, for $\mathbf{x} \in \mathbb{R}^6$ (note that $\frac{d}{dt}(\mathbf{x}) = X_H(\phi_t(\mathbf{x}))$.

Let us define $S = \{\mathbf{x} \in \mathbb{R}^6 | \, g(\mathbf{x}) = 0\}$ a section surface and $T(\mathbf{x})$ the time from $\mathbf{x}$ to intersect transversally S in the direction of $\nabla g(\mathbf{x})$. Then, we can write the system of equations to refine m initial conditions or points on the linear approximation, $\mathbf{x_1}, ..., \mathbf{x_m} \in \mathbb{R}^6$, to a periodic orbit:

$$\begin{cases} \phi_{\tau/m}(\mathbf{x}_i) - \mathbf{x}_{i+1} = 0, \;\; i = 1, \ldots, m-1 \\ \phi_{x_m}(\mathbf{x}_m) - \mathbf{x}_1 = 0 \\ H(\mathbf{x}_1) - h = 0 \\ T(\mathbf{x}_m) - \frac{\tau}{m} = 0, \end{cases} \tag{2.73}$$

where h, $\tau \in \mathbb{R}$ are the energy and the period, respectively, of the refined periodic orbit. Note that this system does not need to be compatible, in fact, the last two equations are related, since given an energy level, there exists an unique (locally) periodic orbit, and at

the same time, a fixed period determines a periodic orbit in the family. Therefore, we can refine a periodic orbit of a given energy level or a given period. Consequently, the way to proceed is to eliminate the equation and the unknown of the corresponding fixed value.

Below, we solve the resulting system using standard Newton's method. Denoting the system obtained as $F(X) = 0$, being $X^{(0)}$ a first approximation, we proceed iteratively in the system

$$\begin{aligned} &DF(X^k)Y^{(k)} = F(X^{(k)}) \\ &X^{(k+1)} = X^{(k)} - Y^{(k)}, \end{aligned} \tag{2.74}$$

stopping at the first k such that $||F(X^{(k)})||$ or $||X^{(k)} - X^{(k-1)}||$ are under a given tolerance. Therefore, we need the derivatives of the system (2.73), to get them we use the first variational equations, which give us the variation of the final state with respect to the initial ones. The derivative of the equation corresponding to the last matching point is calculated by differentiating $g(\phi_{T(\mathbf{x})}(\mathbf{x})) \equiv 0$, which gives

$$DT(\mathbf{x}) = -\frac{Dg(\phi_{T(\mathbf{x})}(\mathbf{x}))D\phi_{T(\mathbf{x})}(\mathbf{x})}{Dg(\phi_{T(\mathbf{x})}(\mathbf{x}))X_H(\phi_{T(\mathbf{x})})}. \tag{2.75}$$

taking into account that the section surface S is a hyperplane, so $Dg(\phi_{T(\mathbf{x})}(\mathbf{x}))$ is a constant row vector. Moreover, let us point out that the system of equations to solve is a full-rank non-square linear system, so a good way to solve it is with a QR factorization or a Singular Value Decomposition (SVD).

Following this procedure, we find a refinement of the linear approximation of the periodic orbit to a periodic orbit, and now we need to continue its family. In order to do this, the idea is basically the same as before, to eliminate equations and unknowns of the system (2.73) so that the resulting system has each orbit of the family as a solution. In this case, we use a prediction-correction strategy to continue the family, choosing whether we want to continue fixing the energy or the period.

To predict a new periodic orbit of the family from a given one, we consider the family as a manifold and move along the tangent space. Let $G(X) = 0$ be the system to solve after elimination, and $KerDG(X)$ the tangent space, given $X^{(k)}$, we compute $Y^{(k)} = X^{(k)} + \delta V^{(k)}$, where $\delta \in \mathbb{R}$, and $V^{(k)} \in KerDG(X^{(k)})$ with norm 1 in the positions. Below, denote $Y^{(k)} =: Y^{(k,0)}$, and by Newton's method:

$$\begin{aligned} &DF(Y^{(k,j)})Z^{(j)} = G(Y^{(k,j)}) \\ &Y^{(k,j+1)} = Y^{(k,j)} - Z^{(j)}. \end{aligned} \tag{2.76}$$

Lastly, we take as a new orbit the first $Y^{(k,j)}$ such that $||G(Y^{(k,j)})||$ or $||Y^{(k,j)} - Y^{(k,j-1)}||$ is under a given tolerance. Remark that the solution obtained is a whole family

of periodic orbits, that is, this last linear system has not a unique solution but a 1-dimensional kernel.

Summarizing, starting from a linear approximation of a periodic orbit around an unstable equilibrium point, we have refined it to a periodic orbit and followed its family either by fixing the energy or the period.

Besides, the linear stability of a periodic orbit is obtained by computing the eigenvalues of its monodromy matrix. This matrix is obtained integrating the variational equations until time τ, being τ the period of the periodic orbit. This monodromy matrix, $\mathbf{M}$, since obtained from a Hamiltonian system, is a 6×6 symplectic matrix, and so if γ is an eigenvalue of M, γ^{-1} is as well. Therefore, the eigenvalues of $\mathbf{M}$ are of the form γ, $1/\gamma$, η, $1/\eta$, ξ, $1/\xi$ and they can be either real or complex.

2.4.1 Invariant manifolds associated to Lyapunov orbits

Once we have described Lyapunov orbits and their continuation method, we can define the invariant manifolds associated to them. As happened with the Lyapunov orbits, the hyperbolic character of the invariant manifolds is related to the hyperbolic behaviour of the base orbits. Therefore, they do not exist around a stable equilibrium point and we can focus on the points L_1 and L_2 of our system.

The goal is to understand the overall dynamics of our system (2.62). Generally speaking, we could say that orbits in the stable, respectively unstable, invariant manifolds are asymptotic orbits that tend to, respectively depart from, the Lyapunov orbit. Knowing these manifolds is crucial as they organize the dynamics on a global scale, for example invariant manifolds may form boundaries of basins of attraction, and intersections between stable and unstable manifolds lead to complicated dynamics and chaos.

Generally, global stable and unstable manifolds can not be found analytically. Moreover, they are not implicitly defined, so it is not possible to find them as the zero-set of some function of the phase space variables. For that reason, points on global invariant manifolds can not be found locally, in their place invariant manifolds must grow from local knowledge, for example from a periodic orbit close to an equilibrium point.

Let us describe the invariant manifolds of orbits around L_1, the L_2 case is symmetric. As we have just described, a family of periodic orbits known as Lyapunov orbits emanates from L_1. The Stable and Unstable Manifold Theorem (Guckenheimer & Holmes, 1986) states that the local stable manifold $W^s_{loc}(\gamma)$ exists in a neighbourhood of γ,

$$W^s_{loc}(\gamma) = \left\{ X \in \mathbb{R}^6 | \lim_{t\to\infty} ||\Psi(t, X) - \gamma|| = 0 \right\}$$

where $\Psi(t, X)$ denotes the orbit that has the state $X = (x, y, z, \dot{x}, \dot{y}, \dot{z})$ at $t = 0$, and $\gamma \in \Gamma$, with Γ the whole family of Lyapunov orbits. Hence, the local stable manifold is the set of orbits that asymptotically tend to the Lyapunov orbit as time tends to infinity. The local unstable manifold is analogously described with respect to the reversed direction of time,

$$W^u_{loc}(\gamma) = \left\{ X \in \mathbb{R}^6 | \lim_{t \to -\infty} ||\Psi(t, X) - \gamma|| = 0 \right\}.$$

That is, the local unstable manifold is the set of orbits that asymptotically tend to the Lyapunov orbit as time tends to minus infinity (i.e., the set of orbits departing from the Lyapunov orbit).

In the same way, we get the global stable and unstable manifolds by letting orbits in $W^s_{loc}(\gamma)$ flow backwards in time and in $W^u_{loc}(\gamma)$ flow forwards in time,

$$W^s_\gamma = \bigcup_{t \leq 0} \Psi(t, W^s_{loc}(\gamma)), \quad W^u_\gamma = \bigcup_{t \geq 0} \Psi(t, W^u_{loc}(\gamma)).$$

W^s_γ and W^u_γ are two-dimensional tubes in phase space that can be parametrized by the angle ϕ and the time t (Gómez et al., 2004, Masdemont & Mondelo, 2004) and the orbits that form them have the same energy as the Lyapunov orbit γ from which they arise. As the energy level varies from that of the equilibrium point C_{L_i}, $i = 1, 2$ to that of its Lyapunov orbit γ, the intermediate energy levels define a family of concentric tubes. These tubes are responsible for the transport of matter that gives shape and important structures to the galaxy.

Let us proceed to explain how to compute the invariant manifolds. Let $\mathbf{M}$ be the monodromy matrix defined previously, we are interested in the asymptotic part represented by two real eigenvalues, ρ_u and ρ_s. The unstable manifold is related to the real eigenvalue such that $||\rho_u|| > 1$, whereas the stable one is related to the real eigenvalue that obeys $||\rho_s|| < 1$. Let us suppose that the associated eigenvectors are $\mathbf{v}_u$ and $\mathbf{v}_s$ respectively.

In the case of the unstable manifold (the stable one is analogous), we need to compute k trajectories which represent the manifold. We define $t_i = \frac{i\tau}{k}, \quad i = 0, \ldots, k$, where $t_k = \tau$ is the period of the Lyapunov orbit. If the orbit γ is parametrized by $\mathbf{x}(t)$, $\mathbf{x}(t_i)$ are k different points on γ ($\mathbf{x}(t_0) = \mathbf{x}(t_k)$). Defining $\mathbf{v}^u(t)$ the vector of the unstable eigenvalue ρ_u such that $\mathbf{v}^u(t) = \mathbf{M}(t)\mathbf{v}_u$, where $\mathbf{M}(0) = \mathbf{Id}$ (the identity matrix) and therefore $\mathbf{v}^u(0) = \mathbf{v}_u$. The k different vectors allow us to have k different points to integrate in the equations of the model:

$$\mathbf{x}_i = \mathbf{x}(t_i) + \delta \mathbf{v}^u(t_i),$$

where the parameter $\delta \in \mathbb{R}$ has to be small ($\delta < 10^{-2}$). In this way we have obtained trajectories which represent the unstable manifold.

Chapter 3

The dynamics of the precessing model

For this precessing model we use a galaxy morphology composed by a Miyamoto-Nagai disc and a Ferrers bar following the equations of motion described in Sect. 2.3. We recall that the potential of the Miyamoto-Nagai disc is modeled by,

$$\phi_d = -\frac{GM_d}{\sqrt{R^2 + (A + \sqrt{B^2 + z^2})^2}} \tag{3.1}$$

where $R^2 = x^2 + y^2$ is the radius in cylindrical coordinates, and z denotes the distance in the out-of-plane component. The parameter G is the gravitational constant and M_d is the mass of the disc. The parameters A and B characterize the shape of the disc. Parameter A measures the radial scale length of the disc while B is a measure of the disc thickness in the z direction. Since galactic discs are larger in the radial direction than in the vertical one, in our models A is greater than B.

The Ferrers bar follows the equation,

$$\rho = \begin{cases} \rho_0(1 - m^2)^{n_h}, & m \leq 1 \\ 0, & m > 1 \end{cases} \tag{3.2}$$

where $m^2 = x^2/a^2 + y^2/b^2 + z^2/c^2$ and, for $n_h = 2$, $\rho_0 = \frac{105}{32\pi}\frac{GM_b}{abc}$ is the central density, being M_b the mass of the bar. The parameters a (semi-major axis) and b, c (semi-minor axes) determine the shape of the bar, while parameter n_h determines the concentration of matter in the bar. With $n_h \geq 2$, this model concentrates matter in the central region and decreases smoothly towards zero at a finite distance.

The density of the bar potential is related with its potential, ϕ_b, by means of the

Poisson equation ($\nabla^2\phi = 4\pi G\rho$):

$$\phi_b = \pi\, G\, abc \frac{\rho_0}{n_h+1} \int_\lambda^\infty \frac{du}{\Delta(u)} (1 - m^2(u))^{(n_h+1)}, \tag{3.3}$$

where G is the gravitational constant, n_h the homogeneity degree for the mass distribution,

$$\Delta(u) = (a^2+u)(b^2+u)(c^2+u) \tag{3.4}$$

and λ the unique positive solution of $m^2(\lambda) = 1$ if $m \geq 1$, (that is, if the particle lies outside the bar), and zero otherwise.

Note that the total potential of the model applied to equation (2.62) is $\phi = \phi_b + \phi_d$ where ϕ_b is the bar potential, and ϕ_d the potential of the disc surrounding the bar.

The length unit used throughout this work is the kpc, the time unit is $\mathrm{u}_t = 2 \times 10^6$ yr and the gravitational constant is $G = 6.674 \times 10^{-11} m^3 kg^{-1} s^{-2}$. In this chapter we take values $A = 3$, $B = 1$ for the disc, and for the bar we are going to consider two different Ferrers bars, one symmetric and another one with the values taken by Pfenniger (1984). For both bars, the distribution of mass is given by $n_h = 2$ and the semi-major axis of the bar by $a = 6$. But, whereas the first bar has revolution symmetry with semi-minor axes $b = c = 0.95$, the second bar has just axial symmetry with $b = 1.5 \neq c = 0.6$. Some other parameters are considered in a range: $GM_d \in [0.6, 0.9]$, $GM_b \in [0.1, 0.4]$, and M_b given by the convention that $G(M_d + M_b) = 1$. Finally we also consider the pattern speed $\Omega \in [0.05, 0.06]$ kpc/[u_t] and the tilt angle of bar, $\varepsilon \in [0, 0.2]$ rad $= [0, 11.46]^\circ$.

3.1 The structure of periodic orbits inside the bar

In order to understand the formation, evolution and properties of any given structure it is essential to first understand its building blocks. In the case of galactic dynamics, and particularly for barred galaxies, it has been clearly demonstrated that some building blocks are periodic orbits elongated along the bar. The study of these building blocks provided answers to a number of crucial questions, like why bars are bisymmetric, why they rotate as rigid bodies, why they can not extend beyond corotation, etc. (see Contopoulos, 1981, Athanassoula et al., 1983, Pfenniger, 1984, Skokos et al., 2002, among others).

In this section we start from the infinitesimal periodic orbits about the central equilibrium point L_3 and considering either period or energy, we continue the families of periodic orbits inside the bar and simultaneously study their stability properties. We obtain evidence that the stable orbits we find give structure to the bar, since stars or particles can be trapped in their neighbourhood.

Proceeding with this aim, we first analyze the stability of the equilibrium point L_3 in the precessing model. Let us consider the differential matrix around any Lagrangian point of the system (2.62):

$$DF(L_i) = \begin{pmatrix} 0 & 0 & 0 & 1 & 0 & 0 \\ 0 & 0 & 0 & 0 & 1 & 0 \\ 0 & 0 & 0 & 0 & 0 & 1 \\ a & \phi_{x_1x_2} & b & 0 & c & 0 \\ \phi_{x_1x_2} & d & \phi_{x_2x_3} & -c & 0 & -e \\ b & \phi_{x_2x_3} & f & 0 & e & 0 \end{pmatrix}_{L_i} \tag{3.5}$$

where

$$\begin{cases} a = \Omega^2 \cos(\varepsilon)^2 + \phi_{x_1x_2}, \\ b = \Omega^2 \sin(\varepsilon)\cos(\varepsilon) + \phi_{x_1x_3}, \\ c = 2\Omega \cos(\varepsilon), \\ d = \Omega^2 + \phi_{x_2x_2}, \\ e = 2\Omega \sin(\varepsilon), \\ f = \Omega^2 \sin(\varepsilon)^2 + \phi_{x_3x_3}. \end{cases} \tag{3.6}$$

For the particular case of L_3, the eigenvalues of (3.5) are of the form $\{\lambda i,\ -\lambda i,\ \mu i,\ -\mu i,\ \omega i,\ -\omega i\}$ ($\lambda,\ \mu,\ \omega \in \mathbb{R}^+$), for any selected value of ε. Since the purely imaginary eigenvalues are associated to infinitesimal librations, the linearised flow around L_3 in the rotating frame of coordinates is characterised by a superposition of three oscillations, and a behaviour of the form center×center×center with two components inside the xy plane and another in the z direction. This is, the L_3 Lagrangian point is a linearly stable elliptic point.

Next, our research on periodic orbits about L_3 is conducted following the work of (Pfenniger, 1984) which is a particular case of the precessing model with $\varepsilon = 0$.

We define the stability indexes, s_1, s_2, s_3 and Δ, of these periodic orbits as in Pfenniger (1984). Let $p(\varsigma)$ be the characteristic polynomial of the monodromy matrix of each orbit, and γ, $1/\gamma$, η, $1/\eta$, ξ, $1/\xi$ its eigenvalues, which can be real or complex. Therefore, the characteristic polynomial is:

$$p(\varsigma) = det(M - \varsigma I) = (\varsigma^2 - s_1\varsigma + 1)(\varsigma^2 - s_2\varsigma + 1)(\varsigma^2 - s_3\varsigma + 1), \tag{3.7}$$

being s_1,s_2 and s_3 the stability indexes defined as

$$s_1 = -(\gamma + 1/\gamma), \quad s_2 = -(\eta + 1/\eta), \quad s_3 = -(\xi + 1/\xi), \quad \Delta = (s_1 - s_2)^2. \tag{3.8}$$

Note that since we are considering a periodic orbit in an autonomous system, at least one of the eigenvalues is equal to 1 with multiplicity 2 (let us suppose that this is ξ). With

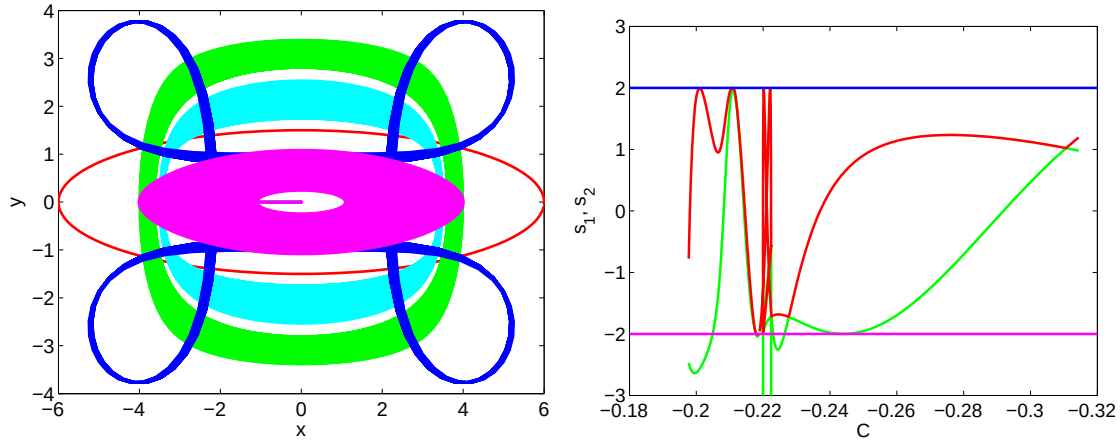

Figure 3.1: Periodic orbits and stability indexes of the precessing model with $b \neq c$ when $\varepsilon = 0$ and $GM_b = 0.1$. Left: family of periodic orbits in the xy plane. Right: stability indexes where C is the Jacobi constant and s_1, s_2 the stability indexes.

these definitions, an orbit is stable only when s_1 and s_2 are real and $|s_1|, |s_2| \leq 2$, otherwise it is unstable. If $|s_1|$ or $|s_2| = 2$ or $\Delta = 0$, the Jacobian matrix of the continuation process is degenerate and bifurcations of the family are allowed. If $s_i = +2$, the bifurcation occurs through period doubling, while if $s_i = -2$, the bifurcation keeps the same period. Moreover, if s_1 or s_2 is complex, then $\Delta < 0$ and we have complex instability, which only happens for 3D orbits.

In Fig. 3.1 we show the results obtained for $GM_b = 0.1, \Omega = 0.05$ and $\varepsilon = 0$, which, for reference, appears in Fig. 4 of Pfenniger (1984). The families of planar periodic orbits about L_3 are stable and responsible for the skeleton of the bar's structure. A continuation process in ε is then used to obtain the corresponding results for a tilt angle $\varepsilon \neq 0$.

The results obtained for $\varepsilon = 0.1$ and $\varepsilon = 0.2$, as well as for reference Pfenniger results ($\varepsilon = 0$), are shown in Fig. 3.2. In the plots we see that the families of periodic orbits change when the tilt angle varies, but the change is mostly in the z component, as expected. The xy projections remain essentially the same and the families of periodic orbits continue giving structure to the bar, as is displayed in Fig. 3.3 where the families for $\varepsilon = 0$ and $\varepsilon = 0.2$ are compared.

As for the stability indexes, in the last row of Fig. 3.2 we find that, for a given value of ε, s_1 and s_2 cross the limits (± 2) an equal number of times and approximately at the same value of the energy. All these facts reinforce again the evidence that the families of periodic orbits about L_3 for any ε are qualitatively the same.

At this moment, we can prove that although the equations given in Chapter 2 are

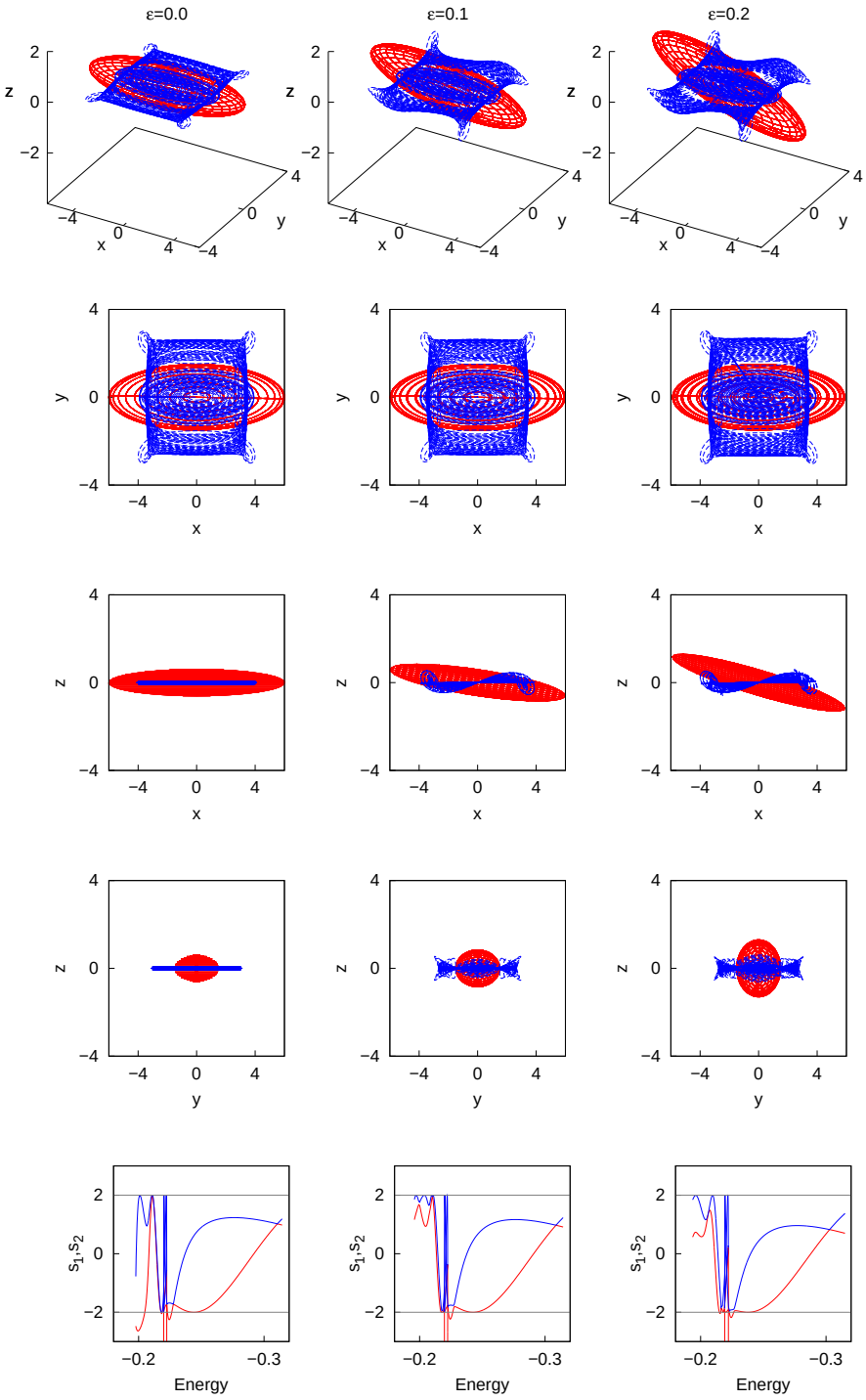

Figure 3.2: x_1 family of periodic orbits of the precessing model with $b \neq c$ and stability indexes for $\varepsilon = [0, 0.1, 0.2]$ and $GM_b = 0.1$.

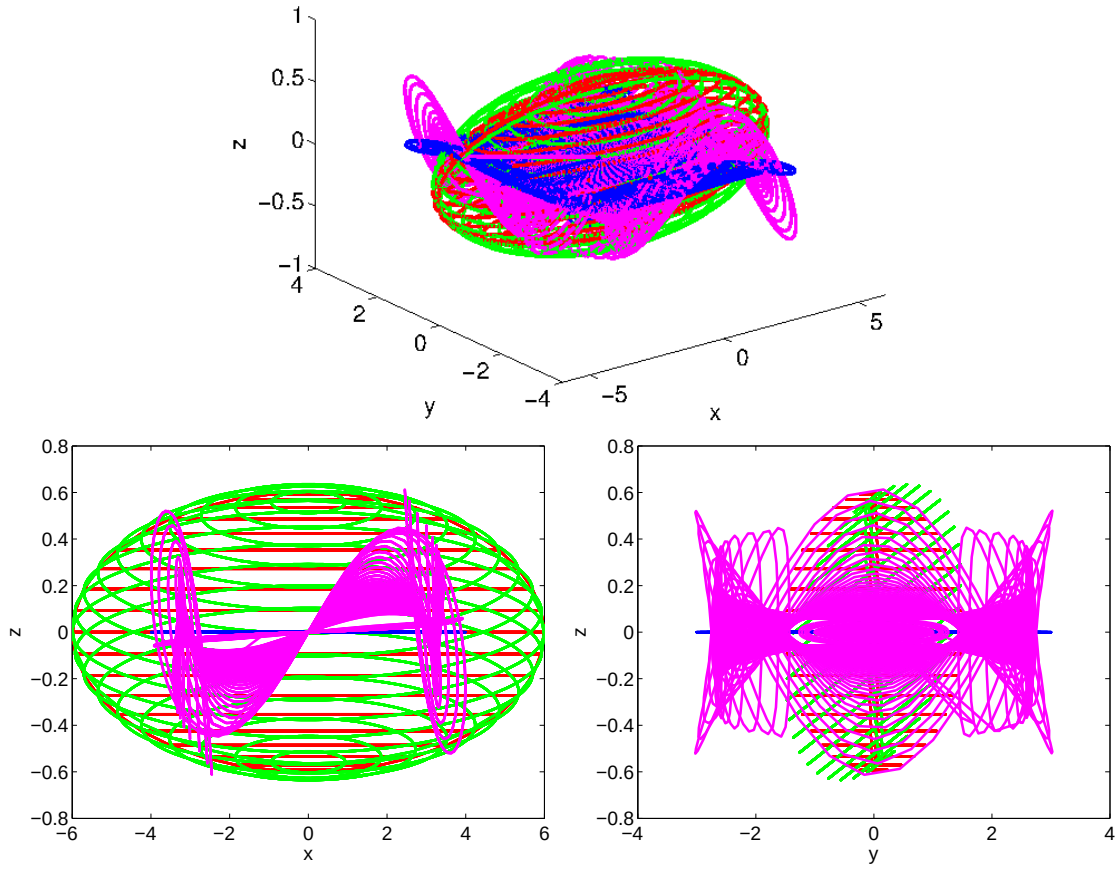

Figure 3.3: x_1 family of periodic orbits of the precessing model with $b \neq c$ for $\varepsilon = 0$ (blue) and $\varepsilon = 0.2$ (purple) and $GM_b = 0.1$. Top: 3D view. Bottom: xz-plane (left), yz-plane (right).

for the case in which $b = c$ in the bar, the results given in this section for the axially symmetric model remain the same. To provide evidence for this statement, we show in Fig. 3.4 how the periodic orbits and the stability indexes remain unchanged for $b = c$. Note that in order to compare the symmetric case ($b = c$) with the non-symmetric one (model given in Pfenniger (1984) with $b = 1.5 \neq c = 0.6$), we impose in both models equal bar mass ($GM_b = 0.1$), equal homogeneity ($n_h = 2$) and therefore equal particle distribution. Thus, we take a symmetric bar where the parameters $\tilde{b}$ and $\tilde{c}$ are the geometric mean of the previous parameters, i.e. $\tilde{b} = \tilde{c} = 0.95 \simeq \sqrt{b \cdot c}$. This results in a gravitational field which is approximately the average along time of the previous one.

Comparing Figs. 3.2 and 3.4, we can confirm that the family of periodic orbits around the central equilibrium point L_3 remain essentially the same regardless of whether we use a symmetric bar or not. Moreover, observing the bottom part of both figures, with regard to the stability indexes for both models, periodic orbits are in a comparable range of energy, the cuts of the indexes within the limits $|\pm 2|$ being qualitatively equal.

Therefore, we can conclude this comparison saying that in both models, namely the revolution symmetric and the merely axially symmetric, the periodic orbits are responsible for maintaining the structure of the bar and giving consistency to the model. In this way, we could use any of both models, but since a bar with parameters $b \neq c$ is more commonly observed and we want to compare with the model given in Pfenniger (1984) to prove that our model is consistent in spite of the tilt applied to it, we prefer to show the rest of results for $b \neq c$.

3.1.1 Other family orbits emanating from L_3

Although the x_1 family of periodic orbits around L_3 is the main family to give structure to the bar, other periodic orbits surrounding the central equilibrium point exist. If we think the x_1 family as the family of orbits along the bar major axis, a perpendicular family also exists. This last family, often called x_2 family, is elongated, perpendicular to the bar and stable. Since this family is, like the x_1 family, also inside the bar, it influences the consistence and structure of the bar. In Fig. 3.5 we can observe the behaviour of this family in the precessing model. As it happened with the previous family, the tilting of the model with an angle ε is related with the behaviour of the family. In this case, the family follows the same tilting of the model, which preserves the width of the bar in its minor axis. Moreover we observe that there are no bifurcations of this family.

Other families that we can remark are those such that, departing from the central equilibrium point L_3, acquire high levels of energy, exiting the bar and surrounding it.

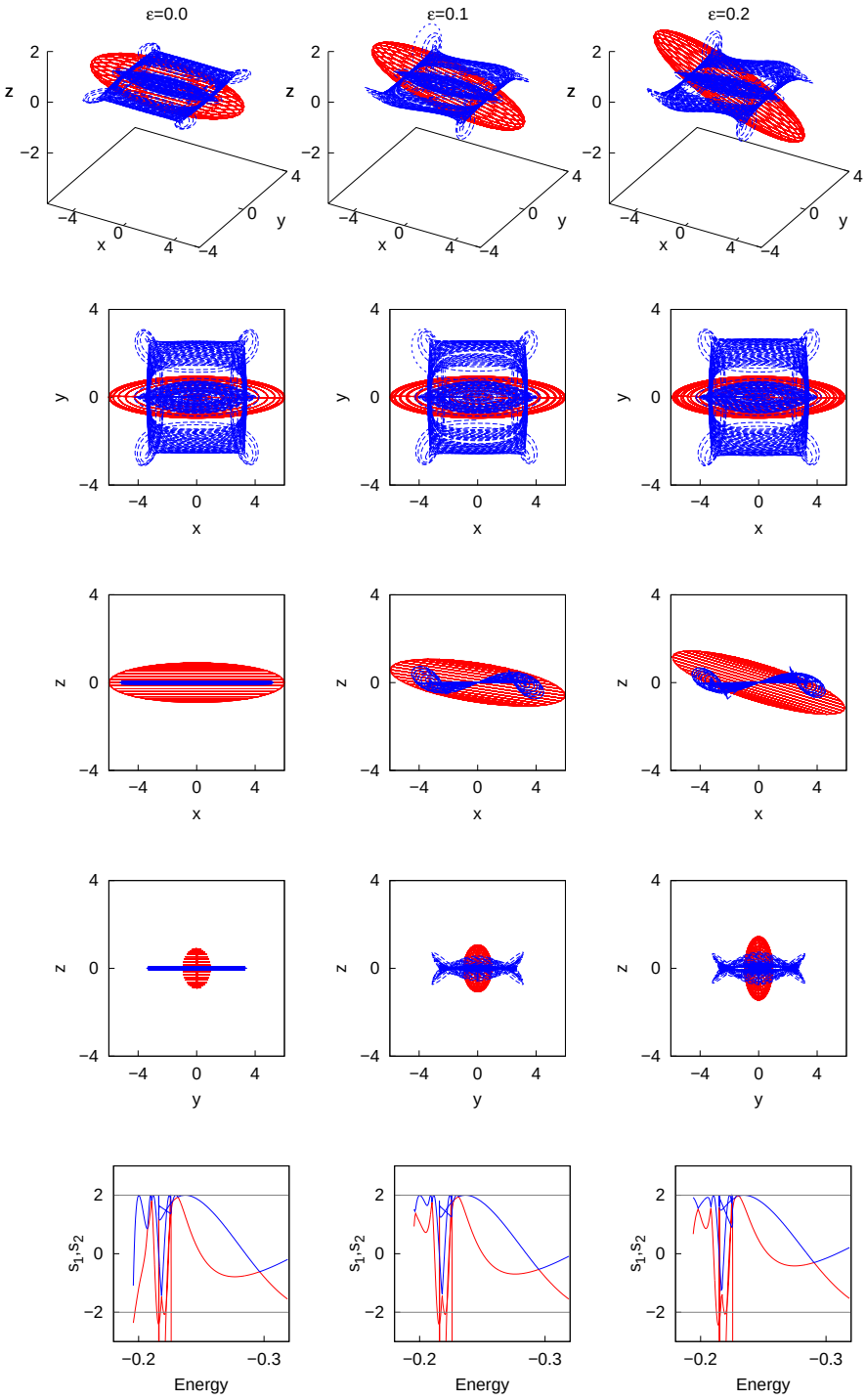

Figure 3.4: x_1 family of periodic orbits and stability indexes for the bar with $b = c = 0.95$ and $\varepsilon = [0, 0.1, 0.2]$ and $GM_b = 0.1$.

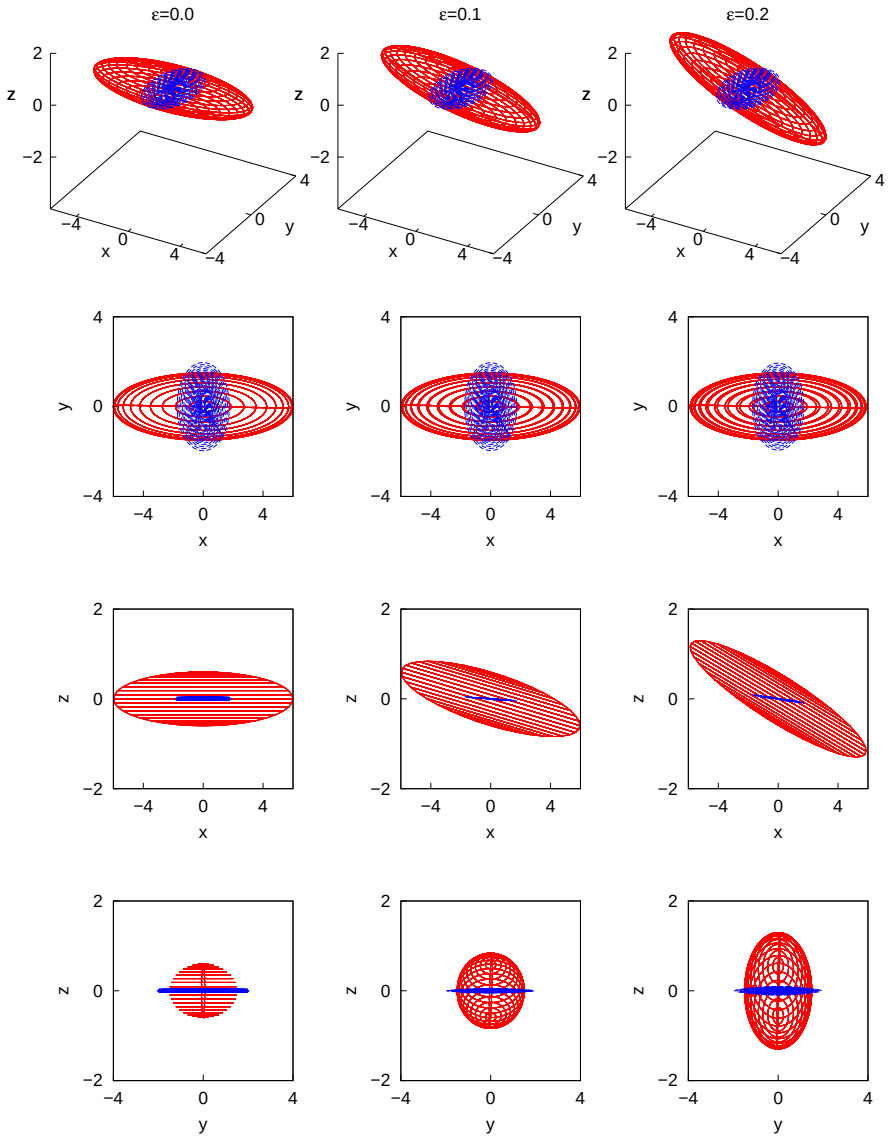

Figure 3.5: x_2 family of vertical periodic orbits inside the bar with $b = 1.5$, $c = 0.6$, $GM_b = 0.1$ and $\varepsilon = [0, 0.1, 0.2]$.

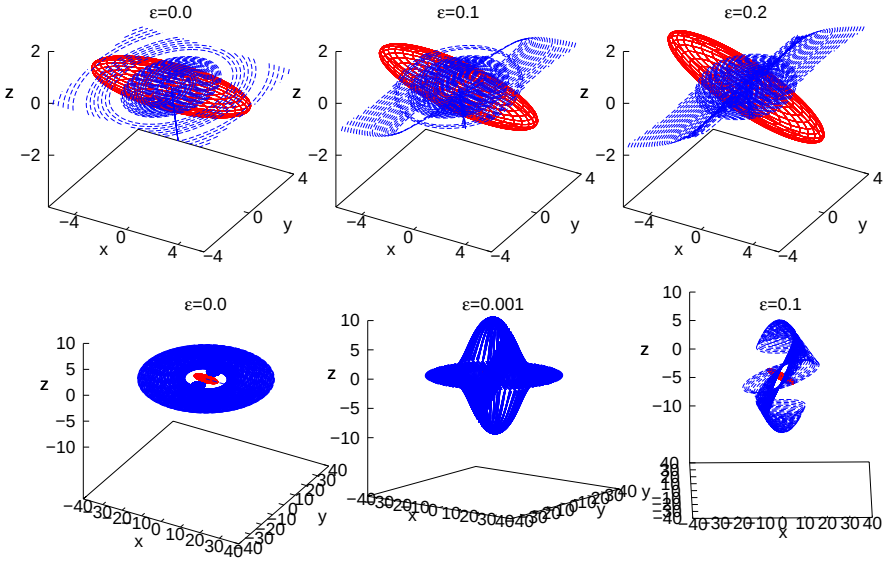

Figure 3.6: Two different families of exterior periodic orbits to the bar with $b = 1.5$, $c = 0.6$, $\varepsilon = [0, 0.1, 0.2]$ for the first family and $\varepsilon = [0, 0.001, 0.1]$ for the second one.

Some of these families do not seem to have any influence either in the structure of the bar or in the motion of the stars around it. But families very close to the bar are possibly important for the deformation of some barred galaxies. Anyway, this is an unexplored question which is not the object of this work. For this reason, we only show some of these families that we have found in Fig. 3.6 for different values of ε. In the bottom of this figure we appreciate a family of periodic orbits which show a deformation similar to two "bulbs" close to the bar for $\varepsilon = 0$, and acquire some curvature when ε reaches 0.001, surrounding completely the bar, whereas when ε takes the value 0.1 rad these periodic orbits cease to close, and the family disappears altogether for greater values of ε.

3.2 Dynamics close to corotation

Once we have analyzed the behaviour of periodic orbits inside the bar, we continue the study considering trajectories outside the bar that are responsible for the main visible building blocks in barred galaxies, i.e. spirals and rings.

Spirals and rings, both inner and outer, are also present in a large fraction of disc galaxies. Identifying their building blocks is important for explaining their formation and evolution, as well as their properties. Moreover they provide information on the properties of the underlying disc galaxy and on the pattern speed and relative strength of the bar.

For this purpose, we aim at finding the building blocks of spiral arms and of inner and outer rings in barred galaxies. In this line, we continue the work done in Romero-Gómez et al. (2006, 2007), Athanassoula et al. (2009), where a new theory is proposed to explain the formation of both rings and spirals in barred galaxies. The theory is based on the chaotic orbital motion driven by the unstable equilibrium points of the rotating bar potential. They suggest that spirals, rings and pseudorings are related to the invariant manifolds associated to the periodic orbits around the Lagrangian equilibrium points L_1 and L_2. To establish this link, the authors compute the unstable and stable manifolds in a large number of cases, covering the relevant parameter space of three simple barred galaxy models and obtain, in a clear way, which parameters of the models are responsible for the morphology of the arms and rings of the galaxy.

Continuing with this line, we start considering the model used in Romero-Gómez et al. (2006), which is a simple, yet realistic, barred galaxy model. But, instead of working with a two-dimensional model as in the cited papers, we need to consider a three-dimensional precessing model to show galaxies in space and to reproduce warped galaxies.

Having this in mind, let us first briefly recall the essential role of the invariant manifolds. In our context, normally hyperbolic invariant manifolds are associated to the unstable character of the libration point orbits about L_1 and L_2 and so, they do not exist about L_3. The set of these orbits consists of trajectories that are asymptotic to the periodic orbit forward in time (stable manifold) or backwards in time (unstable manifold) and are responsible for the transport of matter between the neighborhood of the bar and the exterior part of the galaxy. The stars trapped in these manifolds make visible their structure in the form of rings and arms.

Let us start analysing the stability character of the libration points at corotation. The eigenvalues of the differential matrix (3.5) around L_1 and L_2 are of the form $\{\lambda, -\lambda, \mu i, -\mu i, \omega i, -\omega i\}$ ($\lambda, \mu, \omega \in \mathbb{R}^+$), for any value of ε. This is, the two real eigenvalues are related to a hyperbolic behaviour like a saddle, whereas the purely imaginary are associated to libration motions. This implies that the linearised flow around L_1 and L_2 in the rotating frame of coordinates is characterised by a superposition of a saddle and two harmonic oscillations that is usually described as a saddle×centre×centre behaviour. L_1 and L_2 are unstable and are called hyperbolic points. The dynamics around the unstable equilibrium points in our context are described in detail in Section 2.4 and here just a brief summary follows.

As is well known, around each unstable equilibrium point, L_1 and L_2, there must exist a family of periodic orbits associated with the eigenvalues of the elliptical part. They are the planar and vertical families of Lyapunov periodic orbits. These orbits are unstable

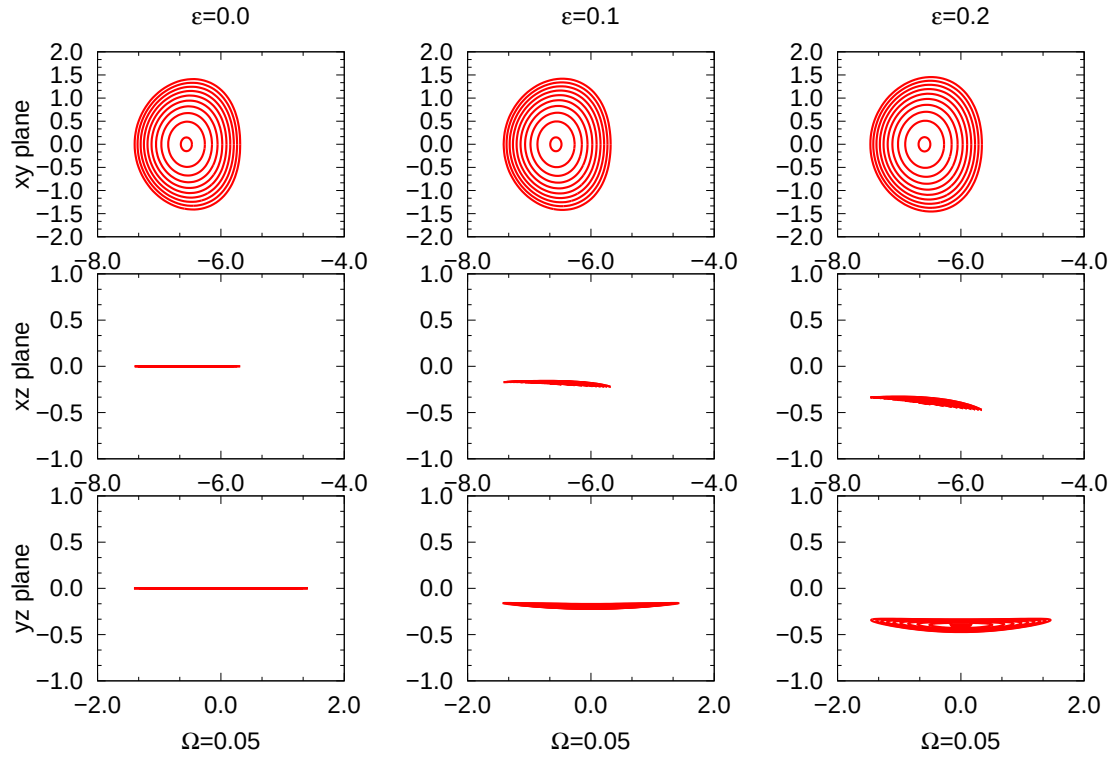

Figure 3.7: Lyapunov family of periodic orbits about L_2 for the model with $GM_b = 0.1$ and for a range of values of the Jacobi constant in $(C_{L_2}, C_{L_2} + 2 \times 10^{-3})$, where $C_{L_2}(\varepsilon = 0) = -0.1879$, $C_{L_2}(\varepsilon = 0.1) = -0.1876$ and $C_{L_2}(\varepsilon = 0.2) = -0.1865$. The tilt angle $\varepsilon \in [0, 0.2]$. Note the varying scale of the vertical axis.

in the vicinity of the equilibrium point and we are interested in the planar family as in Romero-Gómez et al. (2006).

In Fig. 3.7, different projections of Lyapunov orbits are shown. It can be clearly seen from the yz projection that the orbit acquires some out of plane curvature when the parameter ε increases. Moreover, the z component of the orbit decreases with ε (having in mind that we are showing the Lyapunov orbits about L_2, the opposite happens for the ones about L_1). This is, the libration point and the orbit are not strictly contained in the plane $z = 0$ when $\varepsilon \neq 0$. Therefore, the periodic orbits are not strictly planar.

Since the unstable equilibrium points has a saddle×centre×centre behaviour, the two centre factors give rise to a family of quasi-periodic orbits surrounding the unstable equilibrium points, called Lissajous orbits, obtained as the product of the two linear oscillations related with the planar and vertical Lyapunov orbits of the two centre factors. These Lissajous orbits are contained in invariant tori of the same energy level. These

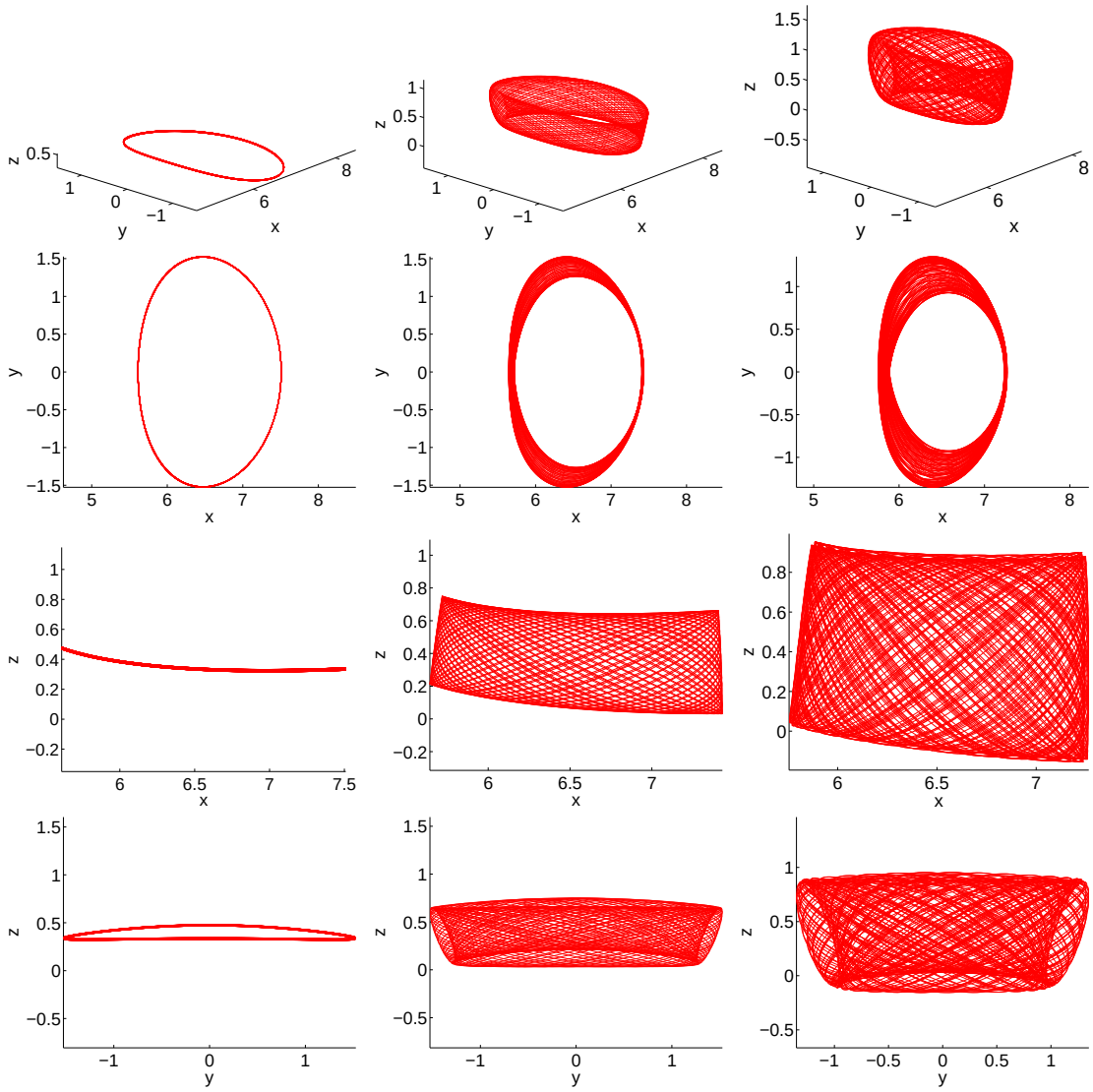

Figure 3.8: Lyapunov orbit (first column) and its associated Lissajous quasi-periodic orbits (second and third columns) around L_1 for the model with $GM_b = 0.1$ and for a Jacobi constant $C_{L_1} + 2 \times 10^{-3}$, where $C_{L_1}(\varepsilon = 0.2) = -0.1865$. The tilt angle is set to $\varepsilon = 0.2$. Note the varying scale of the z axis. Orbits computed in collaboration with Zubin Olikara (IEEC).

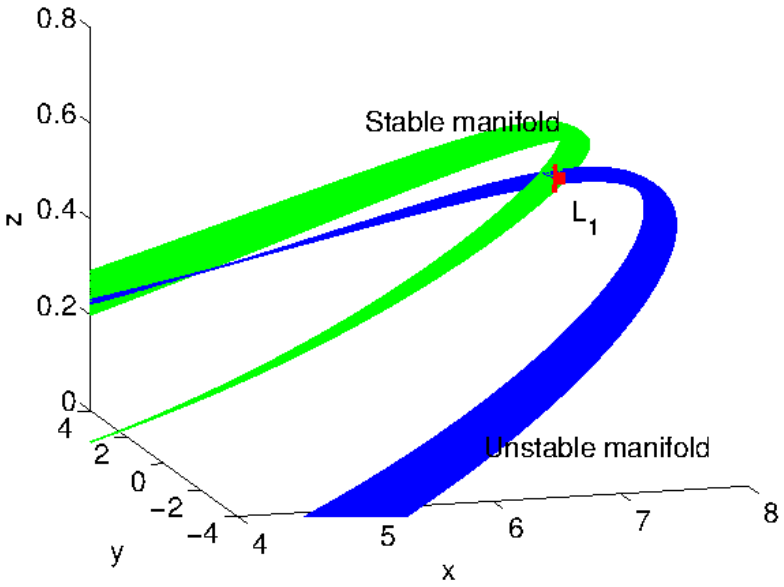

Figure 3.9: Stable and unstable invariant manifold associated to the periodic orbit around L_1 with $\varepsilon = 0.2$ and $GM_b = 0.3$.

orbits have been computed for the equilibrium point L_1 and $\varepsilon = 0.2$ in collaboration with Zubin Olikara (IEEC). Figure 3.8 shows the evolution of the quasi-periodic orbits at an energy level $C_{L_1} + 2 \times 10^{-3}$, starting from the planar Lyapunov orbit. The rows in the figure correspond to different projections, indicated by the axes. The first column shows the projections of the original planar Lyapunov orbit for $\varepsilon = 0.2$ around the L_1 point. The second and third columns present the projection of a Lissajous orbit close to the Lyapunov orbit of the same energy level and the invariant torus that the Lissajous orbit defines, respectively. The out of plane component of the original Lyapunov orbit and of the invariant tori defined by the two Lissajous orbits can be clearly seen in the xz projection shown in the third row.

For a given energy level, two sets of asymptotic orbits emanate from the Lyapunov periodic orbit, they are known as the stable and the unstable invariant manifold respectively and each set has two branches (see Fig. 3.9).

We denote by $W^s_{\gamma_i}$ the stable invariant manifold associated to the periodic orbit γ_i around the equilibrium point L_i, $i = 1, 2$. This stable invariant manifold is the set of orbits that tend to the periodic orbit asymptotically forward in time. On the other hand, we denote by $W^u_{\gamma_i}$ the unstable invariant manifold associated to the periodic orbit γ_i around the equilibrium point L_i, $i = 1, 2$. This unstable invariant manifold is the set of orbits that departs asymptotically from the periodic orbit (i.e. orbits that tend to Lyapunov orbits

backwards in time). Since the invariant manifolds extend well beyond the neighbourhood of the equilibrium points, they are responsible for the global structures and the transport of matter.

As invariant manifolds give rise to external structures, in Figs. 3.10 and 3.11 we show the unstable manifolds for the precessing model. In both figures we have chosen the values $GM_b = 0.1$ and $GM_d = 0.9$ for the first row, $GM_b = 0.2$ and $GM_d = 0.8$ for the second row, $GM_b = 0.3$ and $GM_d = 0.7$ for the third row and, $GM_b = 0.4$ and $GM_d = 0.6$ for the last row. Moreover, we have set the tilt angle $\varepsilon = 0$ in the first column, $\varepsilon = 0.1$ in the second column and $\varepsilon = 0.2$ in the last column for each figure. Also, we have selected the pattern speed $\Omega = 0.05$ for Fig. 3.10, and $\Omega = 0.06$ for Fig. 3.11.

In these figures, we observe the xy projection of the invariant manifolds of Lyapunov orbits around the equilibrium points, L_1 and L_2, varying with the tilt of the model, the angular velocity or the bar mass.

When $\Omega = 0.05$ (Fig. 3.10), we observe that the structure of invariant manifolds (that reproduce the shape of galaxies) is preserved for different values of ε, but with small particularities. For example, the position of the invariant manifolds is not exactly the same in the three columns for a given value of GM_b. In this way, we can see that the structure remains but the spiral arms slowly open up. Moreover, when the bar mass increases, the structure moves from a morphology of a rR_1 ringed galaxy to the one of a spiral galaxy as expected (Romero-Gómez et al., 2007).

When we increase the pattern speed to $\Omega = 0.06$, we appreciate (in Fig. 3.11) that, although the basic structure is preserved, the arms are more open even in the first rows of the figure. And again, the behaviour of the manifolds is the same with respect to the variation of ε.

Figures 3.12 and 3.13 show the previous graphics in three dimensions, in order to better appreciate the variation with respect to the tilt angle of the model. Here, we clearly see the structures that have been discussed before, and we see how the invariant manifolds change in the z-component. In the projections of Figs. 3.18 and 3.19, we even appreciate these changes in a better way.

Intersections between stable and unstable manifolds of periodic orbits of the same energy level give rise to structures responsible for the transport of matter in the galaxy. In this context, we call heteroclinic orbits the orbits which correspond to asymptotic trajectories, ψ, such that $\psi \in W^u_{\gamma_i} \cap W^s_{\gamma_j}$, $i \neq j$, $i, j = 1, 2$. Thus, a heteroclinic orbit departs asymptotically from the periodic orbit γ_i around L_i and approaches asymptotically the periodic orbit around L_j, $i \neq j$. The existence of these heteroclinic orbits makes the

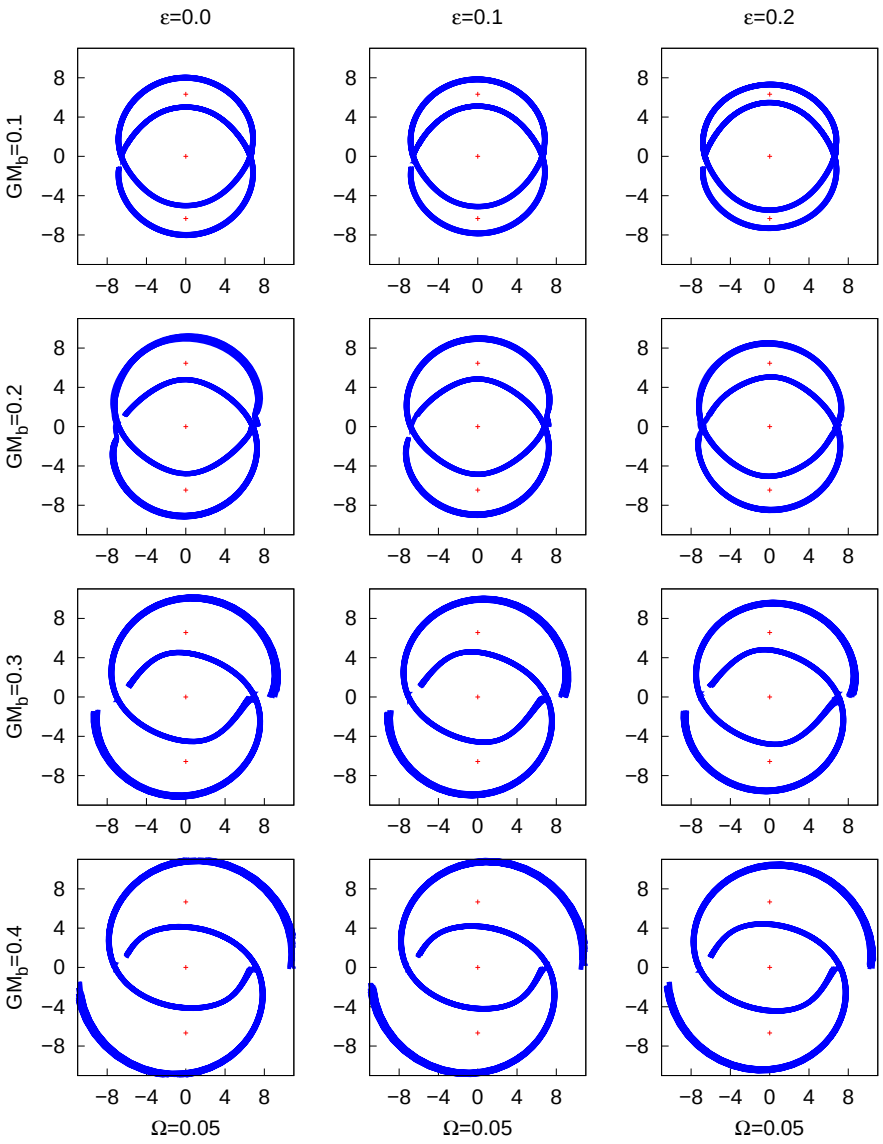

Figure 3.10: Unstable manifold for the Miyamoto-Nagai Ferrers model with $GM_d \in [0.6, 0.9]$, $GM_b \in [0.1, 0.4]$, $\Omega = 0.05$ and the tilt angle $\varepsilon \in [0, 0.2]$.

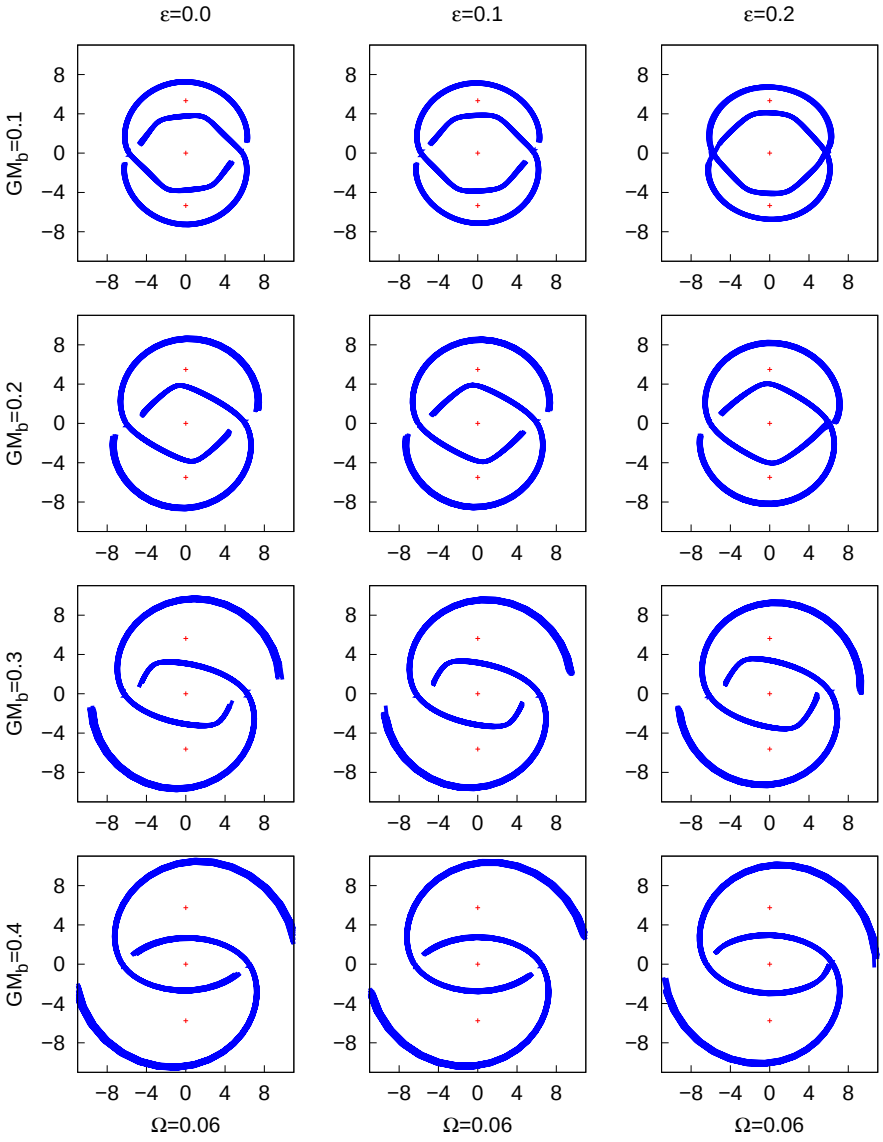

Figure 3.11: As in Fig. 3.10 for $\Omega = 0.06$.

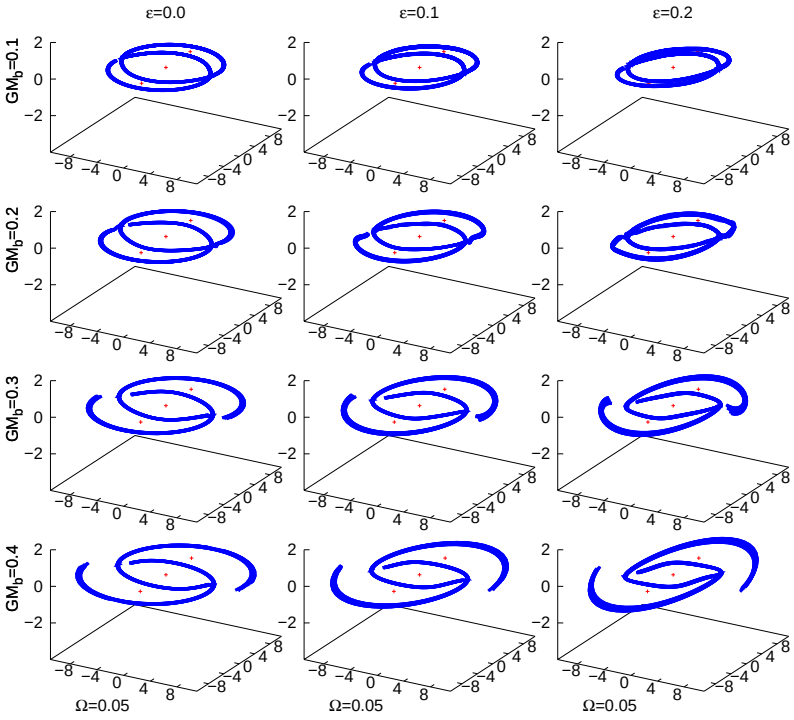

Figure 3.12: 3D view of the plots shown in Fig. 3.10.

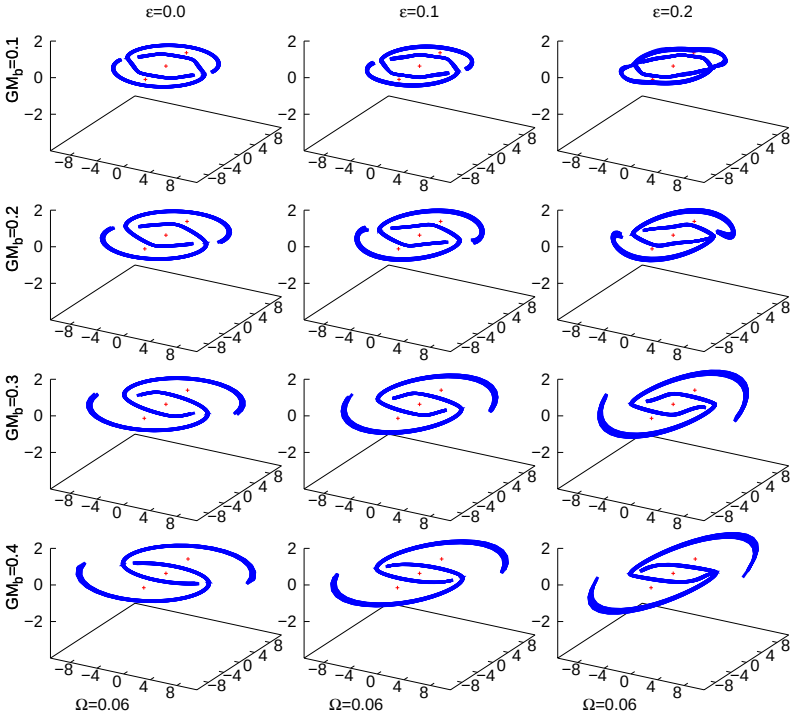

Figure 3.13: 3D view of the plots shown in Fig. 3.11.

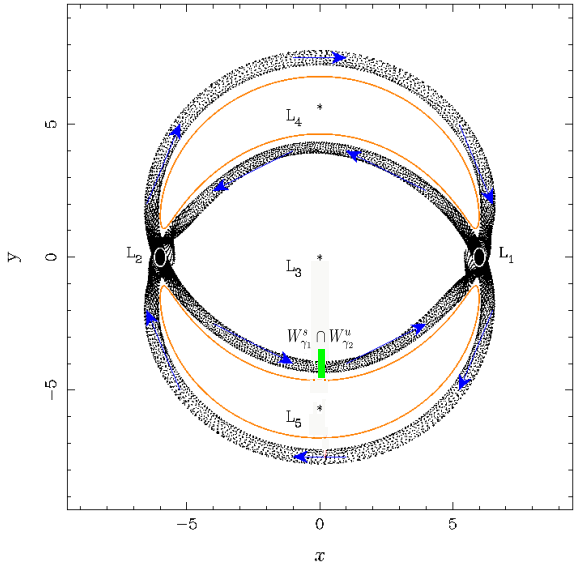

Figure 3.14: Sense of circulation of matter (blue arrows) along a rR_1 ringed galaxy. The green line marks the intersection with the hyperplane S. Image adapted from Athanassoula et al. (2009)

galaxy a rR_1 ringed galaxy, because they establish a closed path along which the matter is transported (Fig. 3.14).

In general, the transfer of matter occurs mainly from the inner region delimited between the bar and the zero velocity curves to the outer region. The transit orbits are responsible for this action. These transit orbits follow the invariant manifolds for a range of energies up to the level of the equilibrium point. For example, the inner branch of the stable invariant manifold from L_1 contains orbits that go from the inner region to the outer region following the outer branch of the unstable invariant manifold of L_1 (see Fig. 3.15). The transit orbits also arise from the intersection of the regions delimited respectively by the inner branch of an unstable manifold from one of the unstable equilibrium points, $W^u_{\gamma_i}$, $i = 1, 2$, and the inner branch of a stable manifold from the other one, $W^s_{\gamma_j}$, $j \neq i$, if this intersection is nonempty. On the other hand, the non-transit orbits are those that stay out of the manifold and move only around the bar without going out to the outer regions.

As the dynamics of our system takes place in a six dimensional phase space, we compute the intersections of the trajectories of the invariant manifolds with the hyperplane S given by the section $x = 0$ in phase space, for a low bar mass model with parameters $GM_b = 0.1$, $GM_d = 0.9$, $\Omega = 0.05$ and $\varepsilon \in [0, 0.2]$ (top row of Fig. 3.12). We consider the inner branch of the stable invariant manifold of the Lyapunov orbit around L_1, $W^s_{\gamma_1}$,

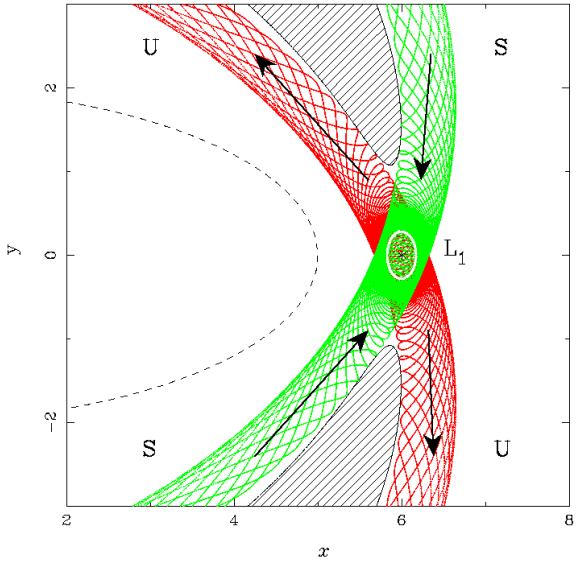

Figure 3.15: Dynamics around L_1. The arrows give the direction of motion along the invariant manifolds (S stable, U unstable) and the stripped areas are the forbidden regions surrounded by the ZVCs. Image taken from Athanassoula et al. (2009).

and the inner branch of the unstable invariant manifold of the Lyapunov orbit around L_2, $W^u_{\gamma_2}$. The intersection of the invariant manifolds with the hyperplane S are two closed curves. We denote by $W^{s,1}_{\gamma_1}$ the closed curve resulting from the first intersection of $W^s_{\gamma_1}$, and by $W^{u,1}_{\gamma_2}$ the closed curve resulting from the first intersection of $W^u_{\gamma_2}$. The intersection $W^{s,1}_{\gamma_1} \cap W^{u,1}_{\gamma_2}$ corresponds to heteroclinic orbits for the given energy level of the invariant manifolds, and if the overlap of the regions bounded by $W^{s,1}_{\gamma_1}$ and $W^{u,1}_{\gamma_2}$ is nonempty it gives rise to transit orbits.

As mentioned, in Fig. 3.16 we plot the intersection of the invariant manifolds in S using coordinates $y\dot{y}$, $z\dot{z}$ and yz for ε ranging from 0 to 0.2 rad. Each trajectory in each invariant manifold intersects the hyperplane S in a unique point $(0, y, z, \dot{x}, \dot{y}, \dot{z})$, that projects onto the planes $y\dot{y}$, $z\dot{z}$ and yz. We are interested in studying the transfer of matter from the inner region around the bar to the outer region.

When the tilt angle ε takes the value $\varepsilon = 0$, the plane $z = 0$ is an invariant, so the phase space is reduced to four dimensions, which, together with the fixed energy level, let us define exactly the intersections between curves in the hyperplane $x = 0$. Therefore, in the left column of Fig. 3.16 we observe that for $\varepsilon = 0$ there are two heteroclinic orbits corresponding to the intersection of $W^{s,1}_{\gamma_1}$ and $W^{u,1}_{\gamma_2}$. Let us note that the curves $W^{s,1}_{\gamma_1}$ and $W^{u,1}_{\gamma_2}$ do not overlap, but they are very close and intersect in two points. The points on the curve $W^{s,1}_{\gamma_1}$ belong to $W^s_{\gamma_1}$, so they are orbits that tend asymptotically to the Lyapunov

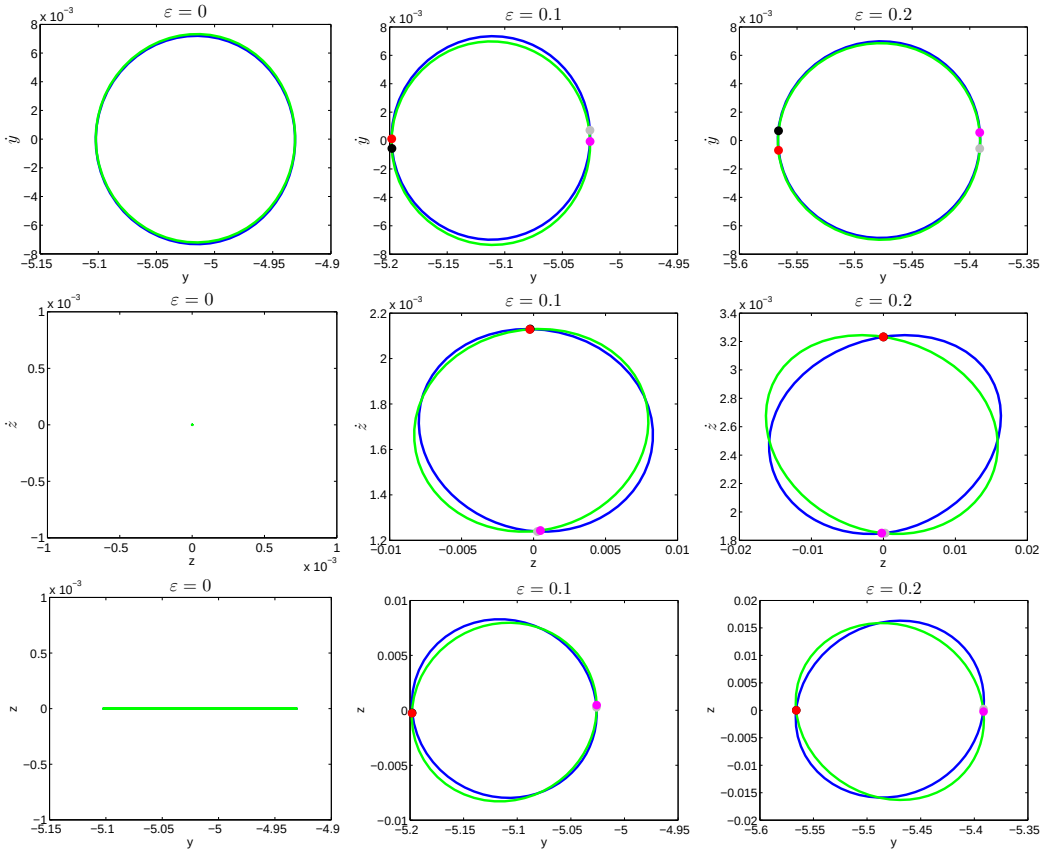

Figure 3.16: For the precessing model with parameters $GM_b = 0.1$, $GM_d = 0.9$, $\Omega = 0.05$, and tilting angle from left to right $\varepsilon = 0$, $\varepsilon = 0.1$ and $\varepsilon = 0.2$, the curves $W^{s,1}_{\gamma_1}$ (in blue) and $W^{u,1}_{\gamma_2}$ (in green) are projected in the plane, from top to down, $(y, \dot{y})$, $(z, \dot{z})$ and (y, z). For $\varepsilon > 0$ the projections of two fixed pairs of near intersection points between the invariant manifolds $W^s_{\gamma_1}$ and $W^u_{\gamma_2}$ are plotted in every plane (one pair in black and red, the other in grey and magenta).

orbit. In the same manner, the points on the curve $W^{u,1}_{\gamma_2}$ belong to $W^{u}_{\gamma_2}$, therefore they are orbits that depart asymptotically to the Lyapunov orbit. The points that project outside both curves, $W^{s,1}_{\gamma_1}$ and $W^{u,1}_{\gamma_2}$, are states whose trajectories remain inside the inner region of the galaxy delimited by the zero velocity curves, i.e. they are non-transit orbits. But the points that project inside the intersection defined by both curves correspond to orbits that transit from the inner region to the outer one, i.e. they are transit orbits. In this way, the invariant manifolds of the Lyapunov orbits drive the motion of the stars from the inner to the outer regions.

When $\varepsilon = 0.1$, 0.2 (center and right columns) we come back to a six dimensional phase space where curve intersections are not transversal, and therefore, numerical techniques will detect only near intersections, i.e. approximations of the curves to very small distances, rather than the intersections themselves. In spite of this fact, the projections into the $y\dot{y}$, $z\dot{z}$, yz planes let us approximate the intersection points between curves. As we observe, the projections of $W^{s,1}_{\gamma_1}$ and $W^{u,1}_{\gamma_2}$ for $\varepsilon \neq 0$ show that there is no strict intersection between the curves (which would appear as a common intersection point in all projections) but there are two points of near intersection between the two curves, namely two pairs of points from each curve at a distance $O(10^{-3})$ (the magenta and grey, and the black and red, in Fig. 3.16). Although there are no strict intersections when ε increases, the closeness of the curves of $W^{s,1}_{\gamma_1}$ and $W^{u,1}_{\gamma_2}$ and the fact that the tilt angle is small, constitute evidence towards the existence of transit orbits.

Although we can only find near intersections between $W^{s,1}_{\gamma_1}$ and $W^{u,1}_{\gamma_2}$ for $\varepsilon > 0$, there are heteroclinic connections between planar Lyapunov orbits and quasi-periodic orbits (Lissajous orbits). For $\varepsilon = 0.2$, Fig. 3.17 shows the heteroclinic connection, computed in collaboration with Zubin Olikara (IEEC), between a Lyapunov orbit around L_1 and a Lissajous orbit around L_2 of small z-amplitude, i.e. close to the corresponding Lyapunov orbit, at the same energy level. The trajectory moves close to the Lissajous orbit around L_2, then it approaches the unstable manifold of the Lissajous orbit and escapes from it reaching the stable manifold of the Lyapunov orbit around L_1. Therefore we have found evidence that there exist heteroclinic connections between the unstable equilibrium points, as happened in the case of $\varepsilon = 0$.

After our discussion of heteroclinic orbits, let us continue with the study of the spatial projections of the invariant manifolds in the precessing model. In Figs. 3.18 and 3.19, we show an approach on the evidence of detected warps in galaxies. Depending on the point of view, and for a tilt angle $\varepsilon > 0$, we observe that the outer branches of the unstable manifold are clearly warped, emulating the shape observed in some catalogued galaxies. This is appreciated in some figures. For example, when we take a bar mass

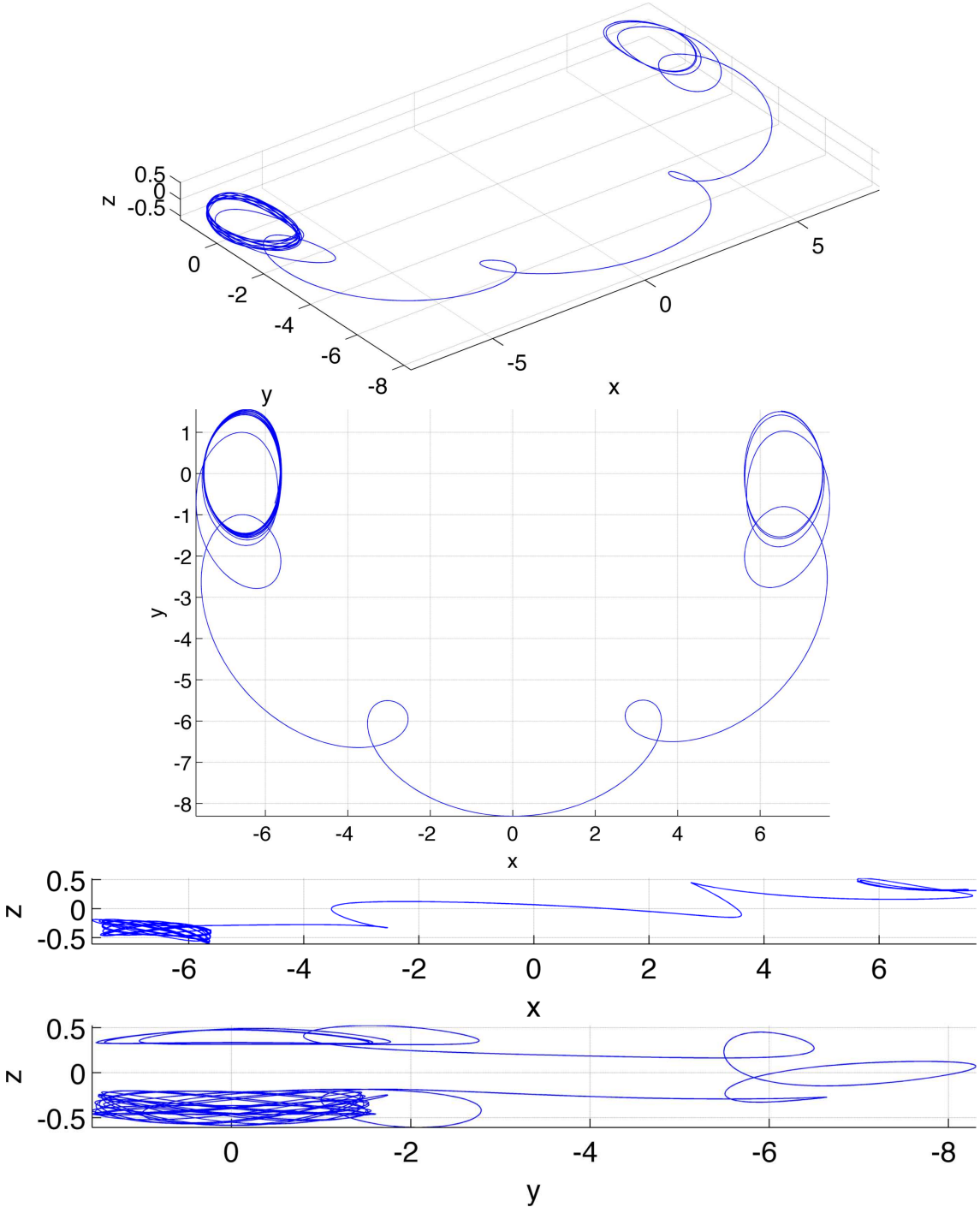

Figure 3.17: For the precessing model with parameters $GM_b = 0.1$, $GM_d = 0.9$, $\Omega = 0.05$, and tilting angle $\varepsilon = 0.2$, a heteroclinic connection between a Lyapunov orbit around L_1 and a Lissajous orbit around L_2 is projected to, from top to down, xyz space, xy plane, xz plane and yz plane. Heteroclinic connection computed in collaboration with Zubin Olikara (IEEC).

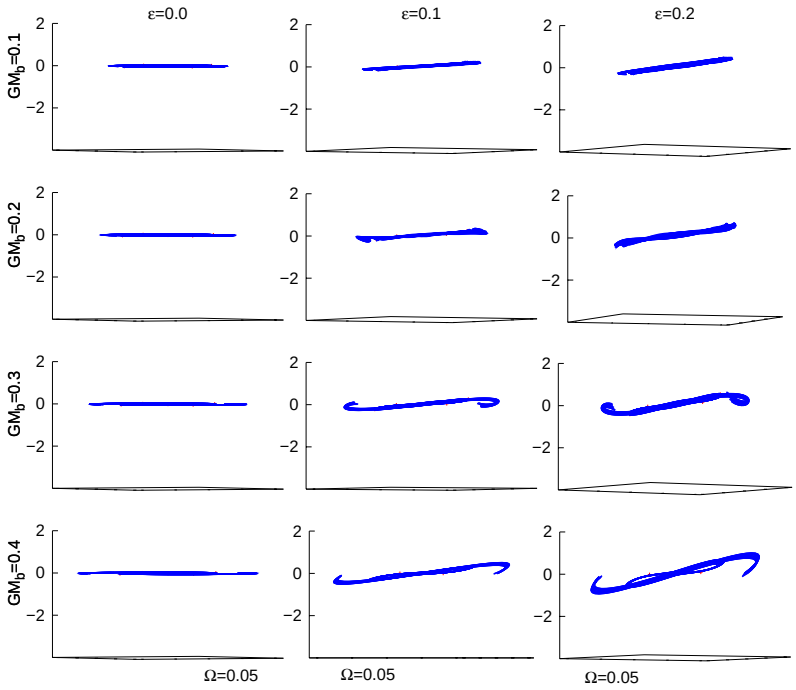

Figure 3.18: Near edge-on view of the plots shown in Fig. 3.10.

$GM_b = 0.2$, all plots present a warped shape, and differences among them are obtained when one varies the inclination and pattern speed.

Looking at Fig. 3.18, we can see that no warped shape appears with $\varepsilon = 0$ as expected. But, when ε is increased, as well as GM_b, different warp shapes are clearly appreciated. With $GM_b = 0.2$, invariant manifolds are just hinting the shape of warps, and when the bar mass reaches $GM_b = 0.3$, the warps are clearly evidenced.

The same phenomenon occurs for the pattern speed $\Omega = 0.06$ (Fig. 3.19). But in this case the warped structure is present for a larger variety of parameter combinations. With $\varepsilon > 0$, a warp is present with already a bar mass of $GM_b = 0.2$. As GM_b increases, the S-shape of the warp becomes more evident, increasing its inclination with respect to the galactic plane, being the most tilted case the one with $\varepsilon = 0.2$ and $GM_b = 0.4$. Note also that the contribution of the inner branches of the invariant manifolds are more evident with a faster pattern speed than with $\Omega = 0.05$.

To get a global vision, in the left part of Fig. 3.20 we show the invariant manifolds for $GM_b = 0.3$, $\Omega = 0.05$ and $\varepsilon = 0.2$, together with the Ferrers bar and the zero velocity surface of the energy level considered. As these parameters are selected in such a way that a noticeable warp is formed, in the right part of Fig. 3.20 the relation of the family of

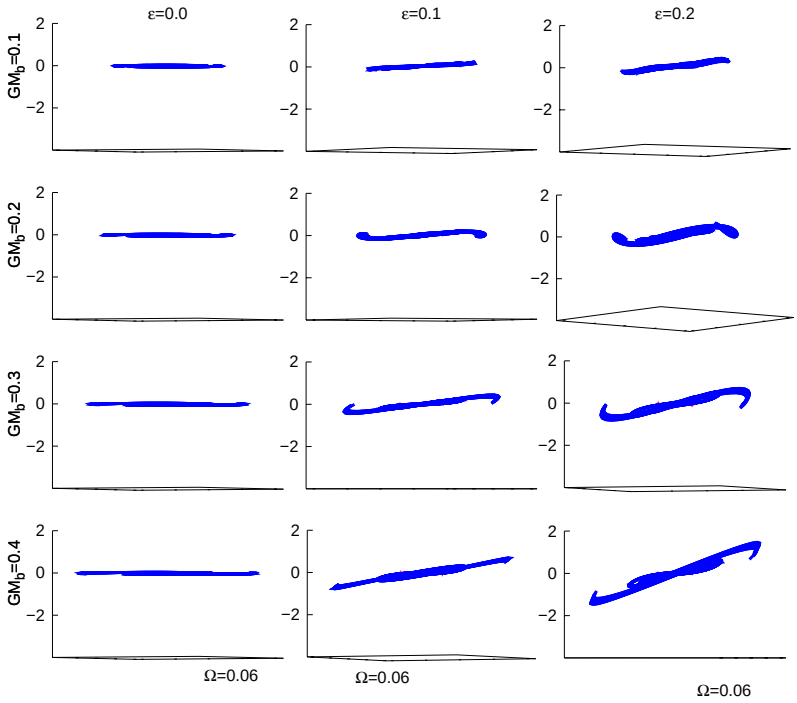

Figure 3.19: Near edge-on view of the plots shown in Fig. 3.11.

periodic orbits inside the bar with the invariant manifolds is shown. Note how the periodic orbits follow the same tilt as the invariant manifolds.

In summary, we deduce that the warp formation is closely related to the pattern speed of the bar, the bar mass and, specially, to the tilt angle of the model, as we expected. We can conclude that the amplitude of the warp increases with the bar mass, pattern speed and, above all, the tilt angle. Also note that if we consider a symmetric bar instead of a bar with $b \neq c$, computations like the ones described show that the results obtained are essentially identical.

As an example, if we select the figure with $\varepsilon = 0.2, \Omega = 0.05$ and $GM_b = 0.3$, we are able to appreciate the strong resemblance with the galaxy warp of the Integral Sign Galaxy (Fig. 3.21).

3.2.1 Warp angles

As already detected in the previous section, there seems to exist a correlation between the warp amplitude and the bar mass and pattern speed. In this section, we study quantitatively this relation.

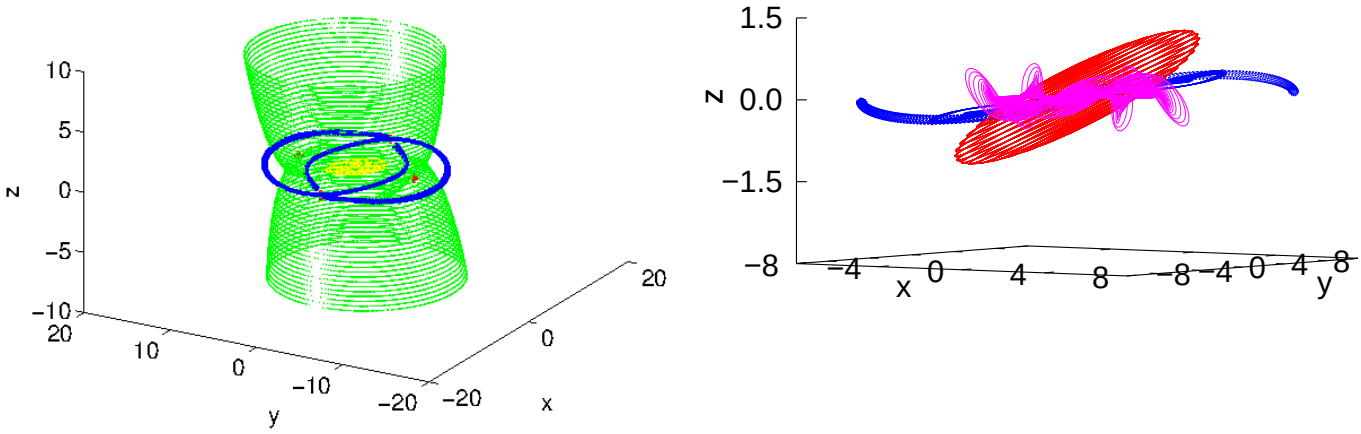

Figure 3.20: Left: Invariant manifold (blue), zero velocity surface (green) and Ferrers bar (yellow) when $GM_b = 0.3$, $\Omega = 0.05$ and $\varepsilon = 0.2$. Right: Invariant manifold (blue), periodic orbits inside the bar (purple) and Ferrers bar (red) with the same parameters.

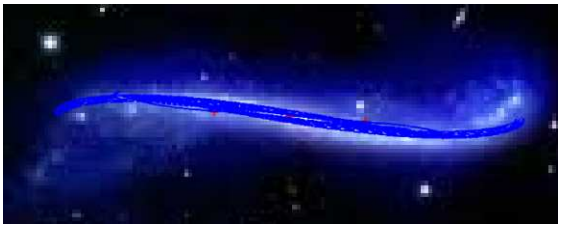

Figure 3.21: Warp obtained with the parameters $\varepsilon = 0.2, \Omega = 0.05$ and $GM_b = 0.3$ (blue) superimposed to the Integral Sign Galaxy, UGC 3697.

ε	Ω	GM_b	θ (°)
0.1	0.05	0.1 - 0.4	1.8 - 3.9
0.1	0.06	0.1 - 0.4	1.8 - 4.8
0.2	0.05	0.1 - 0.4	3.8 - 7.7
0.2	0.06	0.1 - 0.4	3.7 - 9.3

Table 3.1: Warp angles θ (in degrees) obtained in the precessing model.

We define the *maximal amplitude of the warp*, or *warp angle*, as the angle between the outermost detected point and the mean position of the plane of symmetry, as defined by the internal unwarped region (see Fig. 3.22), as in Sánchez-Saavedra et al. (2003).

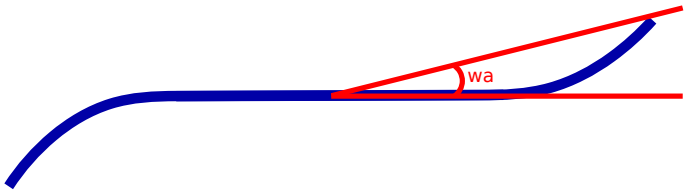

Figure 3.22: Definition of warp angle.

The warp angle obtained in our theoretical analysis varies considerably depending on the pattern speed, bar and disc masses and, above all, the tilt angle ε. As we can observe in Table 3.1, when the pattern speed increases, the warp angle increases too. The same phenomenon occurs when we fix a pattern speed and increase the bar mass, but the biggest increment takes place when the tilt angle ε grows. In this context, there are no warps when $\varepsilon = 0$, but the highest warp angle, $\theta = 9.3°$, is reached when we use the maximum values considered for all the variables. For example, for a pattern speed of $\Omega = 0.05$, the maximum angle obtained is $\theta = 7.7°$, by setting the parameters $\varepsilon = 0.2$, $GM_b = 0.4$, $GM_d = 0.6$. Whereas, if we take a pattern speed of $\Omega = 0.06$, and keep the previous values for the remaining parameters, we obtain a warp angle of $\theta = 9.3°$.

The catalog of warps in the Southern hemisphere (Sánchez-Saavedra et al., 2003) shows that most warps have angles less than 11°, which is very close to the maximum warp angle of $\theta = 9.3°$ which we have obtained with our theoretical model. Let us notice that the tilt angle ε has to be small, since a bigger tilt angle would destabilize the model leading to chaotic dynamics instead of to the formation of a galaxy. The model is stable up to tilt angles slightly above $\varepsilon = 0.25$ rad, which could produce warp angles close to 11°.

3.3 Test particle simulations

The advantage of test particle simulations is that the stars are evolved using a known galactic potential and they have inherited the information on both density and kinematics, that is, the stars are in statistical equilibrium with the imposed potential after a certain integration time. They are used as generators of mock catalogues (Romero-Gómez et al., 2015) or to obtain information about the imposed potential by studying certain aspects of the simulation, for example the moving groups in the Solar Neighbourhood (e.g. Dehnen, 2000, Fux, 2001, Gardner & Flynn, 2010, Minchev et al., 2010, Antoja et al., 2011).

Here we use test particle simulations to check how particles respond to the precessing model. We generate a set of 10^6 particles using the Hernquist method (Hernquist, 1993). The density follows the same Miyamoto-Nagai disc (see Appendix of Romero-Gómez et al. (2015)) as in the analytical computations. We give particles the initial velocity for a circular orbit with zero dispersion. The bar pattern speed is set to $\Omega = 0.05$ kpc/[u$_t$], i.e. 1 bar rotation takes 125 Myr. The bar is introduced adiabatically in $t_1 = 16$ bar rotations, using the same time function as in Dehnen (2000) in the precessing model:

$$A_b = A_f \left(\frac{3}{16}\xi^5 - \frac{5}{8}\xi^3 + \frac{15}{16}\xi + \frac{1}{2} \right), \xi \equiv 2\frac{t}{t_1} - 1, \, t \in (0, t_1), \tag{3.9}$$

and $A_b = 0$ if $t \leq 0$. A_b grows with time in the interval $t \in (0, t_1)$, and assumes its maximal amplitude when $t \geq t_1$, in which $A_b = A_f$, that is, it assumes the total bar amplitude. Since Eq. (3.9) is continuous and derivable, a smooth transition from non-barred to a barred galaxy is guaranteed.

In order to keep the total mass of the system constant when we introduce the bar adiabatically, we transfer mass from the disc to the bar progressively, setting

$$\phi_T = (1 - f(t)f_0)\phi_d + f(t)\phi_b, \tag{3.10}$$

where ϕ_T is the total potential of the system, ϕ_d, ϕ_b the potentials of the disc and bar, respectively, and the time function $f(t)$ is the same polynomial of time t as in the previous equation (3.9). The parameter f_0 takes the value of the final bar mass, $f_0 = GM_b = 0.3$, so that when the integration time reaches the maximum amplitude of the bar, $t = t_1$, the bar mass is $GM_b = 0.3$ and the mass disc $GM_d = 0.7$.

In the case studied here we use the following set of parameters once the final configuration is reached: $A = 3$ kpc, $B = 1$ kpc, $GM_d = 0.7$ for the disc, and $n = 2$, $a = 6$ kpc, $b = 1.5$ kpc, $c = 0.6$ kpc, $GM_b = 0.3$ for the bar ($G(M_d + M_b) = 1$). The tilt angle is $\varepsilon = 0.2$ rad $= 11.46°$. This model corresponds to the panel in third row and third

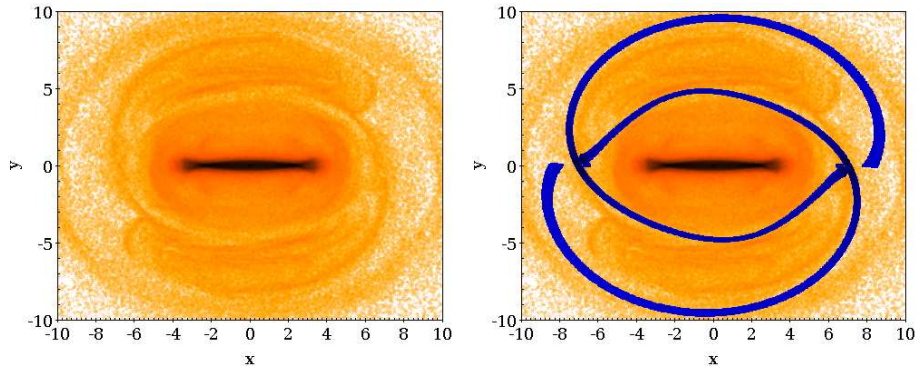

Figure 3.23: Left: Surface density of the xy-projection of the test particle simulation for $GM_d = 0.7$, $GM_b = 0.3$, $\Omega = 0.05$ and $\varepsilon = 0.2$ rad. Right: Overlap of the invariant manifolds for the same parameters (in blue) with Jacobi constant $C = -0.19366$.

column in Fig. 3.18 and to the model shown in Fig. 3.21, where we compare the invariant manifolds with the Integral Sign Galaxy.

The particles in the xy plane adopt the shape seen in Sect. 3.2. The top panel of Fig. 3.23 presents the configuration of the particles, which acquire characteristic features. We observe how some particles are concentrated in the region of the zero velocity curves, which prevents these particles from exiting the region. Also, the particles in the outer parts of the zero velocity curves adopt the shape of the invariant manifolds as we expected. This is shown in the bottom panel of Fig. 3.23, where, for the selected model, we overlap the invariant manifolds of the unstable orbits around L_1 and L_2 with a Jacobi integral C close to that of the equilibrium point L_1 ($C = -0.19366$ and $C_{J,L_1} = -0.19368$).

In Fig. 3.24 we show the surface density and its contour levels in the xz-projection of the test particle simulation (top panel) and we overlap the invariant manifolds of the unstable orbits around L_1 and L_2 (bottom panel). Note how the precessing model tilts the bar and disc and it evidences a warped shape towards the outer parts. Note also the overdensity due to the superposition of the bar and the particles trapped by the inner branches of the invariant manifolds.

If we compare the density contour with some recognized warps, as for example the one shown in Fig. 3 of Debattista & Sellwood (1999) obtained from a N-body simulation, we observe that the tilting of our model is evidently acquiring a similar shape to that in the mentioned figure.

We can also compare our results to observations. As previously mentioned, the invariant manifolds of this model match the profile shown by the Integral Sign Galaxy (Fig. 3.21). In this case, the maximum angle of the warp is $\theta = 6.7°$. This value is in

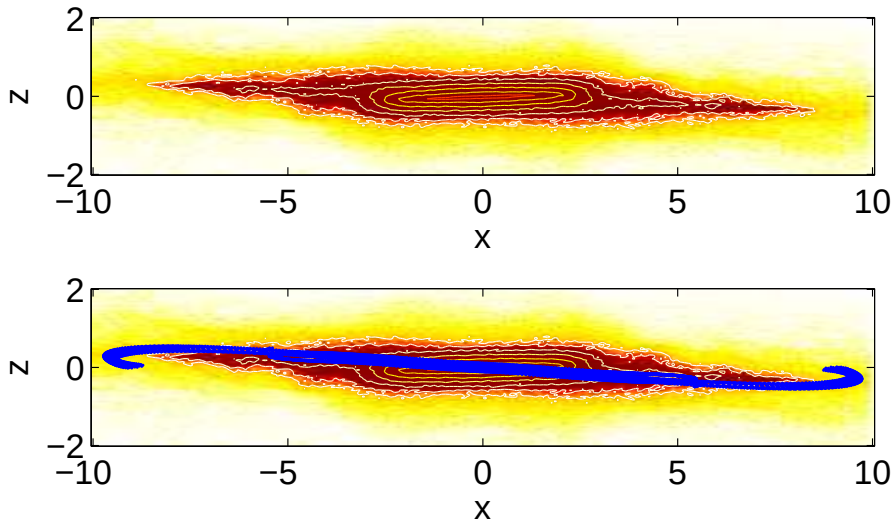

Figure 3.24: Top: Surface density and contours of the xz-projection of the test particle simulation for $GM_d = 0.7$, $GM_b = 0.3$, $\Omega = 0.05$ and $\varepsilon = 0.2$ rad. Bottom: Overlap of the invariant manifolds for the same parameters (in blue) with Jacobi constant $C = -0.19366$.

agreement with warp angles observed in external galaxies (Sánchez-Saavedra et al., 2003), as discussed in the previous Sect. 3.2.1. Using the test particle simulation, we can see that, indeed, the particles integrated in the precessing model get warped in a similar way to that of the Integral Sign Galaxy.

3.4 The case of the tilted bar model

In this chapter we have seen how a model behaves when all its components are tilted. Until now, we had a model composed by a bar and a disc, and applying the equations of motion of the precessing model (Eq. 2.62) the two components are tilted with respect to the plane XY. In this way, we have got warped shapes from invariant manifolds comparable with observed warps. Let us examine now what are the consequences for the formation of warps if we only tilt the bar instead of all the model. From now on we will call this new model the *tilted bar model*.

Let us note however that a galaxy with a bar tilted with respect to the disc is thought to be unlikely in galaxies, because if the bar grows up from the disc no part of the bar can distance itself much from the disc along the common rotation axis. The reason comes from N-body simulations, as is explained for example in Athanassoula et al. (2013). Such simulations of galaxies have shown that, by themselves, rotating disks are highly unstable,

and will spontaneously form bars: if we take a disk where all the stars are rotating on perfectly circular orbits (relative to one another), the stars are not moving. Tweak it just a little, so that there is a little bit of excess density somewhere in the disk. Nearby stars will begin to fall towards this density excess, making it even more excessive. So stars further away will begin to feel the pull, and they will fall in. After a sufficient time every star falls towards the density excess, and a bar is formed. At this point, stars are no longer moving on circular orbits, but on highly elongated orbits along the bar (so the stars are trapped in the bar).

In any case, we think that it is interesting to know the behaviour of the orbits in this tilted bar model, in order to understand in a better way the formation of galaxies and their structure. For this reason, we take a model composed by a Ferrers bar with revolution symmetry and a Miyamoto-Nagai disc. Note that in this case we specifically take a bar with equal semi-minor axes in order to apply our precessing model in an ideal case. Therefore, the parameters that we consider in this model are $A = 3$, $B = 1$ for the disc, and $a = 6$, $b = c = 0.95$ for the bar with homogeneity $n_h = 2$. The rest of parameters are as in the previous precessing model, with $GM_d \in [0.6, 0.9]$, $GM_b \in [0.1, 0.4]$ (but having in mind that $G(M_d + M_b) = 1$), pattern speed $\Omega \in [0.05, 0.06]$ kpc/[u$_t$] and the tilt angle of bar $\varepsilon \in [0, 0.2]$ rad $= [0, 11.46]^\circ$.

We have to emphasize that, whereas in the previous model the system is precessing in a cone about the inertial Z axis where the tilt angle with respect to the XY plane is ε, in this case we consider that the bar continues precessing in a cone about the Z axis but now the plane of the disc is the XY plane. Basically we could think that the bar is tilted an angle ε with respect to the disc, which remains in the XY plane.

To that end, we apply the equations of motion (2.62). For values of $\varepsilon > 0$, the system tilts bar and disc, so now we undo the tilt of the disc with an angle of the same value, $\varepsilon_2 = \varepsilon$. Therefore, we implement the new disc potential as

$$\overline{\phi_d} = \phi_d(R\mathcal{X}), \tag{3.11}$$

where ϕ_d is the previous disc potential, $\mathcal{X} = (x, y, z)$ and R is the rotation inverse to the rotation in the equations of motion. Since we also need the first and second derivatives of the potential, applying the chain rule

$$\begin{aligned} \nabla\overline{\phi_d} &= \nabla\left(\phi_d(RX)\right) = \nabla\phi_d(RX) \cdot R, \\ \nabla^2\overline{\phi_d} &= \nabla^2\left(\phi_d(RX)\right) = R^T \cdot \nabla^2\phi_d(RX) \cdot R. \end{aligned} \tag{3.12}$$

In order to compare with the results of the previous model, we first analyze the periodic orbits inside the bar. Taking the parameters $GM_d = 0.9$ and $GM_b = 0.1$, we study

the stability of the central equilibrium point L_3 in this tilting bar model. Considering the differential matrix (3.5), the eigenvalues obtained are of the form $\{\lambda i,\ -\lambda i,\ \mu i,\ -\mu i,\ \omega i,\ -\omega i\}$ ($\lambda,\ \mu,\ \omega \in \mathbb{R}^+$), for any selected value of ε. So, just as before, the L_3 Lagrangian point is a linearly stable elliptic point.

But it is not enough to know this, since we are interested in that the periodic orbits inside the bar form the skeleton of the model, maintaining the structure of the bar. The next step is to study the shape of the periodic orbits in the bar and its stability indexes. Let us take the same definition for the stability indexes as in the Eq. (3.8), in Fig. 3.25 we show these periodic orbits and their indexes.

Comparing Figs. 3.25 and 3.4 we observe that when $\varepsilon = 0$ and $\varepsilon = 0.1$ rad (left and middle columns), the periodic orbits have the same structure and the stability indexes remain qualitatively comparable. But, when ε increases until 0.2 differences appear. If we observe the second row, the projection in the xy plane, the periodic orbits do not have as many bifurcations as before. After the first family of periodic orbits along the bar, in the case of $\varepsilon = 0.2$ only one more family, which finishes in a small loop, is obtained. In contrast, for smaller values of ε and for the previous model, this first family of orbits along the bar bifurcates in another three families, the last one finishing in an appreciable loop. Moreover, if we pay attention to the first or third row, where the projections in three dimensions or in the xz plane are represented, the periodic orbits suffer a great deformation for $\varepsilon = 0.2$ and escape from the bar.

These facts suggest that periodic orbits inside the bar do not give structure to it, not constituting the backbone of the model when the tilt angle is larger than $\varepsilon = 0.1$, as this model only tilts the bar and for larger tilt angles the system becomes unstable and unravels. Due to the fact that the bar is formed from the disc, a small tilt angle between the bar and the disc could be made possible by dynamical frictions for example, and would not be observable. But a greater tilt angle is not explainable since, as the bar emerges from the disc, a great separation between both is very unlikely. Moreover, great tilt angles would be easily observed, but no instances of them have been reported.

In spite of that, we would like to understand what happens with the invariant manifolds that show the visible external structure in galaxies and help us to obtain warps. To this end, we analyze the stability of the libration points, L_1 and L_2, at corotation for different values of the bar and disc masses, $GM_d \in [0.6, 0.9]$, $GM_b \in [0.1, 0.4]$, with the pattern speed set to $\Omega = 0.05$. The eigenvalues of the differential matrix (3.5) around L_1 and L_2 are of the form $\{\lambda,\ -\lambda,\ \mu i,\ -\mu i,\ \omega i,\ -\omega i\}$ ($\lambda,\ \mu,\ \omega \in \mathbb{R}^+$), for values of $\varepsilon \leq 0.1$. So, the points L_1 and L_2 continue being hyperbolic points until $\varepsilon = 0.1$. But again, differences appear from $\varepsilon > 0.1$ onwards.

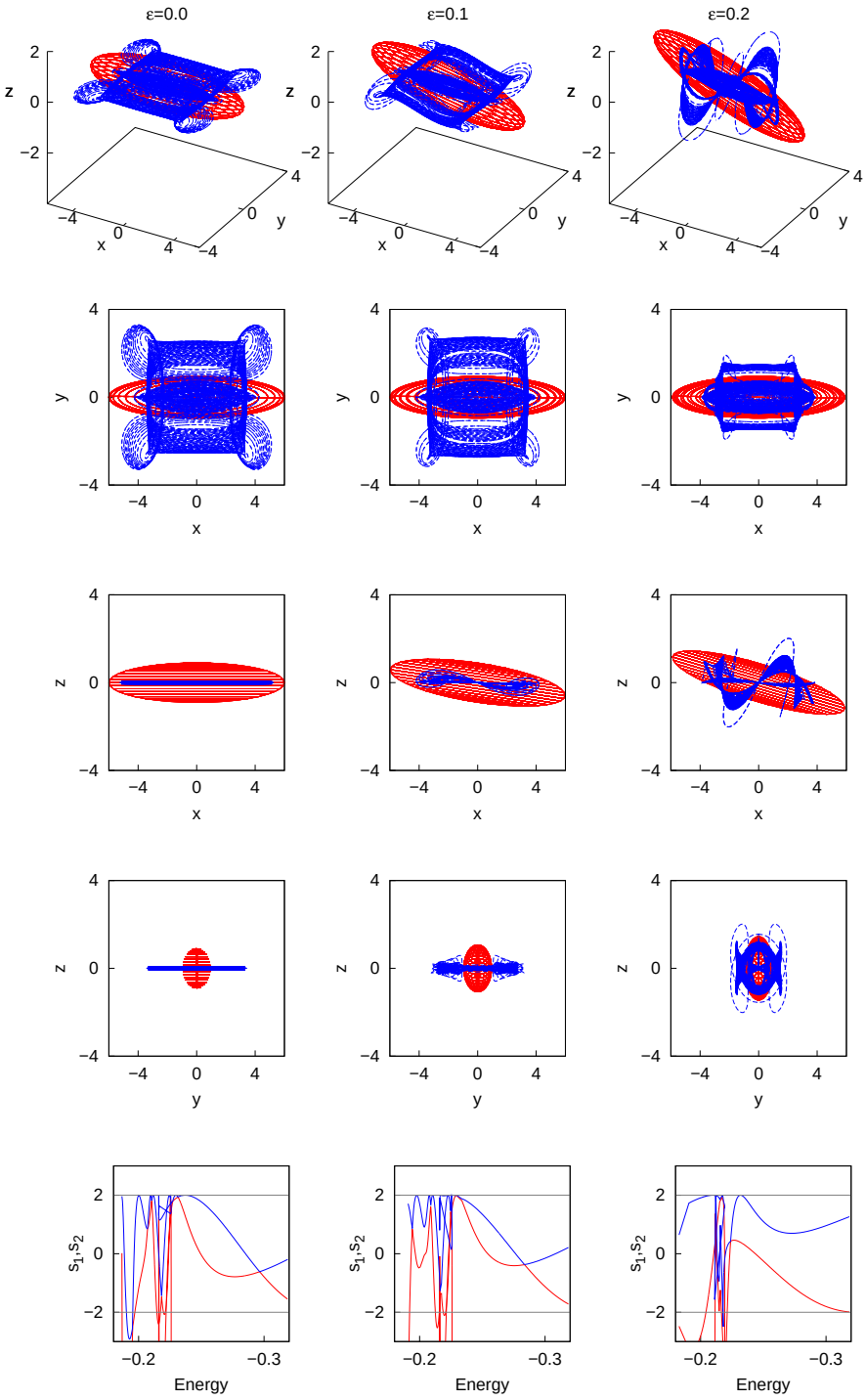

Figure 3.25: Family of periodic orbits and stability indexes for the bar with $b = c = 0.95$ and $\varepsilon = [0, 0.1, 0.2]$ and $GM_b = 0.1$ for the tilted bar model.

When the tilt angle ε increases over 0.1 the type of the critical points may change depending on additional parameters, such as the bar or the disc mass. In the table in the left panel of Fig. 3.26 we show for each value of the bar mass the limit value of ε, up to which L_1 and L_2 continue being unstable, while L_3, L_4, L_5 are stable. This fact reinforces the idea that a tilt angle of the bar respect to the disc greater than $\varepsilon = 0.1$ makes the system acquire a different behaviour, neither natural nor observed.

This study leads to the same conclusion as in the previous precessing model, namely that the tilt angle ε has to be small in order to obtain physically meaningful results.

GM_b	ε
0.1	0.12
0.2	0.17
0.3	0.21
0.4	0.25

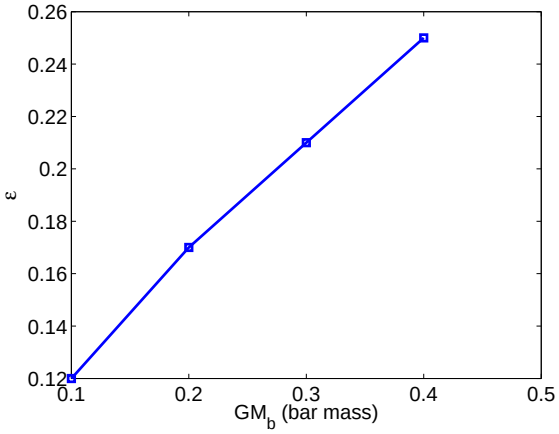

Figure 3.26: Table and plot of the progression of the limit value of ε where the behaviour of the tilted model changes.

To get an idea of how each equilibrium point behaves in this tilted bar model, we show in Fig. 3.27 isodensity curves for the values represented in the table of Fig. 3.26. Note that for these values, the equilibrium points L_1, L_2, L_4, L_5 become unstable and could lead to the formation of four spiral arms instead of two. If these values of ε increase, the equilibrium points L_4 and L_5 continue being unstable, but the points L_1 and L_2 get to be stable as we show in the last plot of Fig. 3.27 for the value of $GM_b = 0.1$ and $\varepsilon = 0.2$.

In order to compare with the first model, for which we have proved that it models a realistic galaxy, in Fig. 3.28 we contrast the isodensity curves with the same parameters in the two models. In the precessing model, left panel, the equilibrium points L_1 and L_2 are saddle points, whereas L_3 and L_4 are stable points. But in the tilted bar model, while L_1 and L_2 continue being unstable points, L_3 and L_4 become unstable as well (right panel).

In spite of the existence of four unstable equilibrium points in the new model, some are more unstable than the others. To check that, a simple way is to observe the effective potential of the model for each point (x, y). Again, the better way is to compare the

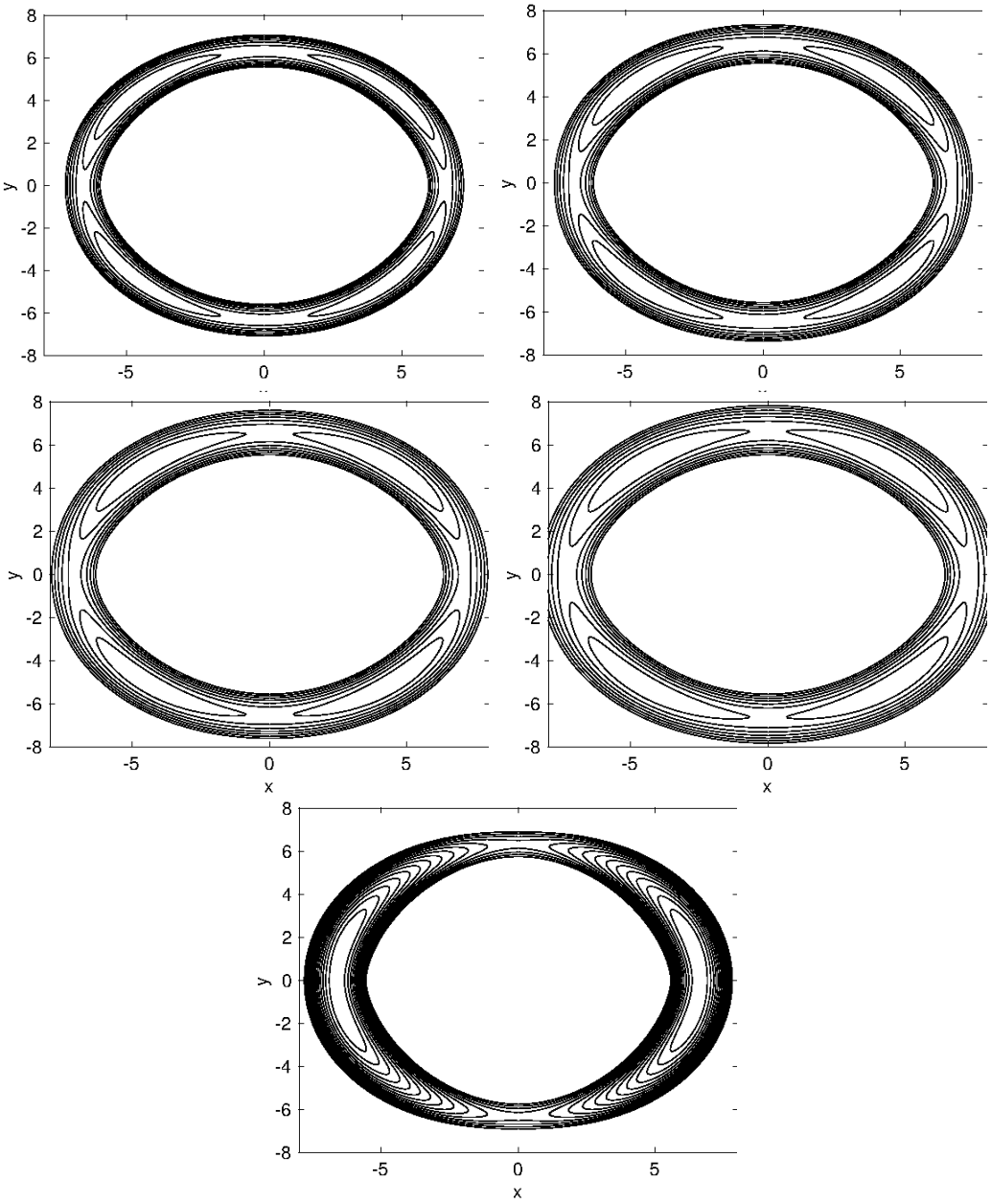

Figure 3.27: Isodensity curves in the xy plane for the tilted bar model. Top: Left plot for $GM_b = 0.1$ and $\varepsilon = 0.12$, right plot for $GM_b = 0.2$ and $\varepsilon = 0.17$. Middle: Left plot for $GM_b = 0.3$ and $\varepsilon = 0.21$, right plot for $GM_b = 0.4$ and $\varepsilon = 0.25$. Bottom: plot for $GM_b = 0.1$ and $\varepsilon = 0.2$ where the behaviour of the equilibrium points has changed.

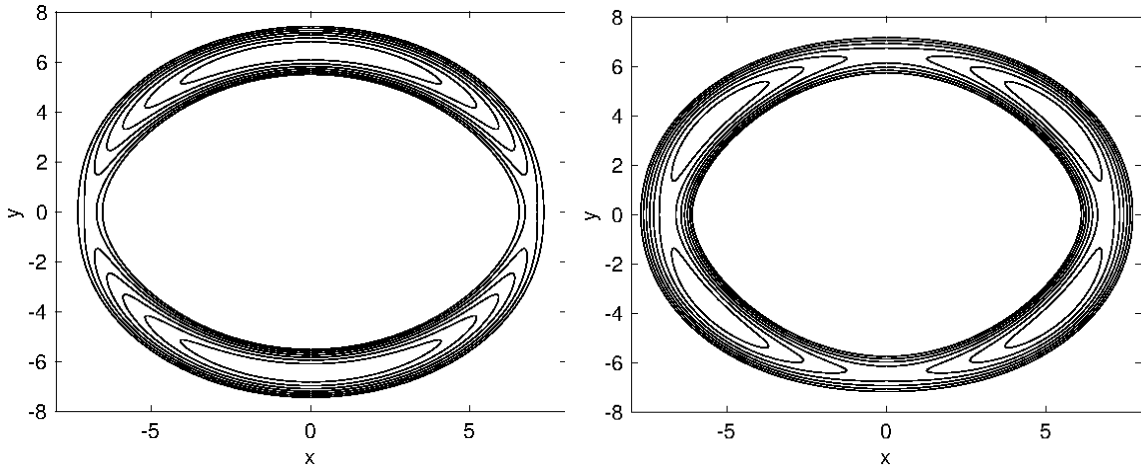

Figure 3.28: Isodensity curves in the xy plane for $GM_b = 0.2$ and $\varepsilon = 0.2$. Left: the precessing model (first model). Right: the tilted bar model (second model).

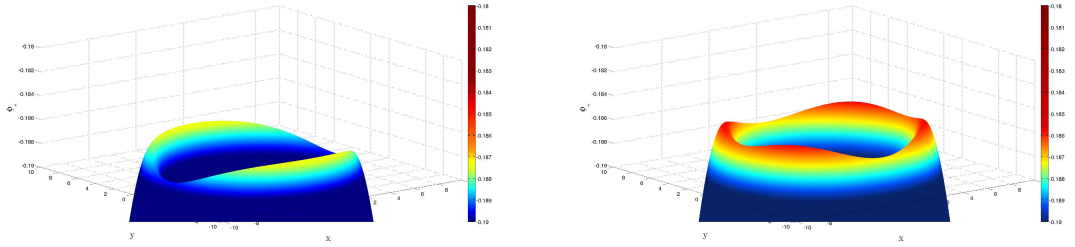

Figure 3.29: Effective potential in each point (x, y), for $GM_b = 0.2$ and $\varepsilon = 0.2$. Left: the precessing model (first model). Right: the tilted bar model (second model).

previous model with this new model. Figure 3.29 shows that the first model has two maxima and two saddle points, all well defined, while on the contrary in the tilted bar model four maxima and four saddle points are present, but they are less marked as critical points.

Finally, we observe the behaviour of the invariant manifolds in this case, where four unstable equilibrium points appear (see Fig. 3.30). Obviously the behaviour of the invariant manifolds has changed with respect to the first model. In this case, we take the invariant manifolds associated to the periodic orbits around L_1 and integrate them until they approach the point L_2, and follow the same procedure for invariant manifolds around L_2. The existence of the unstable equilibrium points L_4 and L_5 makes the approach from L_1 to L_2, and vice versa, difficult compared to the first model with two unstable equilibrium points.

In this Fig. 3.30 we observe the evolution of the invariant manifolds along time.

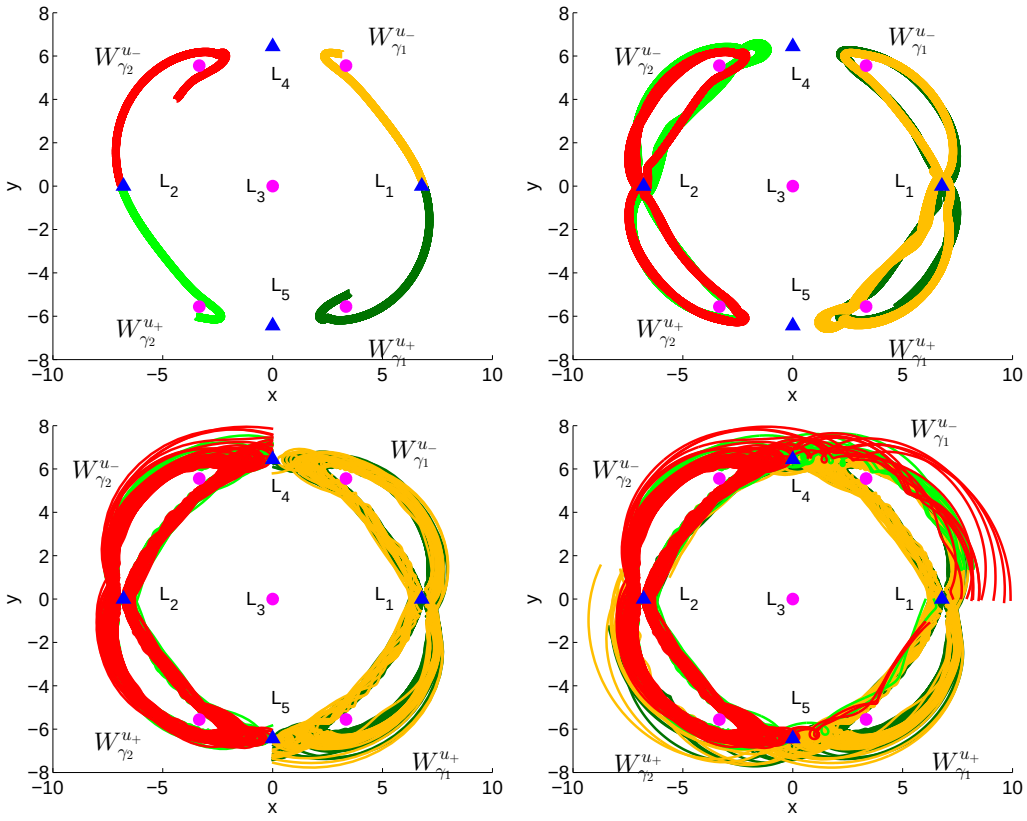

Figure 3.30: Unstable invariant manifolds around L_1 and L_2 for $GM_b = 0.2$ and $\varepsilon = 0.2$ in the tilted bar model (unstable points marked by '▲', stable points marked by '•'). Top left: Integration time $t_1 = 4\,T$. Top right: Integration time $t_2 = 11\,T$. Bottom left: Integration time $t_3 = 349\,T$. Bottom right: Integration time $t_4 = 5674\,T$

For a small integration time, $t_1 = 4\,T$ (top left panel), where T is the bar period, the invariant manifolds start from the equilibrium points L_1 and L_2 and surround the stable equilibrium points (•). As the integration time increases to $t_2 = 11\,T$ (top right panel), the two invariant manifolds of L_1 overlap, as occurs for L_2, but without reaching the unstable points L_4 and L_5. Widening the time span to $t_3 = 349\,T$, the invariant manifolds reach the unstable points L_4 and L_5 overlapping completely. Finally, we observe that for a long integration time $t_4 = 5674\,T$, the unstable invariant manifolds of L_1 and L_2 reach the neighbourhood of L_2 and L_1 respectively. The set of invariant manifolds of L_1 and L_2 thus acquires a particular shape not found in observations of catalogued galaxies.

In conclusion, the tilted bar model suggests a maximal value of the tilt angle in order for the model to be stable, i.e. for the tilted bar to exist. This fairly agrees with N-body simulations, which indicate that the bar grows from the disc and therefore it can

not be greatly tilted with respect to it, and agrees as well with observations, which have not detected galaxies with a bar tilted with respect to the disc, thus indicating that if the bar were tilted it must be so with a small angle.

Chapter 4

The dynamics of the precessing model with halo

The presence of a halo, a spherical distribution of dark matter enveloping the galactic disc, is clear in galaxies, but not its influence in the formation of warps. Some theories propose that the formation of warps is related with the interaction between the galactic disc and the dark matter halo. For example, Sparke & Casertano (1988) use a rigid, flattened halo to obtain persisting warps, which are insensitive to the details of the disc edge. However, dark matter haloes are not rigid, and a responsive halo alters the dynamics in several ways, as established in Binney et al. (1998), where the authors show that a discrete warp in a rigid halo does not survive in a simulation with a responsive halo, concluding that the inner halo could never be significantly misaligned from the inner disc.

Shen & Sellwood (2006) perform simulations with a model composed by a disc, an accreted torus and a halo where the disc is subjected to the torque from the misaligned torus which represents the cosmic infall. Their results show that warp formation does not depend strongly on the choice of halo, being more sensitive to the masses and sizes of the disc and torus than to the density profile or total mass of the halo. The methods used in López-Corredoira et al. (2002) followed this line, where they remark that despite the importance of the halo in the dynamics of galaxies, this may not play an important role in the formation of warps. Their computations confirm that the presence or absence of a massive halo does not affect significantly their results.

In this chapter we observe the influence of a halo, modifying its mass compared to the masses of the disc and the bar, and we compare the results we obtain about the manifolds with those of the first precessing model without halo (Sect. 3.2). Therefore, now, we apply the equations of the precessing model (Eq. 2.62), but in this case the potential

consists of the superposition of a disc, a bar and a spheroidal halo. We will henceforth refer to this model as the *precessing model with halo*.

4.1 Components and description of the model

In the previous precessing model (Sect. 3.2) we have shown how a model composed by a bar and a disc forms warps through the invariant manifolds. Now, in order to make more realistic the model and better fit observations, we add a spheroidal component which performs as a halo of dark matter. In this way, the rotation curve of the galaxy model has a more realistic shape (see Fig. 4.1).

The values for the parameters are chosen in such a way that the rotation curve becomes flat in order to represent the realistic features of galaxies. For that purpose, we start from a model with greater mass in the spheroid than in the disc and bar. We decrease the mass of the spheroid to make different models and compare how much the spheroid affects the different shapes of the galaxy. In the same way, we study the influence of having rotation curves with flat and falling circular velocities in the inner parts of the galaxy.

For this precessing model with halo, we use a morphology to describe the galaxy composed by an axisymmetric component and a bar-like one. The axisymmetric component consists of the superposition of a disc and a spheroid. The disc is modelled as a Miyamoto-Nagai disc with potential:

$$\phi_d = -\frac{GM_d}{\sqrt{R^2 + (A + \sqrt{B^2 + z^2})^2}} \tag{4.1}$$

where $R^2 = x^2 + y^2$ is the squared radius in cylindrical coordinates, and z denotes the distance in the out-of-plane component.

We use a Plummer potential to model a spherical halo,

$$\phi_p = -\frac{GM_p}{\sqrt{r^2 + b^2}}, \tag{4.2}$$

where b characterises the radial scale length of the spheroid, M_p its mass and the radial distance is $r = \sqrt{x^2 + y^2 + z^2}$. Using the Poisson equation $\nabla^2\phi_p = 4\pi G\rho_p$, the density of the Plummer model ρ_p at a radial distance r is

$$\rho_p = \frac{3M_p}{4\pi}\frac{a^2}{(r^2 + a^2)^{5/2}}, \tag{4.3}$$

which scales with radius as $\rho_p \sim r^{-5}$ at large radii.

The bar-like component is modelled, as in previous model, by a Ferrers bar which follows the equation,

$$\rho = \begin{cases} \rho_0(1-m^2)^{n_h}, & m \leq 1 \\ 0, & m > 1 \end{cases} \tag{4.4}$$

where $m^2 = x^2/a^2 + y^2/b^2 + z^2/c^2$ and for $n_h = 2$, $\rho_0 = \frac{105}{32\pi}\frac{GM_b}{abc}$ is the central density, being M_b the mass of the bar. The parameter n_h determines the concentration of matter in the bar. The value $n_h = 2$ indicates that this model concentrates matter in the central region and decreases smoothly towards zero at a finite distance.

In this Chapter, the potential of the system applied to equation (2.62) is $\phi = \phi_b + \phi_d + \phi_p$, where ϕ_b is the bar potential, ϕ_d the potential of the disc and ϕ_p is the potential of the spheroid.

The length unit used in the sequel is the kpc, the time unit is $\mathrm{u}_t = 2 \times 10^6$ yr and the gravitational constant $G = 6.674 \times 10^{-11}$ m^3 kg^{-1} s^{-2}.

We have checked that the shape of the bar (whether it is symmetric or not) in fact does not affect the form of the obtained galaxies. Thus, we prefer to select a symmetric bar (with revolution symmetry) which fits better in our equations. In this model, we fix the shape of the bar with semi-major axis $a = 6$ and semi-minor axes $b = c = 0.95$, and the mass of the bar is in the range $GM_b \in [0.1, 0.2]$. On the other hand, the disc takes values $A = 3$, $B = 1$ and the mass is considered in the range $GM_d \in [0.4, 0.6]$. For the spheroid, its radial scale length is $b = 10$ and its mass is in the range $GM_p \in [0.2, 0.5]$. Note that we take the convention that $G(M_d + M_b + M_p) = 1$.

Finally, we also consider the pattern speed with value $\Omega = 0.06$ since we have evidenced that it gives bigger warp angles. For the tilt angle of the model, we take $\varepsilon \in [0, 0.2]$ rad which is a range that maintains the consistency of the system.

4.2 Characteristics of the model

We define four models, whose free parameters are chosen so that the shape of the rotation curve slightly changes from being flat to gently decreasing. Also, we are interested in ascertaining the influence of the parameters on the warp formation. Therefore, for the different models, we decrease one of the parameters while increasing another one, in order to observe the variations of the results according to their values.

In Fig. 4.1 we observe the rotation curves of the four selected models. For Model A (top left panel) the values are $GM_b = 0.1, GM_d = 0.4, GM_p = 0.5$. The rotation curve of this galaxy model rises linearly inside the bar and becomes flat in the outer parts.

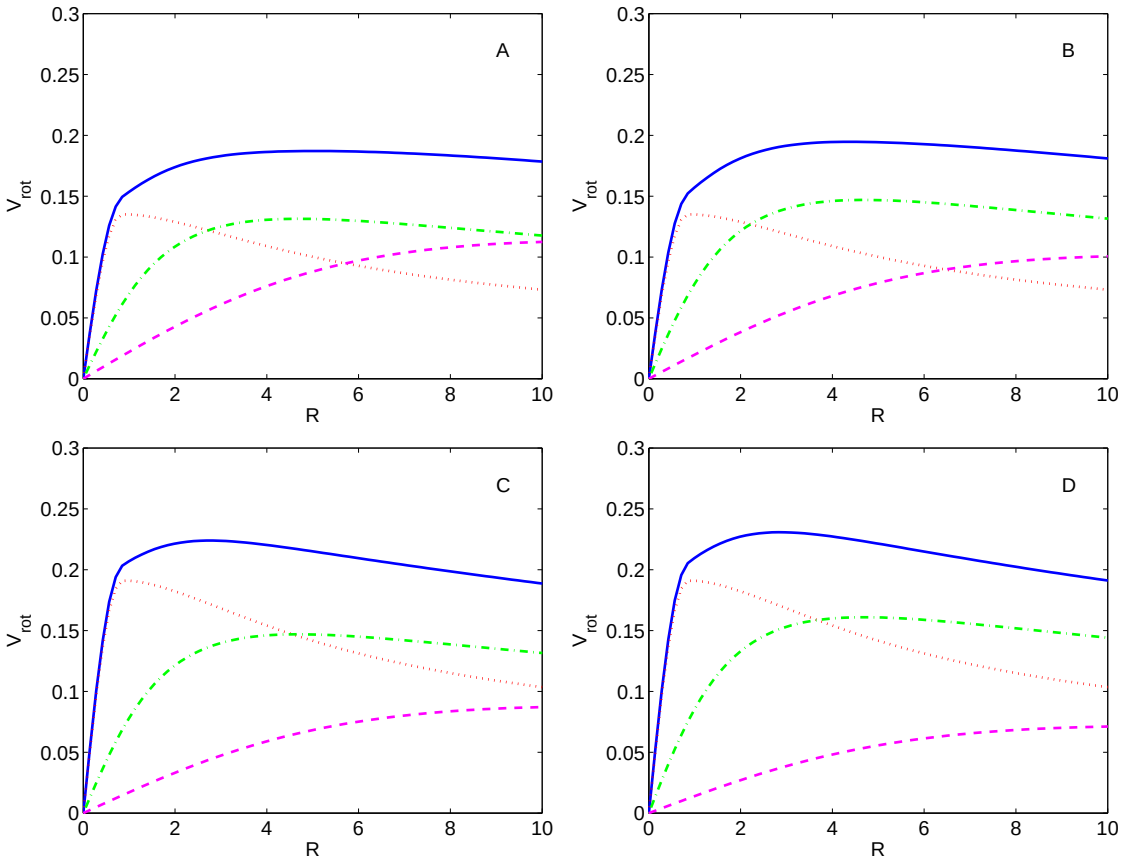

Figure 4.1: Rotation curves of the precessing model with halo. The rotation curve of the composed model is marked in blue (solid line), the one of the bar is in red (dotted line), for the disc is in green (dot-dashed line) and for the spheroid in magenta (dashed line). Model A (top left): $GM_b = 0.1, GM_d = 0.4, GM_p = 0.5$. Model B (top right): $GM_b = 0.1, GM_d = 0.5, GM_p = 0.4$. Model C (bottom left): $GM_b = 0.2, GM_d = 0.5, GM_p = 0.3$. Model D (bottom right): $GM_b = 0.2, GM_d = 0.6, GM_p = 0.2$.

In Model B (top right panel) the spheroid mass decreases while the disc mass increases, $GM_b = 0.1, GM_d = 0.5, GM_p = 0.4$, making the slope of the rotation curve smoothly decrease in the outer parts of the galaxy while it rises in the inner parts. Model C is selected for $GM_b = 0.2, GM_d = 0.5, GM_p = 0.3$ (bottom left panel), in such a way as to increase the bar mass and decrease the spheroid mass, so the circular velocity rises higher inside the bar, but also falls faster in the outer parts of the model. The last model, Model D, in bottom right panel, is for $GM_b = 0.2, GM_d = 0.6, GM_p = 0.2$, in this case the rotation curve reaches its maximum value among all the selected models inside the bar and the slope decreases faster in the outer parts.

When the disc or bar mass increase at the same time as the spheroid mass decreases, the circular velocity continues rising inside the bar but falls in the outer parts, this drop being faster when the spheroid mass reaches its minimum value, $GM_p = 0.2$.

Our purpose is to study the warps that appear with this type of configuration, since we have shown that the equations of motion (2.62) are able to produce this type of galaxy by means of the invariant manifolds. To achieve this aim, we need to analyse the stability of the equilibrium points. The differential matrix around any Lagrangian point of the system is the same as for the disc and bar model (Chapter 3):

$$DF(L_i) = \begin{pmatrix} 0 & 0 & 0 & 1 & 0 & 0 \\ 0 & 0 & 0 & 0 & 1 & 0 \\ 0 & 0 & 0 & 0 & 0 & 1 \\ a & \phi_{x_1x_2} & b & 0 & c & 0 \\ \phi_{x_1x_2} & d & \phi_{x_2x_3} & -c & 0 & -e \\ b & \phi_{x_2x_3} & f & 0 & e & 0 \end{pmatrix}_{L_i} \tag{4.5}$$

where

$$\begin{cases} a = \Omega^2 \cos(\varepsilon)^2 + \phi_{x_1x_2}, \\ b = \Omega^2 \sin(\varepsilon)\cos(\varepsilon) + \phi_{x_1x_3}, \\ c = 2\Omega \cos(\varepsilon), \\ d = \Omega^2 + \phi_{x_2x_2}, \\ e = 2\Omega \sin(\varepsilon), \\ f = \Omega^2 \sin(\varepsilon)^2 + \phi_{x_3x_3}. \end{cases} \tag{4.6}$$

Let us recall that in this case, the potential of the system is $\phi = \phi_b + \phi_d + \phi_p$.

The equilibrium points present the same behaviour as in the precessing model. Around the central equilibrium point L_3, the eigenvalues of this matrix are of the form $\{\lambda i,\ -\lambda i,\ \mu i,\ -\mu i,\ \omega i,\ -\omega i\}$ ($\lambda,\ \mu,\ \omega \in \mathbb{R}^+$), for any selected value of ε. So, this central point continues being linearly stable. But the points we are really interested in are those that are at the ends of the bar, L_1 and L_2. The eigenvalues of the matrix around

these points are of the form $\{\lambda, -\lambda, \mu i, -\mu i, \omega i, -\omega i\}$ ($\lambda, \mu, \omega \in \mathbb{R}^+$), for any value of ε. Therefore, they are unstable, are called hyperbolic points, and there exist families of Lyapunov periodic orbits around each unstable equilibrium point, from which invariant manifolds are obtained.

One interesting comparison with the first model, the precessing model, is to establish how the unstable equilibrium points evolve when ε is increased. To this end, we need to compare two models with potentials as similar as possible. Due to the fact that in one model we had disc and bar, and in the other we have disc, bar and spheroid, there are several possible criteria for comparison between models. In view of the fact that the main component of barred galaxies is the bar, we infer that the two models having the same bar and a similar rotation curve makes the comparison more realistic. We select the first model, the precessing model, with a disc mass of $GM_{d_1} = 0.8$, whereas in the second model, the precessing model with halo, we select Model C which has a disc mass of $GM_{d_2} = 0.5$ and a spheroid mass of $GM_{p_2} = 0.3$. Both models have the bar mass fixed to $GM_b = 0.2$ and the pattern speed $\Omega = 0.06$. Although the position of the unstable equilibrium points in the x axis varies in the two models (since we are not taking the same components), the points of both models are affected by the tilting ε (see Fig. 4.2). In the left part of the plot, we observe the detailed evolution of each L_1 point. The behaviour is different with the tilt angle. In the precessing model with bar, disc and spheroid, the progression of the point acquires some curvature as ε increases. Nevertheless, when the model does not have a spheroid, the evolution of the point has practically the same x-component. This may be due to the presence of the halo making the tilting affect to a greater scale the model.

Regarding how the variation of the spheroid mass affects the equilibrium points in this model, the right part of Fig. 4.2 shows how, for $\varepsilon = 0$, the initial position of the L_1 point increases as GM_p decreases. Let us remark that between the first two lines (cyan and red) and the second ones (blue and black) there is an increment of the bar mass, which makes the z-component of the equilibrium point L_1 increase greatly. Moreover, when the bar mass is small, e.g. $GM_b = 0.1$, the variation of the equilibrium points in their z-component is small compared with the one obtained when the bar mass increases until $GM_b = 0.2$.

Therefore, comparing the left and right panels of this figure, we obtain evidence that the bar mass is the main factor in the out-of-plane z-component displacement of the equilibrium points.

Finally we observe the zero velocity surface of the system for a given energy value, and its cut with the plane $z = 0$ which defines the zero velocity curves (Fig. 4.3). In this case we have chosen an energy value of $C_J = -0.1916$ which is very close to the energy of

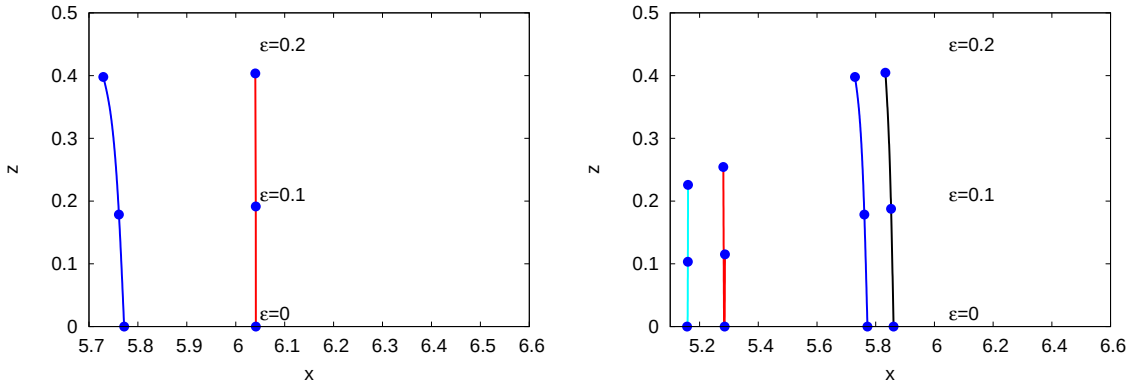

Figure 4.2: Left: Comparison of the evolution of the coordinates of the equilibrium point L_1 for the precessing model with bar and disc (red) with parameters $GM_{b_1} = 0.2$ and $GM_{d_1} = 0.8$, and the precessing model with bar, disc and spheroid (blue) with parameters $GM_{b_2} = 0.2$, $GM_{d_2} = 0.5$ and $GM_{p_2} = 0.3$ respectively, with $\varepsilon \in [0, 0.2]$ for both models. Right: Evolution of the coordinates of the equilibrium point L_1 for the precessing model with bar, disc and spheroid, with $\varepsilon \in [0, 0.2]$, and with spheroid mass from left to right $GM_p = 0.5$ (cyan), $GM_p = 0.4$ (red), $GM_p = 0.3$ (blue), $GM_p = 0.2$ (black).

the unstable equilibrium points L_1 and L_2, $C_{J_{L_1,L_2}} = -0.1966$.

4.3 Dynamics close to corotation

As previously mentioned, the shape of galaxies, and in particular galactic warps, are related to the shape of the invariant manifolds of unstable equilibrium points. As we have seen, around these unstable equilibrium points there exists a family of periodic orbits, called Lyapunov orbits, which at low energies are unstable and give rise to invariant manifolds. For a given energy level, two stable and two unstable branches of asymptotic orbits emanate from the periodic orbit. These branches are the stable and unstable invariant manifolds, and they are responsible for the main visible structures in the galaxy. The stable invariant manifold is the set of orbits that tends to the periodic orbit asymptotically, and the unstable one is the set of orbits that departs asymptotically from the periodic orbit.

Figure 4.4 shows the xy projection of the unstable invariant manifolds of Lyapunov orbits around the equilibrium points L_1 and L_2, for the precessing model with halo for models A, B, C, D (see Fig. 4.1). Thus, from top to bottom, the shape of the rotation curve varies from being flat to slightly decreasing.

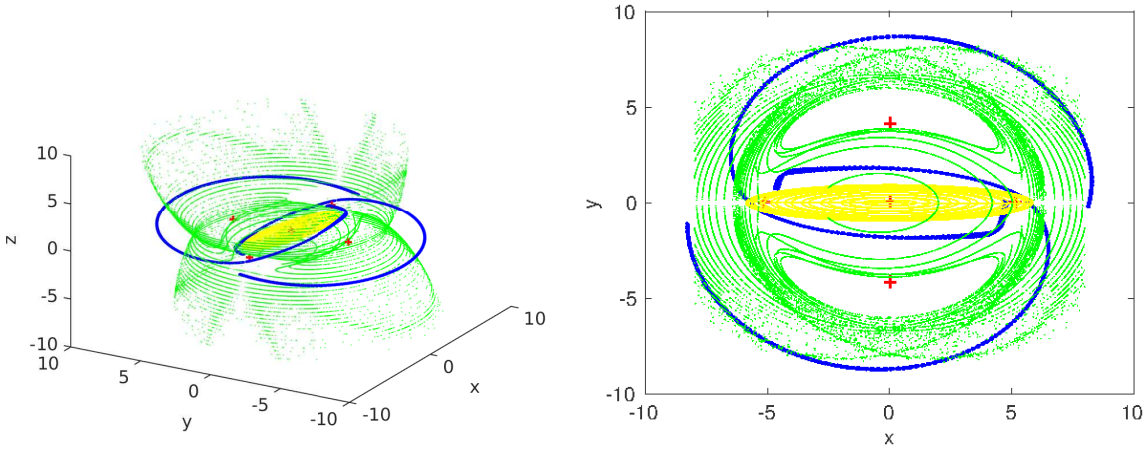

Figure 4.3: Zero velocity surface (left) and zero velocity curves (right) for the precessing model with halo for an energy of $C_J = -0.1916$ (green), unstable invariant manifolds of the points L_1 and L_2 (blue) and Ferrers bar (yellow) for $GM_b = 0.2, GM_d = 0.5, GM_p = 0.3$. The red crosses (+) mark the position of the Lagrangian points.

When the rotation curve is flat (model A, first row), the inner invariant manifolds of L_1 and L_2 are very close, making visible only the exterior branches of the manifolds. As the rotation curve starts decreasing in the outer parts, the inner manifolds move apart, until they form an elliptical structure surrounding the Ferrers bar. A rotation curve which is flat in the inner parts, gives rise to spiral arms, closely resembling the structure of an exterior ring, while the inner manifolds are inside the bar distorting the inner ring. In this case, we do not obtain a clearly ringed structure, since we observe only two arms emanating from the bar ends, and the inner branches of the invariant manifolds add their luminosity to the Ferrers bar. As we select models with an ever decreasing rotation curve, the outer branches of the invariant manifolds open up acquiring a spiral shape. In addition, the slope of the rotation curve in the inner parts is important in order to determine the inner shapes of the structures. When the slope of the rotation curve decreases fast, the inner branches of the invariant manifolds close and form an inner ring, elongated along the bar. As far as the tilt angle is concerned, the effect is better appreciated in this figure for Model C, since when ε increases, the inner branches start falling out, becoming gradually visible.

In order to better appreciate the behaviour of the invariant manifolds with respect to the tilt angle ε, in Fig. 4.5 we show them in three dimensions. Let us notice how the exterior invariant manifolds acquire tilting in the z-component according to the value of ε. The inner branches of the invariant manifolds do not seem to acquire the same tilting, the change being more marked between the inner and outer branches.

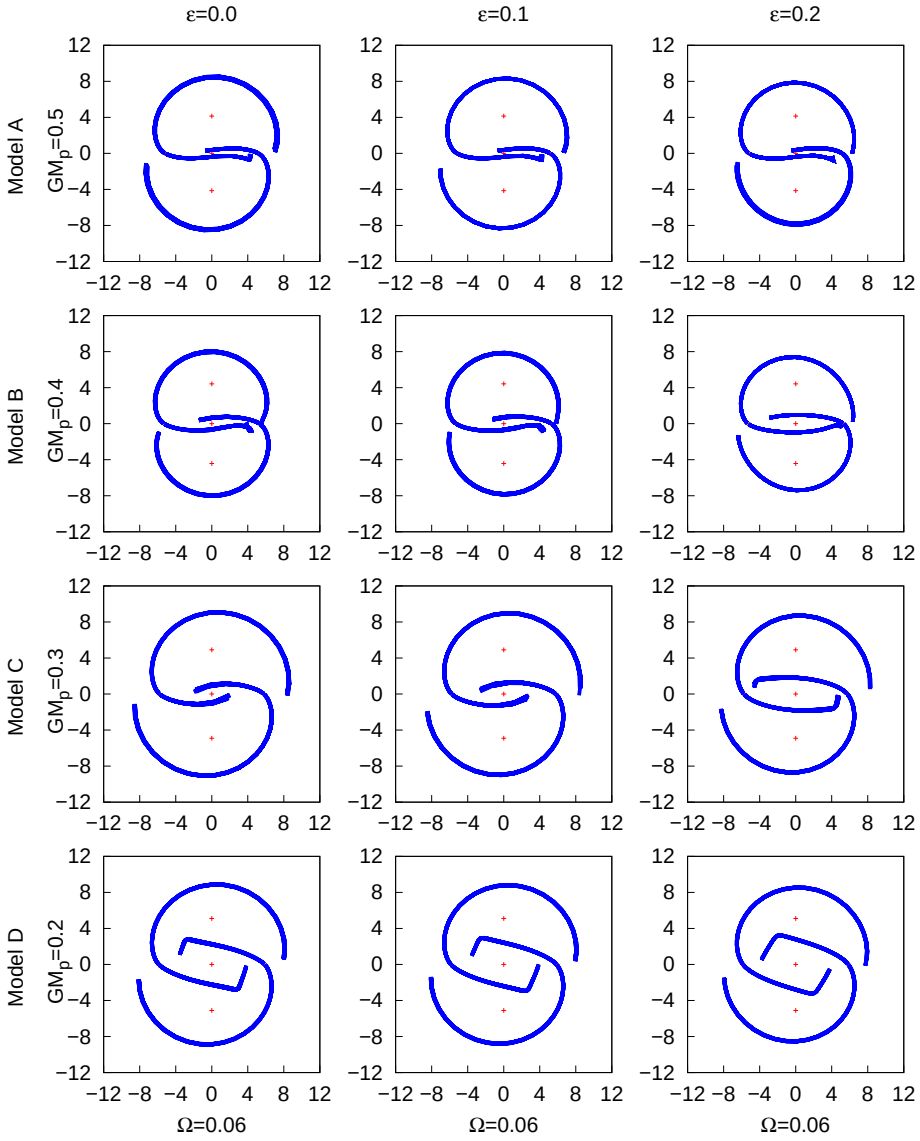

Figure 4.4: Unstable invariant manifolds for the precessing model with halo. Model A (first row): $GM_p = 0.5$, $GM_d = 0.4$, $GM_b = 0.1$. Model B (second row): $GM_p = 0.4$, $GM_d = 0.5$, $GM_b = 0.1$. Model C (third row): $GM_p = 0.3$, $GM_d = 0.5$, $GM_b = 0.2$. Model D (last row): $GM_p = 0.2$, $GM_d = 0.6$, $GM_b = 0.2$. The tilt angle varies with the columns, in the range $\varepsilon \in [0, 0.2]$.

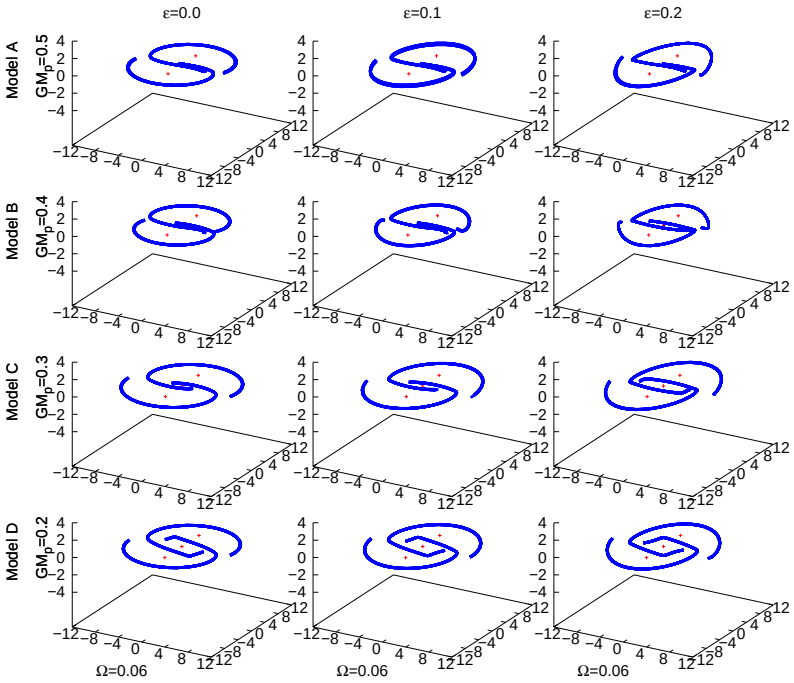

Figure 4.5: 3D view of the plots shown in Fig. 4.4.

Figure 4.6 shows the formation of warps which are similar to those observed in real galaxies. From the point of view taken, we note that the outer branches of the invariant manifolds acquire a warped shape which depends on the tilting angle and the slope of the rotation curve.

For $\varepsilon = 0$ no warped shapes appear, independently of the rotation curve, as expected. For the next value of the tilting angle, $\varepsilon = 0.1$, some warped shapes become discernible, specially when the rotation curve of the model is nearly flat. The inner branches of the invariant manifolds are distinguishable as well. But the most noticeably warped shapes appear when the tilting angle ε reaches the value $\varepsilon = 0.2$. In this case, the outer branches of the invariant manifolds adopt the characteristic curvature of a reclined integral sign, typical of warped galaxies. Let us particularly point out the warp shapes when the rotation curve is flat or nearly. Moreover, the inner branches of the invariant manifolds are clearly observed in the central region forming an almost flat structure, which splits up the two outer branches.

In the previous precessing model with only bar and disc (Sect. 3.2) we have seen that the most important parameter related with the warp formation is the tilt angle ε. Here, we confirm this idea, adding that a flat rotation curve helps to emphasize the characteristic elements of warps.

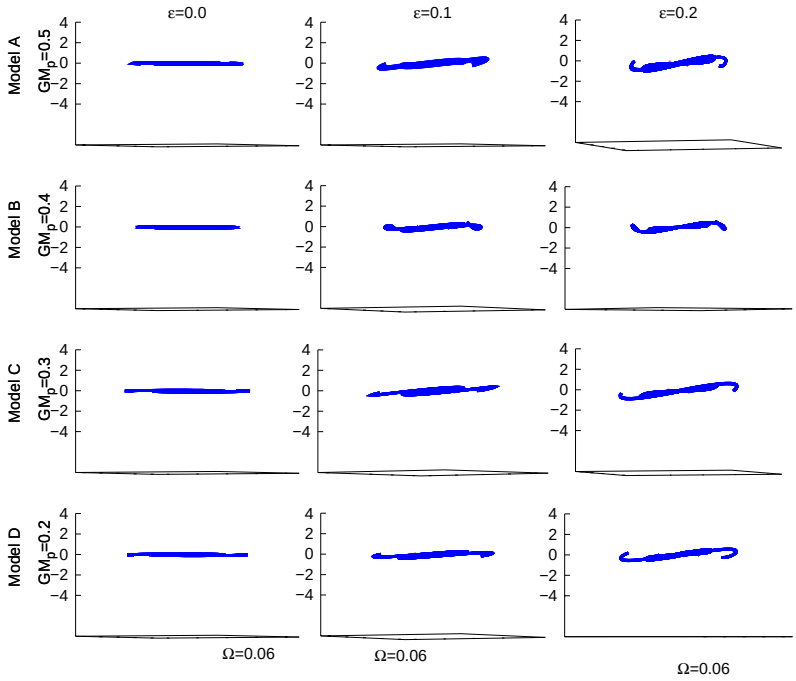

Figure 4.6: Near edge-on view of the plots shown in Fig. 4.4.

4.3.1 Warp angles

The measure of the warp angles has been performed as previously, that is, the warp angle is defined as the angle between the outermost detected point in the warp and the mean position of the plane of symmetry.

The warp angles obtained in this precessing model with halo, composed by a Miyamoto-Nagai disc, a Ferrers bar and a Plummer spheroid, vary greatly with the tilt angle of the model, ε, and with the spheroid mass (note that $G(M_b + M_d + M_p) = 1$, so the variation of the spheroid mass implies in this case the variation of the disc or bar mass as well). Table 4.1 shows the range of warp angles θ obtained.

The slope of the rotation curve of the system also plays an important role. Flat rotation curves help to widen the warp angle, since fixing a value of ε, the maximal warp angles are obtained when the rotation curve of the system is nearly flat in the inner parts, whereas with a descending rotation curve, the warp angle reaches values close to the ones of the previous model.

Comparing with the previous model, for a pattern speed $\Omega = 0.06$ and a tilt angle $\varepsilon = 0.1$, the maximal angle obtained here is $\theta = 7.3°$, when the mass values are $GM_p =$

Model	ε	Ω	GM_p	GM_b	θ (°)
A	0.1	0.06	0.5	0.1	7.3
B	0.1	0.06	0.4	0.1	4.9
C	0.1	0.06	0.3	0.2	5.2
D	0.1	0.06	0.2	0.2	5.0

Model	ε	Ω	GM_p	GM_b	θ (°)
A	0.2	0.06	0.5	0.1	12.3
B	0.2	0.06	0.4	0.1	6.3
C	0.2	0.06	0.3	0.2	9.9
D	0.2	0.06	0.2	0.2	9.8

Table 4.1: Warp angles θ (in degrees) obtained in the precessing model with halo.

$0.5, GM_d = 0.4, GM_b = 0.1$ (Model A). In contrast, in the previous model composed by a bar and a disc, taking the same values for the pattern speed and the tilt angle, the maximum angle obtained was $\theta = 4.8°$, with a bar and a disc mass of $GM_b = 0.4, GM_d = 0.6$, respectively.

However, the maximal values of the warp angles are obtained when the tilt angle reaches the higher value $\varepsilon = 0.2$, as happened in the previous model. In this case, the warp angle reaches the maximal value $\theta = 12.3°$ keeping the previous pattern speed and mass values. With the previous model, the maximum warp angle was $\theta = 9.3°$, also with $\Omega = 0.06, GM_b = 0.4, GM_d = 0.6$.

When we compare results with the catalog Sánchez-Saavedra et al. (2003), most warps have angles up to 11°, with only some outliers exceeding this quantity. Therefore, our theoretical model accurately approximates these measures, and we remark that a flat rotation curve improves this accuracy.

Let us point out the significant reduction of the warp angle between the first and second cases, as we take mass from the spheroid and add it to the disc. This effect is barely noticeable between the third and fourth model, as we take the same amount of mass from the spheroid to the disc but with a more massive bar. The drop of the rotation curve is not much remarkable in either case, so the difference in the behaviour of the warp angles as we transfer mass from the spheroid to the disc seems to be due to the bar mass.

4.4 The effect of a strong bar in the dynamics close to corotation

We have observed the different structure of the galaxy depending on the bar mass in our model. In Fig. 4.4 an increase of the bar mass shows that the galaxy transforms from a nearly ringed galaxy to a spiral one. This effect is clearly correlated with the increment of the bar mass, or equivalently, with a decreasing rotation curve. Nevertheless, the greatest

warp angles have been obtained when the spheroid has most of the system's mass, the bar mass being reduced to $GM_b = 0.1$.

When we studied a model without halo in Sect. 3.2 we found the greatest warp angles in the cases with the greatest bar mass, as a bigger bar mass makes the galaxy acquire a spiral structure, which benefits the warp structure. In the case of a galaxy with halo, disc and bar, Table 4.1 shows that the warp angle is greatly affected by both the bar mass and the halo mass. In order to ascertain which is the main factor in the size of the warp angle we set a fixed bar mass $GM_b = 0.3$ and observe the behaviour of the model depending on the distribution of the rest of the mass between halo and disc.

Considering that sum of the three component masses is fixed, $G(M_b+M_d+M_p) = 1$, and that the disc mass should be greater or equal than the bar mass, the scope for action is reduced. Therefore, we select four models with the bar mass fixed to $GM_b = 0.3$ and the spheroid and disc masses in the range $GM_p \in [0.1, 0.4]$, $GM_d \in [0.3, 0.6]$ respectively. Although the rotation curves with this configuration are not flat, their slopes are not greatly decreasing and fit fairly well with observations.

Figure 4.7 shows the rotation curves of this model where the bar mass is set to $GM_b = 0.3$. Model A' (top left panel) illustrates the rotation curve of a galaxy with components' mass $GM_b = 0.3$, $GM_d = 0.3$ and $GM_p = 0.4$. The curve rises linearly close to the center and begins to decrease at radius 3 kpc approximately. As we increase the disc mass to $GM_d = 0.4$ taking mass of the spheroid, $GM_p = 0.3$, in Model B' (top right panel), the circular velocity falls faster in the outer parts. This decay is more evident in Model C', where we continue taking mass only from the spheroid, so $GM_b = 0.2$, to add it to the disc, $GM_d = 0.5$, as shown in bottom left panel. When the spheroid mass reaches its minimum value at $GM_p = 0.1$, and the disc mass doubles that of the bar, $GM_d = 0.6$, Model D' (bottom right panel), the rate of decay is the fastest. The last observation that we wish to make, comparing Figs. 4.7 and 4.8, is how the invariant manifolds are longer when the rotation curve is flatter, and become shorter as the rotation curve gains negative slope.

The performance of the invariant manifolds with these falling rotation curves, or equivalently, with a more massive bar mass, is shown in Fig. 4.8. The structure of the galaxy has clearly changed due to the presence of the bar. In Model A', where the masses take the values $GM_p = 0.4$, $GM_d = 0.3$, $GM_b = 0.3$, the inner unstable invariant manifolds are together, blending with the bar. The exterior branches of the invariant manifolds are the only ones visible, giving rise to spiral arms wide open. In this case we do not obtain a spiral structure, since we observe only two arms emanating from the bar ends, and the inner branches of the invariant manifolds add their luminosity to the Ferrers bar. As to

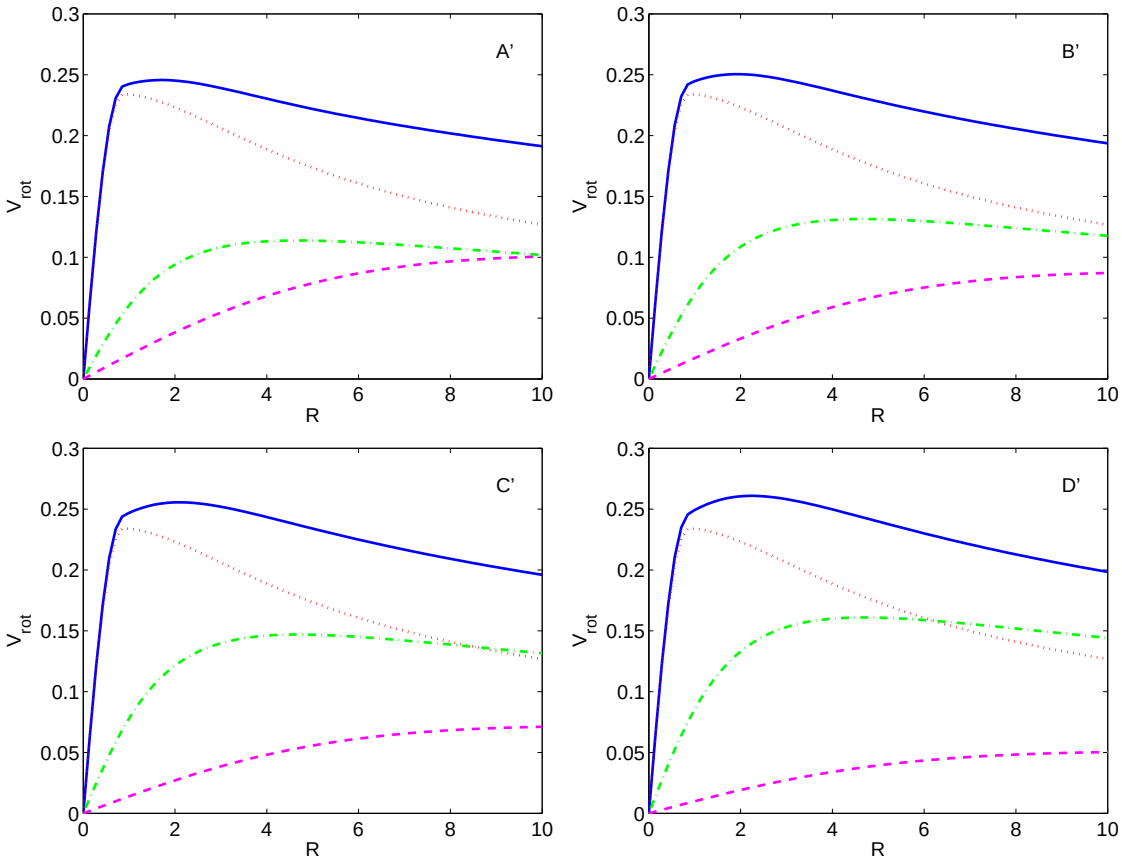

Figure 4.7: Rotation curves of the precessing model with halo, composed by a bar, a disc and a spheroid, when the bar mass is fixed to $GM_b = 0.3$. The rotation curve of the composed model is marked in blue (solid line), the one of the bar is in red (dotted line), for the disc is in green (dot-dashed line) and for the spheroid in magenta (dashed line). Model A' (top left): $GM_b = 0.3, GM_d = 0.3, GM_p = 0.4$. Model B' (top right): $GM_b = 0.3, GM_d = 0.4, GM_p = 0.3$. Model C' (bottom left): $GM_b = 0.3, GM_d = 0.5, GM_p = 0.2$. Model D' (bottom right): $GM_b = 0.3, GM_d = 0.6, GM_p = 0.1$.

the tilt angle effect, we observe that when ε reaches its greatest value, the inner manifolds slowly open up making their structure visible. The spheroid mass decreases in Model B', with values $GM_p = 0.3$, $GM_d = 0.4$, $GM_b = 0.3$. Then the inner branches move away while the exterior ones start to close, making bigger this effect as the tilt angle increases. For Model C', $GM_p = 0.2$, $GM_d = 0.5$, $GM_b = 0.3$, the observed progression continues, the outer branches are closer and the inner ones continue moving apart, forming an elliptical structure surrounding the Ferrers bar. A clearly discernible spiral structure appears. Model D' takes the parameters $GM_p = 0.1$, $GM_d = 0.6$, $GM_b = 0.3$, and, as in the previous cases, the exterior arms continue closing but remain as a spiral structure, whereas the inner ones acquire a wider elliptical structure. Therefore, as we select models with a progressively faster decreasing rotation curve, the outer branches of the invariant manifolds close up but they maintain a spiral shape.

Comparing with Fig. 4.4 of the previous model, we reach the same conclusion as Romero-Gómez et al. (2007), namely that a flat rotation curve makes the galaxy acquire a shape with nearly closed exterior branches, resembling a ringed structure, while a falling rotation curve favours the apparition of spiral arms. The halo component plays an important role in the structure of the galaxies, above all in the structure of the inner branches, since in both models (Figs. 4.4 and 4.8) a greater spheroid mass makes them nearly closed, mixing with the bar structure and making only the outer branches visible. In addition, an increase of the bar mass makes the outer branches of the invariant manifolds reach further out from the centre of the galaxy.

In order to compare the effect of the tilting angle ε in both models, in Fig. 4.9 we display the invariant manifolds of this model, with the bar mass fixed to $GM_b = 0.3$, in three dimensions. The effect appreciated in the previous model (see Fig. 4.5) is confirmed, since the exterior branches clearly acquire a tilting in the z-component as ε increases, whereas the inner branches remain almost flat.

If we change the view point of Fig. 4.9 to approximate to a xz-plane, warped shapes appear as the tilt angle increases (see Fig. 4.10). Obviously the warped shapes are different from those of the previous model in Fig. 4.6, since the shape of the galaxies differs greatly from one to another. The total warp length is clearly bigger in this model with $GM_b = 0.3$, due to the fact that, as we have just mentioned, the outer branches of the invariant manifolds are longer.

As for the warp angles obtained, Table 4.2 allows us to compare whether the warp amplitude, θ, depends on the slope of the rotation curve, the bar mass or the halo mass. When the tilt angle takes values $\varepsilon > 0$, a flat rotation curve (warp angles given in Table 4.1) favours slightly greater angles in most cases. But this effect is not linear, since in the

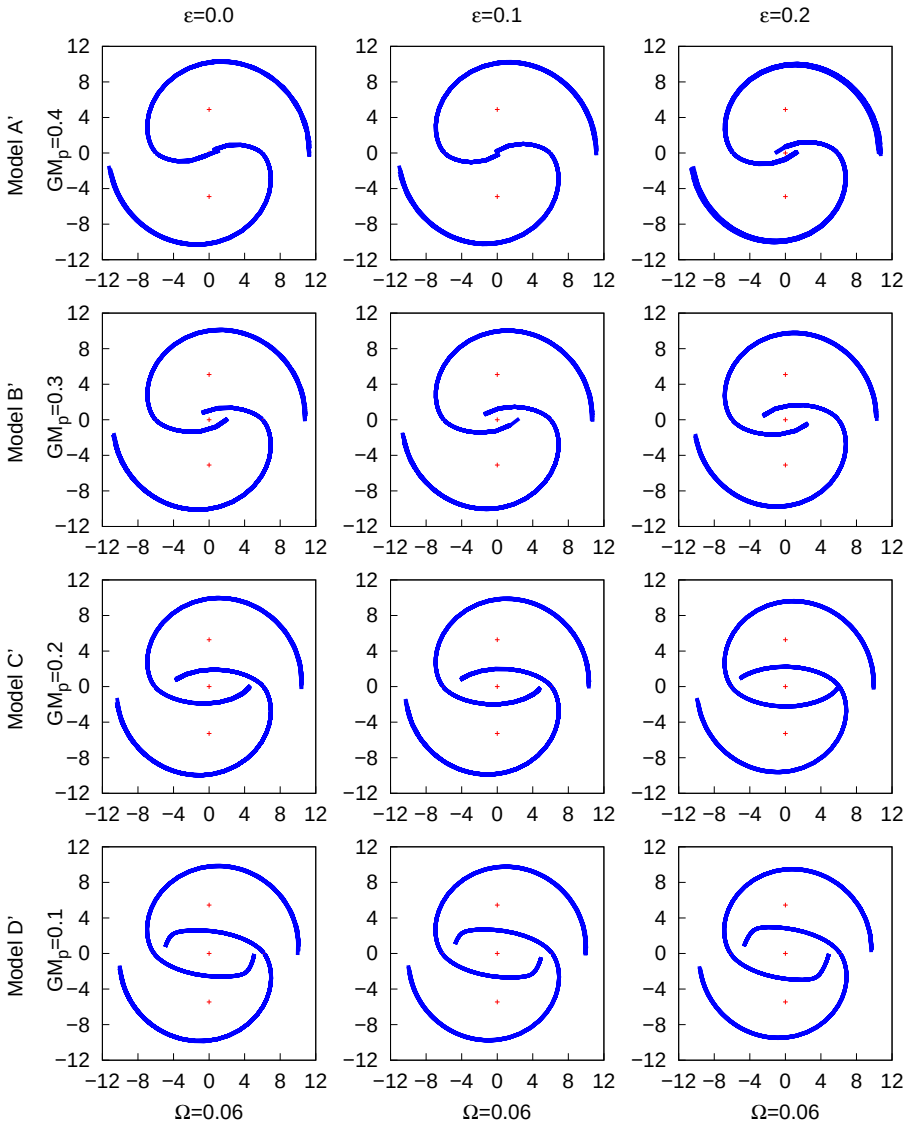

Figure 4.8: Unstable invariant manifolds for the precessing model with halo, when the bar mass is fixed to $GM_b = 0.3$. First row: $GM_p = 0.4$, $GM_d = 0.3$, $GM_b = 0.3$. Second row: $GM_p = 0.3$, $GM_d = 0.4$, $GM_b = 0.3$. Third row: $GM_p = 0.2$, $GM_d = 0.5$, $GM_b = 0.3$. Last row: $GM_p = 0.1$, $GM_d = 0.6$, $GM_b = 0.3$. The tilt angle varies in columns in the range $\varepsilon \in [0, 0.2]$.

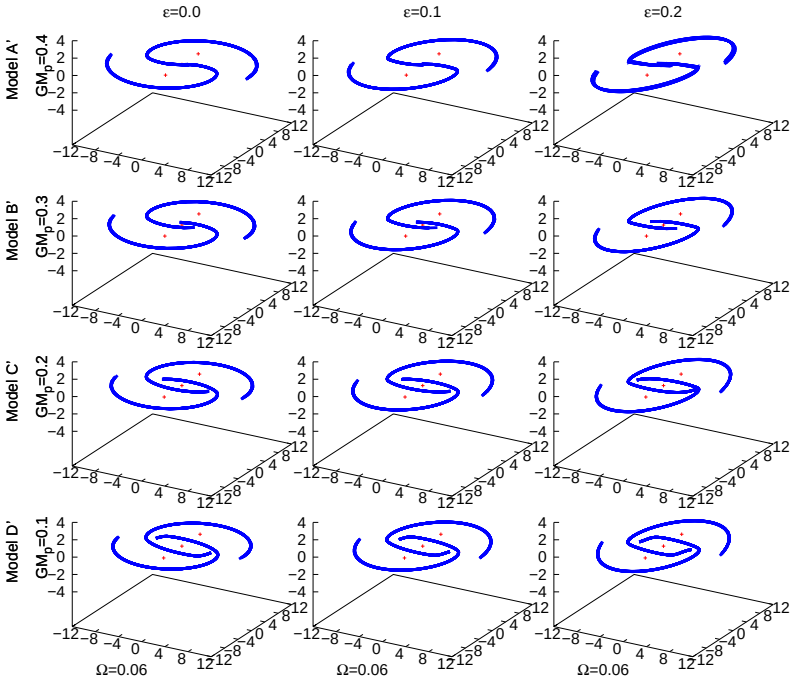

Figure 4.9: 3D view of the plots shown in Fig. 4.8.

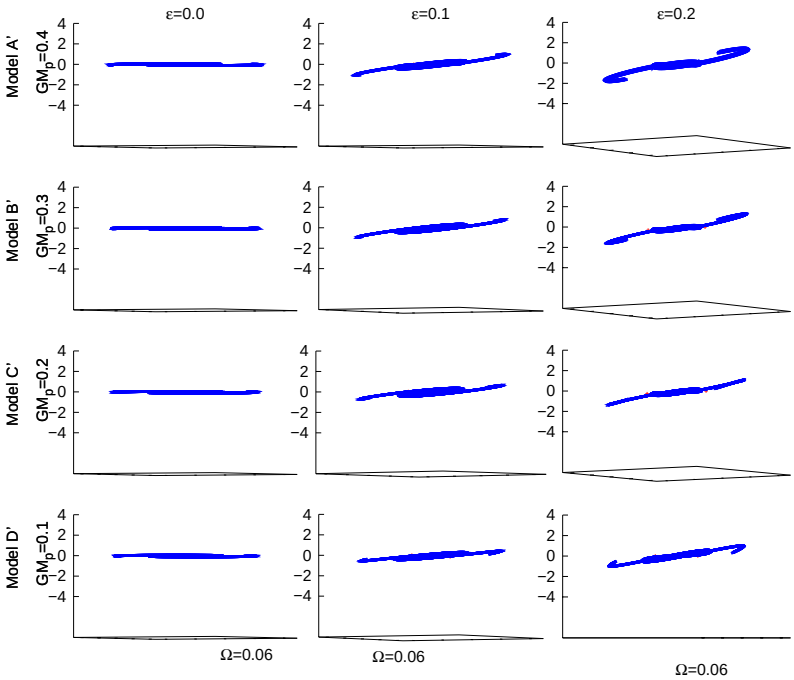

Figure 4.10: Near edge-on view of the plots shown in Fig. 4.8.

Model	ε	Ω	GM_p	θ (°)
A'	0.1	0.06	0.4	5.7
B'	0.1	0.06	0.3	5.2
C'	0.1	0.06	0.2	4.8
D'	0.1	0.06	0.1	4.5

Model	ε	Ω	GM_p	θ (°)
A'	0.2	0.06	0.4	11.3
B'	0.2	0.06	0.3	10.4
C'	0.2	0.06	0.2	9.6
D'	0.2	0.06	0.1	8.9

Table 4.2: Warp angles θ (in degrees) obtained in the precessing model with halo when the bar mass is fixed to $GM_b = 0.3$.

previous model a great reduction of the warp angle is produced when the halo or spheroid mass decreases to $GM_p = 0.4$ to add mass to the disc, $GM_d = 0.5$. In this model with GM_b fixed to 0.3, the decrease of the warp angle is linear, not changing abruptly when the halo loses mass. This fact suggests that the presence of a more massive bar makes the system behave linearly, since the same effect is appreciated in both tables when $\varepsilon = 0.1$ or $\varepsilon = 0.2$. The maximal warp angle obtained for this model is $\theta = 11.3°$ which also fits closely with observations, but it is less than that for a flat rotation curve.

In this way, we verify that a flat rotation curve helps to obtain bigger warp angles, but in order to get a linear behaviour of the system, the model should comprise a bar with substantial mass.

Chapter 5

The effect of double-barred systems on the spiral arms

The existence of double-barred galaxies has been inferred from images taken by the Hubble Space Telescope. Erwin & Sparke (2003) have compiled images of optically barred galaxies, and at least one quarter of them are double-barred. Some examples of these galaxies are in Fig. 5.1. They claim that a typical secondary bar has around 12% of the size of the primary one, and the secondary bar does not always have the same position with respect to the main bar.

N-body simulations and analytical studies have been done in this direction, with or without taking into account the above mass distributions among bars. The authors in Shen & Debattista (2009) study the properties of the double-barred galaxies from their own N-body simulations (Debattista & Shen, 2007), and find that an independently rotating

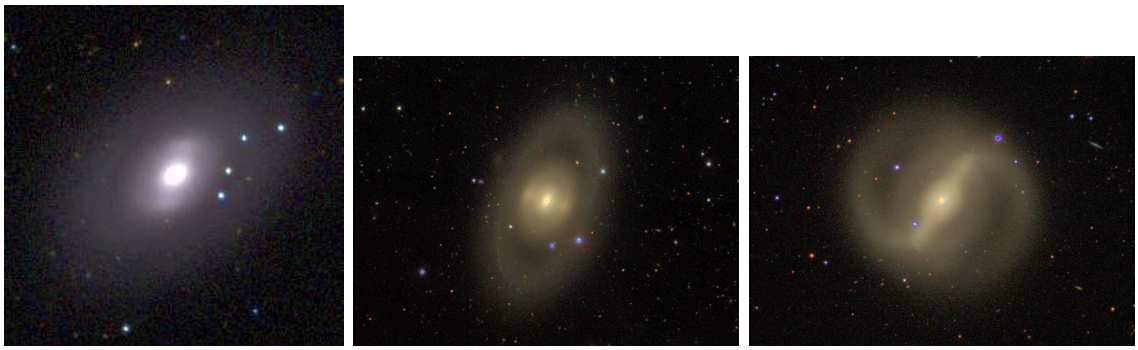

Figure 5.1: Double-barred galaxies. Left: NGC 2950. Center: NGC 3945. Right: NGC 4314. Images taken from SDSS.

secondary bar has a minor effect in the dynamics of the galaxy. Maciejewski & Sparke (2000), Maciejewski & Athanassoula (2007) show that regular orbits give support to the bars in their motion and constitute the backbone of these galaxies with two independently rotating bars. Garzón & López-Corredoira (2014) follow by an analytical method the evolution of two isolated bars oscillating one with respect to the other. The authors study two possible cases, one formed by rigid bars and the other admitting a geometrical deformation of the bars, concluding that in the first case a coupling of the bars is produced, whereas in the second one an exchange of angular momenta between the two bars is obtained.

A considerable difficulty in the study of these galaxies is the same as for single-barred galaxies, namely the fact that for real galaxies only one viewing angle is available for each case, whereas it is possible to visualize a simulation from many viewing angles, in order to realize the geometry of the object. Therefore, in near, face-on galaxies an existing bar is clearly seen, while in near, side-on galaxies, the existence of the bar has to be inferred from the observation of a boxy/peanut bulge which is characteristic of bars.

Most studies on double-barred galaxies are related to the morphology of the Milky Way, which is not clear at the moment. Probably, the Milky Way hosts a double-bar type structure at its centre, consisting of a boxy bulge known as the COBE/DIRBE bar and a long thin bar called simply the Long Bar. The existence of the Long Bar was detected by studies of the near-IR red clump giants (see e.g. López-Corredoira et al., 2007). But the relative orientation of each bar in the inner galaxy is still doubtful. Some researchers consider that the COBE/DIRBE has half-length around 3.1-3.5 kpc, forming an angle of 15° - 30° with respect to the Sun-Galactic Centre direction (see e.g. Binney et al., 1997). Other authors argue that the Long Bar has a half-length of 4-4.5 kpc and forms an angle of around 40° with the said direction (see e.g. López-Corredoira et al., 2007).

The application of invariant manifolds in this study has been made in Romero-Gómez et al. (2011), where the authors analyzed the morphology and kinematics of such manifolds arising from five representative Galactic potentials (two with Ferrers bar, two with a quadrupole bar and another one with a composite bar). They found that the invariant manifolds describe an inner and an outer ring which resemble the observations. But one of the main features of the Milky Way is the presence of two stellar massive spiral arms (Benjamin et al., 2005), which have not been obtained.

Towards this end, and in a more general context, we study how the presence of two bars is related to that of four spiral arms. We do not center ourselves on the Milky Way, but consider a wide range of bar sizes and of angles between them.

5.1 Components and description of the model

Due to the uncertainty surrounding double-barred galaxies or galaxies with four spiral arms, we work with different configurations, all of them composed by two Ferrers bars, and sometimes with a Miyamoto-Nagai disc as well. The Ferrers bars take different size, mass and density, as does the Miyamoto-Nagai disc, and the main idea is that both bars keep a variable angle between them, in order to try to obtain four spiral arms.

Since the invariant manifolds are responsible for the main visible building blocks in galaxies, as we have observed in the cases of spiral arms or rings, we develop the study of the invariant manifolds in the case of double-barred galaxies. To this purpose, we use the equations of motion (2.62) defined in previous models. We are interested in the equilibrium points of the model, since from those that are unstable we obtain the Lyapunov orbits, and consequently the invariant manifolds for each critical point.

Therefore, in order to simplify the problem and to analyze in a better way the dynamics of the system, we concentrate in the motion on the $z = 0$ plane, and in this way, our tilt angle of the equations of motion always takes the value $\varepsilon = 0$. The potential of the system is $\phi = \phi_{b_1} + \phi_{b_2} + \phi_d$ with ϕ_{b_1}, ϕ_{b_2} the potentials of the Ferrers bars for the first and second bar respectively, and ϕ_d the potential of the Miyamoto-Nagai disc. Even though the resulting model will be unrealistic, in order to discern more clearly the role of the two bars in the behaviour of the system, we will conclude the section by studying a model where the mass of the system is distributed exclusively between the two bars.

In addition, as the model is composed by, at least, two Ferrers bars, these should form an angle between them. This angle, namely φ, varies over a wide range in order to accurately study the behaviour of the equilibrium points. To study the trajectories of stars under this potential, we work in a synodic reference frame where the x axis is aligned with the semi-major axis of the first bar, and we assume that the two bars rotate together with the same pattern speed Ω, in order to have an autonomous system (not time depending).

In previous models we have seen that the default number of spiral arms given by the invariant manifolds is two, each of them formed by two branches of the manifold, since they are associated with the number of saddle points of the model. Let us suppose that from each unstable equilibrium point departs a unique unstable invariant manifold, that is, we refer the two branches of each unstable invariant manifold as a single manifold. To get four spiral arms, or equivalently four unstable invariant manifolds, we need four unstable equilibrium points. The easiest configuration for the model, although physically unrealistic, is with two symmetric bars which form an angle of $\varphi = \frac{\pi}{2} \approx 1.57$ rad (90°). In this case, eight equilibrium points plus the central equilibrium point appear, so it is a con-

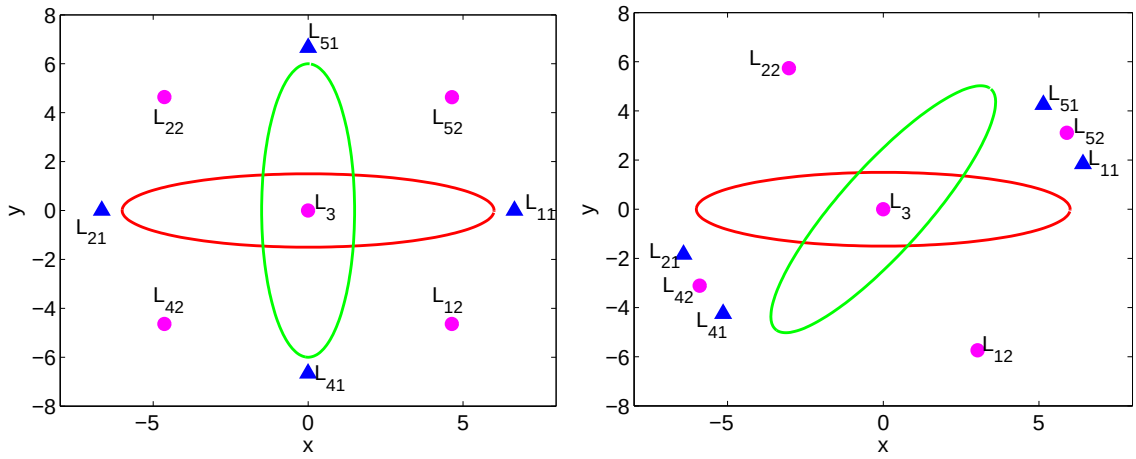

Figure 5.2: Equilibrium points of the model with two bars (unstable points marked by '▲', stable points marked by '•'). Left: Angle between bars of $\varphi = \frac{\pi}{2} \approx 1.57$ rad (90°). Right: Angle between bars of $\varphi = 0.97$ rad ($\approx 56°$).

venient example to obtain all the sought equilibrium points. Since there is no convention about how label all the points, we only follow the order from "main points" to "secondary" ones. Figure 5.2 shows the equilibrium points when the bars are perpendicular, and their behaviour when the angle φ between bars is $\varphi = 0.97$ rad.

5.2 Equilibrium points for different parameter configurations

Let us start analysing the stability character of each equilibrium point, taking into account the nomenclature followed in Fig. 5.2. To this end, we consider the differential matrix around any Lagrangian point of the system (3.5), realizing that $\varepsilon = 0$. The eigenvalues of this matrix in the points L_3, L_{52}, L_{22}, L_{42}, L_{12} are of the form $\{\lambda i, -\lambda i, \mu i, -\mu i, \omega i, -\omega i\}$ (λ, μ, $\omega \in \mathbb{R}^+$). Thus, these points are linearly stable elliptic points, and they do not intervene in the formation of the manifolds.

Next, we analyse the eigenvalues of the previous differential matrix for the rest of the points in this system, L_{11}, L_{51}, L_{21}, L_{41}. Around these points, the eigenvalues take the form $\{\lambda, -\lambda, \mu i, -\mu i, \omega i, -\omega i\}$ (λ, μ, $\omega \in \mathbb{R}^+$), so they are unstable hyperbolic points and are related to the existence of the invariant manifolds.

Once we have described the common dynamics for all the models, we begin to investigate the behaviour of each particular model. We study the distribution of the equi-

librium points depending on the size of the bars, their mass or their density distribution, or whether the disc mass plays any important role in them. Moreover, we see how the equilibrium points vary according to the angle between the bars.

Note that thoroughout this chapter the length unit used is the kpc, the time unit is $\mathrm{u}_t = 2 \times 10^6$ yr and the gravitational constant $G = 6.674 \times 10^{-11}$ m^3 kg^{-1} s^{-2}. Again, we adopt the criterion that $G(M_{b_1} + M_{b_2} + M_d) = 1$ or $G(M_{b_1} + M_{b_2}) = 1$ according to whether the model has a disc or not.

5.2.1 The role of the semi-minor axis of the main bar

We study the variation of the equilibrium points depending on the angle between bars φ and the semi-minor axis of the first bar b_1. In this model the density distribution of the bars is not preserved, since we change the width of the bar but not its mass. The goal is to observe how the distribution of the equilibrium points is related to the size of the bar.

Our model is composed by a Miyamoto-Nagai disc and two Ferrers bars. The shape of the disc is given by $A = 3$ and $B = 1$, while its mass remains constant at $GM_d = 0.8$. Regarding both bars, the first bar takes values $a_1 = 6$, $b_1 \in [1.5, 3.5]$ and $c_1 = 0.6$, with bar mass fixed at $GM_{b_1} = 0.1$, whereas the second one takes the same values but fixing $b_2 = 1.5$ (acquiring the same size as in Pfenniger (1984)). The pattern speed is set to $\Omega = 0.05$ kpc/[u$_t$], and the separation angle between bars is considered in the range $\varphi \in [0.17, \frac{\pi}{2}]$ rad $= [10, 90]^\circ$. Figure 5.3 shows the variation of the equilibrium points as the bars change.

Let us discuss Fig. 5.3. In this figure we plot the first bar in red, the second bar in green, the unstable equilibrium points in blue and the stable one in magenta. The columns correspond to increasing values of the width b_1 of the first bar, and the rows correspond to decreasing values of the separation angle between bars. For the first column, $b_1 = 1.5$, the two bars are symmetrical ($b_1 = b_2$), and the separation angle changes from $\varphi = \frac{\pi}{2}$ to $\varphi = 0.17$ rad. When the bars are perpendicular, nine equilibrium points are perfectly observed. As the angle φ decreases, the central equilibrium point remains in the same position, but the rest of the points change according to the orientation of the second bar. Let us examine each plot separately in its four quadrants. In the first quadrant, the equilibrium points L_{11}, L_{52}, L_{51} gather rapidly, as it happens in the third quadrant for the points L_{21}, L_{42}, L_{41}. On the other hand, in the other two quadrants the points L_{22} and L_{12}, respectively, remain at a considerable distance of the rest. Note that in each group of three points, two points are unstable and one point is stable, located in the middle of the group. Therefore, this is a candidate configuration to yield four invariant manifolds, or four spiral arms, since there are four unstable equilibrium points and besides they are

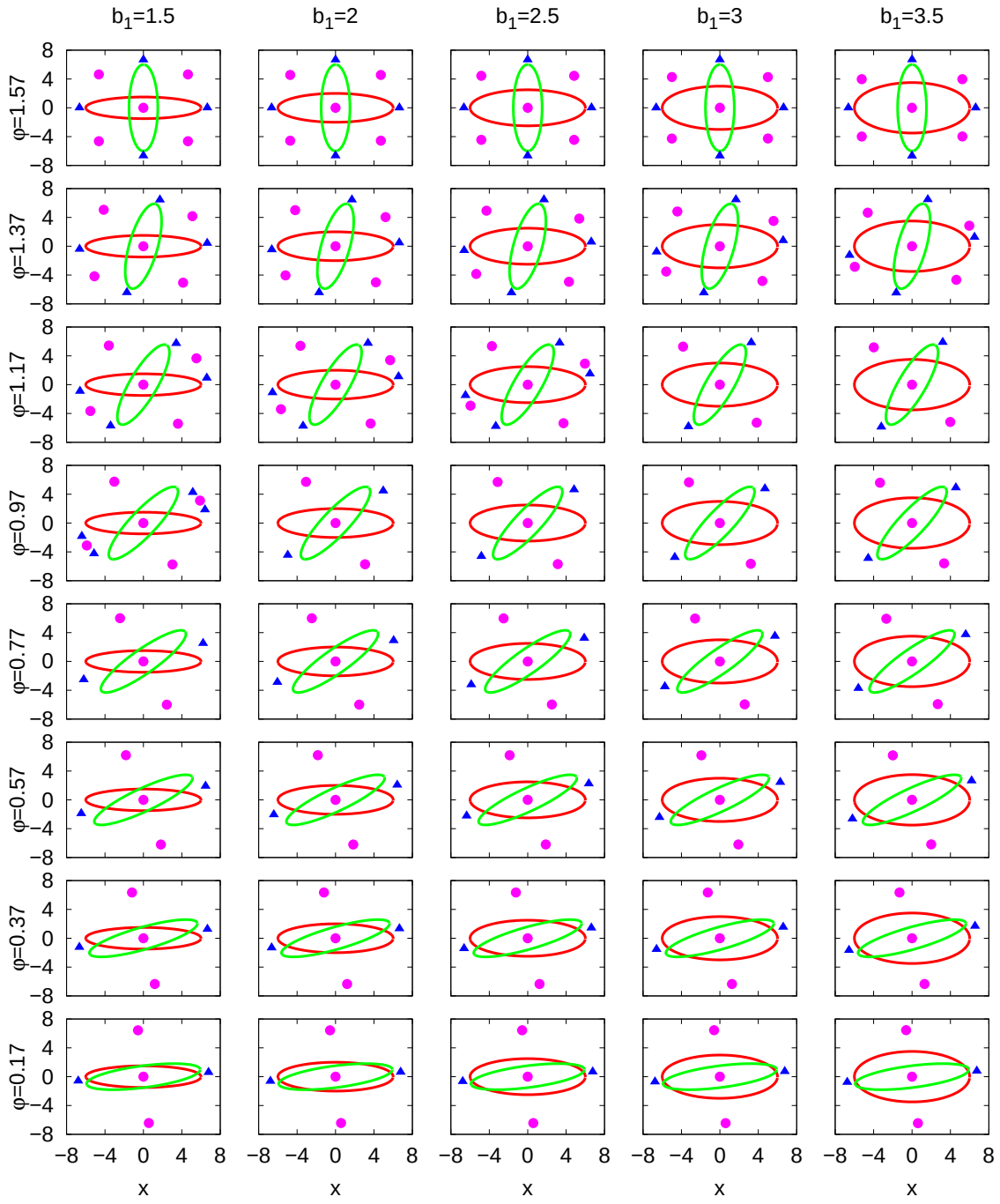

Figure 5.3: Equilibrium points (unstable points marked by '▲', stable points marked by '•') in the xy plane, in a model composed by a Miyamoto-Nagai disc and two Ferrers bars when the width of the first bar and the separation angle between bars vary. The parameters taken are $A = 3$, $B = 1$ and $GM_d = 0.8$ for the disc; $a_1 = 6$, $b_1 \in [1.5, 3.5]$, $c_1 = 0.6$ and $GM_{b_1} = 0.1$ for the first bar; $a_2 = 6$, $b_2 = 1.5$, $c_2 = 0.6$ and $GM_{b_2} = 0.1$ for the second bar. The pattern speed of the system is set to $\Omega = 0.05$.

at an appreciable distance. But, as we observe in the figure, this distribution of points disappears when the separation angle reaches the value $\varphi = 0.77$. From this value, only four equilibrium points appear besides the central equilibrium point, of which two are stable points and two unstable ones, so the distribution of points comes back to that of the previous models.

So wide a separation between bars is unlikely in real galaxies, since observations would have detected it. Thus, we continue to study possible models which fit better with observations. As we increase the width b_1 of the first bar, we discern that the groups of three points disappear more quickly. When $b_1 = 2, 2.5$ the nine equilibrium points become four at a separation angle $\varphi = 0.97$, but if we increase b_1 up to $b_1 = 3, 3.5$, they disappear when $\varphi = 1.17$ rad.

It seems that the equilibrium points are attracted by the wider bar. We may conclude in this first model that the size of the bar, independently of its mass or density, has influence in the distribution of the equilibrium points in the model. However, this model is not appropriate according to observations.

The model with the second bar wider than the first one is a symmetrical problem with the same results and conclusions, so it is not necessary to discuss it separately.

5.2.2 The role of the mass ratio between bars

Once we have seen the performance of the equilibrium points when the width of the bar changes, we continue studying whether this behaviour is modified varying only the mass ratio between bars. Again, we work with two Ferrers bars plus a Miyamoto-Nagai disc. Since we are interested in comparing whether the mass of the bar affects more than the bar width, the parameters of the disc remain as in the previous model, with $A = 3$, $B = 1$ and $GM_d = 0.8$. The size of both bars is $a = 1$, $b = 1.5$, $c = 0.6$, but in this case the mass of the second bar is increased, $GM_{b_2} = 0.1, 0.15, 0.18$, while the mass of the first one decreases, $GM_{b_1} = 0.1, 0.05, 0.02$. The pattern speed of the system is set to $\Omega = 0.05$. Let us notice that this case is the opposite of the previous one, since here we increase the mass in the second bar whereas in the previous model it was the first bar which got an increase in the width. The separation angle varies, again, from $\varphi = \frac{\pi}{2}$ to $\varphi = 0.17$ rad.

Figure 5.4 presents the behaviour of the equilibrium points as the mass of both bars changes. The first column, when $GM_{b_1} = 0.1$ and $GM_{b_2} = 0.1$ is the same case as the first one of the previous figure, so we compare with this first case. When the second bar mass increases up to $GM_{b_2} = 0.15$, and the first bar mass decreases until $GM_{b_1} = 0.05$, an important change is appreciated even when bars are perpendicular. The equilibrium points

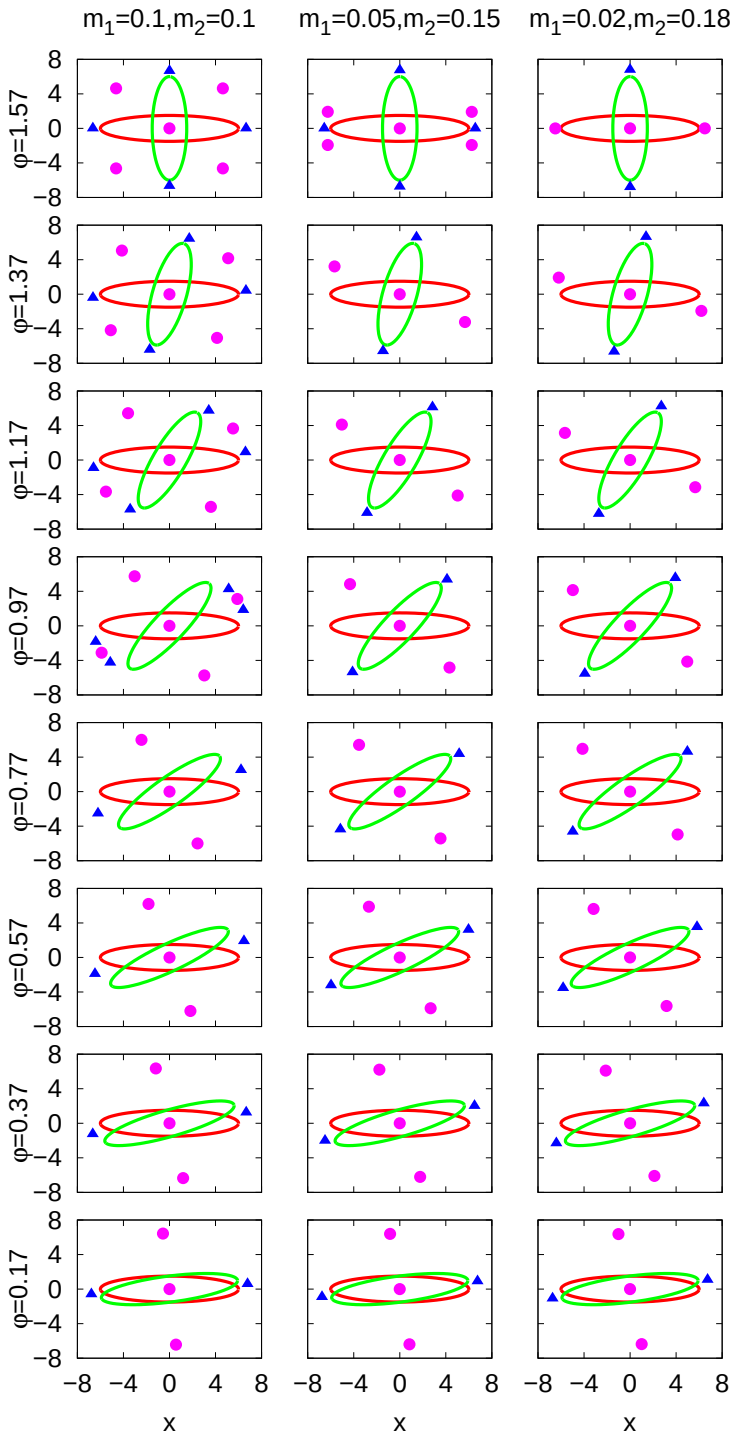

Figure 5.4: Equilibrium points (unstable points marked by '▲', stable points marked by '•') in the xy plane, of a model composed by a Miyamoto-Nagai disc and two Ferrers bars when the mass of the bars and the separation angle between bars vary. The parameters taken are $A = 3$, $B = 1$ and $GM_d = 0.8$ for the disc; $a_1 = 6$, $b_1 = 1.5$, $c_1 = 0.6$ and $GM_{b_1} = 0.1, 0.05, 0.02$ for the first bar; $a_2 = 6$, $b_2 = 1.5$, $c_2 = 0.6$ and $GM_{b_2} = 0.1, 0.15, 0.18$ for the second bar. The pattern speed of the system is set to $\Omega = 0.05$.

which were in the middle of the quadrants, L_{52}, L_{22}, L_{42} and L_{12}, seem to be attracted by the first bar with smaller mass. In fact, what happens is that the model is converging to a model with only the second bar. Let us suppose that we have a model with only the green bar, i.e. the second bar. The equilibrium points would be two unstable points at the ends of the bar, two stable ones in the horizontal direction of the semi-minor axis, and the central stable point. Let us come back to our model with two bars. The equilibrium points which are close to the first bar, the red one, are in fact becoming a stable single point. We check this hypothesis as the separation angle between bars decreases by 0.2 rad, since the equilibrium points become just five, two unstable at the ends of the second bar and two stable in the direction of the minor-axis of this bar, plus the central equilibrium point.

If we continue decreasing the mass of the first bar and increasing the mass of the second one, the change is more abrupt. There are only five equilibrium points even when the bars are perpendicular, with the second bar dominating over the first one. The model where the first bar increases its mass whereas the second bar decreases it, has the symmetrical behaviour, with the first bar dominating over the second one.

We have seen so far that, whether we vary the mass or size of the first or of the second bar, it is always the bigger bar, regardless of its position, the one that essentially determines the distribution of the equilibrium points, as expected. Therefore, if the two bars differ greatly in size, or in mass, the bigger bar predominates over the smaller one. We proceed now to consider separately the influence of the pattern speed and, once its optimal value is determined, we fix the density of the bars and set the value of the angle φ between bars to values likely to yield a configuration of nine equilibrium points.

5.2.3 The role of the pattern speed

We assume that both bars rotate together with the same pattern speed. So, in this model we change the pattern speed, in order to see its effects in the equilibrium points. Since in the previous models we have observed that the best way to preserve nine equilibrium points is to use two symmetric bars, we select here two Ferrers bars of this form, with the same size $a = 6$, $b = 1.5$, $c = 0.6$, and the same mass $GM_b = 0.1$. Also we take a Miyamoto-Nagai disc with parameters $A = 3$, $B = 1$ and $GM_d = 0.8$. Regarding to the pattern speed, it is considered with the values $\Omega = \{0.045, 0.05, 0.054, 0.06\}$, which are the most common values taken in the study of this model. The separation angle is taken as previously, from $\varphi = \frac{\pi}{2}$ to $\varphi = 0.17$ rad.

As we observe in Fig. 5.5 the differences in the distribution of the equilibrium points

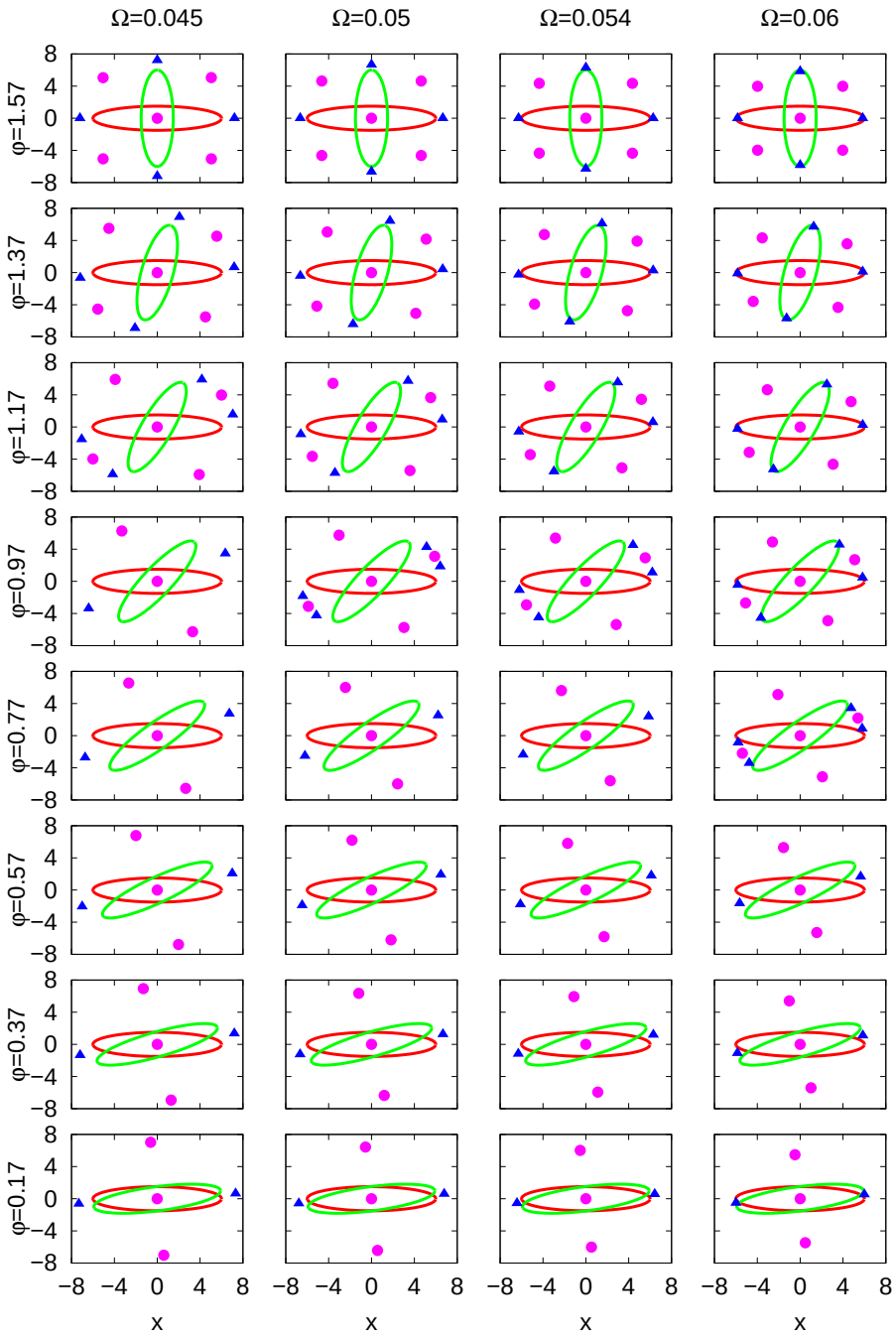

Figure 5.5: Equilibrium points (unstable points marked by '▲', stable points marked by '•') in the xy plane, of a model composed by a Miyamoto-Nagai disc and two Ferrers bars when the pattern speed and the separation angle between bars vary. The parameters taken are $A = 3$, $B = 1$ and $GM_d = 0.8$ for the disc; $a_1 = 6$, $b_1 = 1.5$, $c_1 = 0.6$ and $GM_{b_1} = 0.1$ for the first bar; $a_2 = 6$, $b_2 = 1.5$, $c_2 = 0.6$ and $GM_{b_2} = 0.1$ for the second bar.

appear from $\varphi = 0.97$ rad on. For greater values of the separation angle always nine equilibrium points appear, and their proximity to the bar depends on the corotation radius. At $\varphi = 0.97$ rad, the smallest pattern speed shows only five equilibrium points: the central stable point, two other stable points and two unstable ones. On the other hand, at the same value of φ, and for values of the pattern speed from 0.05 to 0.06, nine equilibrium points continue existing but they are more azimuthally separated, the faster the bar rotates. As the angle is decreased to the next value, $\varphi = 0.77$, nine points only appear for the greatest value of the pattern speed. For the remaining velocities Ω, the equilibrium points are only five. If we continue decreasing the separation angle, there is no more than five equilibrium points in all the models.

Let us underline that the separation angle $\varphi = 0.77$, for the pattern speed of $\Omega = 0.06$, is the smallest angle that we obtain which shows nine equilibrium points.

5.2.4 The role of density for a fixed separation angle

The smallest separation angle in which nine equilibrium points appear is $\varphi = 0.77$, albeit only for a very particular choice of pattern speed. The separation angle usually takes the value of $\varphi = 0.97$ before the number of equilibrium points becomes five. We proceed to study the case of both these angles more deeply.

Since we have studied separately the options of changing the mass or the size of the bars, a next logical step is to fix their density. In this model we depart from two symmetric Ferrers bars with equal bar mass $GM_b = 0.5$ and ellipsoid parameters $a = 6$ and $b = c = 0.95$, and change the bar masses redistributing their total mass to make the first one bigger and the second one smaller, i.e. we set the new masses to be $(1+\lambda_1)\cdot GM_b$, $(1+\lambda_2)\cdot GM_b$ respectively with $\lambda_1 = -\lambda_2 > 0$. This mass redistribution is done by keeping the density constant and rescaling the parameters of the ellipsoid by a factor $\sqrt[3]{1+\lambda_i}$, $i = 1, 2$. When the angle φ between the two bars shrinks, the nine equilibrium points eventually collapse into five equilibrium points. As seen in previous cases (Fig. 5.5), the angle φ at which this transition takes place becomes smaller as the pattern speed becomes greater. Because of this, we now set the pattern speed of the system to $\Omega = 0.06$.

In Fig. 5.6 the separation angle φ is fixed to 0.97 rad. From left to right and top to bottom, we increase the mass of the first bar, the red one, whereas the mass of the second bar, the green one, is decreasing. So, the values of the first bar mass are in the range $GM_{b_1} \in [0.5, 0.9]$, and for the second bar are $GM_{b_2} \in [0.1, 0.5]$. The case in which the bars are symmetrical, i.e. with the same mass, is the only one where nine equilibrium points appear. To the extent that the mass increases in the first bar, and decreases in

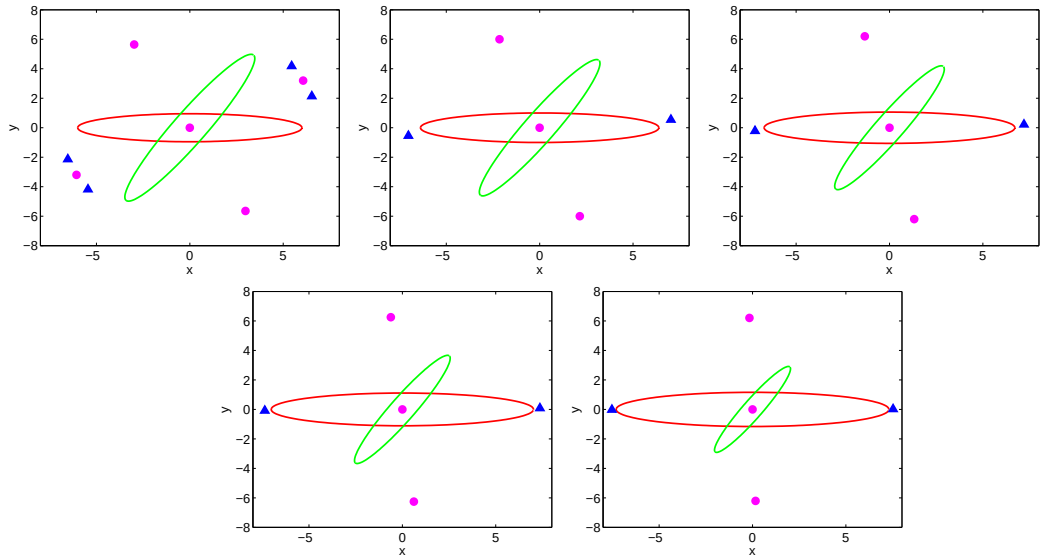

Figure 5.6: Equilibrium points (unstable points marked by '▲', stable points marked by '●') in the xy plane, of a model composed by two Ferrers bars when the pattern speed is fixed to $\Omega = 0.06$ and the separation angle between bars to $\varphi = 0.97$ rad. The parameters taken are in the ratios a:b:c=6:0.95:0.95 for both bars. The masses of the bars vary in the ranges $GM_{b_1} \in [0.5, 0.9]$ for the first one (red), and $GM_{b_2} \in [0.1, 0.5]$ for the second one (green), and their parameters are adjusted keeping constant ratios, according to the density which remains fixed.

the second one, the equilibrium points become just five, as happened in previous models. Following the analysis of these five points, only the two at the ends of the first bar are unstable, whereas the remaining ones are stable.

As the separation angle decreases to $\varphi = 0.77$, just five equilibrium points appear for any given distribution of the masses (see Fig. 5.7). This is in contrast with the results of a previous model consisting of a disc and two bars (Fig. 5.5), where a separation angle ($\varphi = 0.77$) gave rise to nine equilibrium points when $\Omega = 0.06$. The different pattern of the equilibrium points is due to the presence of the disc, containing 80 per cent of the mass of the system.

5.3 Dynamics close to corotation

Although the results achieved with these models do not fit neither observations of galaxies nor N-body simulations, we are interested, from a theoretical point of view, in the behaviour of the invariant manifolds when nine equilibrium points appear.

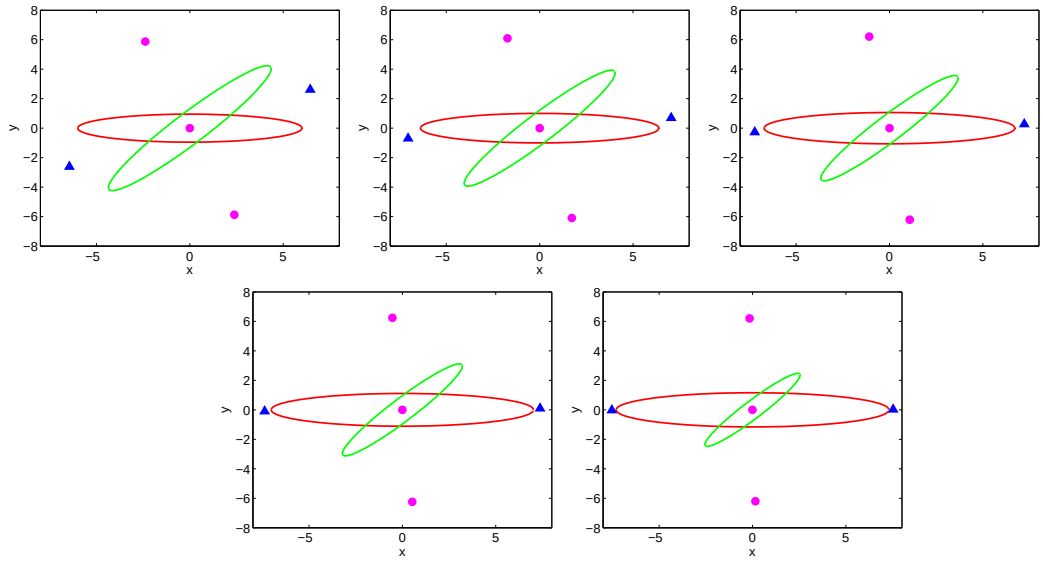

Figure 5.7: Equilibrium points (unstable points marked by '▲', stable points marked by '●') in the xy plane, of a model composed by two Ferrers bars when the pattern speed is fixed to $\Omega = 0.06$ and the separation angle between bars to $\varphi = 0.77$ rad. The parameters taken are in the ratios a:b:c=6:0.95:0.95 for both bars. The masses of the bars vary in the ranges $GM_{b_1} \in [0.5, 0.9]$ for the first one (red), and $GM_{b_2} \in [0.1, 0.5]$ for the second one (green), and their parameters are adjusted keeping constant ratios, according to the density which remains fixed.

In order to compute the invariant manifolds, we select some of the cases considered before. We focus on the models where four unstable equilibrium points appear. Note that the best option to get nine equilibrium points is with two identical bars, thus, in all next models we take this choice. In this way, the first model selected is the one with two symmetrical bars, with the size of both bars fixed to $a = 6$, $b = 1.5$ and $c = 0.6$ and bar mass to $GM_b = 0.1$, and a Miyamoto-Nagai disc with parameters $A = 3$, $B = 1$ and $GM_d = 0.8$. Also, the pattern speed is taken as $\Omega = 0.05$. For this model we take two cases, one where the separation angle φ is 1.17 rad, and another one with $\varphi = 0.97$ rad. Our aim is compare the invariant manifolds in both cases, to observe whether any difference appears between them when there are four unstable points.

The results in the first case are shown in Fig. 5.8. Let us explain the dynamics of this model since it is a bit complex. We begin with the unstable invariant manifold associated to the periodic orbit around the unstable equilibrium point L_{11}. The upper branch of this manifold extends to the vicinity of the unstable point L_{51}, and comes back to the starting equilibrium point L_{11}, surrounding clockwise the stable equilibrium point L_{52} that separates both unstable points. On the other hand, the lower branch of this unstable manifold, goes down to the unstable point on the other side of the bar, avoiding the stable one L_{12}.

The unstable invariant manifold associated to the periodic orbit around the unstable equilibrium point L_{51} has a lower branch that descends to L_{11} avoiding the stable point L_{52}, and an upper branch which moves counterclockwise to the unstable equilibrium point on the other side of the bar.

Finally, the invariant manifolds of Lyapunov orbits around the unstable equilibrium points L_{21} and L_{41} behave symmetrically with respect to those of the equilibrium points L_{11} and L_{51}.

The second model, with a separation angle of $\varphi = 0.97$ shows how the invariant manifolds behave slightly differently than in the previous model (see Fig. 5.9). The fact that the unstable equilibrium points of the first and third quadrant are closer to the corresponding stable ones shows up in the corresponding manifolds. The invariant manifolds cease to surround the stable points L_{52} and L_{42}, and adopt a shape that is very similar to the one obtained in a model with only one bar (see Fig. 3.10).

The next effect we compare is the increase of the pattern speed. The parameters of the bar and disc remain the same, but the pattern speed of the system grows up to $\Omega = 0.06$. Let us remember that in this case the four unstable equilibrium points stayed until the separation angle descended to $\varphi = 0.77$ rad. Figure 5.10 shows the behaviour of the equilibrium points and invariant manifolds with these conditions, taking the value

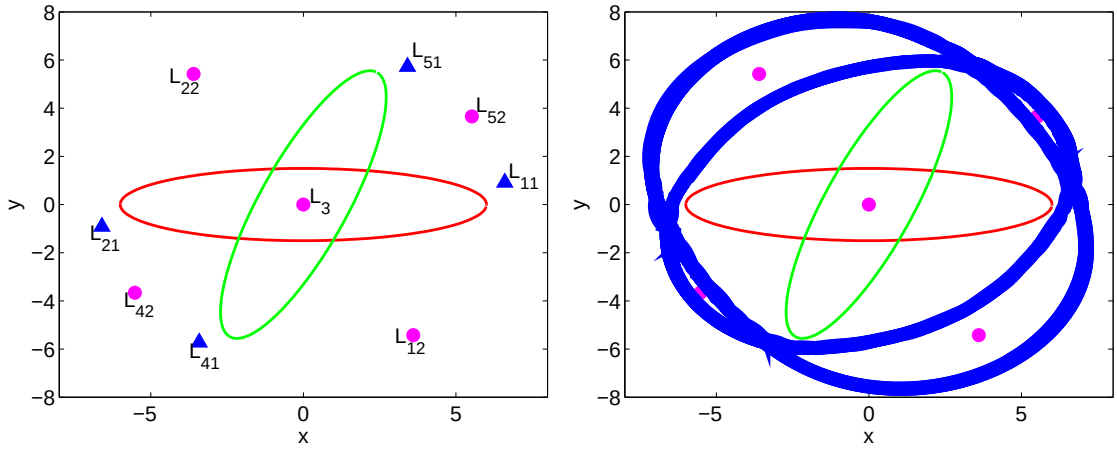

Figure 5.8: Left: Equilibrium points (unstable points marked by '▲', stable points marked by '•') in the xy plane, of a model composed by a Miyamoto-Nagai disc and two Ferrers bars, with parameters $A = 3$, $B = 1$ and $GM_d = 0.8$ for the disc; $a = 6$, $b = 1.5$, $c = 0.6$ and $GM_{b_1} = 0.1$ for both bars, and $\Omega = 0.05$. Right: Invariant manifolds in this model with four unstable equilibrium points. The separation angle is fixed to $\varphi = 1.17$ rad.

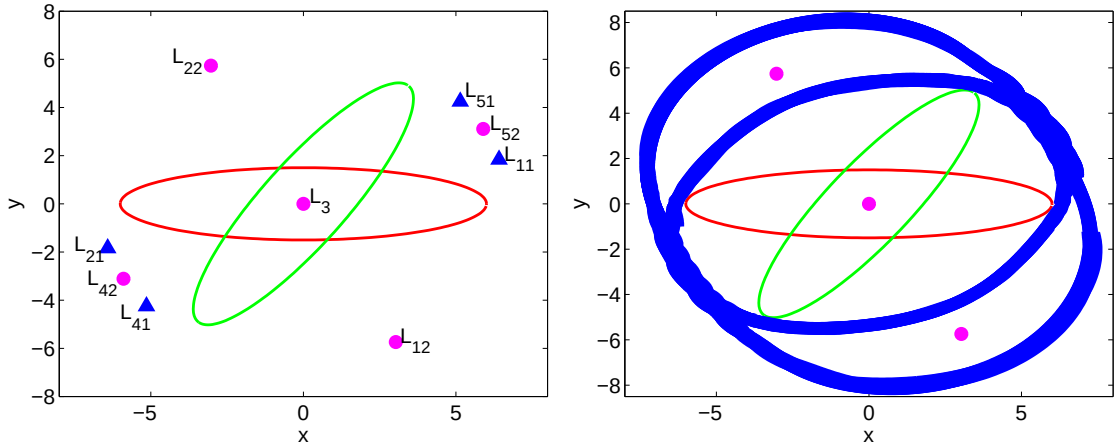

Figure 5.9: Left: Equilibrium points (unstable points marked by '▲', stable points marked by '•') in the xy plane, of a model composed by a Miyamoto-Nagai disc and two Ferrers bars, with parameters $A = 3$, $B = 1$ and $GM_d = 0.8$ for the disc; $a = 6$, $b = 1.5$, $c = 0.6$ and $GM_{b_1} = 0.1$ for both bars, and $\Omega = 0.05$. Right: Invariant manifolds in this model with four unstable equilibrium points. The separation angle is fixed to $\varphi = 0.97$ rad.

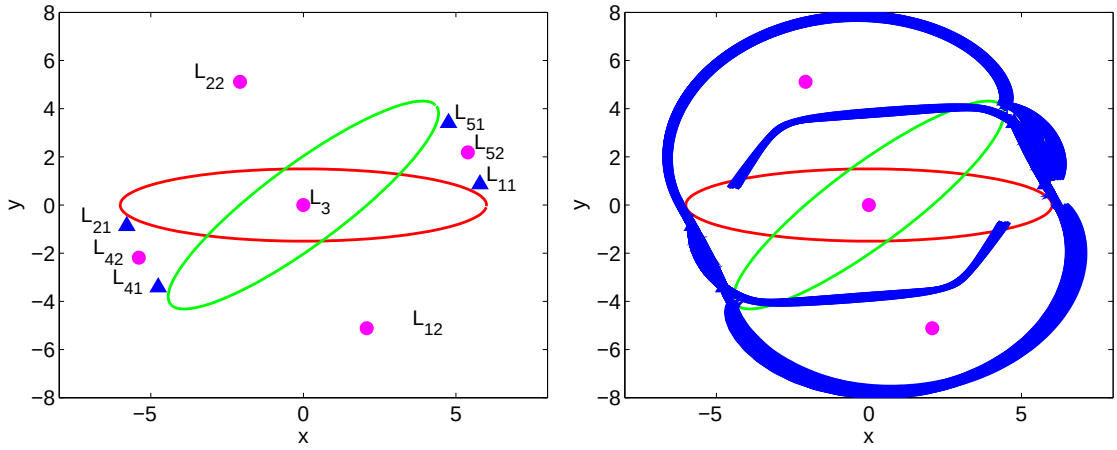

Figure 5.10: Left: Equilibrium points (unstable points marked by '▲', stable points marked by '•') in the xy plane, of a model composed by a Miyamoto-Nagai disc and two Ferrers bars, with parameters $A = 3$, $B = 1$ and $GM_d = 0.8$ for the disc; $a = 6$, $b = 1.5$, $c = 0.6$ and $GM_{b_1} = 0.1$ for both bars, and $\Omega = 0.06$. Right: Invariant manifolds in this model with four unstable equilibrium points. The separation angle is fixed to $\varphi = 0.77$ rad.

$\varphi = 0.77$. The invariant manifolds have a behaviour that markedly differs from that of the previous ones. We note how the outer manifolds still form a ring but the inner ones do not close, because they present an angular slope which turns them into spirals due to the fact that the equilibrium points are closer to both bars. In spite of this fact, four spiral arms still do not show up.

Figures 5.9 and 5.10 present a behaviour similar to that seen in ansae morphologies, with a mass concentration around the equilibrium points at the ends of the bar. This fact is due to that an orbit close to a Lyapunov orbit does not escape from it immediately, moving around the Lyapunov orbit a few times before continuing in the direction of the invariant manifold (Athanassoula et al., 2009).

The last discussion is to investigate what happens when we increase the mass of both bars. In Sect. 3.2, in models with only one bar, a spiral galaxy appeared when the bar mass was higher. Now, let us consider two symmetric bars with size $a = 6$, $b = 1.5$, $c = 0.6$ and with equal mass for each bar $GM_b = 0.3$. Since the total mass of the system is set equal to 1, the disc mass decreases to $GM_d = 0.4$, but we keep it with equal size as before. The minimum value of the separation angle for which four unstable equilibrium points are conserved is $\varphi = 0.97$ rad, so we take this angle as reference. The pattern speed is fixed to $\Omega = 0.06$. Figure 5.11 shows the dynamics of this model, where a spiral galaxy appears, just as it happened in the models of Sect. 3.2. In the figure we note a

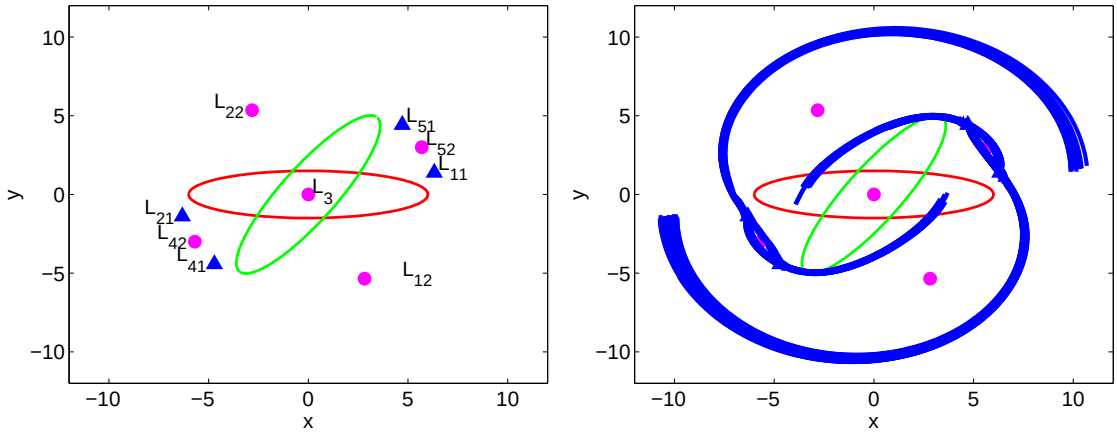

Figure 5.11: Left: Equilibrium points (unstable points marked by '▲', stable points marked by '•') in the xy plane, of a model composed by a Miyamoto-Nagai disc and two Ferrers bars, with parameters $A = 3$, $B = 1$ and $GM_d = 0.4$ for the disc; $a = 6$, $b = 1.5$, $c = 0.6$ and $GM_{b_1} = 0.3$ for both bars, and $\Omega = 0.06$. Right: Invariant manifolds in this model with four unstable equilibrium points. The separation angle is fixed to $\varphi = 0.97$ rad.

small thickening in the regions where one stable and two unstable points coincide, but the shape of the outer and inner manifolds are as in the previously mentioned models. Therefore, the four unstable equilibrium points make the dynamics locally different, but globally similar to those of the model with one bar.

We have analyzed in detail which bar parameters would be necessary for the manifolds to acquire a morphology with four spiral arms. We conclude that the existence of two bars is not closely related to the formation of four spiral arms. This suggests that a possible solution in the manifold framework might be a more complex potential with outer elements such as a spiral part, or, another possibility could be a system formed by the bar, the disc and additional components, which are misaligned with an angle big enough to allow the presence of four unstable equilibrium points, but still small enough for the misalignments to be observationally invisible. An alternative explanation would be that the existence of four spiral arms depends on time-dependent features of the galaxy, which could be reproduced only by means of non-autonomous (i.e. time-dependent) models.

Chapter 6

Towards the non-autonomous problem

Lagrangian Coherent Structures (LCS) are a recently proposed replacement for invariant manifolds in the study of the dynamics of non-autonomous systems. They act as hypersurfaces of maximally attracting or repelling flow, organizing the evolution of the flow in a similar way as invariant manifolds do in autonomous systems.

LCS have been employed notably in the study of problems of fluid dynamics (see Farazmand & Haller, 2012, 2013), or in the elliptic restricted three-body problem (ER3BP) (see Gawlik et al., 2009). The exact concept of what a LCS is, is still evolving. Shadden et al. (2005), Lekien et al. (2007), Gawlik et al. (2009), among others, consider them as ridges of the values of finite-time Lyapunov exponents (FTLE) of the flow, whereas Farazmand & Haller (2012) and therein, Onu et al. (2014), characterize them as critical lines of the averaged material shear, which is an auxiliary autonomous functional also derived from the flow.

We seek to apply the theory of Lagrangian Coherent Structures to the study of the non-autonomous version of the precessing model (2.62). We have developed software to implement the characterization of LCS given by Haller in two dimensions (Onu et al., 2014), as stretch and strainlines. We apply in first place this software to elementary examples to test its robustness and accuracy and to illustrate the meaning of LCS with those examples. Afterwards, we apply our software to determine LCS in both autonomous and non-autonomous versions of our problem.

6.1 Lagrangian Coherent Structures

The starting point to study the local and global structure of a time-dependent flow is the Jacobian given by the variational flow. Let us consider a dynamical system of the form

$$\dot{\mathbf{x}} = \mathbf{v}(\mathbf{x}, t), \quad \mathbf{x} \in U \subset \mathbb{R}^n, \quad t \in [a, b], \tag{6.1}$$

where U denotes an open, bounded subset of $\mathbb{R}^n$, the time t varying over the finite interval $[a, b]$, and $v : U \times [a, b] \to \mathbb{R}^n$ is a sufficiently smooth vector field. For $a \leq t_0 < t \leq b$, define the flow map

$$\mathbf{F}_{t_0}^{t}(\mathbf{x}_0) := \mathbf{x}(t), \tag{6.2}$$

where $\mathbf{x}(t)$ is the solution of equation (6.1) such that $\mathbf{x}(t_0) = \mathbf{x}_0$.

The Jacobian $\nabla \mathbf{F}_{\mathbf{t_0}}^{\mathbf{t}}(\mathbf{x}_0)$ is a linearization of the variation of the flow $\mathbf{F}_{\mathbf{t_0}}^{\mathbf{t}}$ with respect to the initial condition $\mathbf{x}_0$. Its Singular Value Decomposition (SVD) points out the directions in which the flow maximally spreads / is maximally compressed, with the rate of expansion / compression given by the singular values of the Jacobian. For instance, the maximal expansion rate of the flow around $\mathbf{x}_0$ is the first singular value of its Jacobian, which is the Euclidean norm[1] of the Jacobian $||\nabla \mathbf{F}_{\mathbf{t_0}}^{\mathbf{t}}(\mathbf{x}_0)||$, and the direction in which this maximal expansion takes place is given by the first right-singular vector of the SVD.

The SVD of the Jacobian $\nabla \mathbf{F}_{\mathbf{t_0}}^{\mathbf{t}}(\mathbf{x}_0)$ is equivalent to the diagonalization of the Cauchy-Green, or strain, tensor field, widely used in Mechanics,

$$\mathbf{C}_{t_0}^{t} = \left(\nabla \mathbf{F}_{\mathbf{t_0}}^{\mathbf{t}}(\mathbf{x}_0)\right)^T \nabla \mathbf{F}_{\mathbf{t_0}}^{\mathbf{t}}(\mathbf{x}_0), \tag{6.3}$$

where ^{T} stands for matrix transposition.

The eigenvalues of the Cauchy-Green tensor are the *squares* of the singular values of the Jacobian, and the eigenvectors of the Cauchy-Green tensor, $\xi_1, \xi_2, \ldots, \xi_n$, are the right-singular vectors of the Jacobian. In both instances an orthonormal basis of vectors is adopted, but, unfortunately, opposite ordering conventions are followed: It is customary to order the singular values from greatest to smallest, $||\nabla \mathbf{F}_{\mathbf{t_0}}^{\mathbf{t}}(\mathbf{x}_0)|| = \sigma_1 \geq \sigma_2 \geq \ldots \geq \sigma_n$, while the eigenvalues of the Cauchy-Green tensor are usually labelled in increasing order, $\lambda_1 \leq \lambda_2 \leq \ldots \leq \lambda_n$. See Golub & Van Loan (2012) for a mathematical discussion of these concepts.

The concept of a Lagrangian Coherent Structure is recent, and still with much work in progress. Due to this fact, the definition is not settled and several versions with slight differences are found in the literature. Let us present the two main variants of the definition

[1] The Euclidean norm of a matrix A is $||A|| = \sup_{v \neq 0} \frac{||Av||}{||v||}$, or equivalently, the first singular value of A.

of Lagrangian Coherent Structures. We present them only for two dimensional domains, since it is the case that is dealt with in this work, and the definition is simpler in this case.

According to Shadden et al. (2005), a repelling Lagrangian Coherent Structure is a ridge of the FTLE field of the flow $\mathbf{F}_{t_0}^t$, where the finite-time Lyapunov exponent (FTLE) field of $\mathbf{F}_{t_0}^t$ is given by

$$\sigma_{t_0}^t(\mathbf{x}_0) = \frac{1}{t - t_0} \log ||\nabla \mathbf{F}_{t_0}^t(\mathbf{x}_0)||, \tag{6.4}$$

and the ridge corresponds to the intuitive idea of a mountain ridge line for the values of the FTLE field. Concretely, ridges are curves $\mathbf{c}(s)$ in the two dimensional domain such that for all points along the curve, $\mathbf{c}'(s) \,||\, \nabla\sigma(\mathbf{c}(s))$ and $\langle \hat{\mathbf{n}}, \nabla^2\sigma(\mathbf{c}(s))\hat{\mathbf{n}}\rangle < 0$, where $\hat{\mathbf{n}}$ is the unit vector normal to the curve $\mathbf{c}(s)$ and $\sigma = \sigma_{t_0}^t$ (Shadden et al., 2005).

An attracting Lagrangian Coherent Structure is defined in the same way, except that the dynamical system is integrated backwards in time for the computation of the FTLE field. In dynamical systems that are close to an autonomous one with both stable and unstable invariant manifolds, the attracting LCS are the analogue of unstable invariant manifolds, and repelling LCS are the analogue of stable invariant manifolds.

FTLE ridges are associated to separatrices, since neighboring trajectories on opposites sides of a separatrix are quickly distanced by the flow as they are transported to different regions of the domain. Therefore, a segment of initial conditions in the $\mathbf{x}_0$ plane normally intersecting the separatrix is greatly stretched by the flow, giving rise to high, locally maximal, values of the norm of the flow Jacobian, equivalently, of the FTLE field (see Fig. 6.1).

The inability of FTLE ridges in some cases to completely explain the flow pattern, even in some autonomous flows, led Haller to propose an alternative definition in Haller (2001), differing slightly from the previous one. Instead of integrating the dynamical system forwards and backwards in time, and taking in each case the norm of the Jacobian, i.e. the largest eigenvalue of the Cauchy-Green tensor, Haller just integrates forwards in time and considers the largest and the smallest eigenvalues of the Cauchy-Green tensor.

According to Farazmand & Haller (2013) a *strain-surface* or *repelling LCS* is a codimension one hypersurface in the spatial domain of the dynamical system such that at initial time t_0 it is normal everywhere to the eigenvector field of the largest eigenvalue of the Cauchy-Green tensor. A *stretch-surface* or *attracting LCS* is a codimension one hypersurface in the spatial domain of the dynamical system such that at initial time t_0 it is normal everywhere to the eigenvector field of the smallest eigenvalue of the Cauchy-Green tensor.

Roughly speaking, a repelling LCS is a hypersurface that is pointwise more repelling

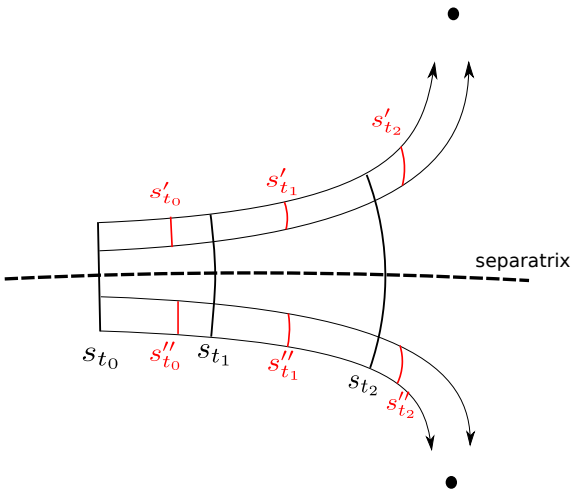

Figure 6.1: The segment s_{t_0} of initial conditions (black) intersects the separatrix. The flow sends the ends of s_{t_0} to different limits, and in the process the transported segments $s_{t_i} = \mathbf{F}_{t_0}^{t_i}(s_{t_0})$ undergo a great stretch. A segment s'_{t_0} (or s''_{t_0}) of initial conditions (red) on one side of the separatrix is transported by the flow to the same limit and suffers less stretch.

over the integration time interval than any nearby hypersurface. On the contrary, an attracting LCS maximizes pointwise attraction when integrating the dynamical system among nearby hypersurfaces.

In our work, we look for Lagrangian Coherent Structures in two dimensional spatial domains. We use the definition of LCS given by Haller and the following characterization of LCS in two dimensions, based on variational theory, from Farazmand & Haller (2012):

A line $\mathcal{M}(t_0)$ in the two dimensional spatial domain of the dynamical system is a repelling LCS (or strainline) for the system over the time interval $[t_0, t]$ if and only if, for every point $\mathbf{x}_0 \in \mathcal{M}(t_0)$ the following conditions hold,

1. $\lambda_1(\mathbf{x}_0) \neq \lambda_2(\mathbf{x}_0) > 1$;
2. $\langle \xi_2(\mathbf{x}_0), \nabla^2 \lambda_2(\mathbf{x}_0) \xi_2(\mathbf{x}_0) \rangle < 0$;
3. $\xi_2(\mathbf{x}_0) \perp \mathcal{M}(t_0)$;
4. $\langle \nabla \lambda_2(\mathbf{x}_0), \xi_2(\mathbf{x}_0) \rangle = 0$,

where λ_1 and λ_2, are the smallest and greatest eigenvalues, respectively, of the Cauchy-Green tensor of the flow, and ξ_1, ξ_2 are the corresponding eigenvector fields.

Condition (1) ensures that the stretching rate of the flow (i.e. the rate at which particular solutions of the system separate when integrated over the time interval $[t_0, t]$) is greater along the normal direction that along the tangential direction. Conditions (3) and (4) assure that the normal stretch rate of the flow along the strainline is a local extremum relative to close material lines. Condition (2) makes this extremum a strict local maximum.

The characterization of an attracting LCS (or stretchline) is analogous to that of a strainline, but replacing the second eigenvalue and vector of the Cauchy-Green tensor by the first ones, and reversing the inequality in condition 2 above. Although, alternatively, the same authors give another variant of the definition of a stretchline as a strainline when integrating backwards in time the dynamical system (Haller, 2011, Farazmand & Haller, 2012).

The two definitions of LCS presented here are similar but not equal. Let us note that the conditions (2) and (4) of the last characterization of repelling LCS are satisfied by ridges of the FTLE field. Therefore, such a ridge is a repelling LCS according to the last characterization of Farazmand & Haller (2012) if and only if the remaining two conditions of the characterization hold, i.e. the values of the FTLE field are strictly positive along the ridge; the minimal and maximal FTLE exponents are not equal along the ridge; and the ridge is pointwise normal to the maximal strain eigenvector field, $\xi_2(\mathbf{x}_0)$. These additional conditions, (2) and (4), are not trivial and Haller (2011) presents examples of repelling LCS which are not FTLE ridges, and of FTLE ridges that are not repelling LCS.

6.2 The computation of Lagrangian Coherent Structures

It is convenient to relax conditions (2) and (4) characterizing a repelling LCS in the previous section because of numerical computation reasons. Condition (2) is problematic because the eigenvalue $\lambda_2(\mathbf{x}_0)$ may be locally constant over part of the domain, it is adviceable in such cases to allow the LCS to have non-zero thickness. In the case of the condition (4), it is often numerically sensitive according to Farazmand & Haller (2012), which replaces this local condition by its averaging along the strainline. Relaxing condition (4) in this way is consistent with numerical and laboratory observations of tracer mixing in two-dimensional flows (Farazmand & Haller, 2012).

So, recalling that ξ_1, ξ_2 form an orthonormal basis of the plane, the alternative conditions to (1) - (4) are

(i) $\lambda_1(\mathbf{x}_0) \neq \lambda_2(\mathbf{x}_0) > 1$;

(ii) $\langle \xi_2(\mathbf{x}_0), \nabla^2 \lambda_2(\mathbf{x}_0) \xi_2(\mathbf{x}_0) \rangle \leq 0$;

(iii) $\xi_1(\mathbf{x}_0) \,||\, \mathcal{M}(t_0)$;

(iv) $\bar{\lambda}_2(\gamma)$, the average of λ_2 over a curve γ, is maximal on $\mathcal{M}(t_0)$ among all nearby curves γ satisfying $\dot{\gamma}(t_0) \,||\, \xi_1(\mathbf{x}_0)$.

In order to create our software package for the computation of LCS, we follow the algorithm given in Onu et al. (2014), which implements a characterization shown in Farazmand et al. (2014) to be equivalent to conditions (1) - (4), and based in the integration of the autonomous vector fields given by the eigenvectors of the Cauchy-Green tensor (i.e. the left-singular vectors of the Jacobian $\nabla \mathbf{F}_{t_0}^t$).

A strainline or repelling LCS is obtained by taking as initial point $\mathbf{x}_0$ a local maximum of the greatest eigenvalue λ_2 and integrating from $\mathbf{x}_0$ the eigenvector field ξ_1 forwards and backwards in time.

Analogously, a stretchline or attracting LCS is obtained by taking as initial point $\mathbf{x}_0$ a local minimum of the smallest eigenvalue λ_1 and integrating from $\mathbf{x}_0$ the eigenvector field ξ_2 forwards and backwards in time.

Let us detail the procedure followed by our software package in order to compute these strain and stretchlines for the flow $\mathbf{F}_{t_0}^t$ of a sufficiently smooth dynamical system over a rectangular spatial domain Γ.

First, the Jacobian of the flow $\mathbf{F}_{t_0}^t$ must be computed. We define a regular rectangular grid, henceforth called the main grid, covering the domain Γ with steps Δx, Δy along the x, y axes respectively, and for each point $\mathbf{x}_i = (x, y)$ in the main grid we select four neighboring points $\mathbf{x}_i^r = (x, y) + (\delta_x, 0)$, $\mathbf{x}_i^l = (x, y) - (\delta_x, 0)$, $\mathbf{x}_i^u = (x, y) + (0, \delta_y)$, $\mathbf{x}_i^d = (x, y) - (0, \delta_y)$, where δ_x, δ_y are suitably small distances (see Fig. 6.2).

The flow $\mathbf{F}_{t_0}^t$ is computed numerically, using an adaptive Runge-Kutta-Fehlberg method of order 7-8, with initial conditions the list of neighboring points of all points in the main grid. The accuracy of this computation is crucial because the Jacobian of the flow $\mathbf{F}_{t_0}^t$ on each (x, y) of the main grid is computed by centered differences of the flow in its four neighboring points, according to the formula,

$$\nabla \mathbf{F}_{t_0}^t(\mathbf{x}_i) \approx \left(\frac{\mathbf{F}_{t_0}^t(\mathbf{x}_i^r) - \mathbf{F}_{t_0}^t(\mathbf{x}_i^l)}{2\delta_x}, \frac{\mathbf{F}_{t_0}^t(\mathbf{x}_i^u) - \mathbf{F}_{t_0}^t(\mathbf{x}_i^d)}{2\delta_y} \right), \tag{6.5}$$

and this finite difference scheme to approximate the derivative is very sensitive to small fluctuating errors in the value of the flow.

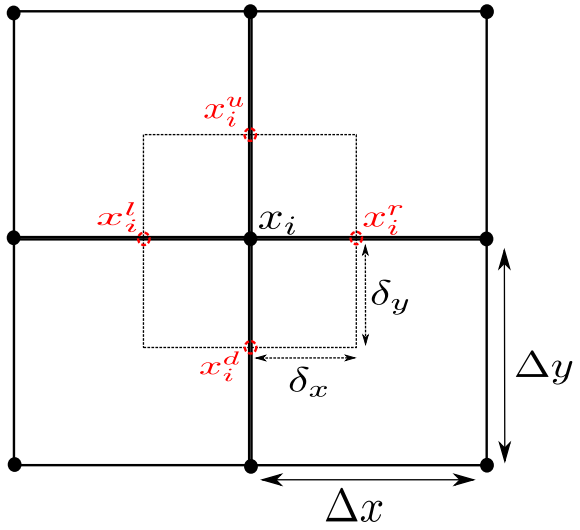

Figure 6.2: The four neighboring points (red) to a point $\mathbf{x}_i$ of the main grid which are used to compute the Jacobian of the flow $\mathbf{F}_{t_0}^t(\mathbf{x}_i)$ by finite differences.

The next step, after the computation of the Jacobian of the flow $\mathbf{F}_{t_0}^t$ in the points of the main grid, is to perform the Singular Value Decomposition (SVD) on each Jacobian. The result of this operation is to obtain the singular values $\sigma_1(\mathbf{x}_i) = ||\nabla \mathbf{F}_{t_0}^t|| \geq \sigma_2(\mathbf{x}_i)$, and the corresponding right-singular vectors, $\eta_1(\mathbf{x}_i), \eta_2(\mathbf{x}_i)$, for each point of the main grid. We compute directly the SVD of the Jacobian rather than the Cauch-Green tensor and its diagonalization, to minimize error transmission from the values of the Jacobian to the result of the computation. In addition, in the cases when the Jacobian is singular, the SVD yields a singular value very close to zero and positive, while the diagonalization of the Cauchy-Green tensor produces an eigenvalue that is close to zero but may have positive or negative sign.

When the spatial domain U has dimension greater than 2, the computation of 2-dimensional LCS (strain and stretchlines) can still yield a great deal of information about the dynamics of the system by parametrizing strategically chosen surfaces S inside the domain U,

$$\begin{array}{rccc} \Psi: & \Gamma & \longrightarrow & S \subset U \\ & (\alpha, \beta) & \longmapsto & \mathbf{x}(\alpha, \beta) \end{array} \tag{6.6}$$

with Γ a rectangle. The flow $\tilde{\mathbf{F}}_{t_0}^t = \mathbf{F}_{t_0}^t \circ \Psi$ is now a flow defined on $\Gamma \subset \mathbf{R}^2$ to which the above computation can be applied. But in this case care must be taken to discount the effects of the parametrization Ψ, because $\nabla \tilde{\mathbf{F}}_{t_0}^t = \nabla \mathbf{F}_{t_0}^t \cdot \nabla \Psi$, and the Jacobian $\nabla \Psi$ of the parametrization introduces its own compression or spreading of tangent directions, which does not belong to the original flow $\mathbf{F}_{t_0}^t$ but has been artificially inserted by the

parametrization Ψ (e.g. the compression towards the North and South poles of a sphere introduced by standard spherical coordinates). The solution to this problem is to apply the SVD to the Jacobian $\nabla \mathbf{F}_{t_0}^t$, using for it an orthonormal basis w_1, w_2 of the tangent space to the parametrised surface $S = \Psi(\Gamma)$ at each point $\mathbf{x}$, which depends only on the surface S and the point $\mathbf{x}$ and not on the parametrization Ψ. If C is the base change from this orthonormal basis w_1, w_2 to the original one in our parametrization $\nabla\Psi(\partial_\alpha), \nabla\Psi(\partial_\beta)$, we will perform the SVD to the matrix

$$(\nabla \mathbf{F}_{t_0}^t)_{|S}(\mathbf{x}) = \nabla \tilde{\mathbf{F}}_{t_0}^t(\mathbf{x}) \cdot C \tag{6.7}$$

which is the Jacobian of the flow $\mathbf{F}_{t_0}^t$ restricted to the surface S using as a departure basis for the tangent space, $T_{\mathbf{x}}S$, the orthonormal basis w_1, w_2 which does not introduce distortions to the flow.

According to the above conditions (i) - (iv), the strainlines are computed taking the local maxima of the greatest singular value σ_1 in the main grid as initial condition, and integrating the right-singular vector field η_2 forwards and backwards in time. The stretchlines are computed taking the local minima of the least singular value σ_2 in the main grid as initial condition, but now integrating the right-singular vector field η_1 forwards and backwards in time.

Let us note that the vector fields η_1, η_2 to be integrated in the computation of strain and stretchlines are known only in the discrete main grid. Because of this, the use of a variable step integrator requires interpolation of the fields and does not result in greater accuracy for the computed solution. Therefore, we have selected an order 4 Runge-Kutta (RK4) integrator with fixed step, taken smaller than the main grid step.

The choice of a fixed step RK4 integrator has been made not only to speed up the computation but also to handle an added difficulty of the discrete vector fields η_1, η_2. Pointwise, the vectors $\eta_1(\mathbf{x}_i), \eta_2(\mathbf{x}_i)$ are defined up to sign, which means that the orientation of the field can suddenly reverse. In practice this is indeed the case, since the SVD algorithm produces singular vectors that do not vary continuously, but suddenly change orientation when crossing certain boundaries in the domain. This is unavoidable if the vector field is not parallelizable (see Abraham et al., 1988), which happens for instance when the two singular values σ_1, σ_2 become equal at a point in the domain Γ. We avoid this discontinuity in the sign of the vectors, which would make the integrator oscillate back and forth, by making our integrator compare the orientation of the value of the vector field it uses with the orientation of the last previously used value, and reverse orientation of the current vector if an orientation discontinuity is detected.

Finally, in order to avoid local extremal values of the singular values σ_1, σ_2 intro-

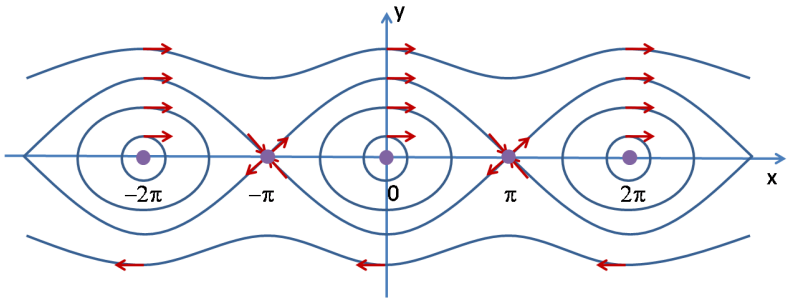

Figure 6.3: Phase portrait of the autonomous pendulum (taken from the Mathematical Garden web page).

duced by fluctuation errors in their computation, our algorithm fixes a minimal radius such that only points that are extremal for the singular value within this radius at least are considered as a starting point for a LCS. Moreover, if one such point lies within this critical distance of an already computed LCS of its type (strainlines for maxima of the main value σ_1, stretchlines for minima of the smaller value σ_2), then it is discarded as a starting condition of a LCS because it would produce a line that is superfluous because it would be closely parallel to an already computed LCS of the same type.

6.2.1 Basic test examples

In order to verify the accuracy of our software package, we have applied it to compute LCS in a simple example such as the pendulum. We consider the autonomous equation of the pendulum,

$$\begin{cases} \dot{x} = y \\ \dot{y} = -\sin(x), \end{cases} \tag{6.8}$$

with critical points $(k\pi, 0)$, for $k \in \mathbb{Z}$, which are elliptic points when k is even and hyperbolic when k is odd (see Fig. 6.3 for the phase portrait). The invariant manifolds of the unstable equilibrium points are given by the curve $y^2 = 2 + 2\cos(x)$.

The spatial domain Γ used in the computation of LCS for the autonomous problem is $[-\pi, \pi] \times [-\frac{3}{4}\pi, \frac{3}{4}\pi]$. We integrate the system over the time intervals $T = [0, 6]$ and $T = [0, 12]$, in order to study the dependence of the LCS with respect to the integration time length.

In the figures of stretch and strainlines in the sequel, the black dots signal the local extremum of the singular value determining the line, and the red and green dots mark the points at which integration of the line has stopped forwards and backwards in time respectively.

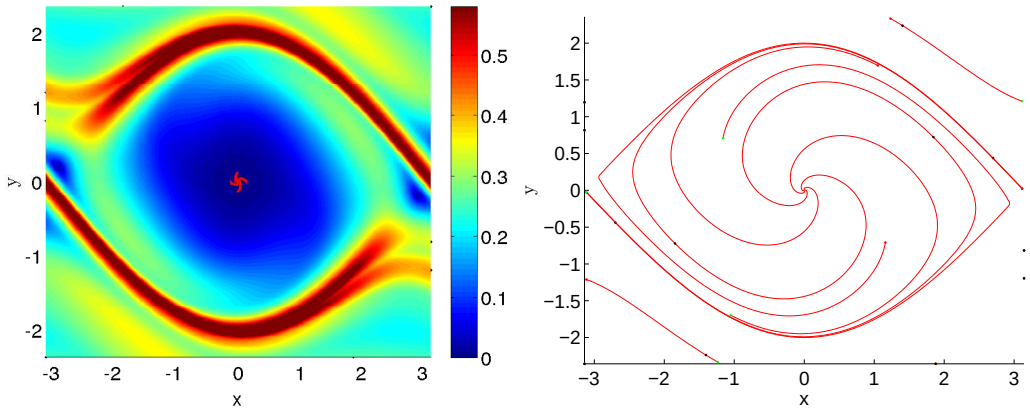

Figure 6.4: FTLE (left) and strainlines (right) of the autonomous pendulum for time $T = [0, 6]$

In Fig. 6.4 we show the FTLE and the strainlines for the time $T = [0, 6]$. Let us point out that the main concentration of strainlines is found on the main ridges of the FTLE field (or equivalently of the main singular value σ_1, or equivalently of the main eigenvalue λ_2 of the Cauchy-Green tensor), which are located in the invariant manifolds of the flow. Neither the strainlines nor the FTLE ridges cover the entire invariant manifolds, due to the short integration time. There are additional strainlines that spiral out of the central equilibrium point which do not correspond to the invariant manifolds, but reflect fluctuations in angular velocity of the solutions around the central point over the integration time.

Figure 6.5 shows the field of values of the smaller singular value σ_2 and the stretchlines for an integration time of $T = [0, 6]$. The invariant manifolds mark the position of a trench where σ_2 has its minimal values. This is the starting point for every stretchline, which then spirals to the center where σ_2 has its maximal values and continues to the edge of the domain when it is integrated backwards in time.

Taking the time interval $T = [0, 12]$ the ridge of the FTLE field completely covers the invariant manifolds, and the main strainlines almost cover them as well (see Fig. 6.6). There are secondary strainlines corresponding to secondary ridges of the FTLE field. The coincidence of the main FTLE ridges or strainlines with the invariant manifolds is a consequence of the longer integration time span, which also gives rise to secondary FTLE ridges and strainlines. The description of the dynamics of the system by LCS becomes more sofisticated as the integration time span grows, showing a stratification of the system according to the stretching of the flow. This description with increasing sofistication is possible in this example because the pendulum is a well conditioned system which can be

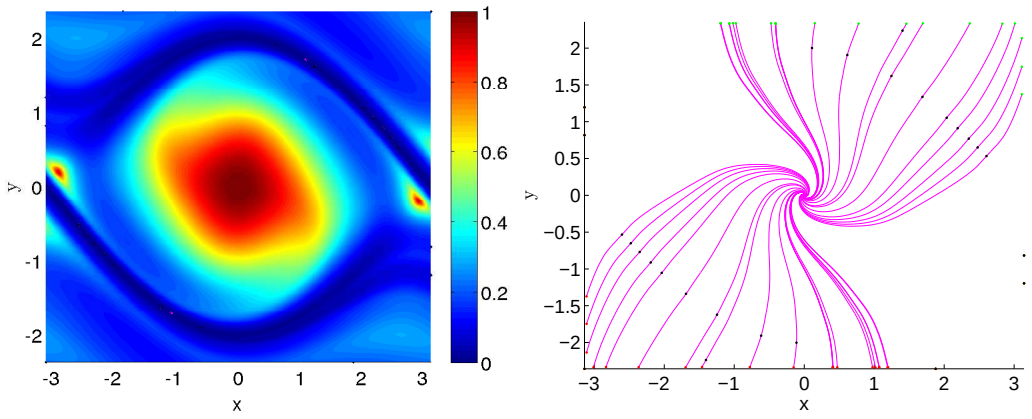

Figure 6.5: Smaller singular value σ_2 (left) and stretchlines (right) of the autonomous pendulum for time $T = [0, 6]$.

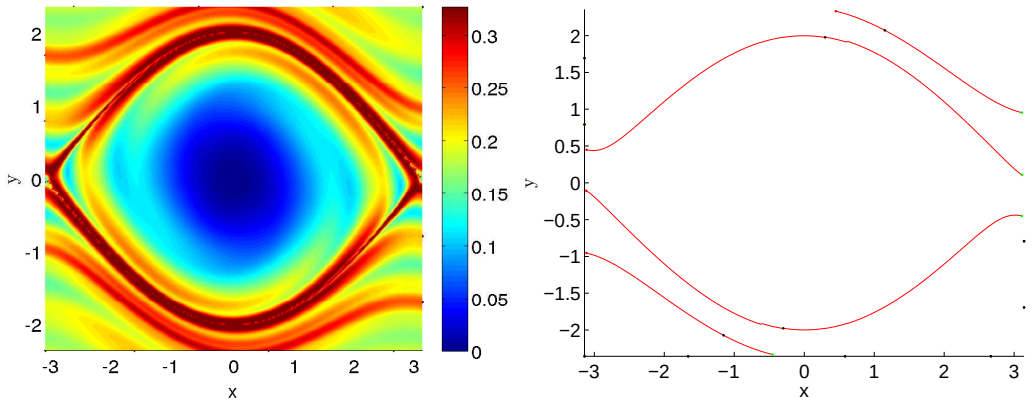

Figure 6.6: FTLE (left) and strainlines (right) of the autonomous pendulum for time $T = [0, 12]$.

integrated for a long time with moderate error.

The field of small singular values σ_2 changes little when the integration time span is increased to $T = [0, 12]$ (see Fig. 6.7). The trench formed by the minimal values of the field now completely covers the invariant manifolds. The stretchlines behave as in the previous case when the integration time was $T = [0, 6]$ but now approach the central equilibrium points from all directions.

In order to check our software package and the capability of the LCS in non-autonomous problems, we consider the pendulum with a small time dependent pertur-

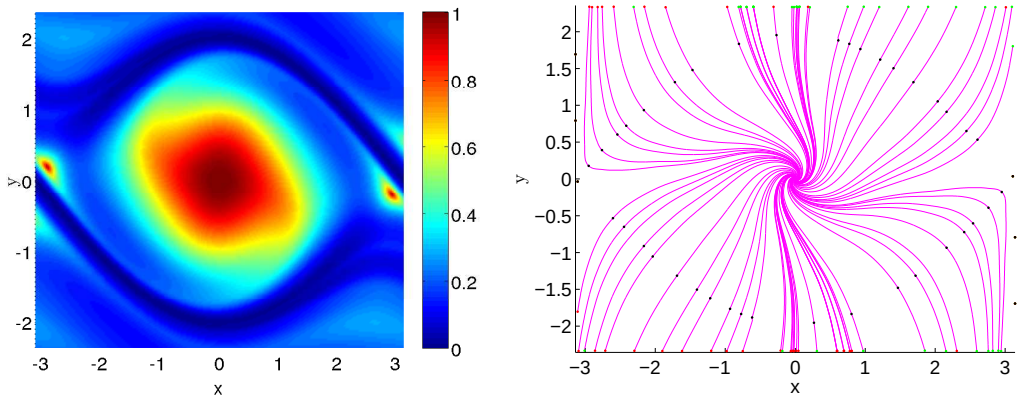

Figure 6.7: Smaller singular value σ_2 (left) and stretchlines (right) of the autonomous pendulum for time $T = [0, 12]$.

bation,

$$\begin{cases} \dot{x} = y \\ \dot{y} = -\sin(x) - ky, \end{cases} \tag{6.9}$$

where the parameter k represents the non-autonomous friction, $k = 0.1 \cdot (1 + 0.05t)$. Let us note that we have selected a perturbation in order to compare the LCS with the autonomous problem.

We select the spatial domain Γ as previously, $[-\pi, \pi] \times [-\frac{3}{4}\pi, \frac{3}{4}\pi]$. As for the integration time span, since in the autonomous problem we have observed that time plays an important role, and that the time necessary to show the LCS completely is $T = [0, 12]$, we choose this interval for the non-autonomous case.

Figure 6.8 shows the FTLE field and the LCS for this non-autonomous pendulum. As in the previous case, the main ridges of the FTLE field present the main concentration of strainlines, representing what we might call the "invariant manifolds" in the non-autonomous system. In this non-autonomous problem, the ridges of the FTLE field are clearly delimited, showing the dynamics of the system. Let us observe that the ridges of the FTLE field and the strainlines are a perturbation of those in Fig. 6.6, with a small tilt with respect to the autonomous pendulum, but that the shape of the ridges and strainlines remains.

The corresponding smaller singular value σ_2 presents its main set of minima along the "invariant manifolds" of the non-autonomous problem (Fig. 6.9). The field of values of σ_2 does not form a trench over the "invariant manifolds" now, but rather a saw blade alternating local minima and maxima. The starting point of the main set of stretchlines is placed in the troughs of the saw blade of the σ_2 field, and these stretchlines spiral towards

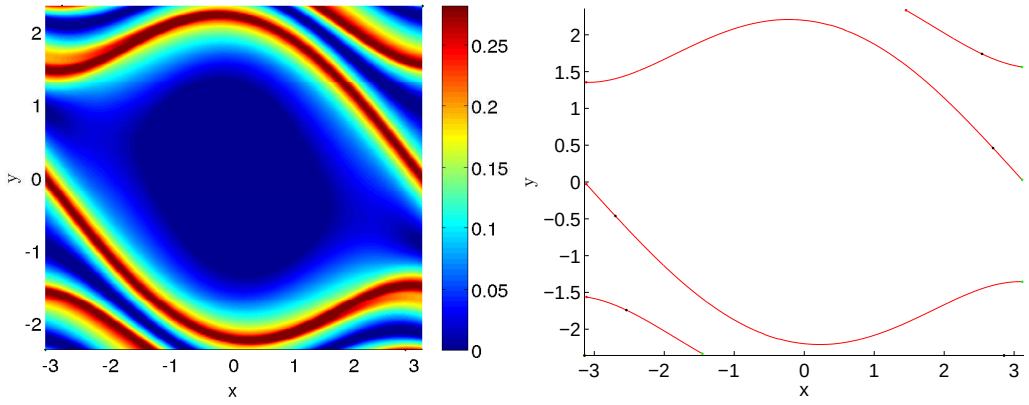

Figure 6.8: FTLE (left) and strainlines (right) of the non-autonomous pendulum for time $T = [0, 12]$.

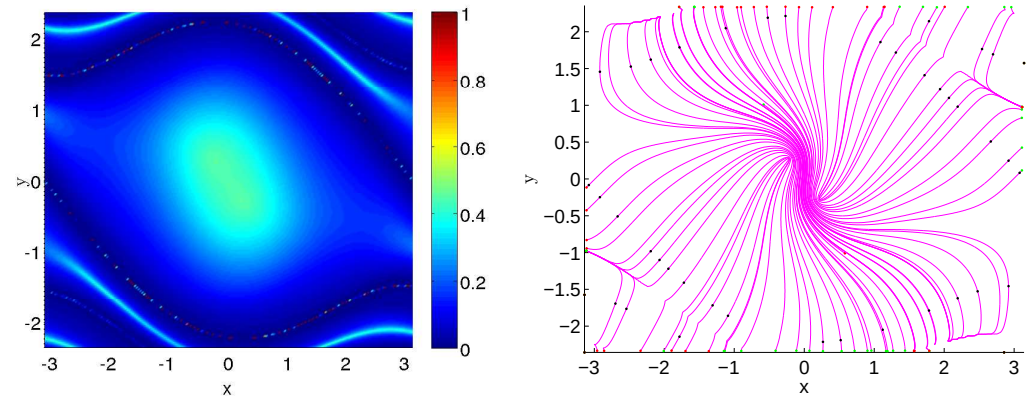

Figure 6.9: Smaller singular value σ_2 (left) and stretchlines (right) of the non-autonomous pendulum for time $T = [0, 12]$.

the central point. There are two secondary trenches/saw blades towards the corners of the figure, parallel to the main one and separated from it by ridges of maxima of σ_2. The stretchlines defined by these secondary saw blades follow the ridge of maxima of σ_2.

The examples presented so far already point out to one conclusion: stretchlines are not a robust invariant of the dynamical system because very small changes in parameters of the system such as integration time or friction result in a large variation in the number and geometry of the set of stretchlines. This sensitivity reflects the fact that the smaller singular value σ_2 is a less well conditioned invariant of the Jacobian than the main singular value σ_1. This problem worsens in case of taking the Cauchy-Green tensor for its diagonalization instead of computing the SVD of the Jacobian, because the condition number of

the system increases. Furthermore, in the presented examples, there is no straightforward relation between the stretchlines and the dynamics of the system.

6.3 Lagrangian Coherent Structures in the precessing model

Let us now apply our computation of Lagrangian Coherent Structures to the autonomous precessing model formed by a bar and a disc (Chapter 3), in order to compare the results of the computation to the structure of the invariant manifolds of the model.

Our precessing model produces a 6-dimensional dynamical system,

$$\begin{cases} \dot{x_1} = x_4 \\ \dot{x_2} = x_5 \\ \dot{x_3} = x_6 \\ \dot{x_4} = 2\Omega\cos(\varepsilon)x_5 + \Omega^2\cos^2(\varepsilon)x_1 + \Omega^2\sin(\varepsilon)\cos(\varepsilon)x_3 - \phi_{x_1} \\ \dot{x_5} = -2\Omega\cos(\varepsilon)x_4 - 2\Omega\sin(\varepsilon)x_6 + \Omega^2 x_2 - \phi_{x_2} \\ \dot{x_6} = 2\Omega\sin(\varepsilon)x_5 + \Omega^2\sin(\varepsilon)\cos(\varepsilon)x_1 + \Omega^2\sin^2(\varepsilon)x_3 - \phi_{x_3}. \end{cases} \tag{6.10}$$

Since our computation of strain and stretchlines is performed on 2-dimensional domains, we must parametrise a surface in the 6-dimensional space $(x, y, z, \dot{x}, \dot{y}, \dot{z})$ to reduce to two degrees of freedom our dynamical system. We select this surface with the same criterion used in Chapter 3 to find heteroclinic orbits of the precessing model, as we wish to compare our LCS to these orbits.

We set the tilt angle $\varepsilon = 0$ so that the dynamics of the system becomes independent of $z, \dot{z}$, and then fix the values $z = 0, \dot{z} = 0$. In order to obtain a surface containing the heteroclinic orbits, corresponding to the two unstable equilibrium points L_1 and L_2 of the model in our surface, we set $x = 0$ and fix an energy level $C_{L_1} + \delta$ slightly above that of the equilibrium point L_1 (or L_2). The resulting surface may be parametrised by $(y, \dot{y})$ using the Jacobi constant of the system,

$$\begin{aligned} C(x, y, z, \dot{x}, \dot{y}, \dot{z}) = &- (\dot{x}^2 + \dot{y}^2 + \dot{z}^2) + 2\Omega^2\sin(\varepsilon)\cos(\varepsilon)xz \\ &+ (\Omega^2\cos^2(\varepsilon)x^2 + \Omega^2 y^2 + \Omega^2\sin^2(\varepsilon)z^2) - 2\phi, \end{aligned} \tag{6.11}$$

from which we deduce when $x, z, \dot{z} = 0$ and $C = C_{L_1} + \delta$ that

$$\dot{x} = \sqrt{-\dot{y}^2 + \Omega^2 y^2 - 2\phi(0, y, 0) - (C_{L_1} + \delta)}. \tag{6.12}$$

In this way we obtain a surface $S \subset \mathbb{R}^6$ parametrised by

$$\Psi(y, \dot{y}) = (0, y, 0, \sqrt{-\dot{y}^2 + \Omega^2 y^2 - 2\phi(0, y, 0) - (C_{L_1} + \delta)}, \dot{y}, 0), \tag{6.13}$$

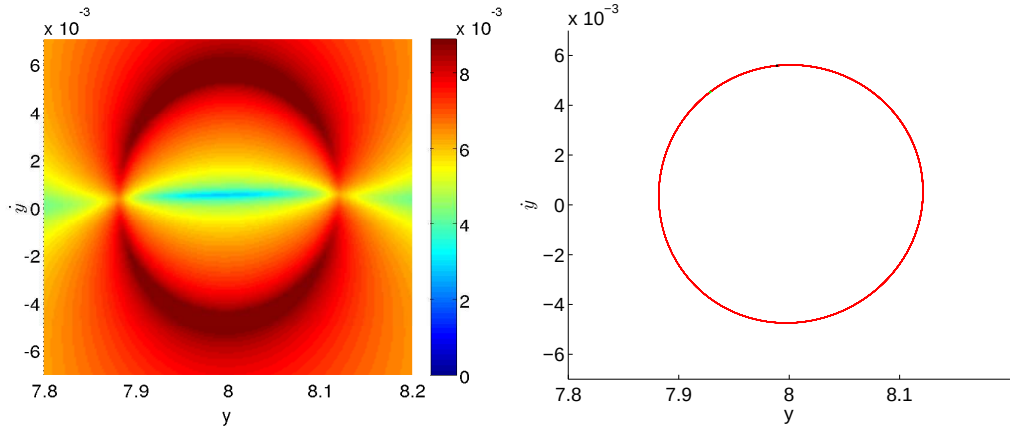

Figure 6.10: FTLE (left) and strainlines (right) of the precessing model for time $T = [0, 505]$.

where we have chosen the positive value of $\dot{x}$, to obtain the plane containing the above mentioned heteroclinic orbits.

We take the parameters, $A = 3, B = 1, GMd = 0.9$ for the disc and $a = 6, b = 1.5, c = 0.6$ for the bar with a pattern speed $\Omega = 0.05$. Unless otherwise indicated, the spatial domain for our parametrization is $\Gamma = [7.8, 8.2] \times [-0.007, 0.007]$. Figure 6.10 shows the FTLE field and the strainlines corresponding to this model for an integration time $T = [0, 505]$, where $t = 505$ is the time of the first intersection of the upper branch of the stable invariant manifold with the $x = 0$ plane. As previously, the concentration of strainlines is found on the main ridges of the FTLE field, forming a closed curve.

Recall that to obtain the cuts of the heteroclinic orbits with the $\{x = 0,\ y \geq 0\}$ semiplane, we consider the outer branches of the stable invariant manifold of the Lyapunov orbit around L_1, $W^s_{\gamma_1}$, and the unstable invariant manifold of the Lyapunov orbit around L_2, $W^u_{\gamma_2}$. The intersection of the invariant manifolds with the $\{x = 0,\ y \geq 0\}$ semiplane are two closed curves. We denote by $W^{s,1}_{\gamma_1}$ the closed curve resulting from the first intersection of $W^s_{\gamma_1}$, and by $W^{u,1}_{\gamma_2}$ the closed curve resulting from the first intersection of $W^u_{\gamma_2}$. The intersection $W^{s,1}_{\gamma_1} \cap W^{u,1}_{\gamma_2}$ corresponds to heteroclinic orbits for the given energy level of the invariant manifolds. The second intersection of the invariant manifolds $W^s_{\gamma_1}$, $W^u_{\gamma_2}$ with the $\{x = 0,\ y \geq 0\}$ semiplane are denoted by $W^{s,2}_{\gamma_1}$ and $W^{u,2}_{\gamma_2}$ respectively.

Let us superimpose the FTLE field, the strainlines and the first cuts of the heteroclinic orbits with the $\{x = 0,\ y \geq 0\}$ semiplane, for the same level of energy ($C_{L_1} + \delta$, with δ small). Figure 6.11 shows in the top left panel how the strainlines follow the main ridge of the FTLE field. If we observe $W^{s,1}_{\gamma_1}$ and $W^{u,1}_{\gamma_2}$ (top right panel), the one corresponding to the stable manifold follows as well the main ridge of the FTLE field, whereas the

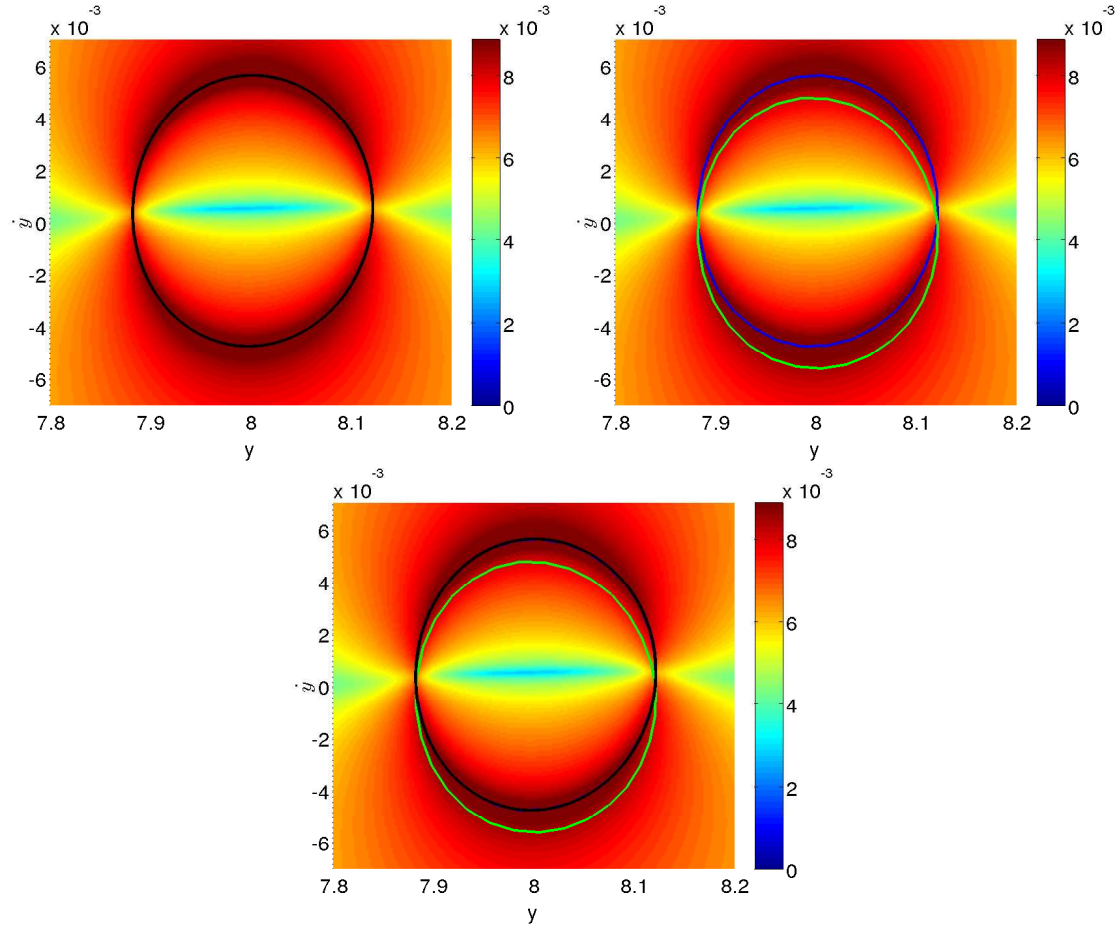

Figure 6.11: Precessing model with tilt angle $\varepsilon = 0$ for time $T = [0, 505]$. Top left: FTLE field and strainlines in black. Top right: FTLE field and heteroclinic orbits ($W^{s,1}_{\gamma_1}$ in blue, $W^{u,1}_{\gamma_2}$ in green). Bottom: FTLE field, strainlines (in black) and heteroclinic orbits (in blue and green).

one corresponding to the unstable manifold is associated with the boundary of the ridge. When we join both figures, in the bottom panel, the strainlines correspond exactly with the heteroclinic orbit of the stable manifold. Therefore, we confirm that the strainlines are associated with the stable invariant manifolds, and concretely with $W^{s,1}_{\gamma_1}$, at least in the autonomous problem. Let us remark that as the stretchlines are by definition perpendicular to the strainlines, they do not seem to carry any relevant dynamic information in our problem.

As the integration time is increased, the accuracy of the description of the FTLE field and strainlines is gradually lost. This is due not only to the loss of precision in the integration of the dynamical system in order to compute the LCS, but also to the fact

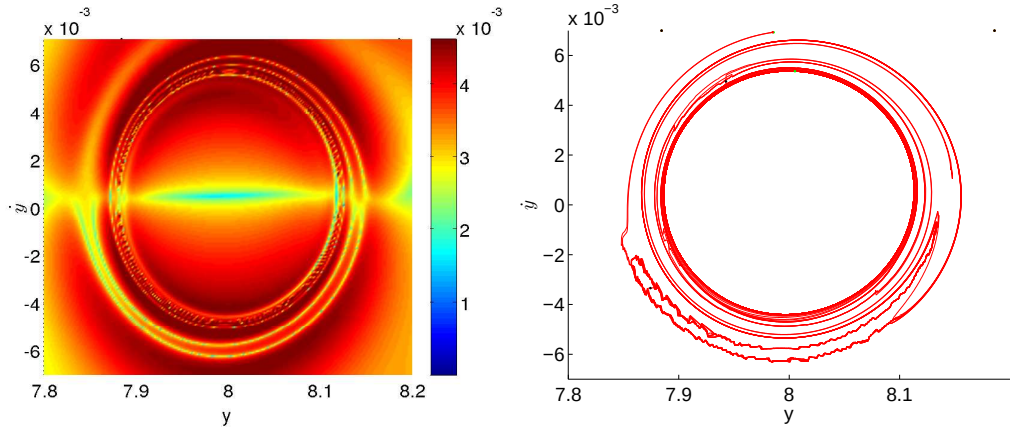

Figure 6.12: FTLE (left) and strainlines (right) of the precessing model with tilt angle $\varepsilon = 0$ for time $T = [0, 1000]$.

that, in the precessing model, the successive intersections of the invariant manifolds with the $\{x = 0,\, y \geq 0\}$ semiplane become increasingly blurred. Taking an integration time $T = [0, 1000]$ the ridges of the FTLE field are not so remarked, but the strainlines continue following these ridges, although the dynamics of the system is less clear (see Fig. 6.12).

In order to observe the second intersection of the invariant manifolds with the $\{x = 0,\, y \geq 0\}$ semiplane, $W^{s,2}_{\gamma_1}$ and $W^{u,2}_{\gamma_2}$, and the corresponding LCS, we take a time interval for the integration of $T = [0, 1570]$. Figure 6.13 shows the FTLE field, where the ridges are even less marked than in the previous case, and the strainlines associated with these ridges. We observe some artifices in the integration of strainlines that do not correspond to ridges of the FTLE field, but are due to the long time of integration, for example in the top right part of the figure of strainlines.

In Fig. 6.14 we observe how the strainlines (in black) follow the main ridges of the FTLE field, although some of the strainlines do not match these ridges (top left panel). In the top right panel we show the cuts of the heteroclinic orbits, $W^{s,2}_{\gamma_1}$ and $W^{u,2}_{\gamma_2}$, superimposed to the FTLE field, where we mark this second intersection of the invariant manifolds with dots in order to clarify the figure, since they do not follow a clear closed curve. We observe that the second intersection of the stable manifold (in blue) follows approximately the ridges of the FTLE field. To join this stable manifold to the strainlines and the FTLE field (bottom panel), the stable manifold (the first intersection with the plane $x = 0$ in magenta, the second one in blue) is closely approximated by the strainlines and the ridges of the FTLE field in its main components. Let us point out that both the strainlines and the ridges of the FTLE field also give false positives as time increases, i.e. not all the strainlines follow the ridges of the FTLE field and furthermore some ridges of

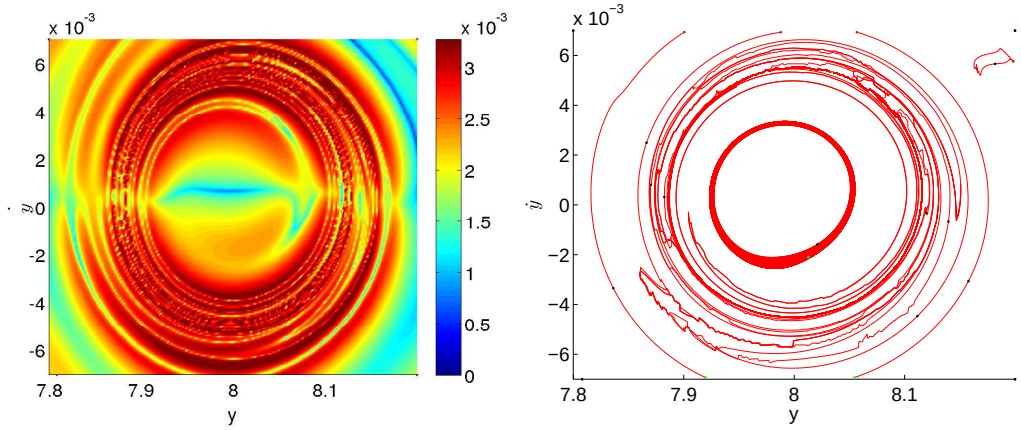

Figure 6.13: FTLE (left) and strainlines (right) of the precessing model with tilt angle $\varepsilon = 0$ for time $T = [0, 1570]$.

the FTLE field do not correspond to a defined structure of the dynamics of the model. This fact suggests that for long integration times the FTLE field and the strainlines lose its precision, a fact that is also stated by Haller (see e.g. Farazmand & Haller, 2012).

Let us widen now the spatial domain Γ in the computation of LCS, for an integration time of $T = [0, 505]$ which considerably improves the accuracy (Fig. 6.15). The left part of both plots, in dark blue in the FTLE field, shows the region of forbidden movement, where the black dots indicate starting points in the computation of LCS. In the FTLE field as well as in the strainlines, we observe structures within the fixed energy level reflecting the dynamics of the system, corresponding to the heteroclinic orbits and probably to further features, such as intersections of the parametrised surface with other invariant manifolds.

Figure 6.16 represents the superposition of the FTLE field and the strainlines (top left panel), the FTLE field and the heteroclinic orbits (top right panel) and the three elements in the bottom panel. The heteroclinic orbits correspond to the central closed curve, whereas the rest of the main ridges of the FTLE field are followed by the strainlines. This suggests that there are stable manifolds with the same level of energy associated to other structures, which are easily captured by the main ridges of the FTLE field and the corresponding strainlines.

6.3.1 Lagrangian Coherent Structures in the non-autonomous case

The aim of the Lagrangian Coherent Structures is to study the dynamics of non-autonomous problems, where they describe the organization of movement. In the autonomous problem

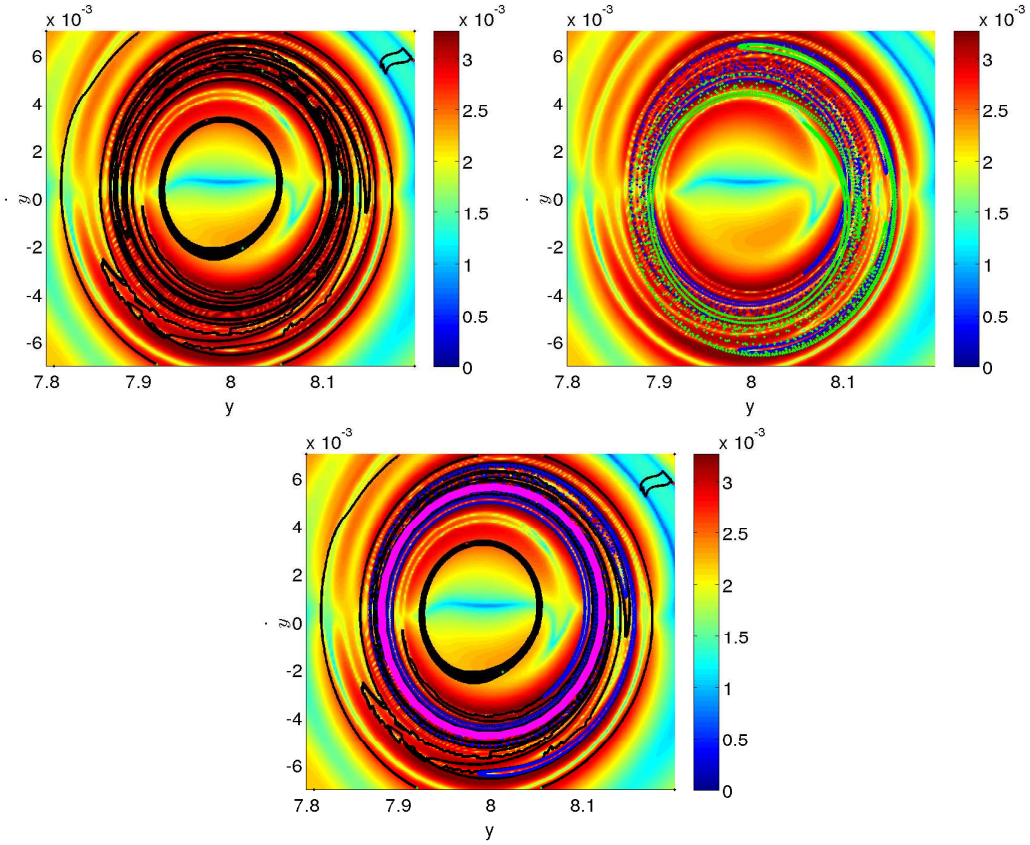

Figure 6.14: Precessing model with tilt angle $\varepsilon = 0$ for time $T = [0, 1570]$. Top left: FTLE field and strainlines in black. Top right: FTLE field and heteroclinic orbits for the second intersection of the $\{x = 0,\ y \geq 0\}$ semiplane ($W^{s,2}_{\gamma_1}$ in blue, $W^{u,2}_{\gamma_2}$ in green). Bottom: FTLE field, strainlines (in black) and heteroclinic orbits for the first intersection (in magenta), $W^{s,1}_{\gamma_1}$, and for the second one (in blue), $W^{s,2}_{\gamma_1}$, of the stable manifold.

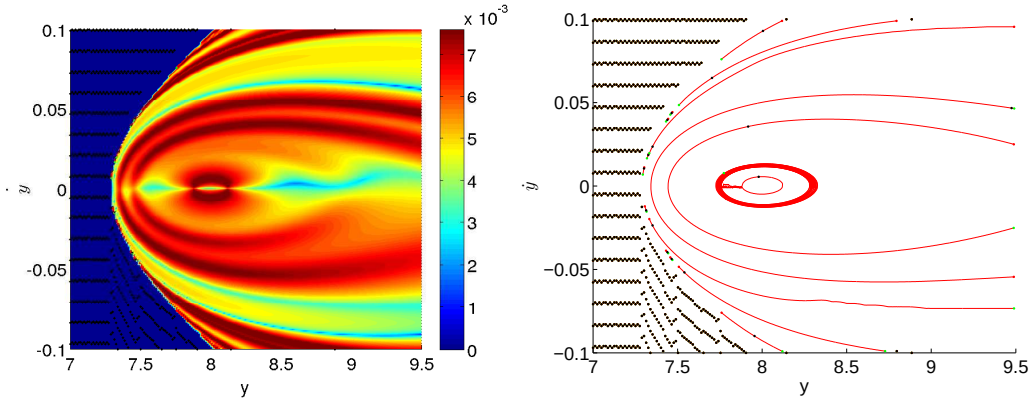

Figure 6.15: FTLE (left) and strainlines (right) of the precessing model with tilt angle $\varepsilon = 0$ for time $T = [0, 505]$ in the spatial domain $[7, 9.5] \times [-0.1, 0.1]$.

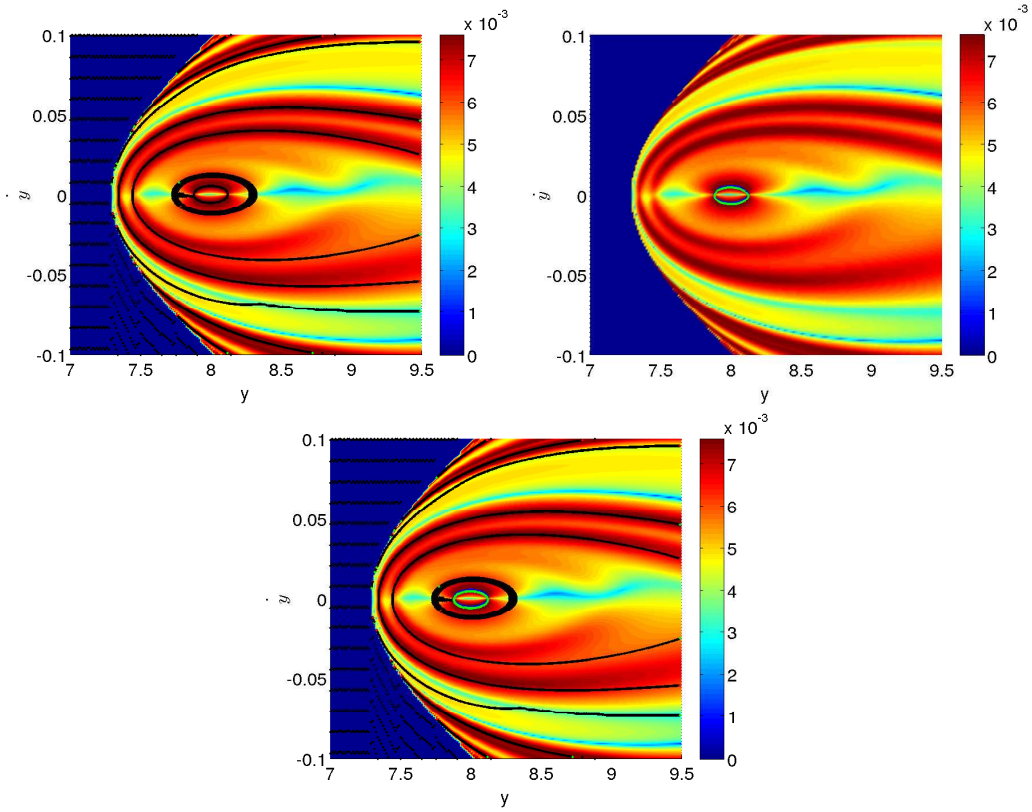

Figure 6.16: Precessing model with tilt angle $\varepsilon = 0$ for time $T = [0, 505]$ in the spatial domain $[7, 9.5] \times [-0.1, 0.1]$. Top left: FTLE field and strainlines in black. Top right: FTLE field and heteroclinic orbits ($W^{s,1}_{\gamma_1}$ in blue, $W^{u,1}_{\gamma_2}$ in green). Bottom: FTLE field, strainlines (in black) and heteroclinic orbits (in blue and green).

we have observed that the FTLE field and its corresponding strainlines are the "analogue" of the stable invariant manifolds. With this idea we transform our precessing model into a non-autonomous model to observe the behaviour of its dynamics.

A parameter which can reasonably be made dependent on time in the precessing model is its pattern speed, so from now we consider a pattern speed $\widetilde{\mathbf{\Omega}}_{\mathbf{p}} = \mathbf{\Omega}_{\mathbf{p}}(t)$. The pattern speed depends now on time, and this dependence introduces changes to the equations of the model. The vectorial form of the equations of motion in the rotating reference frame is now,

$$\ddot{\mathbf{r}} = -\nabla\phi - 2(\widetilde{\mathbf{\Omega}}_{\mathbf{p}} \times \dot{\mathbf{r}}) - \widetilde{\mathbf{\Omega}}_{\mathbf{p}} \times (\widetilde{\mathbf{\Omega}}_{\mathbf{p}} \times \mathbf{r}) - \dot{\widetilde{\mathbf{\Omega}}}_{\mathbf{p}} \times \mathbf{r}, \tag{6.14}$$

where the new summand $-\dot{\widetilde{\mathbf{\Omega}}}_{\mathbf{p}} \times \mathbf{r}$ is the inertial force of rotation (see Binney & Tremaine, 2008, for further details). Taking $\widetilde{\mathbf{\Omega}}_{\mathbf{p}}$ as in Chapter 2, but now with $\widetilde{\Omega} = \widetilde{\Omega}(t)$ depending on time,

$$\widetilde{\mathbf{\Omega}}_{\mathbf{p}} = (-\widetilde{\Omega}\sin(\varepsilon), 0, \widetilde{\Omega}\cos(\varepsilon)), \tag{6.15}$$

the new equations of motion are given by

$$\begin{cases} \dot{x_1} = x_4 \\ \dot{x_2} = x_5 \\ \dot{x_3} = x_6 \\ \dot{x_4} = 2\widetilde{\Omega}\cos(\varepsilon)x_5 + \widetilde{\Omega}^2\cos^2(\varepsilon)x_1 + \widetilde{\Omega}^2\sin(\varepsilon)\cos(\varepsilon)x_3 + \dot{\widetilde{\Omega}}\cos(\varepsilon)y - \phi_{x_1} \\ \dot{x_5} = -2\widetilde{\Omega}\cos(\varepsilon)x_4 - 2\widetilde{\Omega}\sin(\varepsilon)x_6 + \widetilde{\Omega}^2 x_2 - \dot{\widetilde{\Omega}}\cos(\varepsilon)x - \dot{\widetilde{\Omega}}\sin(\varepsilon)z - \phi_{x_2} \\ \dot{x_6} = 2\widetilde{\Omega}\sin(\varepsilon)x_5 + \widetilde{\Omega}^2\sin(\varepsilon)\cos(\varepsilon)x_1 + \widetilde{\Omega}^2\sin^2(\varepsilon)x_3 + \dot{\widetilde{\Omega}}\sin(\varepsilon)y - \phi_{x_3}. \end{cases} \tag{6.16}$$

Let us remark that this system is non-autonomous, it has no integrals of motion, and in particular it does not conserve energy, so there are no constant-energy surfaces as in the autonomous precessing model. In order to parametrise a surface to compute the FTLE field and the strainlines, we consider the same conditions as previously, taking the "energy" of this system as the Jacobi constant of the autonomous problem,

$$\begin{aligned} C(x, y, z, \dot{x}, \dot{y}, \dot{z}) = &-(\dot{x}^2 + \dot{y}^2 + \dot{z}^2) + 2\widetilde{\Omega}^2\sin(\varepsilon)\cos(\varepsilon)xz \\ &+ (\widetilde{\Omega}^2\cos^2(\varepsilon)x^2 + \widetilde{\Omega}^2 y^2 + \widetilde{\Omega}^2\sin^2(\varepsilon)z^2) - 2\phi. \end{aligned} \tag{6.17}$$

The parameters taken for the bar and disc as the same as previously, but now the pattern speed varies linearly from $\widetilde{\Omega}_{t_0} = 0.05$ to $\widetilde{\Omega}_{t_f} = 0.04$ for $[t_0, t_f] = [0, 1500]$ time units, i.e. with slope $\dot{\widetilde{\Omega}} = -\frac{2}{3}\cdot 10^{-5}$. This decreases in the pattern speed over time has been observed in galaxies, due to the transfer of angular momentum from the bar to the other components of the galaxy (Widrow et al., 2008). In addition, the fixed "energy" level continues to be $C_{L_1} + \delta$, where C_{L_1} is the Jacobi constant for the equilibrium

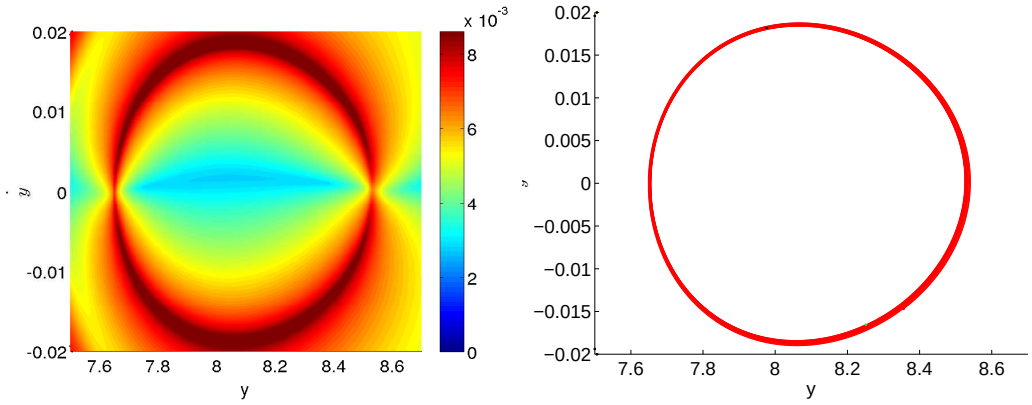

Figure 6.17: FTLE (left) and strainlines (right) of the non-autonomous precessing model with tilt angle $\varepsilon = 0$ for time $T = [0, 505]$.

point L_1 in the autonomous problem. The selected spatial domain for the integration is $\Gamma = [7.5, 8.7] \times [-0.02, 0.02]$.

In order to compare the results with the ones obtained for the autonomous precessing model, we take the same integration times. The first computation of LCS is for the time interval $T = [0, 505]$ (Fig. 6.17). We observe that although the problem is non-autonomous, the shape of the main ridges of the FTLE field and the strainlines continues being that of a closed curve, and that the strainlines still follow the main ridges of the FTLE field. But, if we superimpose the cuts $W^{s,1}_{\gamma_1}$ and $W^{u,1}_{\gamma_2}$ of the invariant manifolds of the autonomous precessing model, we observe that the width of the FTLE field and strainlines has increased (Fig. 6.18). Since the integration time is the same as the one taken in the autonomous problem (Fig. 6.11), the different range in the spatial domain is due to a variation of energy when integrating the initial conditions. This variation takes place because the "energy" chosen to parametrise the surface of initial conditions is not an integral of motion of the non-autonomous precessing model, and therefore the energy of the system in fact changes, as we observe in the bottom right panel of Fig. 6.18. Let us point out that in this figure the strainlines are associated with an abrupt change of energy.

Figure 6.19 displays the FTLE field and the strainlines for an integration time of $T = [0, 1000]$, and the same spatial domain as in the previous integration for time $T = [0, 505]$ of the non-autonomous problem. While in the integration of the autonomous precessing model both FTLE ridges and strainlines became blurred and separated from heteroclinic orbits when the integration time increased to 1000, here they suffer a much smaller deformation compared to their position for integration time $T = [0, 505]$.

Figure 6.20 presents the strainlines overimposed on the FTLE field (left panel) and

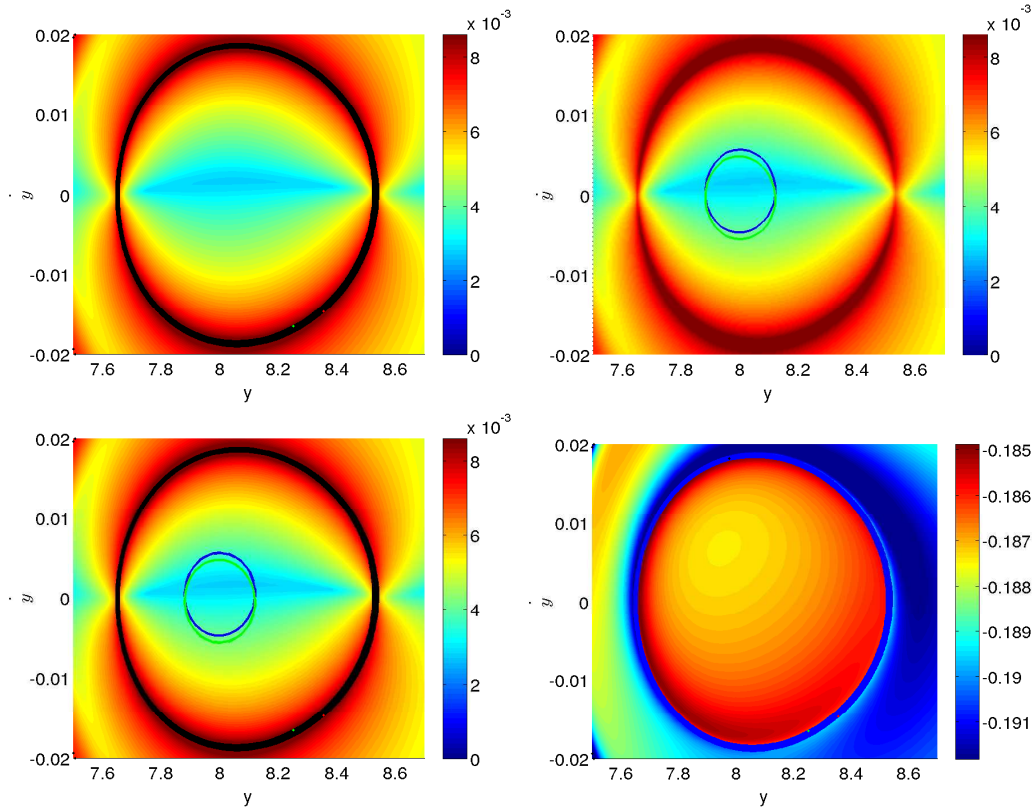

Figure 6.18: Non-autonomous precessing model with tilt angle $\varepsilon = 0$ for time $T = [0, 505]$. Top left: FTLE field and strainlines in black. Top right: FTLE field and heteroclinic orbits of the autonomous precessing model ($W^{s,1}_{\gamma_1}$ in blue, $W^{u,1}_{\gamma_2}$ in green). Bottom left: FTLE field, strainlines (in black) and heteroclinic orbits of the autonomous precessing model (in blue and green). Bottom right: Energy at the endpoint of each orbit.

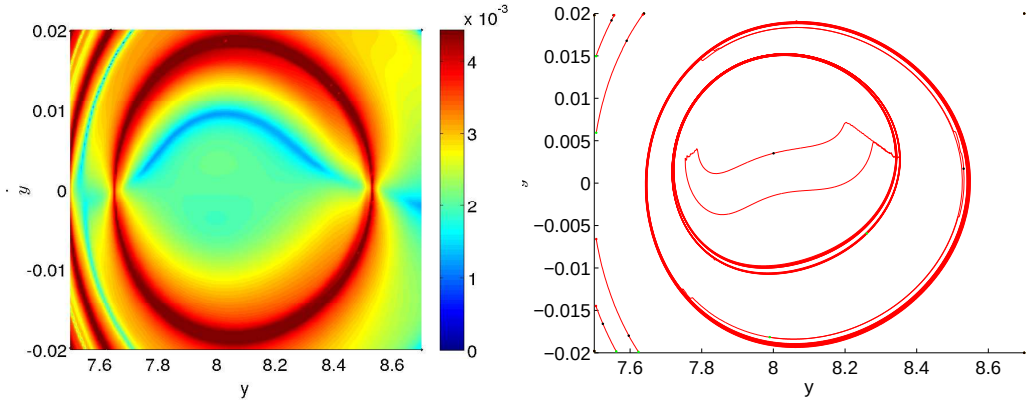

Figure 6.19: FTLE (left) and strainlines (right) of the non-autonomous precessing model with tilt angle $\varepsilon = 0$ for time $T = [0, 1000]$.

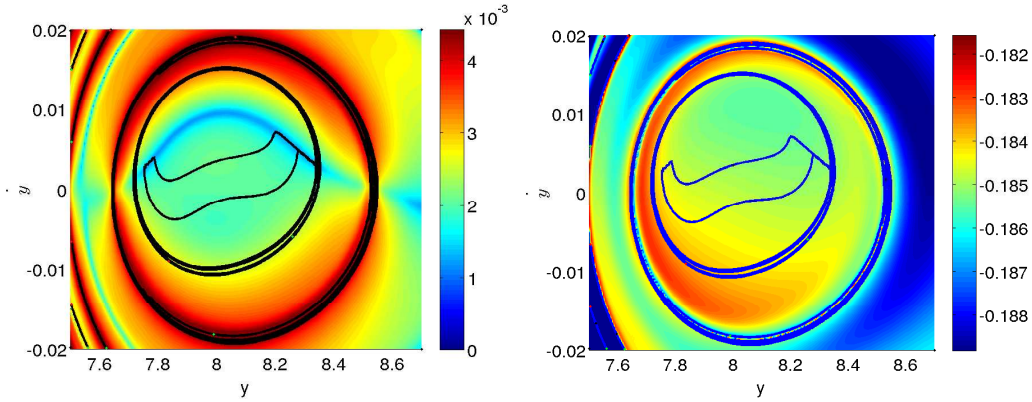

Figure 6.20: Non-autonomous precessing model with tilt angle $\varepsilon = 0$ for time $T = [0, 1000]$. Left: FTLE field and strainlines in black. Right: Energy at the endpoint of each orbit.

overimposed on the final value of the energy in each orbit (right panel). Comparing the results with those of integration time $T = [0, 505]$, we notice that an FTLE ridge-cum-strainline appears for values of y up to 7.7. The main strainlines follow the ridges of the FTLE field, but there is a secondary ring of central strainlines inside the main FTLE ridge that does not correspond to any feature of the FTLE field. In the right panel we observe that the main strainlines coincide with an abrupt variation of the final energy level of each orbit, and the central strainlines are placed over a smoother variation of the final energy level. An isolated central strainline diverging from the inner ring seems an artifice introduced by inaccuracies accumulated over the long integration time.

Figure 6.21 shows the FTLE field and the strainlines for an interval of integration of $T = [0, 1570]$. The distribution of values of the FTLE field is very similar to that of the interval of integration $T = [0, 1000]$. Regarding the strainlines, they cover the ridges of the FTLE field and there is a further inner ring of strainlines inside the main ridge of the FTLE field following a lesser ridge that borders areas of decrease of the FTLE field.

Figure 6.22 illustrates that the behaviour of the strainlines in relation to the final energy of the orbits for integration time $T = [0, 1570]$ is the same as for integration time $T = [0, 1000]$. Therefore, the main rings of strainlines border on the steepest variations of energy level and the inner ring of strainlines also borders on a secondary area of variation of the energy level.

Final Fig. 6.23 shows the strainlines, FTLE field and final energy level for the orbits for a wider parametrised surface in the spatial domain $(y, \dot{y}) \in \Gamma = [7, 9.5] \times [-0.1, 0.1]$, for integration times $T = [0, 505]$ in the left column and $T = [0, 1000]$ in the right column. Looking at the FTLE field and the strainlines (top row) we see that there are more ridges

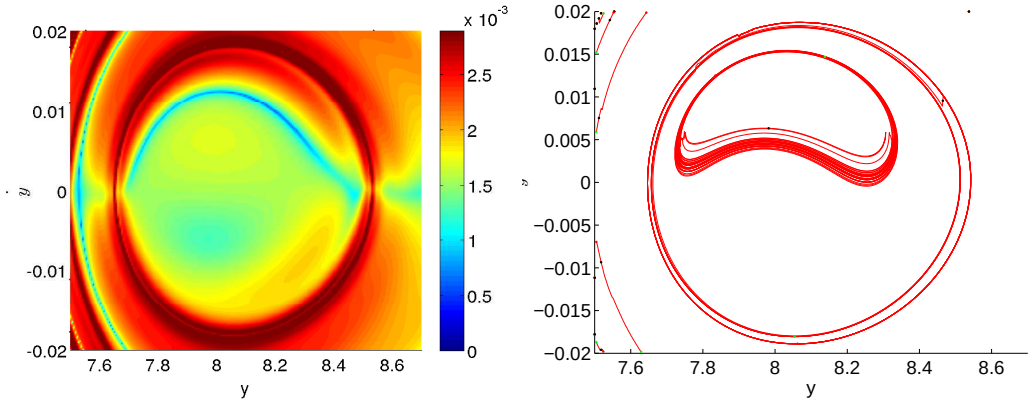

Figure 6.21: FTLE (left) and strainlines (right) of the non-autonomous precessing model with tilt angle $\varepsilon = 0$ for time $T = [0, 1570]$.

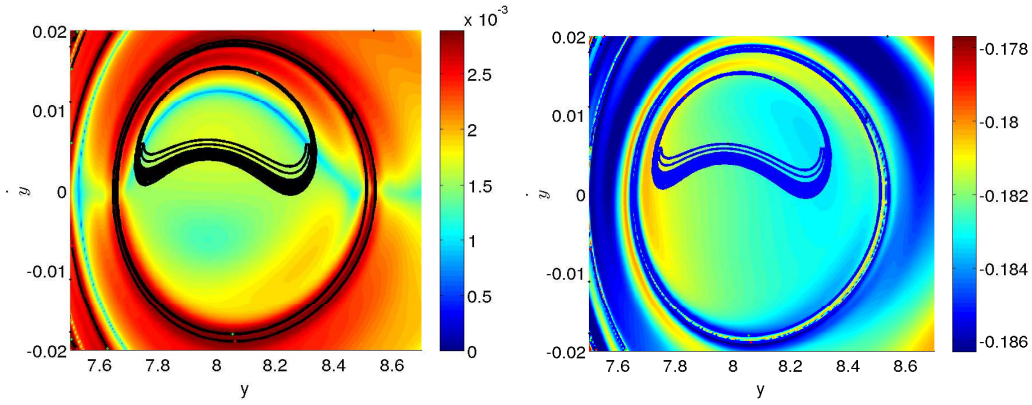

Figure 6.22: Non-autonomous precessing model with tilt angle $\varepsilon = 0$ for time $T = [0, 1570]$. Left: FTLE field and strainlines in black. Right: Energy at the endpoint of each orbit.

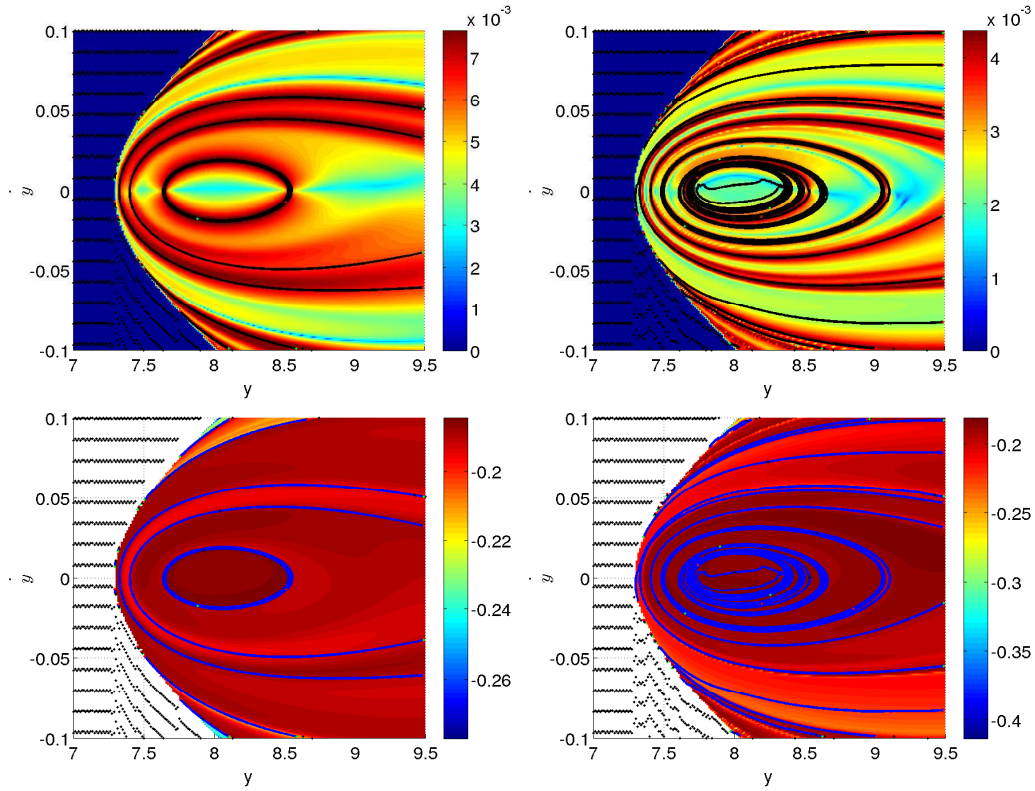

Figure 6.23: Non-autonomous precessing model with tilt angle $\varepsilon = 0$ for time $T = [0, 505]$ and $T = [0, 1000]$. Top: FTLE field and strainlines in black for time $T = [0, 505]$ (left) and $T = [0, 1000]$ (right). Bottom: Energy at the endpoint of each orbit for time $T = [0, 505]$ (left) and $T = [0, 1000]$ (right), and strainlines (in blue).

of the FTLE field and strainlines surrounding the main one seen on the previous figures. A longer integration time leads to the apparition of further features (FTLE ridges and strainlines) of this type. The comparison of the final energy level of the orbits with the strainlines (bottom row) establishes that the strainlines point out curves of steepest variation for the final energy level of the orbits.

To sum up the computations of this section, we can state that FTLE ridges are covered by strainlines, that there appear some further strainlines associated to secondary features of the FTLE field (typically abrupt descents of the field value) and that strainlines in both cases mark curves of steepest descents of the final energy level of the orbits.

Our computations also show that the non-autonomous precessing model presents more stable FTLE field and strainlines than the autonomous version. This greater stability might be due to the energy-dissipative character of our non-autonomous model.

Chapter 7

Conclusions

Although warps are a common feature in galaxies, there is still no agreement on how they are formed. This thesis is based on the fact that spirals and rings in barred galaxies can be driven by the invariant manifolds associated to Lyapunov periodic orbits around the unstable equilibrium points in the rotating bar potential. Here we investigate the effect of tilting the model with respect to the XY plane, i.e. to the rotation axis of the galaxy, which produces a small misalignment between the angular momentum and the angular velocity of the system. Since invariant manifolds behave like tubes transporting matter, we have been able to observe that due to the small misalignment these manifolds reproduce warped shapes such as those observed in warped galaxies, not only qualitatively, but up to such detail as the warp angle. In addition, we have shown the consistency of the model despite its tilting thanks to the periodic orbits inside the bar (around the central equilibrium point), which continue being responsible for the bar structure and constitute its backbone.

The above misalignment is produced in a natural way, when we consider the bar as a rigid body. The relation between the angular momentum and the angular velocity, $\mathbf{L} = \mathbf{I} \cdot \omega$, means that they are aligned only in the case that the three components of the inertia tensor $\mathbf{I}$ are equal. Such a thing can be possible only when a spherical symmetry with uniform density exists. In this case, $\mathbf{I}$ would be proportional to the identity matrix, providing a perfect alignment between the angular momentum and the angular velocity. In our case, the bar is an ellipsoid, so, at least, one of the components of the inertia tensor is different from the others.

There are other theories which seek to explain the formation of warps through a misalignment, but they suppose it is due to the misalignment of the angular momentum between two components of their models. Such theories assume that this misalignment

is produced thanks to the contribution of a third element. In some cases, this element is considered, for example, as an accretion of material due to the cosmic infall (see e.g. Ostriker & Binney, 1989, Jiang & Binney, 1999), possibly aided by dynamical frictions between the components (see e.g. Debattista & Sellwood, 1999). However, our theory does not assume external contributions, since our misalignment is produced between the angular momentum and the angular velocity of a rigid body, something very common in dynamics.

To make sure that our principal results are not model-dependent, we prove our theory with two versions of a precessing bar and disc model: one composed by a bar with revolution symmetry, the other where the bar has just axial symmetry, in addition to a Miyamoto-Nagai disc in both versions. Some considerations have to be made at this point. A bar rotating around its major axis should have revolution symmetry ($b = c$): is this observable? Are all bars rotating, and does this motion form other structures such as bulges? How can we interpret the model given by Pfenniger, where the bar has just axial symmetry ($b \neq c$), when the bar is rotating around itself? In both models, the periodic orbits around the central point L_3 contribute to the backbone of the bar, the family of periodic orbits being qualitatively the same in both cases, and although the shape of the graphs of the stability indexes varies, the range of energies in which the orbits are stable is the same. But the main point is that the invariant manifolds in both models are very similar and acquire the same warped form, in the sense that if we take equal values for the free parameters (bar mass, bar disc, tilt angle and pattern speed) we obtain equivalent warped shapes.

Comparing with observations, we can confirm that the warp angles obtained with this precessing model closely approximate observed warps. We observe that the tilt angle ε, which is responsible for the misalignment between the angular momentum and the angular velocity is also responsible for the warp shape, albeit this also depends to a smaller extent on the pattern speed and bar mass. We show that if the bar mass grows or the pattern speed is faster, the warp angle increases.

In the precessing bar and disc model we tilt all the components of the model, i.e. the bar and the disc, a small angle ε. But a ramification of this theory could be to only tilt the bar, since it is the main component from which the manifolds emerge, we refer to it as the tilted bar model. Although a tilt of the bar only is unlikely in external galaxies, due to the fact that the bar is formed from the particles of the disc as N-body simulations show, we are interested in the study of the behaviour of the model in this case, for a greater understanding of the problem. The periodic orbits inside the bar are obviously the same as the previous ones when $\varepsilon = 0$, and this performance remains with a little tilt of the bar,

up to $\varepsilon = 0.1$ rad. The differences appear for larger values of the tilt angle, which shows the first signs of the low viability of tilting only the bar. The periodic orbits around the central equilibrium point gradually vanish as the tilt angle grows, and those that remain are seriously deformed and do not give structure to the model, that is, they do not form the backbone of the system. The next step is to study the arrangement of the invariant manifolds. But, whereas in the previous model there are only two unstable equilibrium points at the ends of the bar, this configuration is lost at early stages, from $\varepsilon = 0.1$ rad, in the tilting bar model. Two more unstable points appear, making the invariant manifolds acquire configurations not seen in external galaxies. Therefore, a model where only the bar is tilted with respect to the other components is not plausible from the point of view of the invariant manifolds, reinforcing the results obtained in N-body simulations and seen in observations.

Carrying on with the question of the dependency on the model, we add a third component to the first model, the precessing disc and bar model, to show if warps survive. This third component is a halo, whose presence is clear in galaxies due to its influence in making the rotation curve flat. We study how the existence of a halo affects the shape of the invariant manifolds. To begin with, let us point out that the position of the equilibrium points varies with the presence or absence of the halo, and with its mass. But the behaviour of these points does not change: the two equilibrium points at the ends of the bar continue being unstable, whereas the rest remain stable. As for the invariant manifolds, the halo affects to a greater extent the inner than the outer branches of the invariant manifolds. An increase of the mass of the halo makes the inner branches join and the outer ones become more open, while if its mass decreases the inner branches open up forming a ring and the outer branches slowly close. The halo also influences the formation of warps, favouring the apparition of a larger warp angle. In addition, the presence of the halo increases the length of the warps, less so as the mass of the halo decreases or, equivalently, when the slope of the rotation curve becomes smaller.

To sum up conclusions about the formation of warps, we can confirm that a misalignment between the angular momentum and the angular velocity of the bar produces warped galaxies as those seen in observations. A simple model composed by a bar and a disc, seen from suitable viewpoints, already shows the shape of warps in its invariant manifolds with warp angles close to the values observed in external galaxies. Adding a halo to this model, warped shapes are present in all the cases studied, whenever the tilt angle of the model is greater than zero, as in the previous precessing bar and disc model. The bigger warp angles have been obtained with the maximal halo mass and the greatest pattern speed considered. But, above all, the bigger warp angles occur with the greatest tilt angle of the system. Let us remark that this tilt angle has been taken with a maximal

value of $\varepsilon = 0.2$ rad, which is not a wide angle, and it is not possible to take greater values because the system loses its stability. This fact is due to that, indeed, the bar is not a rigid body and therefore the tilt angle must be small in order for the bar and disc to remain together during the precession. Thus our study concludes that the stability of the galactic system limits tilt angles, and in consequence produces warp angles also limited to the $0^\circ - 12.3^\circ$ range. This is the range of warp angles found by astronomical observation, so the invariant manifold method provides an explanation not only for warps but also for their observed magnitude.

Next, we apply the theory of the invariant manifolds to the formation of four-armed galaxies. Double-barred galaxies have been clearly observed, but its relation with galaxies with four arms is not so clear. One of these galaxies is the Milky Way itself, but despite being there in, its morphology is not clear at all. Recent observations have detected two bars in our galaxy, one also referred to as a triaxial bulge, but observations suggest two other structures in its inner parts as well. Nevertheless, our study does not center in the configuration of the Milky Way. We make a general enquiry with several bar sizes, in order to try finding a structure with four spiral arms. Several options for the configuration of the model have been tested, but the results are not satisfactory. Considering a wide range of separation angles between two bars, from almost coincident to perpendicular, we study the performance of the equilibrium points when the size, mass, density or pattern speed of the bars vary.

Applying the theory of the invariant manifolds, the possibility of four spiral arms appearing is related to the existence of four unstable equilibrium points. Four unstable points only exist when the two bars are well separated. Two perpendicular bars always yield this number of unstable points, but as the separation angle decreases the rest of parameters considered gain importance. The fact that one bar is bigger than the other, either in size, mass or density, considerably affects the position of the equilibrium points, since they are attracted to the bigger bar. Already at early stages of inequality the configuration of four unstable equilibrium points is lost. The pattern speed of the bars also influences this configuration. The minimal separation angle between bars at which we obtain four unstable points is $\theta = 0.77$ rad when the pattern speed reaches its maximal value $\Omega = 0.06$, and when the bars are symmetrical.

Although two bars so separated are unlikely, we study the invariant manifolds formed in this configuration and the results are still unpromising. The dynamics of these invariant manifolds, one from each unstable equilibrium point, are locally different from those previously studied due to the apparition of new stable equilibrium points, but globally have similar characteristics. Consequently, we consider that the four spiral arms appearing in

some galaxies are not closely related to the morphology of a double-barred galaxy, but either require at least other elements, such as a complex potential with an outer spiral component, or the time evolution plays an important role.

The last chapter of this thesis deals with the study of the non-autonomous version of the precessing model in 2 dimensions by means of the Lagrangian Coherent Structures (LCS). This is a recently developed theory to find out dynamical structures, either attracting or repelling, reflecting the dynamics of the system in non-autonomous problems. To apply this theory to our precessing model we have created our own LCS computation software, made as accurate and efficient as possible, and capable of computing LCS in general 2-dimensional dynamical systems and in parametrized surfaces in dynamical systems of any dimension. The LCS are based on the singular values and vectors of the Jacobian of the flow, equivalent to the eigenvalues and the eigenvectors of the Cauchy-Green tensor. In particular, the Finite Time Lyapunov Exponent (FTLE) field is determined by the main singular value, i.e. the norm, of the Jacobian of the flow. These LCS give us the repulsion and attraction zones. In 2-dimensional domains, we obtain strainlines and stretchlines which are the maximally repelling or attracting lines, respectively. Whereas for the strainlines we have found that they give us relevant information about the dynamics of the system, the strecthlines have turned out to be more ill-conditioned and less connected to the global dynamics of the system. Let us also remark that the LCS must be applied to "smooth problems", in the sense that the problems have no abrupt changes in its behaviour, since the computation of the flow Jacobian and, above all, of the stretchlines, is very sensitive to sudden variations of the integrated vector field.

We first apply the LCS to the well known pendulum problem in order to validate our software. In its autonomous version, the ridges of the norm of the flow Jacobian and the strainlines are the invariant manifolds. In its non-autonomous version, adding a small perturbation depending on time, the ridges of the norm of the flow Jacobian and the strainlines are perturbations of the invariant manifolds, and they play an analogous role in organizing the dynamics of the system.

In order to better understand the information given by the FTLE field and the LCS, we apply it to the autonomous precessing model. Selecting a parametrized surface given by the energy of the system in one of the equilibrium points (L_1 or L_2), and initial conditions in the $(y, \dot{y})$ plane, we obtain that the flow Jacobian norm field points to the zones where the stable invariant manifold is placed, and the strainlines accurately overlap with this stable manifold. As the integration time increases, the unavoidable build up of error in the computation of the flow causes it to lose precision in the related flow Jacobian norm field and therefore in the strainline computations, but these still approximate the related

stable manifolds. Moreover, the flow Jacobian norm field and the LCS give information about other zones of maximal repulsion placed in a bigger spatial domain, which seem to correspond to invariant manifolds caused by other structures.

But the main point of this final chapter is a first approach to finding the behaviour of our precessing model in its non-autonomous version. This version is a small perturbation of the autonomous problem, making the pattern speed of the system decrease slightly, and linearly on time. The way of dealing with the problem is the same as in the autonomous one, although the energy is not preserved in this version. Selecting the same time intervals of integration as previously, we observe that the flow Jacobian norm field and the strainlines continue remarking the zones of maximal repulsion, with a shape analogous to the previous stable invariant manifold, but now somewhat wider. In this non-autonomous precessing model, the flow Jacobian norm field and the strainlines are not distorted as the integration time increases. This stronger stability may be a consequence of the energy-dissipative character of the selected model. In addition, the other zones of maximal repulsion found in the autonomous problem continue existing in this time-dependent model, but now we observe that these zones are placed where a steepest change on the energy of the system occurs.

7.1 Future work

In this thesis we have satisfactorily explained the formation of warps through the study of the invariant manifolds in the dynamical system defined by the motion equations of a precessing model describing a barred galaxy. We have concentrated on the formation of S-shaped warps, by means of a potential composed by a Ferrers bar, a Miyamoto-Nagai disc and optionally a Plummer spheroid. The other types of warps observed in galaxies, namely U-shaped and L-shaped warps, ought to admit an explanation of their origin and shape by the same method, studying the invariant manifolds of the dynamical system defined by suitable potentials reflecting the asymmetry in the mass distributions of such galaxies.

Another problem studied in this work is the existence of galaxies with four spiral arms. We have found that the development of four spiral arms in a galaxy is not closely related to the presence of two bars in it. An alternative line of study for this problem could be to work with more complex potentials, with outer elements such as a spiral parts. Another possibility would be to continue studying the precessing of the model when some of its components are slightly tilted in a physically plausible way and inducing four unstable equilibrium points in the resulting dynamical system. However, it is also possible that the

occurrence of four spiral arms in a galaxy depends on non-autonomous (time-dependent) features of the galaxy. The study of such non-autonomous systems requires tools going beyond the invariant manifolds of autonomous dynamical systems, such as Lagrangian Coherent Structures (LCS) and Finite Time Lyapunov Exponent (FTLE) fields.

After our ground study of non-autonomous versions of the precessing model of a galaxy by means of LCS and FTLE fields, the next natural steps would be to develop non-autonomous potentials that match more closely the physical properties of observed galaxies, and to find the LCS in the entire phase space of any dimension rather than just their intersection with strategically placed surfaces. This will require the extension of the LCS and FTLE field computation software package developed in this thesis from parametrized surfaces in a phase space of any dimension to the phase space itself. The algorithm used in the package extends readily to higher dimensions, but this extension is much more computationally expensive.

Bibliography

Abraham, R., Marsden, J. E., Ratiu, T. S., 1988, *Manifolds, tensor analysis, and applications*, Springer, Berlin.

Antoja, T., Figueras, F., Romero-Gómez, M., Pichardo, B., Valenzuela, O., Moreno, E. 2011, *Understanding the spiral structure of the Milky Way using the local kinematic groups*, MNRAS, 418, 1423.

Arnold, V. I., 1989, *Mathematical methods of classical mechanics*, Graduate Texts in Mathematics, Vol. 60, Springer, New York.

Athanassoula, E., 1992, *Morphology of barred orbits*, MNRAS, 259, 328.

Athanassoula, E., Martinet, L., 1980, *A correlation between the lengths of bars and the sizes of bulges*, A&A, 87, 10.

Athanassoula, E., Bienaymé, O., Martinet, L., Pfenniger, D., 1983, *Orbits as building blocks of a barred galaxy model*, A&A, 127, 349.

Athanassoula, E., Machado, Rubens E. G., Rodionov, S. A., 2013, *Bar formation and evolution in disc galaxies with gas and a triaxial halo: morphology, bar strength and halo properties*, Mon. Not. R. Astron. Soc., 429, 1949.

Athanassoula, E., Romero-Gómez, M., Masdemont, J.J., 2009, *Rings and spirals in barred galaxies - I. Building blocks*, Mon. Not. R. Astron. Soc., 394, 67.

Benjamin, R. A., et al., 2005, *First GLIMPSE Results on the Stellar Structure of the Galaxy*, ApJ, 630, L149.

Binney, J., Gerhard, O., Spergel, D., 1997, *The photometric structure of the inner Galaxy*, MNRAS, 288, 365.

Binney J., Jiang I.-G., Dutta S., 1998, *The persistence of warps in spiral galaxies with massive haloes*, MNRAS, 297, 1237.

Binney, J., Tremaine, S., 2008, *Galactic Dynamics, Second Edition, Princeton Univ. Press*, Princeton.

Bosma, A. 1981, *21-cm line studies of spiral galaxies. I - Observations of the galaxies NGC 5033, 3198, 5055, 2841, and 7331. II - The distribution and kinematics of neutral hydrogen in spiral galaxies of various morphological types*, AJ, 86, 1791.

Briggs F. H., 1990, *Rules of behavior for galactic warps*, ApJ, 352, 15.

Buta, R., 1995, *The catalogue of southern ringed galaxies*, ApJS, 96, 39.

Buta, R., Crocker, D., 1992, *Integrated photometric properties of early-type ringed galaxies*, AJ, 103, 1804.

Buta, R., Crocker, D., 1993, *Metric characteristics of nuclear rings and related features in spiral galaxies*, AJ, 105, 1344.

Combes, F., 1994, *How Galaxies Accrete Mass and Evolve: Spiral Waves and Bars, Warps and Polar Rings*, in Muñoz-Tuñón, C. and Sánchez, F.,eds., *The Formation and Evolution of Galaxies, Cambridge University Press, Cambridge*, p. 317.

Combes, F., Sanders, R.H., 1981, *Formation and properties of persisting stellar bars*, A&A, 96, 164.

Combes, F., Boissé, P., Mazure, A., Blanchard, A., 1995, *Galaxies and cosmology*, Springer-Verlag, Berlin Heidelberg.

Contopoulos, G., 1980, *How far do bars extend?*, A&A, 81, 198.

Contopoulos, G., 1981, *The effects of resonances near corotation in barred galaxies*, A&A, 102, 265.

Cox A. L., Sparke L. S., van Moorsel G., Shaw M., 1996, *Optical and 21 CM Observations of the Warped, Edge-On Galaxy UGC 7170*, AJ, 111, 1505.

de Jong, R. S., 1996, *Near-infrared and optical broadband surface photometry of 86 face-on disk dominated galaxies. III. The statistics of the disk and bulge parameters*, A&A, 313, 45.

de Vaucouleurs, G. 1959, *Classification and morphology of external galaxies*, Handb. der Phys., 53, 275.

de Vaucouleurs, G., Buta, R., 1980, *Diameters of nuclei, lenses, and inner and outer rings in 532 galaxies*, AJ, 85, 637.

Debattista, V.P., Sellwood, J.A.,1999, *Warped Galaxies from Misaligned Angular Momenta*, The Astrophisical Journal, 513, 107110.

Debattista, V., Shen, J., 2007, *Long-lived Double-barred Galaxies from Pseudobulges*, ApJ, 654, L127.

Dehnen, W.,2000, *The Effect of the Outer Lindblad Resonance of the Galactic Bar on the Local Stellar Velocity Distribution*, The Astronomical Journal, 119, 800-812.

Duval, M.F., Athanassoula, E., 1983, *Photometry, kinematics, and dynamics of the barred spiral galaxy NGC 5383*, A&A, 121, 297.

Erwin, P., Sparke, L., 2003, *An imaging survey of early-type barred galaxies*, ApJS, 146, 299.

Eskridge, P.B., Frogel, J.A., Podge, R.W., Quillen, A.C., Davies, R.L., DePoy, D.L., Houdashelt, M.L., Kuchinski, L.E., Ramírez, S.V., Sellgren, K., Terndrup,D.,M., Tiede, G.P. 2000, *The frequency of barred spiral galaxies in the near-infrared*, AJ, 119, 536.

Farazmand, M., Haller, G., 2012, *Erratum and addendum to "A variational theory of hyperbolic Lagrangian coherent structures"*, Physica D, 241, 439.

Farazmand, M., Haller, G., 2012,, *Computing Lagrangian coherent structures from their variational theory*, Chaos, 22, , 013128.

Farazmand, M., Haller, G., 2013,, *Attracting and repelling Lagrangian coherent structures from a single computation*, Chaos, 23, , 023101.

Farazmand, M., Blazevski, D., Haller, G., 2014, *Shearless transport barriers in unsteady two-dimensional flows and maps*, Physica D, 278, 44.

Ferrers, N. M. 1877, *On the potentials of ellipsoids, ellipsoidal shells, elliptic laminae and elliptic rings of variable densities*, Q.J. Pure Appl. Math., 14, 1.

Fux, R., 2001, *Order and chaos in the local disc stellar kinematics induced by the Galactic bar*, A& A, 373, 511.

García-Ruiz, I., Sancisi, R., Kuijken, K., 2002, *Neutral hydrogen and optical observations of edge-on galaxies: Hunting for warps*, A&A, 394, 769.

Gardner, E., Flynn, C., 2010, *Probing the Galaxy's bars via the Hercules stream*, MNRAS, 405, 545.

Garzón, F., López-Corredoira, M., 2014, *Dynamical evolution of two associated galactic bars*, arXiv:1409.1916, to appear in AN.

Gawlik, E. S., Marsden, J. E., Du Toit, P. C., Campagnola, S, 2009, *Lagrangian coherent structures in the planar elliptic restricted three-body problem*, Celestial mechanics and dynamical astronomy, 103, 227.

Giovanelli, R., Haynes, M., 1988, *Extragalactic neutral hydrogen* in Verschuur, Gerrit L., Kellermann, Kenneth I (eds.) *Galactic and extra-galactic radio astronomy, Berlin, Springer, Second Edition.*

Golub, G. H., Van Loan, C. F., 2012, *Matrix computations*, *3rd Ed., JHU Press*, London.

Gómez, G., Koon, W.S., Lo, M.W., Marsden, J.E., Masdemont, J.J., Ross, S.D., 2004, *Connecting orbits and invariant manifolds in the spatial restricted three-body problem*, Nonlinearity, 17, 1571.

Guckenheimer, J., Holmes, P., 1986, *Nonlinear oscillations, dynamical systems, and bifurcations of vector fields*, *Second edition, Springer-Verlag*, NY.

Haller, G., 2001, *Distinguished material surfaces and coherent structures in three-dimensional fluid flows*, Physica D, 149, 248.

Haller, G., 2011, *A variational theory of hyperbolic Lagrangian coherent structures*, Physica D, 240, 574.

Hand, L., Finch, J., 1998, *Analytical mechanics*, Cambridge University Press, Cambridge.

Hernquist, L., 1993, *N-body realizations of compound galaxies*, ApJS, 86, 389.

Hubble, E.P., 1958, *The realm of nebulae*, Dover Publications Inc.

Hunter C., Toomre A., 1969, *Dynamics of the bending of the Galaxy*, ApJ, 155, 747.

Jiang, I. G., Binney, J., 1999, *Warps and cosmic infall*, MNRAS, 303, L7.

Kormendy, J., 1982, in Morphology and Dynamics of galaxies, 12th SAAS-FEE Course. Ed. by Martinet, L. and Mayor, M. Geneva Observatory, p. 115-270.

Lekien, F., Shadden, S. C., Marsden, J. E., 2007, *Lagrangian coherent structures in n-dimensional systems*, Journal of Mathematical Physics, 48, 065404.

Levine E. S., Blitz L., Heiles C., 2006, *The vertical structure of the outer Milky Way HI disk*, ApJ, 643, 881.

López-Corredoira, M., Betancort-Rijo, J., Beckman, J.E., 2002, *Galactic disc warps due to intergalactic accretion flows onto the disc*, Astronomy and Astrophysics, 386, 169186.

López-Corredoira, M., Cabrera-Lavers, A., Mahoney, T. J., Hammersley, P. L., Garzón, F., González-Fernández, C., 2007, *The Long Bar in the Milky Way: Corroboration of an Old Hypothesis*, AJ, 133, 154.

Lynden-Bell D., 1965, *Free precession for the galaxy*, MNRAS, 129, 299.

Lynden-Bell, D., 1979, *On a mechanism that structures galaxies*, MNRAS, 187, 101.

Maciejewski, W., Athanassoula, E., 2007, *Regular motions in double bars - I. Double-frequency orbits and loops*, MNRAS, 380, 999.

Maciejewski, W., Sparke, L. S., 2000, *Orbits supporting bars within bars*, MNRAS, 313, 745.

Masdemont, J., Mondelo J.M., 2004, *Notes for the Numerical and Analitycal Techniques Lectures*, in Advanced Course in Astrodynamics, Barcelona.

Miller, R.H., Smith, B.F., 1979, *Dynamics of a stellar bar*, ApJ, 227, 785.

Minchev, I., Boily, C., Siebert, A., Bienaymé, O. 2010, *Low-velocity streams in the solar neighbourhood caused by the Galactic bar*, MNRAS, 407, 2122.

Miyamoto, M., Nagai, R. 1975, *Three-dimensional models for the distribution of mass in galaxies*, PASJ, 27, 533.

Onu, K., Huhn, F., Haller, G., 2014, *LCS Tool : A Computational Platform for Lagrangian Coherent Structures*, preprint, arXiv:1406.3527 [nlin.CD].

Ostriker, E. C., Binney, J., 1989, MNRAS, *Warped and tilted galactic discs*, 237, 785.

Papayannopoulos, T., Petrou, M., 1983, *On the nature of orbits in realistic bar potentials*, A&A, 119, 21.

Patsis, P., Skokos, Ch., Athanassoula, E., 2003, *Orbital dynamics of threedimensional bars - IV. Boxy isophotes in face-on views*, MNRAS, 342, 69-78.

Pfenniger, D., 1984, *The 3D dynamics of barred galaxies*, A&A, 134, 373.

Read, J. I., Lake, G., Agertz, O., Debattista, V. P., 2008, *Thin, thick and dark discs in* ΛCDM, MNRAS, 389, 1041.

Reshetnikov, V., Combes, F., 1998, *Statistics of optical warps in spiral disks*, A&A, 337, 9-16.

Revaz, Y., Pfenniger D., 2001, *Periodic orbits in warped disks*, A&A, 372, 784-792.

Revaz, Y., Pfenniger D., 2004, *Bending instabilities at the origin of persistent warps: A new constraint on dark matter halos*, A&A, 425, 67.

Romero-Gómez, Athanassoula, E., M., Masdemont, J.J., García-Gómez, C., 2007, *The formation of spiral arms and rings in barred galaxies*, A&A, 472, 63.

Romero-Gómez, M., Athanassoula, E., Antoja, T., Figueras, F., 2011, *Modelling the inner disc of the Milky Way with manifolds - I. A first step*, MNRAS, 418, 1176.

Romero-Gómez, M., Masdemont, J.J., Athanassoula, E., García-Gómez, C., 2006, *The origin of rR_1 ring structures in barred galaxies*, A&A, 453, 39.

Romero-Gómez M., Figueras, F., Antoja, T., Abedi, H., Aguilar, L., 2015, *The analysis of realistic stellar Gaia mock catalogues - I. Red clump stars as tracers of the central bar*, MNRAS, 447, 218.

Rubin, V. C., Burstein, D., Ford, W. K., Jr., Thonnard, N., 1985, *Rotation velocities of 16 SA galaxies and a comparison of Sa, Sb, and SC rotation properties*, ApJ, 289, 81.

Sánchez-Saavedra, M. L., Battaner, E., Florido, E., 1990, *Frequency of warped spiral galaxies at visible wavelengths*, MNRAS, 246, 458.

Sánchez-Saavedra, M. L., Battaner, E., Guijarro, A., López-Corredoira, M., Castro-Rodríguez, N., 2003, *A catalog of warps in spiral and lenticular galaxies in the Southern hemisphere*, A&A 399, 457.

Sellwood, J.A., 1980, *Galaxy models with live halos*, A&A, 89, 296.

Sellwood, J.A., 1980, *Bar instability and rotation curves*, A&A, 99, 362.

Sellwood J. A., 2013, *Dynamics of Disks and Warps*, in Oswalt T. D., Gilmore G., eds., *Planets, Stars and Stellar Systems Vol. 5, Springer, Dordrecht*, p. 923.

Shadden, S. C., Lekien, F.; Marsden, J. E., 2005, *Definition and properties of Lagrangian coherent structures from finite-time Lyapunov exponents in two-dimensional aperiodic flows*, Physica D, 212, 271.

Shen, J., Debattista, V., 2009, *Observable Properties of Double-Barred Galaxies in N-Body Simulations*, ApJ, 690, 758.

Shen, J., Sellwood, J.A.,2006, *Galactic warps induced by cosmic infall*, Mon. Not. R. Astron. Soc. 370, 214.

Simó, C., 1990, *Les Méthodes Modernes de la Mécanique Céleste*, D. Benest and C. Froeschlé, eds., *Editions Frontiéres, Paris*, p. 285-329.

Skokos, Ch., Patsis, P.A., Athanassoula, E., 2002, *Orbital dynamics of three-dimensional bars. I - The backbone of three-dimensional bars*, MNRAS, 333, 847.

Sparke L. S., Casertano S., 1988, *A model for persistent galactic warps*, MNRAS, 234, 873.

Sparke L. S., Gallagher, J. S., 2000, *Galaxies in the Universe*, Cambridge University Press, Cambridge, UK.

van Albada, T.S., Sanders, R.H., 1982, *Periodic orbits and gas flow in barred spirals*, MNRAS, 201, 303.

Widrow, L. M., Pym, B., Dubinski, J., 2008, *Dynamical blueprints for galaxies*, ApJ, 679, 1239.